Scuola Normale Superiore
Classe di scienze matematiche e naturali

Tesi di perfezionamento in fisica
(PhD thesis)

Search for time-dependent CP violation in $D^0 \to K^+K^-$ and $D^0 \to \pi^+\pi^-$ decays

Candidate:
Tommaso Pajero

Advisor:
Dr. Michael J. Morello

Academic year 2020–2021

Abstract

A search for time-dependent violation of the charge-parity (CP) symmetry in $D^0 \to K^+K^-$ and $D^0 \to \pi^+\pi^-$ decays is performed at the LHCb experiment using proton–proton collision data recorded in 2015–2018 at a centre-of-mass energy of 13 TeV, corresponding to an integrated luminosity of $5.7\,\text{fb}^{-1}$. The D^0 meson is required to originate from $D^*(2010)^+ \to D^0\pi^+$ decays, such that its flavour at production is identified by the charge of the pion meson. The slope of the time-dependent asymmetry of the decay rates of D^0 and $\overline{D}^0$ mesons, ΔY, into the final states under consideration is measured to be

$$\Delta Y_{K^+K^-} = (-2.3 \pm 1.5 \pm 0.3) \times 10^{-4},$$
$$\Delta Y_{\pi^+\pi^-} = (-4.0 \pm 2.8 \pm 0.4) \times 10^{-4},$$

where the first uncertainties are statistical and the second are systematic. Neglecting possible final-state dependent contributions, these results are combined yielding

$$\Delta Y = (-2.7 \pm 1.3 \pm 0.3) \times 10^{-4},$$

which is compatible with the CP-invariance hypothesis at the level of 2σ. This result improves by nearly a factor of two on the precision of the world average of the parameter A_Γ, which is approximately equal to the negative of ΔY. Thus, it sets the strongest bound on the value of the phase ϕ_2^M, which parametrises dispersive CP-violating contributions to D^0-meson mixing.

Contents

Introduction

Therefore, let us not undervalue small signs; perhaps by means of them we will succeed in getting on the track of greater things. I agree with you that the larger problems of the world and of science have the first claim on our interest. But it is generally of little avail to form the definite resolution to devote oneself to the investigation of this or that problem. Often one does not know in which direction to take the next step. In scientific research it is more fruitful to attempt what happens to be before one at the moment and for whose investigation there is a discoverable method. If one does that thoroughly without prejudice or predisposition, one may, with good fortune, and by the virtue of the connection which links each thing to every other (hence also the small to the great) discover even from such modest research a point of approach to the study of the big problems.

— Sigmund Freud, *Introduction to Psychoanalysis*

The attempt to understand and organize the various and apparently chaotic complex of natural phenomena that surround us, and shape our lives by determining the possibilities and the limits of our field of action, is among the most ancient and urgent aspirations of mankind. Since the very birth of Greek philosophy, one of the main directions of this quest has been that of establishing what are the basic constituents of the Universe and the laws that govern the interactions among them. The Standard Model of particle physics (SM), a theory able to describe all phenomena observed to date in laboratory except for gravity, is the latest and most advanced product of this thousand-year old progress in understanding. Yet, few years after the crowning of its success by the discovery of the last of its predicted particles — the Higgs boson —, achieved at the Large Hadron Collider of Geneva in 2012, the SM is in a rather awkward position. Despite its success in describing a wealth of experimental results to an amazing level of precision, its building blocks account for less than 5% of the energy of the Universe and are not able to explain fundamental astrophysical and cosmological observations. In particular, the SM provides no hints about what might be the nature of Dark Matter, the invisible massive substance that is known to be 5–to–6 times more abundant than ordinary matter, but has never been observed directly in laboratory; nor that of Dark Energy, the mysterious form of energy that is believed to make up the remaining 70% or the Universe energy budget. Finally, it leaves without explanation the much larger abundance of matter over antimatter in the Universe, commonly known as baryonic asymmetry. These are only some of the reasons that suggest that the SM will not be the final word on our understanding of fundamental interactions.

Two kinds of experimental projects are currently pursued to overcome this impasse. On one hand, direct searches try to produce new particles or to measure the interactions of Dark

Matter particles passing though the Earth with ordinary particles. On the other hand, precision measurements of known phenomena are performed to highlight possible deviations from the SM predictions due to new interactions. The second approach, which has contributed in a crucial way to give shape to the current formulation of the SM and is sensitive to the existence of particles much heavier than those that can currently be produced at particle colliders, is the one pursued in this thesis.

The noninvariance of fundamental interactions under the combined charge conjugation (C) and parity (P) transformations, commonly named CP violation, is a required condition to explain the much larger abundance of matter with respect to antimatter in the Universe [1]. Within the SM, the weak interaction provides a source of CP violation, namely a single complex phase in the Cabibbo–Kobayashi–Maskawa (CKM) matrix that governs the interaction of quarks with the W boson [2, 3]. However, while the CKM mechanism has been tested successfully in the decay of down-type quarks in K and B mesons [4–12], it is too small to explain the observed matter–antimatter asymmetry [13], suggesting the existence of additional sources of CP violation beyond the SM.

Charm hadrons are the only particles where CP violation and flavour-changing neutral currents (FCNC) involving up-type quarks can be studied, and provide a unique opportunity to detect new interactions beyond the SM that leave down-type quarks unaffected [14]. Both CP violation and FCNC are predicted to be extremely suppressed for charm hadrons within the SM, implying sensitivity to higher energy scales with respect to those achievable with beauty hadrons [15, 16]. In particular, the combination of CKM matrix elements responsible for CP violation in charm decays is $\mathrm{Im}(V_{cb}V_{ub}^*/V_{cs}V_{us}^*) \approx -6 \times 10^{-4}$, corresponding to CP asymmetries typically of the order of 10^{-4} to 10^{-3} [14]. Processes involving FCNC, like the quantum oscillation of a D^0 meson (made up of a $c\overline{u}$ quarks pair) into its $\overline{D}^0$ antiparticle companion, known as mixing, are similarly predicted to happen less than 1 time in 10^4.

Therefore, precision studies of these phenomena require the collection and analysis of a huge number of decays. This has become possible only during the last two decades, which witnessed a renaissance of charm-quark physics thanks to the activities of the Belle, BaBar and CDF experiments. A further, decisive leap forward has been allowed by the start of operations of the LHCb experiment in 2010. Thanks to the huge $c\overline{c}$ production cross-section at the Large Hadron Collider where it is installed, this experiment collected the largest sample ever produced of charm-hadron decays and provided a wealth of results in the field, including the first single-experiment observation of D^0-meson mixing in 2012 [17] and the first observation of CP violation in the decay of D^0 mesons in 2019 [18]. Despite these successes, the experimental potential of the LHCb experiment has not exploited at full yet, and additional investigations are crucial to solve open theoretical puzzles. In particular, theoretical uncertainties on low-energy strong-interaction effects do not allow a rigorous assessment of the compatibility of the observation of CP violation with the SM [19–27]. Complementary searches for time-dependent CP violation in charm-hadron decays [28, 29], which has not been observed so far, might help clarify the picture and determine whether LHCb has discovered a new fundamental interaction or if the observation is due to an enhancement of strong interaction effects above the expectation.

This thesis reports the most precise measurement to date of the parameter ΔY, that is the slope of the time-dependent asymmetry of the decay rates of D^0 and $\overline{D}^0$ mesons into K^+K^- or $\pi^+\pi^-$ final states, performed by employing the data collected by the LHCb experiment during 2015–2018. The result achieves the unprecedented precision of 1.3×10^{-4}, at the upper edge of the SM expectations, and allows to improve the precision on the world average of ΔY by nearly a factor of two. Thus, it sets the strongest bound on the value of the phase ϕ_2^M, which parametrises dispersive CP-violating contributions to D^0-meson mixing. In addition, it provides a crucial input to the determination of CP violation in the D^0-meson decay amplitude into the final state K^+K^-, based on the measurements of the time-integrated CP asymmetry of $D^0 \to K^+K^-$ decays that are performed at the LHCb experiment [30]. The text is structured as follows. Chapter 1 details the theoretical formalism and the predictions for the size of mixing and CP violation in two-body D^0 decays, including the first explicit calculation of the $D^0 \to K^-\pi^+$ decay rate as a function of time. The decay-rate deviation from an exponential function, while smaller than that of the Cabibbo-suppressed decays $D^0 \to K^+K^-$ and $D^0 \to \pi^+\pi^-$, cannot be completely neglected. In fact, it is shown to bias significantly most of the measurements of the y_{CP} parameter performed to date, as detailed in Chap. 2. This chapter describes the experimental status of the searches for CP violation in charm-hadron decays, and concludes by summarising the analysis procedure of the measurement of ΔY. This is detailed in Chaps. 4–8 after a brief sketch of the experimental apparatus in Chap 3. Finally, Chap. 9 concludes by presenting the final results, their impact on the world average of the parameters quantifying mixing and CP violation in charm-hadrons decays, and the prospects for the development of the field thanks to the upgrade of the LHCb experiment that is foreseen in the next few years.

Chapter 1

CP violation in charm-quark decays

This chapter briefly describes the origin and phenomenology of CP violation in the Standard Model of particle physics, and its relation with the phenomenon of mixing of neutral flavoured mesons. The discussion is focused on the charm quark, whose unique features are highlighted in contrast with the strange and beauty mesons, where CP violation has been discovered and thoroughly studied. A detailed description of the decays of D^0 mesons into two charged hadrons, which are the subject of this thesis and provide a privileged experimental access to charm CP violation parameters, concludes this brief theory overview. The last section includes expressions for the time-dependent decay rates of $D^0 \to K^-\pi^+$ decays that had never been shown in literature before, but are an essential input to the measurement subject of this thesis.

The *CP* transformation is defined as the combination of the charge conjugation (C) and the parity (P) transformations, where the first reverses the sign of all particles internal quantum numbers and the second the direction of the Cartesian axis and, consequently, the handedness of the spatial coordinates. These two transformations have separately been considered exact symmetries of fundamental interactions for a long time. No evidence of P- or C-symmetry violation in electromagnetic or strong interactions has been found to date. However, in 1956 the weak interaction was shown to violate the P and C symmetries in the strongest possible way [31–33], with the W boson interacting only with left-handed particles and right-handed antiparticles. Nevertheless, the combination of the two transformations, denoted as *CP*, seemed to remain a respected symmetry of weak interactions. Therefore, it was with great surprise that the *CP* symmetry was observed to be violated, although only at the two-per-mil level, in the weak decay of kaon mesons in 1964 [4]. This phenomenon, generally known as *CP* violation, implies the possibility to distinguish unambiguously matter from antimatter, and its discovery represented a major turning point in the study of fundamental interactions. In particular, it suggested the existence of a third generation of quarks, subsequently discovered only in 1977 (b quark) and 1995 (t quark). Just a couple of years later, in 1967, the violation of the *CP* symmetry by fundamental interactions was indicated as one of the necessary conditions to explain the generation of the matter–antimatter asymmetry observed in the Universe in a dynamical way [1].

Today, the Standard Model of particle physics (SM) encompasses only two sources of *CP* violation. The first origins from the strong-interaction Lagrangian (see Ref. [34] for a review). However, upper bounds of the electric dipole moment of the neutron constrain the coefficient of this *CP*-violating Lagrangian term to be less than 10^{-10} [35], an unnatural fact commonly referenced to as the "strong *CP* problem", which has motivated the proposal of the existence and the search of new particles or interactions such as the axion. Thus, the only source of *CP*

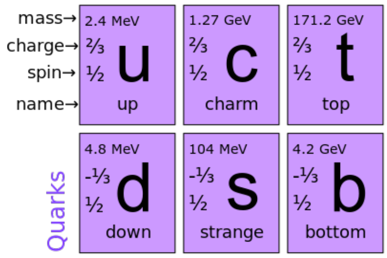

Figure 1.1: Summary of the main properties of the six quarks. The bottom quark is also named beauty quark. Each quark is identified by a flavour quantum number denoted with the letter reported in the corresponding box, but in upper-case character.

violation measured so far is a single complex phase in the Cabibbo–Kobayashi–Maskawa (CKM) matrix [2, 3], which quantifies the interaction of the W^- boson with quarks. However, while the CKM mechanism has been tested successfully in the decay of down-type quarks in K and B mesons [4–12], it is too small to explain the observed matter–antimatter asymmetry [13], suggesting the existence of additional sources of *CP* violation beyond the SM. One possible source, which will be tested in the next few years, is *CP* violation in the oscillation probabilities of neutrinos (see Ref. [36] for a review). Another possibility is given by *CP*-violating interactions of new particles with the SM ones, which can influence the decay of SM particles *via* so-called "virtual interactions", even in the case that their masses are much larger than those that can be currently produced directly at colliders like the Large Hadron Collider at CERN. The latter category of models can be tested with high-precision measurements of *CP* violation in the decay of SM particles. The measurement presented in this thesis falls into this experimental program. The background information necessary to understand the unique role and potentiality of searches of *CP* violation in the decay of the charm quark in the context of precision measurements of the SM is provided in the next sections.

1.1 Quarks decays and *CP* violation in the Standard Model

The SM encompasses three generations of quarks, see Fig. 1.1, each composed of an up-type quark with electric charge $+2/3$ and a down-type quark with electric charge $-1/3$. Each quark has a different mass and is identified by a flavour quantum number. Flavour quantum numbers can be changed only by interactions with the W^- boson, which interacts with all possible pairs of up- and down-type quarks according to the Lagrangian

$$\mathcal{L}_{W^-,\,\text{quarks}} = \sum_{i,j=1,2,3} \frac{g}{\sqrt{2}} W^+_\mu \bar{u}^i_{\mathrm{L}} \gamma^\mu V^{i,j}_{\mathrm{CKM}} d^j_{\mathrm{L}} + \text{h.c.}, \tag{1.1}$$

where g is the gauge coupling of the $SU(2)$ weak-isospin group of the SM, γ^μ are the Dirac matrices, the indices i, j run over the three generations, $\bar{u}_{\mathrm{L}}$ and d_{L} are left-handed spinors, "h.c." denotes the Hermitian conjugate and the unitary CKM matrix

$$\mathbf{V}_{\mathrm{CKM}} \equiv \begin{pmatrix} V_{ud} & V_{us} & V_{ub} \\ V_{cd} & V_{cs} & V_{cb} \\ V_{td} & V_{ts} & V_{tb} \end{pmatrix} \tag{1.2}$$

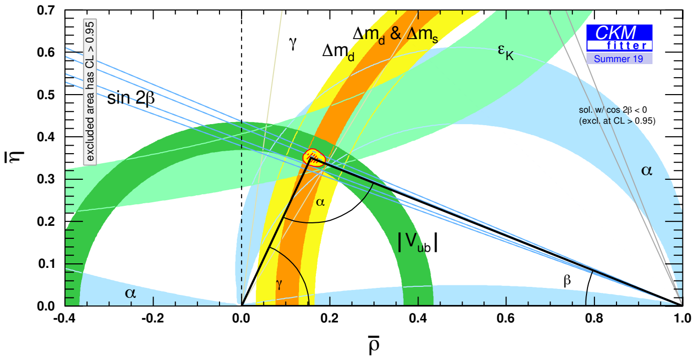

Figure 1.2: Constraints on the $(\overline{\rho},\overline{\eta})$ plane. The red hashed region of the global combination corresponds to 68% CL. Figure taken from Ref. [41].

quantifies the strength of the interaction between each pair of quarks.[1] By choosing a convenient definition of the unobservable quark-fields phases, this can be parametrised in terms of four observable real parameters.[2] These are conventionally chosen to be three angles, θ_{12}, θ_{13} and θ_{23}, and a single complex phase δ, defined as [38]

$$\begin{aligned} V_{\text{CKM}} &= \begin{pmatrix} 1 & 0 & 0 \\ 0 & c_{23} & s_{23} \\ 0 & -s_{23} & c_{23} 0 \end{pmatrix} \begin{pmatrix} c_{13} & 0 & s_{13}e^{-i\delta} \\ 0 & 1 & 0 \\ -s_{13}e^{i\delta} & 0 & c_{13} \end{pmatrix} \begin{pmatrix} c_{12} & s_{12} & 0 \\ -s_{12} & c_{12} & 0 \\ 0 & 0 & 1 \end{pmatrix} \\ &= \begin{pmatrix} c_{12}c_{13} & s_{12}c_{13} & s_{13}e^{-i\delta} \\ -s_{12}c_{23} - c_{12}s_{23}s_{13}e^{i\delta} & c_{12}c_{23} - s_{12}s_{23}s_{13}e^{i\delta} & s_{23}c_{13} \\ s_{12}s_{23} - c_{12}c_{23}s_{13}e^{i\delta} & -c_{12}s_{23} - s_{12}c_{23}s_{13}e^{i\delta} & c_{23}c_{13} \end{pmatrix}, \end{aligned} \tag{1.3}$$

where c_{ij} and s_{ij} are abbreviations for $\cos\theta_{ij}$ and $\sin\theta_{ij}$. Experimentally, the following hierarchy among the angles is measured, $s_{13} \ll s_{23} \ll s_{12} \ll 1$. The corresponding hierarchy between the CKM-matrix elements can be made more explicit by employing the alternative Wolfenstein parametrisation [39–41]. This is obtained by performing the following parameters redefinition,

$$s_{12} \equiv \lambda, \qquad s_{23} \equiv A\lambda, \qquad s_{13}e^{-i\delta} \equiv A\lambda^3(\overline{\rho}+i\overline{\eta})\frac{\sqrt{1-A^2\lambda^4}}{\sqrt{1-\lambda^2}[1-A^2\lambda^4(\overline{\rho}+i\overline{\eta})]}, \tag{1.4}$$

where the λ, A, $\overline{\rho}$ and $\overline{\eta}$ parameters are measured to be equal to [41]

$$\begin{aligned} \lambda &= 0.22650 \pm 0.00048, & A &= 0.790\,^{+0.017}_{-0.012}, \\ \overline{\rho} &= 0.141\,^{+0.016}_{-0.017}, & \overline{\eta} &= 0.357 \pm 0.011. \end{aligned}$$

The experimental constraints on the values of $\overline{\rho}$ and $\overline{\eta}$ are displayed in Fig. 1.2. Neglecting terms of $\mathcal{O}(\lambda^6)$, the CKM matrix is equal to

$$\mathbf{V}_{\text{CKM}} = \begin{pmatrix} 1-\frac{\lambda^2}{2}-\frac{\lambda^4}{8} & \lambda & A\lambda^3(\overline{\rho}-i\overline{\eta})(1+\frac{\lambda^2}{2}) \\ -\lambda + A^2\lambda^5(\frac{1}{2}-\overline{\rho}-i\overline{\eta}) & 1-\frac{\lambda^2}{2}-\frac{\lambda^4(1+4A^2)}{8} & A\lambda^2 \\ A\lambda^3(1-\overline{\rho}-i\overline{\eta}) & -A\lambda^2\left(1-\frac{\lambda^2}{2}\right) - A\lambda^4(\overline{\rho}+i\overline{\eta}) & 1-\frac{A^2\lambda^4}{2} \end{pmatrix}. \tag{1.5}$$

[1] Lorentz–Heaviside units are adopted throughout this chapter.

[2] A concise but clear derivation of the expression of the quark charged currents from the complete Lagrangian of the SM can be found in Ref. [37].

The parameter λ is historically referenced to as the sine of the Cabibbo angle. The weak decays are classified into Cabibbo favoured (CF), Cabbbo suppressed (CS) or doubly Cabibbo supressed (DCS) decays, depending on the lowest power of λ that appears in any of their decay amplitudes being zero, one or two.

Having introduced these preliminary notions, the conditions for observing *CP* violation in hadron decays can be presented. Let us consider the decay amplitudes of an initial hadron, whose state is denoted by $|i\rangle$, into a general final state $|f\rangle$, and its *CP*-conjugate amplitude, describing the decay of its antiparticle into the *CP*-conjugated final state,

$$A_f \equiv \langle f|\, \mathcal{H}\, |i\rangle\,, \qquad \bar{A}_{\bar{f}} \equiv \langle \bar{f}|\, \mathcal{H}\, |\bar{i}\rangle\,, \tag{1.6}$$

where $\mathcal{H}$ is the effective Hamiltonian governing the decay. In general, two types of phases can enter in the amplitudes contributing to the transitions of Eq. (1.6). The *strong phases* are defined as the phases that do not change sign under *CP* transformation, while *weak phases* are defined as those that change sign under *CP* transformation. The nomenclature follows from the observation that all phases due to strong interactions, which arise for example from rescattering — that is nonperturbative quantum-chromodynamics (QCD) interactions involving on-shell particles —, are invariant under the *CP* transformation. For this reason, these phases are also known as "scattering phases". On the contrary, the only measured source of *CP*-odd phases in the SM is given by the complex phases δ of the CKM matrix, and thus pertains to the weak interaction. In fact, if a given matrix element $V_{\rm CKM}^{i,j}$ appears in A_f, the corresponding element entering in $\bar{A}_{\bar{f}}$ is seen from Eq. (1.1) to be $(V_{\rm CKM}^{i,j})^*$, which is obtained from $V_{\rm CKM}^{i,j}$ with the substitution $\delta \to -\delta$.

The strong and weak phases of a single amplitude are not observable, since only the amplitudes magnitude and the phase differences between different amplitudes are observable in quantum mechanics. However, most decay processes receive contributions from multiple amplitudes,

$$A_f = \sum_n |A_n|\, e^{i(\phi_n+\delta_n)}, \qquad\qquad \bar{A}_{\bar{f}} = \sum_n |A_n|\, e^{i(-\phi_n+\delta_n)}, \tag{1.7}$$

where ϕ_i and δ_i are the weak and strong phases, respectively.[3] The *CP* violation arises if the squared magnitudes of the total amplitudes differ, and is effectively quantified by their asymmetry,

$$\frac{|A_f|^2 - |\bar{A}_{\bar{f}}|^2}{|A_f|^2 + |\bar{A}_{\bar{f}}|^2} = -\frac{\sum_{n\neq m} |A_n|\,|A_m| \sin(\phi_n - \phi_m)\sin(\delta_n - \delta_m)}{\sum_n |A_n|^2 + \sum_{n\neq m} |A_n|\,|A_m| \cos(\phi_n - \phi_m)\cos(\delta_n - \delta_m)}. \tag{1.8}$$

From this expression, it follows that the required condition to observe *CP* violation is that the process receives contributions by at least two distinct interfering amplitudes with both different weak phases and different strong phases. The size of *CP* violation is determined by the differences of the phases, as well by the ratio of the product of the magnitudes of the amplitudes responsible of *CP* violation at numerator of Eq. (1.8), to the squared magnitude of the largest amplitudes at denominator.

Although *CP* violation can be measured in the decay of many particles, the richest phenomenology of *CP* violation and many of most precise measurements of its size concern the decay of flavoured neutral mesons. The phenomenology of these particles is described in the next section.

[3] In the SM and in the SM effective field theory, under the assumption of *CPT* invariance, each term of the Hamiltonian has a corresponding *CP*-conjugate term, which can differ only by the phase of its complex coefficient. Therefore, in this framework the expansion in Eq. (1.7), where to each amplitude contributing to A_f corresponds an amplitude with equal magnitude but possible different phases contributing to $\bar{A}_{\bar{f}}$, is completely general.

1.2 Mixing of flavoured neutral mesons

In the SM there are exactly four neutral mesons (plus their antiparticles) that are unable to decay into lighter particles *via* the electromagnetic or strong interaction, namely the K^0 ($d\bar{s}$), D^0 ($c\bar{u}$), B^0 ($d\bar{b}$) and B_s^0 ($s\bar{b}$) mesons.[4] They owe this property to possessing nonzero flavour quantum numbers, and are thus often named *flavoured neutral mesons*. Owing to the nonconservation of flavour quantum numbers by the weak interaction, the flavour eigenstates listed above are not eigenstates of the effective Hamiltonian, H, that governs their time evolution. As a consequence, flavoured neutral mesons have a nonzero probability of oscillating into their antiparticles *via* a $\Delta F = 2$ transition, which changes their flavour quantum numbers by two units, before decaying. This phenomenon is commonly named *mixing*. This section presents the formalism to describe the evolution of a generic flavoured neutral meson M^0, both employing the standard phenomenological parametrisation and the theoretical parametrisation introduced by Refs. [42, 43]. Finally, the mixing phenomenology of the four flavoured neutral mesons is briefly described.

1.2.1 Formalism

Let us consider an initial state that is a pure superposition of the neutral-meson flavour eigenstates M^0 and $\overline{M}^0$, where M^0 stands for K^0, D^0, B^0 or B_s^0, at time equal to zero,

$$\left|\psi(0)\right\rangle = a(0)\left|M^0\right\rangle + b(0)\left|\overline{M}^0\right\rangle . \tag{1.9}$$

The time evolution of this state is determined by the Schrödinger equation,

$$i\frac{\mathrm{d}}{\mathrm{d}t}\left|\psi(t)\right\rangle = H\left|\psi(t)\right\rangle , \tag{1.10}$$

where H is the Hamiltonian governing its dynamics and $\left|\psi(t)\right\rangle$ is a linear superposition of $\left|M^0\right\rangle$, $\left|\overline{M}^0\right\rangle$ and all final states $\left|f_k\right\rangle$ in which these two mesons can decay,

$$\left|\psi(t)\right\rangle \equiv a(t)\left|M^0\right\rangle + b(t)\left|M^0\right\rangle + \sum_k c_k(t)\left|f_k\right\rangle . \tag{1.11}$$

If one is interested only in the values of $a(t)$ and $b(t)$ and not in distinguishing the final states to which the mesons decay, and if the times t under consideration are much larger than the typical time scale of the strong interaction, the problem can be solved with a simplified formalism using the Wigner–Weisskopf approximation [44, 45]. The evolution of the state in the M^0–$\overline{M}^0$ subspace is described with a 2×2 effective Hamiltonian $\boldsymbol{H}$,

$$i\frac{\mathrm{d}}{\mathrm{d}t}\begin{pmatrix} a(t) \\ b(t) \end{pmatrix} = \begin{pmatrix} H_{11} & H_{12} \\ H_{21} & H_{22} \end{pmatrix}\begin{pmatrix} a(t) \\ b(t) \end{pmatrix} . \tag{1.12}$$

This Hamiltonian is non-Hermitian, reflecting the fact that the probability is not conserved in the M^0–$\overline{M}^0$ subspace (the two mesons can decay). However, it can be conveniently split into a Hermitian and an anti-Hermitian part,

$$\boldsymbol{H} = \boldsymbol{M} - \tfrac{i}{2}\boldsymbol{\Gamma}, \tag{1.13}$$

[4] The short lifetime of the t quark prevents it from hadronising into quarks bound states.

Table 1.1: Constraints on the $\boldsymbol{H}$ matrix elements if the parametrised interactions are invariant under the CPT, CP or T transformations.

Invariance	Constraints		
CPT	$\mathrm{M}_{11} = \mathrm{M}_{22}$,	$\Gamma_{11} = \Gamma_{22}$	
CP	$\mathrm{M}_{11} = \mathrm{M}_{22}$,	$\Gamma_{11} = \Gamma_{22}$,	$\mathcal{I}m(\Gamma_{12}/\mathrm{M}_{12}) = 0$
T	$\mathcal{I}m(\Gamma_{12}/\mathrm{M}_{12}) = 0$		

where $\boldsymbol{M} \equiv (\boldsymbol{H} + \boldsymbol{H}^{\dagger})/2$ and $\boldsymbol{\Gamma} \equiv i(\boldsymbol{H} - \boldsymbol{H}^{\dagger})$ are the Hermitian mass and decay matrices, which describe dispersive transitions through virtual (off-shell) intermediate states, and absorptive transitions through real (on-shell) intermediate states, respectively.[5] In particular, the decay of the projection of $|\psi\rangle$ on the M^0–$\overline{M}^0$ subspace, indicated with $\left|\psi^{(2)}\right\rangle$, is regulated by

$$\frac{\mathrm{d}}{\mathrm{d}t} \langle\psi^{(2)}|\psi^{(2)}\rangle = i \langle\psi^{(2)}| \left(\boldsymbol{H}^{\dagger} - \boldsymbol{H}\right) |\psi^{(2)}\rangle = - \langle\psi^{(2)}| \boldsymbol{\Gamma} |\psi^{(2)}\rangle . \tag{1.14}$$

As this value must be negative, $\boldsymbol{\Gamma}$ is positive definite. In general, $\boldsymbol{H}$ is defined by eight free parameters, while $\boldsymbol{M}$ and $\boldsymbol{\Gamma}$ are each described by four parameters (each of them being Hermitian, the following relations hold, $M_{ij} = M^*_{ji}$ and $\Gamma_{ij} = \Gamma^*_{ji}$). If the interactions described by $\boldsymbol{H}$ are invariant under some combinations of discrete transformations, further relations among the matrix elements of $\boldsymbol{M}$ and $\boldsymbol{\Gamma}$ hold, as listed in Tab. 1.1, and reduce the number of parameters needed to describe $\boldsymbol{H}$. The CPT invariance is assumed in the following, implying $M_{11} = M_{22} \equiv M$ and $\Gamma_{11} = \Gamma_{22} \equiv \Gamma$. Under this assumption, which is motivated by central role of the CPT invariance in the formulation of quantum field theory and by the conservation of the CPT symmetry in all measurements performed to date, the expressions to describe the M^0-meson mixing are greatly simplified.

Phenomenological parametrisation

Let us define the (normalised) eigenstates of $\boldsymbol{H}$ to be

$$\begin{aligned} |M_1\rangle &\equiv p \left|M^0\right\rangle + q \left|\overline{M}^0\right\rangle , \\ |M_2\rangle &\equiv p \left|M^0\right\rangle - q \left|\overline{M}^0\right\rangle , \end{aligned} \tag{1.15}$$

where p and q are complex numbers satisfying $|p|^2 + |q|^2 = 1$ and

$$\left(\frac{q}{p}\right)^2 = \frac{H_{21}}{H_{12}} = \frac{M^*_{12} - \frac{i}{2}\Gamma^*_{12}}{M_{12} - \frac{i}{2}\Gamma_{12}}. \tag{1.16}$$

As the matrix $\boldsymbol{H}$ is not Hermitian, $|M_1\rangle$ and $|M_2\rangle$ are not necessarily orthogonal. These interaction eigenstates evolve according to $|M_{1,2}(t)\rangle = e^{-i\omega_{1,2}t} |M_{1,2}(0)\rangle$, where the eigenvalues $\omega_{1,2} \equiv \omega_0 \mp \frac{1}{2}\Delta\omega$ are conveniently split into a real and an imaginary part,

$$\omega_{1,2} \equiv M_{1,2} - \tfrac{i}{2}\Gamma_{1,2}, \tag{1.17}$$

corresponding to the masses and decay widths of the two eigenstates. In fact, the definition of Eq (1.17) implies the usual time evolution of unstable particle states, $|M_{1,2}(t)\rangle =$

[5] The explicit expressions for $\boldsymbol{M}$ and $\boldsymbol{\Gamma}$ are given, for example, in Ref. [46].

$e^{-iM_{1,2}t-\frac{1}{2}\Gamma_{1,2}t}\,|M_{1,2}(0)\rangle$. The averages of the masses and of the decay widths are equal to the diagonal matrix elements of $\boldsymbol{M}$ and $\boldsymbol{\Gamma}$,

$$\omega_0 = \frac{M_1 + M_2}{2} - \frac{i}{2}\frac{\Gamma_1 + \Gamma_2}{2} = M - \frac{i}{2}\Gamma, \tag{1.18}$$

while their differences $\Delta M = M_2 - M_1$ and $\Delta\Gamma = \Gamma_2 - \Gamma_1$, or equivalently $\Delta\omega \equiv \Delta M - \frac{i}{2}\Delta\Gamma$, satisfy

$$H_{12}H_{21} = \frac{1}{4}\left(\Delta M - \tfrac{i}{2}\Delta\Gamma\right)^2. \tag{1.19}$$

Usually, the mass and width splits of the eigenstates are parametrised in units of the average decay width, through the two dimensionless mixing parameters $x \equiv \Delta M/\Gamma$ and $y \equiv \Delta\Gamma/2\Gamma$.

The time evolution of a particle created in its flavour eigenstate at time zero is given by

$$\begin{aligned} \left|M^0(t)\right\rangle &= g_+(t)\left|M^0\right\rangle + \frac{q}{p}\,g_-(t)\left|\overline{M}^0\right\rangle, \\ \left|\overline{M}^0(t)\right\rangle &= g_+(t)\left|\overline{M}^0\right\rangle + \frac{p}{q}\,g_-(t)\left|M^0\right\rangle, \end{aligned} \tag{1.20}$$

where $\left|M^0(t)\right\rangle$ ($\left|\overline{M}^0(t)\right\rangle$) indicates the time-evolved at time t of the M^0 ($\overline{M}^0$) state at time zero and $g_\pm(t)$ are defined by

$$g_\pm(t) \equiv \frac{e^{-i\omega_1 t} \pm e^{-i\omega_2 t}}{2}. \tag{1.21}$$

The probability of measuring at time t the same particle that was produced in its flavour eigenstate at time $t = 0$ is equal to

$$\left|\left\langle M^0\middle|M^0(t)\right\rangle\right|^2 = \left|\left\langle \overline{M}^0\middle|\overline{M}^0(t)\right\rangle\right|^2 = |g_+(t)|^2, \tag{1.22}$$

whereas the probability of measuring the particle with opposite flavour quantum numbers is

$$\begin{aligned} \left|\left\langle \overline{M}^0\middle|M^0(t)\right\rangle\right|^2 &= \left|\frac{q}{p}\right|^2 \cdot |g_-(t)|^2, \\ \left|\left\langle M^0\middle|\overline{M}^0(t)\right\rangle\right|^2 &= \left|\frac{p}{q}\right|^2 \cdot |g_-(t)|^2, \end{aligned} \tag{1.23}$$

with

$$|g_\pm(t)|^2 = \tfrac{1}{2}e^{-\Gamma t}\left[\cosh(y\Gamma t) \pm \cos(x\Gamma t)\right]. \tag{1.24}$$

Thus, the probability of the M^0 and $\overline{M}^0$ mesons to preserve their flavour quantum numbers as a function of time is the same for both mesons, whereas the probability to oscillate into their antiparticle can be different, provided that $|q/p| \neq 1$ and that at least one of the mixing parameters x and y is nonzero.

In this parametrisation, a convention choice is needed to resolve the ambiguity arising from the definitions of $|M_1\rangle$ and $|M_2\rangle$ in Eq. (1.15), which can be interchanged by redefining $q \to -q$. This corresponds to choosing the sign for the solutions of the Eqs. (1.16) and (1.19). For example, this ambiguity can be solved by defining the $|M_2\rangle$ meson as the short-lived eigenstate or, equivalently, by forcing the y parameter to be positive. Once one such convention choice is done, all ambiguities are removed, apart from the phases of q and p. In fact, their relative phase still depends on the convention for the CP transformation of the M^0 an $\overline{M}^0$ mesons, whereas their global phase is arbitrary.

Theoretical parametrisation

The results of the previous section can be obtained also by using an alternative parametrisation, introduced in Refs. [42, 43] and usually referenced to as "theoretical", which is convention-independent and quantifies directly the magnitudes and the phase difference between the dispersive and absorptive transition amplitudes. In particular, the theoretical mixing parameters and the mixing phase are defined as

$$x_{12} \equiv \frac{2|M_{12}|}{\Gamma}, \qquad y_{12} \equiv \frac{2|\Gamma_{12}|}{\Gamma}, \qquad \phi_{12} \equiv \arg\left(\frac{M_{12}}{\Gamma_{12}}\right), \tag{1.25}$$

and are all observable quantities. While x_{12} and y_{12} are *CP*-even observables, ϕ_{12} is a *CP*-odd weak phase.

In this parametrisation, the time evolution of the flavour eigenstates can obtained by solving directly Eq. (1.12), obtaining

$$\begin{aligned}\begin{pmatrix} a(t) \\ b(t) \end{pmatrix} &= e^{-i\boldsymbol{H}t}\begin{pmatrix} a(0) \\ b(0) \end{pmatrix} \\ &= e^{-i\left(M-i\frac{\Gamma}{2}\right)t}\begin{pmatrix} \cos\left(\sqrt{H_{12}H_{21}}t\right) & -i\sqrt{\frac{H_{12}}{H_{21}}}\sin\left(\sqrt{H_{12}H_{21}}t\right) \\ -i\sqrt{\frac{H_{21}}{H_{12}}}\sin\left(\sqrt{H_{12}H_{21}}t\right) & \cos\left(\sqrt{H_{12}H_{21}}t\right) \end{pmatrix}\begin{pmatrix} a(0) \\ b(0) \end{pmatrix}.\end{aligned} \tag{1.26}$$

The transition amplitudes are thus given by

$$\begin{aligned}\left\langle M^0\middle|M^0(t)\right\rangle = \left\langle \overline{M}^0\middle|\overline{M}^0(t)\right\rangle &= e^{-i\left(M-\frac{i}{2}\Gamma\right)t}\cos\left[\tfrac{1}{2}\left(\Delta M - \tfrac{i}{2}\Delta\Gamma\right)t\right], \\ \left\langle \overline{M}^0\middle|M^0(t)\right\rangle &= e^{-i\left(M-\frac{i}{2}\Gamma\right)t}\frac{\sin\left[\frac{1}{2}\left(\Delta M - \frac{i}{2}\Delta\Gamma\right)t\right]}{\frac{1}{2}\left(\Delta M - \frac{i}{2}\Delta\Gamma\right)t}\left(e^{-i\frac{\pi}{2}}M_{12}^* - \tfrac{1}{2}\Gamma_{12}^*\right)t,\end{aligned} \tag{1.27}$$

where Eq. (1.19) has been used, with $\left\langle \overline{M}^0\middle|M^0(t)\right\rangle$ obtained from $\left\langle M^0\middle|\overline{M}^0(t)\right\rangle$ with the substitutions $M_{12}^* \to M_{12}$ and $\Gamma_{12}^* \to \Gamma_{12}$.

The theoretical and phenomenological mixing parameters are related as

$$x^2 - y^2 = x_{12}^2 - y_{12}^2, \tag{1.28}$$

$$xy = x_{12}y_{12}\cos\phi_{12}, \tag{1.29}$$

$$\left|\frac{q}{p}\right|^{\pm 2}(x^2+y^2) = x_{12}^2 + y_{12}^2 \pm 2x_{12}y_{12}\sin\phi_{12}, \tag{1.30}$$

where the first two equations and the third are obtained by equating the expressions of $H_{12}H_{21}$ and $|H_{12}|^2$, $|H_{21}|^2$ in terms of the two sets of mixing parameters (see Eqs. (1.16) and (1.19) for the phenomenological mixing parameters).

The ratio $|q/p|$ is measured to be very close to unity for all flavoured neutral mesons, corresponding to small values of $\sin\phi_{12}$. Therefore, the x_{12} and y_{12} parameters are equal to the magnitude of the x and y parameters, $x_{12} \approx |x|$ and $y_{12} \approx |y|$, up to corrections quadratic in $\sin\phi_{12}$. The x and y parameters have the same sign only if $\phi_{12} \approx 0$ rather than π. Finally, $|q/p| - 1$ is approximately equal to

$$\left|\frac{q}{p}\right| - 1 \approx \frac{x_{12}y_{12}}{x_{12}^2 + y_{12}^2}\sin\phi_{12}, \tag{1.31}$$

up to corrections quadratic in $\sin\phi_{12}$.

Table 1.2: Value of the mixing parameters of the four flavoured neutral mesons (values taken from Ref. [36] for kaon and from Ref. [47] for c and b mesons). The global sign of the two mixing parameters is convention dependent.

System	$x = \Delta M/\Gamma$	$y = \Delta\Gamma/2\Gamma$
K^0–$\overline{K}^0$	-0.946 ± 0.004	0.99650 ± 0.00001
D^0–$\overline{D}^0$	$(3.4 \pm 1.2) \times 10^{-3}$	$(6.8\,^{+0.6}_{-0.7}) \times 10^{-3}$
B^0–$\overline{B}^0$	0.769 ± 0.004	$(0.1 \pm 1.0)\%$
B_s^0–$\overline{B}_s^0$	26.89 ± 0.07	$(12.9 \pm 0.6)\%$

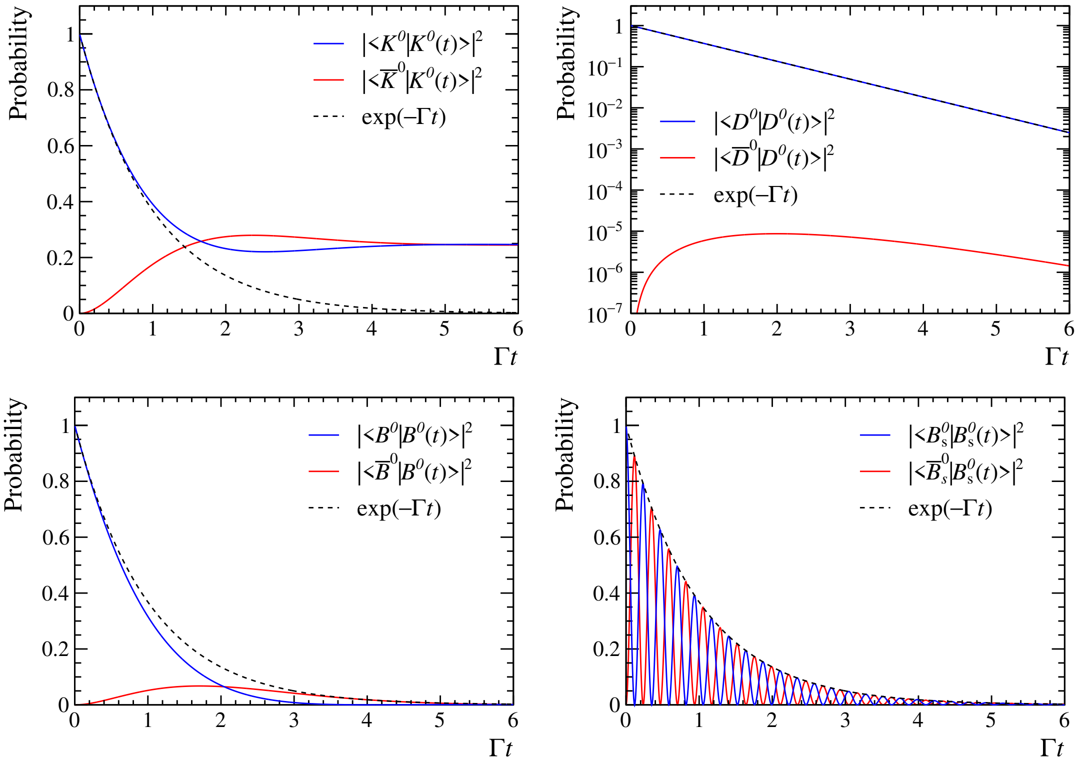

Figure 1.3: Probability for a neutral flavoured meson to oscillate in its relative antimeson (red) or to preserve its flavour quantum numbers (blue) as a function of time, under the assumption that $|q/p| = 1$. The plots correspond, from left to right and from top to bottom, to K^0, D^0 (in logarithmic scale), B^0 and B_s^0 mesons. The exponential function that would be measured in absence of mixing is drawn as well as a black-dashed line.

1.2.2 Phenomenology

The formalism introduced in Sect. 1.2.1 describes the mixing of all K^0, D^0, B^0 and B_s^0 mesons. However, the phenomenology, which is governed by the size of the mixing parameters x and y summarised in Table 1.2, varies considerably among different particles. This is displayed in Fig. 1.3, where the probability for the mesons to preserve their flavour quantum numbers or to change them, oscillating into their antiparticles, is plotted as a function of time.

These different behaviours can be traced down to largely different interactions contributing

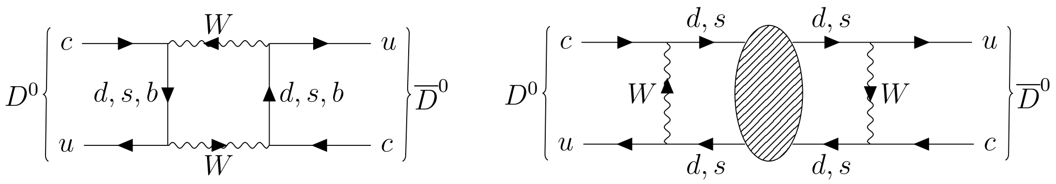

Figure 1.4: Feynman diagrams of (left) short-distance and (right) long-distance contributions to D^0-meson mixing. In the right diagram, the blob stays for low-energy QCD interactions, possible involving the exchange of hadrons on the mass shell.

to the matrix elements responsible for the transitions, M_{12} and Γ_{12}. These are fourth-order interactions in the weak coupling, and are usually classified in two categories, namely *short-distance* and *long-distance* contributions, depending on whether they receive significant contributions from long-distance nonperturbative QCD interactions or not. In particular, while short-distance amplitudes involve the exchange of virtual particles off the mass shell only, and can be calculated with good precision, long-distance amplitudes can be significantly enhanced by the exchange of hadrons on the mass shell, as shown in Fig. 1.4, and pose several challenges to theory predictions.

Box diagrams responsible for the $\Delta F_1 = -2$, $\Delta F_2 = 2$ neutral currents that provoke the mixing of mesons with $F_1\bar{F}_2$ flavour content, similar to those of Fig. 1.4 (left), are roughly proportional to $\lambda^q_{F_1F_2}(\lambda^{q'}_{F_1F_2})^*(m_q/m_W)^2$, where $\lambda^q_{F_1F_2}$ is defined as $\lambda^q_{F_1F_2} \equiv V_{qF_1}V^*_{qF_2}$ and q and q' are the internal quarks of the diagram, with q the lightest one [48]. The absence of $\Delta F = 2$ transitions at tree level, and the suppression of possible contributions from loops involving internal light quarks due to the $(m_q/m_W)^2$ factor, is known as GIM mechanism [49] and follows from the unitarity of the CKM matrix.[6] Furthermore, the GIM mechanism predicts that $\Delta F = 2$ transitions would be zero also at loop level, if the masses of all of the three possible internal quarks were equal.

For B^0 and B^0_s mesons, the only relevant contribution to mixing involves the exchange of two internal top quarks, owing to the large breaking of the GIM mechanism by the top-quark mass ($m_t/m_W \approx 1$, while $m_q/m_W \ll 1$ for $q \neq t$), and to the favourable hierarchy of the relevant CKM-matrix elements ($\lambda^t_{bs} \approx \lambda^c_{bs} \gg \lambda^u_{bs}$ and $\lambda^t_{bd} \approx \lambda^c_{bd} \approx \lambda^u_{bd}$). Moreover, these amplitudes are nearly completely short-distance, since the large B mass is off the region of hadronic resonances. Since the top-quark exchanges are off the mass shell, in the SM the magnitude of M_{12} (and of the x parameter) of B mesons is expected to be much larger than that of Γ_{12} (and of the y parameter). In addition, since the magnitude of V_{td} is much smaller than that of V_{ts}, the magnitude of the mixing parameters of the B^0_s meson is larger than that of the B^0 meson, and its oscillations are much faster. Finally, explicit calculations provide $\phi_{12} \approx \pi$, implying opposite signs for x and y, and predict that the ratio of x to y is the same for B^0 and B^0_s mesons. The fact that y is smaller for B^0 than for B^0_s mesons can also be understood based on the total branching fraction of B decays that are shared with $\overline{B}$ decays. These are dominated by $b \to c\bar{c}q$ transitions, which are Cabibbo favoured for B^0_s decays ($q = s$) and Cabibbo suppressed for B^0 decays ($q = d$).

A completely different dynamics is at play in K^0-meson mixing. Since the K^0-meson mass is of the same order of many hadronic resonances, the contributions to Γ_{12} are dominated by long-distance amplitudes. In particular, the y parameter is approximately equal to unity since,

[6] See for example Refs. [50–52] for a modern exposition of the GIM mechanism.

neglecting *CP*-violating effects of order of 10^{-3}, only the approximately *CP*-even K eigenstate can decay into two pion mesons, whereas the semileptonic decays and the decays into three pion mesons of the approximately *CP*-odd eigenstate have very low rates owing to phase-space suppression. On the contrary, only approximately 20% of the M_{12} amplitude is due to long-distance contributions. However, unlike in B-meson mixing, the short-distance contributions to M_{12} involving charm quarks are larger than those due to top quarks, owing to the large CKM suppression of the top-quark transitions ($\lambda^t_{sd}/\lambda^c_{sd} \ll m_c/m_t$).

The interactions governing the mixing of D^0 mesons, which are the only flavoured neutral mesons where the mixing of up-type quarks can be observed, are very different from those of K and B mesons. The size of mixing is here extremely small, as shown in Fig. 1.3, owing to a severe GIM suppression which is due to two accidental features. First, the masses of the internal down-type quarks circulating in the box diagrams, which break the exact GIM cancellation at loop level, are much smaller than that of the top quark (the largest mass is $m_b/m_W \approx 5\%$). Second, owing to the accidental hierarchy of the CKM-matrix elements, the third generation of quarks is nearly decoupled from the first two. In fact, $|\lambda^b_{cu}/\lambda^s_{cu}| \approx |\lambda^b_{cu}/\lambda^d_{cu}| \ll \Lambda/m_b$, where Λ is a dynamical hadronic scale of order Λ_{QCD} that replaces $m_{s,d}$ in the evaluation of box diagrams with internal s and d quarks (the charm-quark mass is not distant from that of light-quarks hadronic resonances and long-distance effects cannot be neglected). Another consequence of the aforementioned hierarchy of the CKM-matrix elements is that the submatrix relative to the first two generations of quarks is accidentally nearly unitary, so that the GIM mechanism applies with good approximation also to the first two generations only. Thus, the breaking of the GIM suppression coincides to good approximation with the breaking of the flavour $SU(3)_{\mathrm{F}}$ symmetry of the strong interactions or, more precisely, of their U-spin symmetry.[7] In particular, the y parameter is generated only at second order in the breaking of the U-spin symmetry [53, 54]. On the other hand, it is not excluded that the x parameter, which is sensitive to dispersive amplitudes, receives contributions also from beauty-quark loops. In fact, the smaller size of λ^b_{cu} might be compensated by the absence of the suppression due to the approximate U-spin symmetry.

Both x and y mixing parameters of the D^0 meson are experimentally less than than 1% [55–62]. However, while the y parameter has been measured to differ significantly from zero, the significance for x to differ from zero is only around 3σ. In particular, the latest world averages of these parameter are $y = (6.8\,^{+0.6}_{-0.7}) \times 10^{-3}$ and $x = (3.7 \pm 1.2) \times 10^{-3}$.

Different approaches have been employed in the literature to estimate the size of the mixing parameters of D^0 mesons. The inclusive approach relies on the heavy-quark expansion (HQE). This is an effective field theory of QCD, which describes the dynamics of beauty or charm hadrons through an expansion in powers of Λ/m_Q around the assumption that the heavy quark Q is static within the hadron (see Ref. [63] and references therein for a review). While the HQE is able to explain the value of the lifetime ratio τ_{D^+}/τ_{D^0} [64, 65], suggesting that a perturbative expansion in terms of the parameter $\Lambda/m_c \approx 0.3$ might be well founded, it has difficulties in calculating the values of the mixing parameters, owing to the huge GIM cancellations at play in $\Delta C = 2$ transitions. Nonperturbative matrix elements have been calculated up to dimension-six HQE operators [15, 65–67]. While their single-quark contributions to mixing is around five times larger than the experimental value of y, the GIM suppression mechanism provokes huge cancellations in their sum, and a consequent suppression of the prediction for the y parameter

[7] The U-spin group is the $SU(2)$ subgroup of $SU(3)_{\mathrm{F}}$ that concerns the quarks d and s. Therefore, the U-spin symmetry coincides with the invariance of the strong interaction under the transformation $d \to s$ and $s \to d$, under the assumption that the two masses m_d and m_s are equal.

by up to five orders of magnitude [68]. However, the large disagreement with experimental data can be due to a violation of the quark–hadron duality (the HQE assumption that hadron decays can be described at the quark level) as low as 20% [69], or to a lifting of the GIM suppression for dimension-9 or -12 operators, which would overcompensate their larger suppression in terms of Λ/m_Q [70–73]. The latter hypothesis has been qualitatively verified in Ref. [74] for dimension-9 operators, although the size of the lifting seems too small to explain the observed value of y. Calculations of higher-order operators, initiated in Refs. [75, 76], might help clarify the picture. Finally, recently Ref. [68] pointed out that a more careful setting of the normalisation scales for box diagrams containing different internal quarks could also lift the disagreement between predictions and data.

The alternative exclusive approach aims to calculate the mixing amplitudes at the hadron level, by summing the contributions of all possible intermediate virtual states [53, 54, 77–80]. Overall, these studies hint at values of y and x of the order of few times 10^{-3}, even if the limited precision in the knowledge of some branching fractions and the current inability to perform first-principle calculations of nonperturbative matrix elements limit the precision of such approach. In particular, Ref. [53] argued that contributions to the mixing parameters from a given $SU(3)_{\mathrm{F}}$ multiplet cancel in the $SU(3)_{\mathrm{F}}$-symmetry limit. However, the only $SU(3)_{\mathrm{F}}$ breaking that arises from the different phase space of different multi-body final states within the same multiplet, can account for values of y as large as 1%. On the contrary, resonances close to the D^0-mass threshold are thought to play a less important role in the breaking of the $SU(3)_{\mathrm{F}}$ symmetry.

On the long term, the D^0-meson mixing parameters might be calculated on the lattice, by building on the methods described in Ref. [81]. In addition, a dispersion relation between the two mixing parameters has been derived in Ref. [82] under the heavy quark limit, predicting values of x between 10^{-3} and 10^{-2} if y is approximately equal to 10^{-2}. These predictions seem in agreement with the latest experimental data.

Even in absence of precise SM predictions, the peculiarly small size of the D^0 mixing parameters can be employed to set stringent limits on models of new interactions beyond the SM, typically tighter than those set thanks to the analysis of B-meson mixing, as shown in Fig. 1.5. These can be obtained by neglecting the SM contributions, and by saturating the measured values with the new dynamics, obtaining limits on energy scales as high as 10^4 TeV in Refs. [83] and [16] (the latter being based on Ref. [84]).

1.2.3 Classification of *CP* violation

The phenomenology of *CP* violation is particularly rich in flavoured neutral mesons, thanks to the fact that weak and strong phases can appear both in the mixing or in the decay amplitudes. Depending on which of these factors is responsible for *CP* violation, *CP* violating effects are conventionally classified into three categories. The first is *CP violation in the decay*, and arises if the magnitude of the decay amplitudes of *CP*-conjugated processes are different. It is defined as

$$a_f^d \equiv \frac{|A_f|^2 - |\bar{A}_{\bar{f}}|^2}{|A_f|^2 + |\bar{A}_{\bar{f}}|^2}, \tag{1.32}$$

and is the only type of *CP* violation that can be observed also in charged hadrons. The second category is *CP violation in the mixing*, and occurs if the probability of the M^0 meson to oscillate after a time t into its anti-meson $\overline{M}^0$ is different from that for the *CP*-conjugate process, where a $\overline{M}^0$ meson oscillates into a M^0 meson. This happens if and only if the magnitude of the ratio

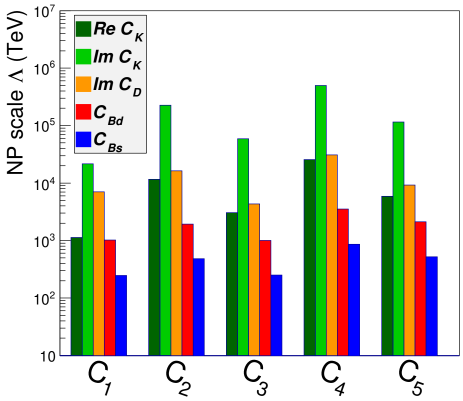

Figure 1.5: Summary of the 95% probability lower bound on the scale of new-physics (NP) interactions beyond the SM, λ, for strongly-interacting NP. Results from all of the neutral meson systems are shown. Figure taken from Ref. [16].

of the coefficients of M^0 and $\overline{M}^0$ in the expression of the mass eigenstates differs from unity, $|q/p| \neq 1$, see Eq. (1.20). In the theoretical parametrisation, this corresponds to the condition $\sin\phi_{12} \neq 0$, see Eq. (1.31). Finally, the *CP violation in the interference* arises only for final states shared by M^0 and $\overline{M}^0$ mesons, and is due to the interference between the decay without mixing, $M^0 \to f$, and the decay following mixing, $M^0 \to \overline{M}^0 \to f$. This condition occurs if

$$\mathcal{I}m(\lambda_f) + \mathcal{I}m(\lambda_{\bar{f}}) \neq 0, \tag{1.33}$$

where λ_f is defined as

$$\lambda_f \equiv \frac{q}{p}\frac{\bar{A}_f}{A_f}, \tag{1.34}$$

and $\lambda_{\bar{f}}$ is obtained from the last equation through the substitution $f \to \bar{f}$.

An alternative classification of CP violation employs only two categories, *direct* and *indirect* CP violation. Indirect CP-violating effects are those that can be described by assuming that the only source of CP violation is given by interactions of new heavy particles contributing to the mixing-matrix element M_{12}, the so-called superweak approximation [85]. On the contrary, direct CP violation encompasses all effects that cannot be explained through the assumption above. While CP violation in the mixing is indirect and CP violation in the decay is direct, CP violation in the interference can be either indirect or direct. However, although the superweak scenario has been experimentally ruled out for all of the neutral mesons, it is still used in the study of D^0 mesons to set bounds on new interactions beyond the SM, based on measurements of CP violation in the mixing and in the interference. In fact, the contribution of direct CP violation in time-dependent measurements of D^0-meson decays is still below their experimental precision.

1.3 Time-dependent CP violation in $D^0 \to h^+h^-$ decays

The discussion is now specialised to the time-dependent decay rates of D^0 and $\overline{D}^0$ mesons into two-body charged final states, where each of the two final-state particles can be either a kaon or a pion meson. These decays are the main subject of the present thesis. The $D^0 \to K^-\pi^+$

($D^0 \to K^+\pi^-$) decays are usually referenced as right-sign (wrong-sign) decays, since when the D^0 meson originates from $D^*(2010)^+ \to D^0\pi^+$ decays — the most common case in present experimental studies — the sign of the electric charges of the pions from the $D^*(2010)^+$ and D^0 decays are the same (opposite). While the $D^0 \to K^+K^-$ and $D^0 \to \pi^+\pi^-$ decays are Cabibbo suppressed (CS), right-sign decays receive mainly contributions from Cabibbo-favoured (CF) decays without mixing, and wrong-sign decays receive contributions of nearly equal size from doubly Cabibbo-suppressed (DCS) decays without mixing and CF decays following mixing.

The following exposition employs the theoretical parametrisation of Ref. [28], given the clearer insights that it provides on the dynamics at play. The corresponding expressions in the phenomenological parametrisation employed by Refs. [36, 47] are reported in Appendix A for completeness. The reader interested in a general introduction to the dynamics of the quark charm can refer to Ref. [86], which includes a historical overview of charm physics as well, while an up-to-date review of the most recent experimental and theoretical advances in D-meson mixing and *CP* violation can be found in Ref. [87].

1.3.1 Decay rates

Let us denote the amplitudes of D^0- and $\overline{D}^0$-meson decays into the final state f as

$$A_f \equiv \langle f|\, \mathcal{H} \,|D^0\rangle\,, \qquad \bar{A}_f \equiv \langle f|\, \mathcal{H} \,|\overline{D}^0\rangle\,, \tag{1.35}$$

where $\mathcal{H}$ is the $|\Delta C| = 1$ weak-interaction effective Hamiltonian that governs the decay of D^0 mesons. The time-dependent rates of D^0- and $\overline{D}^0$-meson decays into the final state f are equal to

$$\Gamma(D^0 \to f, t) = \mathcal{N}_f \left| \langle f|\mathcal{H}|D^0(t)\rangle \right|^2, \qquad \Gamma(\overline{D}^0 \to f, t) = \mathcal{N}_f \left| \langle f|\mathcal{H}|\overline{D}^0(t)\rangle \right|^2, \tag{1.36}$$

where $\mathcal{N}_f$ is a common, time-independent normalisation factor that includes the result of the phase space integration. By employing the definitions of Eq. (1.35), the last equation can be rewritten as

$$\begin{aligned} \Gamma(D^0 \to f, t) &= \mathcal{N}_f \left| A_f \langle D^0|D^0(t)\rangle + \bar{A}_f \langle \overline{D}^0|D^0(t)\rangle \right|^2, \\ \Gamma(\overline{D}^0 \to f, t) &= \mathcal{N}_f \left| A_f \langle D^0|\overline{D}^0(t)\rangle + \bar{A}_f \langle \overline{D}^0|\overline{D}^0(t)\rangle \right|^2, \end{aligned} \tag{1.37}$$

where the first and second term of the sums correspond to decays with and without flavour oscillation, respectively, which can interfere giving rise to *CP* violation in the interference. The oscillation amplitudes are given in Eq. (1.27), and can be expanded to second order in the small mixing parameters for all practical aims,

$$\begin{aligned} \langle D^0|D^0(t)\rangle = \langle \overline{D}^0|\overline{D}^0(t)\rangle &\approx e^{-i\left(M - i\frac{\Gamma}{2}\right)t} \left[1 - \frac{1}{8}(x_{12}^2 - y_{12}^2 - 2ix_{12}y_{12}\cos\phi_{12})\right] (\Gamma t)^2, \\ \langle \overline{D}^0|D^0(t)\rangle &\approx e^{-i\left(M - i\frac{\Gamma}{2}\right)t} \left(e^{-i\frac{\pi}{2}} M_{12}^* - \frac{\Gamma_{12}^*}{2}\right) t, \\ \langle D^0|\overline{D}^0(t)\rangle &\approx e^{-i\left(M - i\frac{\Gamma}{2}\right)t} \left(e^{-i\frac{\pi}{2}} M_{12} - \frac{\Gamma_{12}}{2}\right) t, \end{aligned} \tag{1.38}$$

where the following relation was used in the first equation,

$$\begin{aligned}\cos\left[\frac{1}{2}\left(\Delta m - i\frac{\Delta\Gamma}{2}\right)t\right] &= 1 - \frac{1}{2}H_{12}H_{21}t^2 + \mathcal{O}(t^4)\\ &= 1 - \frac{1}{2}\left(|M_{12}|^2 - \frac{|\Gamma_{12}|^2}{4} - i\,\mathrm{Re}\,(M_{12}\Gamma_{12}^*)\right)t^2 + \mathcal{O}(t^4)\\ &= 1 - \frac{1}{8}(x_{12}^2 - y_{12}^2 - 2ix_{12}y_{12}\cos\phi_{12})(\Gamma t)^2 + \mathcal{O}(t^4).\end{aligned} \tag{1.39}$$

Substituting the Eqs. (1.38) in the Eqs. (1.37), the time-dependent decay rates can be written as

$$\begin{aligned}\Gamma(D^0(t)\to f) = \mathcal{N}_f e^{-\tau}|A_f|^2\Big\{&1 - \tau\mathcal{R}e[ix_{12}/\lambda_f^M + y_{12}/\lambda_f^\Gamma]\\ &+ \frac{\tau^2}{4}\big(x_{12}^2\left(1/|\lambda_f^M|^2 - 1\right) + y_{12}^2\left(1/|\lambda_f^\Gamma|^2 + 1\right) + 2x_{12}y_{12}\mathcal{I}m[1/(\lambda_f^{M*}\lambda_f^\Gamma)]\big)\Big\},\\ \Gamma(\bar{D}^0(t)\to f) = \mathcal{N}_f e^{-\tau}|\bar{A}_f|^2\Big\{&1 - \tau\mathcal{R}e[ix_{12}\lambda_f^M + y_{12}\lambda_f^\Gamma]\\ &+ \frac{\tau^2}{4}\big(x_{12}^2\left(|\lambda_f^M|^2 - 1\right) + y_{12}^2\left(|\lambda_f^\Gamma|^2 + 1\right) + 2x_{12}y_{12}\mathcal{I}m[\lambda_f^{M*}\lambda_f^\Gamma]\big)\Big\},\end{aligned} \tag{1.40}$$

where terms of order higher than two in $\tau \equiv \Gamma t$ are neglected, and the following parameters are introduced,

$$\lambda_f^M \equiv \frac{M_{12}}{|M_{12}|}\frac{A_f}{\bar{A}_f}, \qquad \lambda_f^\Gamma \equiv \frac{\Gamma_{12}}{|\Gamma_{12}|}\frac{A_f}{\bar{A}_f}. \tag{1.41}$$

The $\lambda_f^{M(\Gamma)}$ parameter corresponds to decay amplitudes proceeding through dispersive (absorptive) mixing, respectively.

The analogue of all of the expressions and definitions given above for the final state f, can be obtained for the CP-conjugate final state $\bar{f}$ by substituting $f \to \bar{f}$. Note that the normalisation factor $\mathcal{N}_f$ is shared by the D^0- and $\bar{D}^0$-meson decay widths separately for each final state f and, in addition, is equal for the f and $\bar{f}$ final states ($\mathcal{N}_f = \mathcal{N}_{\bar{f}}$).

1.3.2 Cabibbo-suppressed final states

In this section f indicates either of the two CS final states K^+K^- and $\pi^+\pi^-$, and the parameters $\lambda_f^{M(\Gamma)}$ are parametrised as

$$\begin{aligned}\lambda_f^M &= \frac{M_{12}}{|M_{12}|}\frac{A_f}{\bar{A}_f} \equiv \left|\frac{A_f}{\bar{A}_f}\right| e^{i\phi_f^M},\\ \lambda_f^\Gamma &= \frac{\Gamma_{12}}{|\Gamma_{12}|}\frac{A_f}{\bar{A}_f} \equiv \left|\frac{A_f}{\bar{A}_f}\right| e^{i\phi_f^\Gamma},\end{aligned} \tag{1.42}$$

where the CP-violating weak phases ϕ_f^M and ϕ_f^Γ satisfy $\phi_f^M - \phi_f^\Gamma = \phi_{12}$, and no strong phases appear, since the final states are CP even.[8] The time-dependent decay rates are conveniently parametrised as

$$\begin{aligned}\Gamma(D^0\to f,t) &\equiv \mathcal{N}_f e^{-\tau}|A_f|^2\left(1 + c_f^+\tau + c_f'^+\tau^2\right),\\ \Gamma(\bar{D}^0\to f,t) &\equiv \mathcal{N}_f e^{-\tau}\left|\bar{A}_f\right|^2\left(1 + c_f^-\tau + c_f'^-\tau^2\right),\end{aligned} \tag{1.43}$$

[8]Since $(CP)^2 = 1$, in general a state $|f\rangle$ transforms under CP violation as $CP\,|f\rangle = \eta_{CP}^f\,|\bar{f}\rangle$, and its CP-conjugate as $CP\,|\bar{f}\rangle = (\eta_{CP}^f)^*\,|\bar{f}\rangle$, where η_{CP}^f is a complex number whose magnitude is equal to unity. For CP eigenstates, η_{CP}^f is equal to plus (minus) unity for CP-even (CP-odd) final states.

up to second order in the mixing parameters, where the parameters $c_f^{\pm}$ and $c_f'^{\pm}$ are equal to

$$\begin{aligned}
c_f^{\pm} &= \left|\frac{\bar{A}_f}{A_f}\right|^{\pm 1} (\mp x_{12}\sin\phi_f^M - y_{12}\cos\phi_f^\Gamma) \approx \mp x_{12}\sin\phi_f^M - y_{12}\cos\phi_f^\Gamma(1\mp a_f^d), \\
c_f'^{\pm} &= \frac{1}{4}(y_{12}^2 - x_{12}^2) + \frac{1}{4}(x_{12}^2 + y_{12}^2 \pm 2x_{12}y_{12}\sin\phi_{12}) \left|\frac{\bar{A}_f}{A_f}\right|^{\pm 2} \\
&\approx \tfrac{1}{2}\left[y_{12}^2 \pm x_{12}y_{12}\sin\phi_{12} \mp (x_{12}^2 + y_{12}^2)a_f^d\right].
\end{aligned} \tag{1.44}$$

The approximate expressions correspond to the limit of small *CP* violation. In particular, the parameter

$$a_f^d \equiv \frac{|A_f|^2 - |\bar{A}_f|^2}{|A_f|^2 + |\bar{A}_f|^2} \approx 1 - \left|\frac{\bar{A}_f}{A_f}\right| \tag{1.45}$$

is the *CP* asymmetry in the decay, and terms multiplying it have been expanded to first order in the *CP* violation parameters a_f^d, $\sin\phi_f^M$ and $\sin\phi_f^\Gamma$.

Finally, the following *CP*-odd and *CP*-even combinations of c_f^+ and c_f^-,

$$\Delta Y_f \equiv \frac{c_f^+ - c_f^-}{2} \approx -x_{12}\sin\phi_f^M + y_{12}\cos\phi_f^\Gamma a_f^d, \tag{1.46}$$

$$y_{CP}^f \equiv -\frac{c_f^+ + c_f^-}{2} \approx y_{12}\cos\phi_f^\Gamma, \tag{1.47}$$

are particularly convenient from an experimental point of view, and are often employed as experimental observables instead of c_f^+ and c_f^-.

1.3.3 Right-sign and wrong-sign decays

For the D^0-meson decays into RS and WS final states, denoted as $f = K^-\pi^+$ and $\bar{f} = K^+\pi^-$, respectively, the $\lambda_f^{M(\Gamma)}$ and $\lambda_{\bar{f}}^{M(\Gamma)}$ parameters are parametrised as

$$\begin{aligned}
\lambda_f^M &= \frac{M_{12}}{|M_{12}|}\frac{A_f}{\bar{A}_f} \equiv -\left|\frac{A_f}{\bar{A}_f}\right| e^{i(\phi_f^M - \Delta_f)}, \qquad &\lambda_f^\Gamma &= \frac{\Gamma_{12}}{|\Gamma_{12}|}\frac{A_f}{\bar{A}_f} \equiv -\left|\frac{A_f}{\bar{A}_f}\right| e^{i(\phi_f^\Gamma - \Delta_f)}, \\
\lambda_{\bar{f}}^M &= \frac{M_{12}}{|M_{12}|}\frac{A_{\bar{f}}}{\bar{A}_{\bar{f}}} \equiv -\left|\frac{A_{\bar{f}}}{\bar{A}_{\bar{f}}}\right| e^{i(\phi_f^M + \Delta_f)}, \qquad &\lambda_{\bar{f}}^\Gamma &= \frac{\Gamma_{12}}{|\Gamma_{12}|}\frac{A_{\bar{f}}}{\bar{A}_{\bar{f}}} \equiv -\left|\frac{A_{\bar{f}}}{\bar{A}_{\bar{f}}}\right| e^{i(\phi_f^\Gamma + \Delta_f)},
\end{aligned} \tag{1.48}$$

where the *CP*-violating weak phases ϕ_f^M and ϕ_f^Γ always satisfy $\phi_f^M - \phi_f^\Gamma = \phi_{12}$, but in general are different from those of Eq. (1.42), and Δ_f is a strong *CP*-conserving phase. The minus sign in the right-hand side of the definitions ensures that ϕ_f^M and ϕ_f^Γ are equal to their analogues for CS decays (rather than being shifted by π) in the limit of no *CP* violation in the decay, when adopting the convention that Δ_f is equal to zero rather than π in the U-spin symmetry limit.[9] Furthermore, it is useful to denote the ratio of the DCS to CF branching ratios of D^0 and $\overline{D}^0$ mesons, as well as their average, as

$$R_f^+ \equiv |A_{\bar{f}}/A_f|^2, \qquad R_f^- \equiv |\bar{A}_f/\bar{A}_{\bar{f}}|^2, \qquad R_f \equiv \frac{R_f^+ + R_f^-}{2}, \tag{1.49}$$

[9] In particular, it stems from the relative minus sign between the CKM factors involved in the CF and DCS amplitudes, see Eq. (1.5).

while the CP asymmetry in the decay of CF and DCS decays are defined as

$$a^d_f \equiv \frac{|A_f|^2 - |\bar{A}_{\bar{f}}|^2}{|A_f|^2 + |\bar{A}_{\bar{f}}|^2} \approx 1 - \left|\frac{\bar{A}_{\bar{f}}}{A_f}\right|, \qquad a^d_{\bar{f}} \equiv \frac{|A_{\bar{f}}|^2 - |\bar{A}_f|^2}{|A_{\bar{f}}|^2 + |\bar{A}_f|^2} \approx 1 - \left|\frac{\bar{A}_f}{A_{\bar{f}}}\right|, \tag{1.50}$$

respectively.

The time-dependent rates of RS decays are parametrised as

$$\begin{aligned} \Gamma(D^0 \to f, t) &\equiv \mathcal{N}_f e^{-\tau} |A_f|^2 \left(1 + \sqrt{R_f} c^+_f \tau + c'^+_f \tau^2\right), \\ \Gamma(\overline{D}^0 \to \bar{f}, t) &\equiv \mathcal{N}_f e^{-\tau} |\bar{A}_{\bar{f}}|^2 \left(1 + \sqrt{R_f} c^-_f \tau + c'^-_f \tau^2\right), \end{aligned} \tag{1.51}$$

such that the suppression of the interference term with respect to CS decays — owing to the interference of a DCS amplitude with a CF amplitude, instead of two CS amplitudes of equal size —, is absorbed by the $\sqrt{R_f}$ term and not by the $c^\pm_f$ coefficients, which are approximately equal in size to their analogues for CS decays. The coefficients $c^\pm_f$ and $c'^\pm_f$ are equal to

$$\begin{aligned} c^\pm_f &= \sqrt{\frac{R^\pm_f}{R_f}} \left|\frac{\bar{A}_f}{A_{\bar{f}}}\right|^{\pm 1} \left[-x_{12} \sin\left(\Delta_f \mp \phi^M_f\right) + y_{12} \cos\left(\Delta_f \mp \phi^\Gamma_f\right)\right] \\ &\approx \left[1 \mp \tfrac{1}{2}(a^d_{\bar{f}} + a^d_f)\right](-x_{12} \sin\Delta_f \cos\phi^M_f + y_{12} \cos\Delta_f \cos\phi^\Gamma_f) \\ &\qquad \pm x_{12} \cos\Delta_f \sin\phi^M_f \pm y_{12} \sin\Delta_f \sin\phi^\Gamma_f, \\ c'^\pm_f &= \frac{1}{4}(y^2_{12} - x^2_{12}) + \frac{1}{4} R^\pm_f \left|\frac{\bar{A}_f}{A_{\bar{f}}}\right|^{\pm 2} (x^2_{12} + y^2_{12} \pm 2 x_{12} y_{12} \sin\phi_{12}) \\ &\approx \tfrac{1}{4}(y^2_{12} - x^2_{12}) + \tfrac{1}{4} R_f \left[1 \mp (a^d_{\bar{f}} + a^d_f)\right](x^2_{12} + y^2_{12}) \pm \tfrac{1}{2} R_f x_{12} y_{12} \sin\phi_{12}, \end{aligned} \tag{1.52}$$

where in the last passage the expressions are expanded to first order in the CP violation parameters a^d_f, $a^d_{\bar{f}}$, $\sin\phi^M_f$ and $\sin\phi^\Gamma_f$. The analogues of the ΔY_f and y^f_{CP} observables of CS decays for RS decays are defined as

$$\begin{aligned} \Delta Y_f \equiv \sqrt{R_f} \times \frac{c^+_f - c^-_f}{2} \approx \sqrt{R_f} \Big[& x_{12} \cos\Delta_f \sin\phi^M_f + y_{12} \sin\Delta_f \sin\phi^\Gamma_f \\ & + \tfrac{1}{2}(a^d_{\bar{f}} + a^d_f)(x_{12} \sin\Delta_f \cos\phi^M_f - y_{12} \cos\Delta_f \cos\phi_\Gamma)\Big], \end{aligned} \tag{1.53}$$

$$y^f_{CP} \equiv -\sqrt{R_f} \times \frac{c^+_f + c^-_f}{2} \approx \sqrt{R_f} \Big[x_{12} \sin\Delta_f \cos\phi^M_f - y_{12} \cos\Delta_f \cos\phi^\Gamma_f\Big]. \tag{1.54}$$

For WS decays, the time-dependent decay rates are parametrised as

$$\begin{aligned} \Gamma(D^0(t) \to \bar{f}) &\equiv \mathcal{N}_f e^{-\tau} |A_f|^2 \left(R^+_f + \sqrt{R^+_f} c^+_{\bar{f}} \tau + c'^+_{\bar{f}} \tau^2\right), \\ \Gamma(\overline{D}^0(t) \to f) &\equiv \mathcal{N}_f e^{-\tau} |\bar{A}_{\bar{f}}|^2 \left(R^-_f + \sqrt{R^-_f} c^-_{\bar{f}} \tau + c'^-_{\bar{f}} \tau^2\right), \end{aligned} \tag{1.55}$$

where the suppression of the rates with respect to RS decays is again absorbed by the $R^\pm_f$

coefficients, and the $c_{\bar f}^{\pm}$ and $c_{\bar f}^{\prime\pm}$ coefficients are equal to

$$\begin{aligned}
c_{\bar f}^{\pm} &= \left|\frac{\bar A_{\bar f}}{A_f}\right|^{\pm 1}\left[x_{12}\sin\bigl(\Delta_f \pm \phi_f^M\bigr) + y_{12}\cos\bigl(\Delta_f \pm \phi_f^\Gamma\bigr)\right] \\
&\approx (1 \mp a_f^d)(x_{12}\sin\Delta_f\cos\phi_f^M + y_{12}\cos\Delta_f\cos\phi_f^\Gamma) \pm x_{12}\cos\Delta_f\sin\phi_f^M \mp y_{12}\sin\Delta_f\sin\phi_f^\Gamma, \\
c_{\bar f}^{\prime\pm} &= \frac{1}{4}(x_{12}^2 + y_{12}^2 \pm 2x_{12}y_{12}\sin\phi_{12})\left|\frac{\bar A_{\bar f}}{A_f}\right|^{\pm 2} + \frac{1}{4}R_f^{\pm}(y_{12}^2 - x_{12}^2) \\
&\approx \tfrac{1}{4}\left[(x_{12}^2 + y_{12}^2)(1 \mp 2a_f^d) \pm 2x_{12}y_{12}\sin\phi_{12}\right] + \tfrac{1}{4}R_f^{\pm}(y_{12}^2 - x_{12}^2).
\end{aligned} \tag{1.56}$$

Again, terms multiplying a_f^d or $a_{\bar f}^d$ have been expanded to first order in the *CP* violation parameters in the last passage.

1.3.4 Theoretical predictions and final-state dependence

For the purposes of this discussion, it is useful to parametrise the decay amplitudes of D^0 and $\overline{D}^0$ mesons into the final states f and $\bar f$ as

$$\begin{aligned}
A_f &\equiv A_f^0 e^{+i\phi_f^0}[1 + r_f e^{i(\delta_f + \phi_f)}], \quad A_{\bar f} \equiv A_{\bar f}^0 e^{i(\Delta_f^0 + \phi_{\bar f}^0)}[1 + r_{\bar f} e^{i(\delta_{\bar f} + \phi_{\bar f})}], \\
\bar A_{\bar f} &\equiv A_f^0 e^{-i\phi_f^0}[1 + r_f e^{i(\delta_f - \phi_f)}], \quad \bar A_f \equiv A_{\bar f}^0 e^{i(\Delta_f^0 - \phi_{\bar f}^0)}[1 + r_{\bar f} e^{i(\delta_{\bar f} - \phi_{\bar f})}].
\end{aligned} \tag{1.57}$$

Here, A_f^0 and $A_{\bar f}^0$ are the magnitudes of the dominant SM amplitudes, r_f and $r_{\bar f}$ are the relative magnitudes of the subleading amplitudes (either from the SM or from interactions beyond the SM) with respect to the dominant ones, ϕ_f^0 and $\phi_{\bar f}^0$ are unobservable weak phases, and Δ_f^0 is a strong phase. Finally, ϕ_f and $\phi_{\bar f}$ (δ_f and $\delta_{\bar f}$) are the relative weak and strong phases between the subleading and dominant decay amplitudes. For CS decays into self-conjugate *CP*-even final states, the expressions for A_f and $\bar A_f$ are simplified, yielding

$$\begin{aligned}
A_f &\equiv A_f^0 e^{+i\phi_f^0}[1 + r_f e^{i(\delta_f + \phi_f)}], \\
\bar A_f &\equiv A_f^0 e^{-i\phi_f^0}[1 + r_f e^{i(\delta_f - \phi_f)}],
\end{aligned} \tag{1.58}$$

where a minus sign would have appeared on the right-hand side of the second expression if the final states had been *CP*-odd. Employing these definitions, the angles ϕ_f^M and ϕ_f^Γ defined in Eqs. (1.42) for CS decays can be written as

$$\phi_f^{M(\Gamma)} \approx \phi^{M(\Gamma)} + 2\phi_f^0 + 2r_f\cos\delta_f\sin\phi_f \tag{1.59}$$

to first order in r_f, while their analogues and the strong phase Δ_f of CF and DCS decays are equal to

$$\begin{aligned}
\phi_f^{M(\Gamma)} &\approx \pi + \phi^{M(\Gamma)} + \phi_f^0 + \phi_{\bar f}^0 + r_f\cos\delta_f\sin\phi_f + r_{\bar f}\cos\delta_{\bar f}\sin\phi_{\bar f}, \\
\Delta_f &\approx \Delta_f^0 - r_f\sin\delta_f\cos\phi_f + r_{\bar f}\sin\delta_{\bar f}\cos\phi_{\bar f},
\end{aligned} \tag{1.60}$$

where the term π in the first equation takes into account the relative minus sign between the CKM coefficients of the DCS and CF decay amplitudes, and ensures that the $\phi_f^{M(\Gamma)}$ angles are equal to their analogues for CS decays in the limit of no *CP* violation. Also the *CP* violation in the decay can be easily calculated in terms of the introduced parameters, yielding

$$a_f^d \approx -2r_f\sin\delta_f\sin\phi_f \tag{1.61}$$

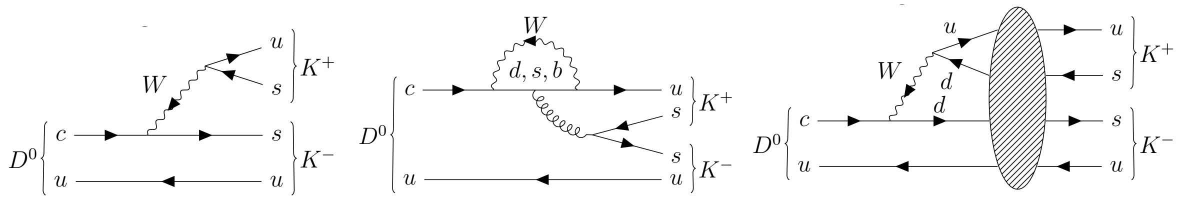

Figure 1.6: Examples of Feynman diagrams contributing to the $D^0 \to K^+K^-$ decay. The tree diagram (left) is proportional to λ^s_{cu}, while the electroweak-loop diagram (centre) is proportional to λ^q_{cu}, where q is the internal quark of the loop. Finally, the rightmost diagram represents one of the possible contributions to rescattering, where the blob is a placeholder for the rescattering of the $\pi^+\pi^-$ state into the K^+K^- final state through strong interactions. This diagram is proportional to $\lambda^d_{cu} = -\lambda^s_{cu} - \lambda^b_{cu}$.

to first order in r_f, for all categories of decays (with the only substitution $f \to \bar{f}$ for WS decays).

In the SM the factors r_f and $r_{\bar{f}}$ in Eq. (1.57), and consequently the CP violation in the decay, can be neglected for CF and DCS decays, since these decays are not sensitive to QCD electroweak-loop and chromomagnetic dipole operators. On the contrary, the factor r_f of CS decays cannot be neglected in Eq. (1.58). Here, there is an ambiguity in the choice of the division between the dominant and subleading decay amplitudes, which is determined by the choice of the CKM coefficient of the dominant amplitude (in any case, the choice does not affect the observable quantities). Thanks to the unitarity of the CKM matrix, only two of the three λ^d_{cu}, λ^s_{cu} and λ^b_{cu} coefficients contributing to $c \to u$ transitions are independent. Conventionally, the dominant amplitude is chosen to be proportional to the U-spin odd quantity $\Sigma \equiv (\lambda^s_{cu} - \lambda^d_{cu})/2 \approx \lambda$. The subleading amplitudes are thus proportional to $(\lambda^s_{cu} + \lambda^d_{cu})/2 = -\lambda^b_{uc}/2 = -\lambda^5 A^2(\bar{\rho} - i\bar{\eta})/2$ in the SM (see Refs. [22, 88] for a discussion of the amplitudes parametrisation). This result is general and does not depend on the chosen convention. Therefore, the factor r_f in Eq. (1.61) is proportional to $|\lambda^b_{cu}/\Sigma|$, and the angle ϕ_f is approximately equal to $\pi - \gamma$, where the γ angle is defined as $\gamma \equiv \arg(V_{cb}V^*_{ub}) \approx \operatorname{atan}(\bar{\eta}/\bar{\rho}) \approx 66°$ [89]. A rough upper bound on the size of CP violation in the decay for CS final states is thus given by $2r_f|\sin\phi_f| \approx |\mathrm{Im}(\lambda^b_{cu}/2\Sigma)| = |\lambda^b_{cu}/2\Sigma|\sin\gamma \approx 6 \times 10^{-4}$ [47] (note, however, that this value might be significantly enhanced in $D^0 \to K^0_S K^0_S$ and $D^0 \to K^0_S K^{*0}$ decays [90, 91]). The size of CP violation is further suppressed by the sine of the relative strong phase between the subleading ($\Delta U = 0$, $\Delta U_3 = 0$) and dominant ($\Delta U = 1$, $\Delta U_3 = 0$) amplitudes, and by the ratio of their magnitudes (excluding the CKM factors). To provide predictions for these nonperturbative quantities is very challenging. The dominant amplitude A^0_f is mostly determined by tree-level decays, plus subleading electroweak-loop contributions and possible rescattering effects. On the other hand, the subleading decay amplitudes are only due to electroweak-loop diagrams or to rescattering effects. Some examples of these diagrams are shown in Fig. 1.6 for the $D^0 \to K^+K^-$ decay. The strong phase difference δ is expected to be of order of unity due to large scattering at the charm-mass scale, and does not necessarily lead to a large suppression. On the other hand, the ratio of the magnitudes of subleading to dominant amplitudes has been estimated using dynamical methods of QCD in Refs. [14, 92–94] and is expected to lead a suppression of up to one order of magnitude of the asymmetry. The predictions for the magnitudes of $a^d_{K^+K^-}$ and $a^d_{\pi^+\pi^-}$ are accordingly in the range between 10^{-4} and 10^{-3}. However, all of the predictions rely on model assumptions, like for example the quark-hadron duality, and it cannot be excluded that the suppression is smaller due to large rescattering at the charm-mass scale, as already noted in 1989 in Ref. [95]. Finally, U-spin symmetry implies that $a^d_{K^+K^-}$ and $a^d_{\pi^+\pi^-}$ are approximately equal in magnitude and opposite in sign.

Alternative theoretical studies have been performed to estimate the size of the various topological amplitudes that contribute to the dominant and subleading amplitudes. They parametrise the branching fractions and the *CP* asymmetries of all of the D-meson final states in terms of these topological amplitudes, and fit them to their measured values. All of these studies, see Refs. [88, 95–100], rely on perturbative parametrisations of the amplitudes in $SU(3)_{\mathrm{F}}$ or U-spin breaking, and are necessarily data driven. Some of them further rely on rescattering models [19, 101, 102]. However, while the values of the branching fractions fix the size of the dominant amplitudes A_0^f, they are only not able to predict the absolute size of *CP* violation, but only to relate its size among decays into different final states. In fact, the size of the electroweak-loop diagrams and of rescattering effects, which are responsible for *CP* violation, contribute only marginally to the branching fractions (or, in the case of rescattering, cannot be distinguished unambiguously from the tree-level-like amplitudes).

The LHCb collaboration reported in 2019 the first observation of *CP* violation in charm-hadron decays — a landmark result for particle physics —, by measuring the difference between the *CP* asymmetries of $D^0 \to K^+K^-$ and $D^0 \to \pi^+\pi^-$ decays,

$$a^d_{K^+K^-} - a^d_{\pi^+\pi^-} = (-15.7 \pm 2.9) \times 10^{-4}.$$

This observable is very convenient from an experimental point of view, since most nuisance asymmetries cancel in the difference, and allows to achieve a much better precision than the measurements in the single decay channels [103]. The magnitude of the measured value lies at the upper edge of the SM predictions, and challenges the predictions based on first-principle QCD dynamics [14, 94]. However, it is not excluded that the discrepancy is due to a mild enhancement of rescattering beyond expectations. This possibility had already been proposed in 2012, see Refs. [88, 96, 97, 99, 100], to explain the large value of $a^d_{K^+K^-} - a^d_{\pi^+\pi^-}$ measured by the LHCb collaboration in that same year, $(-8.2 \pm 2.4) \times 10^{-3}$ [104], which later turned out to be due to a large statistical fluctuation. Technically, it would correspond to a mild enhancement of the $\Delta U = 0$ over $\Delta U = 1$ decay amplitudes (analogous but smaller in size than the $\Delta I = 1/2$ rule of kaon mesons[10]), and it has been explored in detail recently in Ref. [22]. An explicit proposal of a possible source of rescattering enhancement has been put forward in Ref. [23], while the global fits relying on $SU(3)_{\mathrm{F}}$ symmetry have been updated after the first observation of *CP* violation in Refs. [24, 26]. However, like after the 2012 measurement [98], other authors question the possibility of such an enhancement, and attribute the effect to new interactions beyond the SM [20]. The impact of possible contributions of interactions beyond the SM to the asymmetry had already been analysed in Refs. [14, 97, 100, 106] before the LHCb discovery, and has been further explored recently in Refs. [20, 25, 27].

Therefore, further measurements of *CP* asymmetries in D-meson decays are crucial to shed light on the dynamics underlying the measurement of $a^d_{K^+K^-} - a^d_{\pi^+\pi^-}$ [107]. In particular, measuring the *CP* asymmetries separately in the two decay channels would allow to test the U-spin predictions, which might be violated by new interaction beyond the SM. Another important goal is to improve the precision with which the branching fractions and *CP* asymmetries of other CS decay channels of D^0 and $D^+_{(s)}$ mesons are known. This would allow to test the sum rules relating the *CP* asymmetries of different decay channels, and to improve the precision of the predictions provided by the global fits to the topological decay amplitudes, see for example Refs. [21, 24, 99, 100]. New interactions beyond the SM can in general violate the sum rules, and cause inconsistencies within the fits. However, currently there are only few channels where precisions below 10^{-3} for the *CP* asymmetries can be achieved [103, 108].

[10]See Ref. [105] and references therein for an introduction to the $\Delta I = 1/2$ rule.

On the other hand, complementary information might be gained from measurements of CP violation in the mixing, which is expected to be smaller than CP violation in the decay by around one order of magnitude [28, 29, 73, 109, 110]. The CP violation in the mixing originates from the transitions amplitudes Γ_{12} and M_{12}, which in the SM can be written as

$$\Gamma_{12}^{\rm SM} = -\sum_{i,j=d,s} \lambda_{cu}^i \lambda_{cu}^j \Gamma_{ij}, \qquad M_{12}^{\rm SM} = -\sum_{i,j=d,s,b} \lambda_{cu}^i \lambda_{cu}^j M_{ij}, \tag{1.62}$$

where Γ_{ij} (M_{ij}) is identified, at the quark level, with a box diagram containing internal on-shell (off-shell) quarks i and j. Therefore, only the M_{ij} amplitudes receive contributions from internal b quarks. Employing the CKM unitarity, the absorptive mixing amplitude can be written as

$$\Gamma_{12}^{\rm SM} = \frac{(\lambda_{cu}^s - \lambda_{cu}^d)^2}{4}\Gamma_2 + \frac{(\lambda_{cu}^s - \lambda_{cu}^d)\lambda_{cu}^b}{2}\Gamma_1 + \frac{(\lambda_{cu}^b)^2}{4}\Gamma_0, \tag{1.63}$$

where $\Gamma_{2,1,0}$ are the $\Delta U_3 = 0$ elements of the $\Delta U = 2, 1, 0$ multiplets, respectively. Explicitly, they are equal to

$$\begin{aligned} \Gamma_2 &= \Gamma_{ss} + \Gamma_{dd} - 2\Gamma_{sd} \sim (s\bar{s} - d\bar{d})^2 = \mathcal{O}\big(\epsilon^2\big), \\ \Gamma_1 &= \Gamma_{ss} - \Gamma_{dd} \sim (s\bar{s} - d\bar{d})(s\bar{s} + d\bar{d}) = \mathcal{O}(\epsilon), \\ \Gamma_0 &= \Gamma_{ss} + \Gamma_{dd} + 2\Gamma_{sd} \sim (s\bar{s} + d\bar{d})^2 = \mathcal{O}(1), \end{aligned} \tag{1.64}$$

where the two rightmost terms of the equalities represent the flavour structure of the diagrams ($\Gamma_{ij} \sim (i\bar{i})(j\bar{j})$) and their suppression in terms of the U-spin breaking parameter $\epsilon \sim 0.4$ [28]. Even though Γ_2 is second order in ϵ, it is expected to provide the dominant contribution to $\Gamma_{12}^{\rm SM}$, owing to the hierarchy among the CKM elements that multiply $\Gamma_{2,1,0}$. In fact, the values of $(\lambda_{cu}^s - \lambda_{cu}^d)/2$ and $\lambda_{cu}^b/2$ are equal to

$$\begin{aligned} \frac{\lambda_{cu}^s - \lambda_{cu}^d}{2} &\approx \lambda - \frac{\lambda^3}{2} - \lambda^5\frac{1+4A^2}{8} + \frac{A^2\lambda^5}{2}(\bar{\rho} - i\bar{\eta}) \approx +0.22 - i\,6.6\times10^{-5}, \\ \frac{\lambda_{cu}^b}{2} &\approx \frac{A^2\lambda^5}{2}(\bar{\rho} - i\bar{\eta}) \approx +2.6\times10^{-5} - i\,6.6\times10^{-5}, \end{aligned} \tag{1.65}$$

where terms of order $\mathcal{O}\big(\lambda^6\big)$ are neglected. Therefore, the coefficients that multiply $\Gamma_{2,1,0}$ are equal to

$$\begin{aligned} \tfrac{1}{4}(\lambda_{cu}^s - \lambda_{cu}^d)^2 &\approx +4.9\times10^{-2} - i\,2.9\times10^{-5}, \\ \tfrac{1}{2}(\lambda_{cu}^s - \lambda_{cu}^d)\lambda_{cu}^b &\approx +1.2\times10^{-5} - i\,2.9\times10^{-5} \\ \tfrac{1}{4}\lambda_{cu}^b &\approx -3.7\times10^{-9} - i\,3.5\times10^{-9}, \end{aligned} \tag{1.66}$$

respectively. The coefficients of Γ_1 and Γ_0 are suppressed by three and seven orders or magnitude with respect to that of Γ_2. Thus, the smaller U-spin suppression is not able to compensate for the CKM suppression. On the other hand, these terms are essential to give rise to CP violation in the mixing and it is worth noting that, differently by the coefficient of Γ_2, they possess significant complex phases. The decomposition of $M_{12}^{\rm SM}$ is analogous to that of $\Gamma_{12}^{\rm SM}$ in Eq. (1.63), but differently from Eq. (1.67), the M_1 and M_0 elements receive contributions also from internal b quarks,

$$\begin{aligned} M_2 &= M_{ss} + M_{dd} - 2M_{sd} \sim (s\bar{s} - d\bar{d})^2 = \mathcal{O}\big(\epsilon^2\big), \\ M_1 &= M_{ss} - M_{dd} + M_{sb} - M_{db} \sim (s\bar{s} - d\bar{d})(s\bar{s} + d\bar{d} + b\bar{b}) = \mathcal{O}(\epsilon), \\ M_0 &= M_{ss} + M_{dd} + 2M_{sd} + M_{sb} + M_{db} + M_{bb} \sim (s\bar{s} + d\bar{d})(s\bar{s} + d\bar{d} + b\bar{b}) + (b\bar{b})^2 = \mathcal{O}(1). \end{aligned} \tag{1.67}$$

However, the U-spin hierarchy among the elements remains the same.

It is now possible to introduce two observable mixing phases to parametrise the *CP* violation in the mixing and in the interference. These are defined as the phases of the transition amplitudes with respect to their dominant $\Delta U = 2$ components,

$$\phi_2^M \equiv \arg\left[\frac{M_{12}}{\frac{1}{4}(\lambda_{cu}^s - \lambda_{cu}^d)M_2}\right], \qquad \phi_2^\Gamma \equiv \arg\left[\frac{\Gamma_{12}}{\frac{1}{4}(\lambda_{cu}^s - \lambda_{cu}^d)\Gamma_2}\right]. \tag{1.68}$$

These phases can receive contributions also from new interactions beyond the SM and satisfy $\phi_2^M - \phi_2^\Gamma = \phi_{12}$. Their magnitude can be estimated in the SM, for example for ϕ_2^Γ, by observing that the phase of $\Gamma_{12}^{\rm SM}$ in Eq. (1.63) is mainly due to the small imaginary part of the term linear in U-sping breaking. Therefore, it is approximately equal to [28, 29]

$$|\phi_2^\Gamma| \approx \left|2\,\mathrm{Im}\left(\frac{\lambda_{cu}^b}{\lambda_{cu}^s - \lambda_{cu}^d}\right)\frac{\Gamma_1}{\Gamma_2}\right| \approx \left|\frac{\lambda_{cu}^b}{\lambda}\right| \sin\gamma \frac{1}{\epsilon} \approx (2.2\times 10^{-3}) \times \frac{0.3}{\epsilon}, \tag{1.69}$$

with the phase ϕ_2^M expected to be of the same order as well. These results hold up to a shift of π, which is however disfavoured by experimental data, as shown in the next chapter.

The phases ϕ_f^M and ϕ_f^Γ defined in Eqs. (1.42) and (1.48) are approximately equal to these intrinsic mixing phases, apart from a subleading correction $\delta\phi_f \equiv \phi_f^M - \phi_2^M = \phi_f^\Gamma - \phi_2^\Gamma$ which depends on the final state but is shared by the absorptive and dispersive phases. These final-state corrections $\delta\phi_f$ for right-sign and wrong-sign decays are of order of 10^{-6} and can be neglected [28]. On the contrary, they are suppressed only by one further order of magnitude in U-spin breaking with respect to $\phi_2^{M(\Gamma)}$ for the CS final states [28, 29]. In fact, if there is a large rescattering contribution to the decay amplitude, its *CP* violating contribution is not suppressed by U-spin breaking like the electroweak-loop diagrams (or the box diagrams of mixing) with internal d and s quarks; furthermore, *CP* violation can arise from electroweak-loop diagrams with an internal b quark as well. In particular, employing Eq. (1.59) and noting that the convention-dependent phase $2\phi_f^0$ cancels in the difference with $\phi_2^{M(\Gamma)}$, the misalignment can be written as

$$\delta\phi_f = 2r_f \cos\delta_f \sin\phi_f \approx -\cot\delta_f a_f^d, \tag{1.70}$$

where Eq. (1.61) has been used.

This result allows to separate the final-state dependent contributions from the final-state independent ones in the observables defined in Sects. 1.3.2 and 1.3.3. In particular, for the ΔY observable defined in Eq. (1.46), which is the subject of the present thesis, the result is

$$\Delta Y_f \approx -x_{12}\sin\phi_2^M + y_{12}\cos\phi_2^\Gamma a_f^d \left(1 + \frac{\cos\phi_2^M}{\cos\phi_2^\Gamma}\frac{x_{12}}{y_{12}}\cot\delta_f\right), \tag{1.71}$$

where the first term is universal and the second encloses the final-state dependence. As already mentioned, the SM predictions of ϕ_2^M are of order of 2 mrad [28, 29] or less [110]. Given the current experimental measurements on the mixing parameter x_{12} [47], the final-state independent contribution is expected to be around few times 10^{-5} in the SM, even though values as high as 10^{-4} cannot be excluded given the approximations in the estimate presented above [29]. On the other hand, using available experimental data [18, 47] and the minimal assumption (motivated by U-spin symmetry) that $a_{K^+K^-}^d$ and $a_{\pi^+\pi^-}^d$ have opposite signs, $y_{12}|a_f^d|$ is estimated to be less than 0.13×10^{-4} at 90% confidence level. The factor $\frac{x_{12}}{y_{12}}\cot\delta_f$ could enhance the dependence on the final state, even though this effect is expected to be small since x_{12}/y_{12} is measured to be smaller than unity [47], and the phase δ_f is expected to be of $\mathcal{O}(1)$ due to large rescattering at the charm-mass scale (in particular, the smaller $\sin\delta_f$ is, the more difficult it is to explain the value of $a^d_{K^+K^-} - a^d_{\pi^+\pi^-}$ within the SM, see Eq. (1.61)).

Thus, on the whole the magnitude of ΔY_f is expected to lie in the range 10^{-5}–10^{-4} in the SM. At the current level of experimental precision, approximately 1×10^{-4}, final-state dependent contributions to ΔY_f can be neglected. Therefore, measurements of $\Delta Y_{K^+K^-}$ and $\Delta Y_{\pi^+\pi^-}$ are expected to agree with each other, and a nonzero measurement of their combination ΔY would be interpreted in terms of a single dispersive mixing phase ϕ_2^M common to all time-dependent charm decays, $\Delta Y \approx -x_{12}\sin\phi_2^M$. The limit in which the final-state dependent contributions to the weak phases ϕ_f^M and ϕ_f^Γ are neglected has been named *approximate universality* in Ref. [28]. The corresponding parametrisation of CP violation in terms of the two phases ϕ_2^M and ϕ_2^Γ is equivalent to that based on $|q/p|$ and ϕ_2 employed by the HFLAV collaboration, as proven in Ref. [28]. The main methods employed to measure the parameters of mixing and time-dependent CP violation in charm decays, x_{12}, y_{12}, ϕ_2^M and ϕ_2^Γ, are presented in the next chapter.

Chapter 2

Experimental status

This chapter describes the experimental strategies used to measure the parameters of mixing and time-dependent CP violation introduced in the previous chapter by employing two-body D^0 decays. A detailed review of the approaches used to measure the parameter ΔY is provided. Then, it is pointed out that neglected effects in the past measurements of the y_{CP} parameter caused biases of around 6%, which is similar in size to the uncertainty of the world average, approximately 16%. The relative sensitivities of the different observables and measurements are discussed, and the experimental status is reviewed. Finally, a brief overview of the measurement presented in this thesis is sketched.

2.1 Observables of time-dependent CP violation in charm-quark decays

The following sections describe the various methods employed to measure the theoretical observables ΔY and y_{CP}, as well as the time-dependence of the WS decay rate. The approximations inherent to each method are highlighted. The less sensitive $\Delta Y_{K^-\pi^+}$ observable is discussed as well, and the measurement of the slope of the time-dependent untagged asymmetry of $K^-\pi^+$ decays is proposed as a possible complementary experimental observable. Finally, the main time-dependent measurements of multibody decays and the measurement of the strong phase $\Delta_{K^-\pi^+}$ at charm-factory experiments are sketched. In the sections that discuss CS decays, the ratio of the squared decay amplitudes of $D^0 \to K^+\pi^-$ to $D^0 \to K^-\pi^+$ decays is denoted with $R_{K\pi}$ instead of R_f or $R_{K^-\pi^+}$ to avoid ambiguities with the CS final state f and to keep the notation compact. With the same aim, the strong phase $\Delta_{K^-\pi^+}$ is indicated with $\Delta_{K\pi}$.

2.1.1 $\Delta Y_{K^+K^-}$ and $\Delta Y_{\pi^+\pi^-}$

The parameter ΔY_f introduced in Sect. 1.3.2, where f is equal to K^+K^- or $\pi^+\pi^-$, has been measured with two alternative approaches. In the first, the time distributions of D^0 and $\overline{D}^0$ mesons into CS and RS final states are modelled with an exponential function, $\exp(-\hat{\Gamma}\tau)$, neglecting the coefficients quadratic in the mixing parameters in Eqs. (1.43) and (1.51). The effective decay widths of CS decays are thus approximately equal to $\hat{\Gamma}_{D^0/\overline{D}^0\to f} \approx 1 - c_f^{\pm}$, while those of RS decays are equal to $\hat{\Gamma}_{D^0\to f/\overline{D}^0\to \bar{f}} \approx 1 - \sqrt{R_f}c_f^{\pm}$. The parameter ΔY_f can be measured as

$$\frac{\Delta Y_f}{1+y_{CP}^{K^-\pi^+}} \approx -\frac{\hat{\Gamma}_{D^0\to f} - \hat{\Gamma}_{\overline{D}^0\to f}}{\hat{\Gamma}_{D^0\to K^-\pi^+} + \hat{\Gamma}_{\overline{D}^0\to K^+\pi^-}}, \tag{2.1}$$

where $y_{CP}^{K^-\pi^+}$, which is defined in Eq. (1.54), can be neglected in the denominator of the left-hand side, or in other words the approximation that $\hat{\Gamma}$ is equal to unity for RS decays can be employed. In fact, $y_{CP}^{K^-\pi^+}$ provides a multiplicative correction to the measurement of ΔY_f which is smaller than 10^{-3} ($\sqrt{R_f}$ is equal $(5.87 \pm 0.02)\%$, and both mixing parameter are less than 1% [47]). This approach was first employed, although with a relative minus sign in the definition of ΔY_f, in Ref. [57]. The A_Γ observable, which has been used as alternative to ΔY_f in Refs. [59,111,112], is similarly defined as the asymmetry of the effective decay widths of D^0 and $\overline{D}^0$ mesons into final state f,

$$A_\Gamma^f \equiv \frac{\hat{\Gamma}_{D^0\to f} - \hat{\Gamma}_{\overline{D}^0\to f}}{\hat{\Gamma}_{D^0\to f} + \hat{\Gamma}_{\overline{D}^0\to f}}, \tag{2.2}$$

and is related to ΔY_f by

$$A_\Gamma^f \approx -\frac{\Delta Y_f}{1+y_{CP}^f}. \tag{2.3}$$

Since the y_{CP}^f parameter is less than 1% [57,59,61], the negative of A_Γ^f coincides with ΔY_f up to 1% relative corrections. This approach is more convenient than that of Eq. (2.1), since it does not require to measure of the effective lifetime of $D^0 \to K^-\pi^+$ decays, but implies essentially the same experimental challenges.

While the measurements based on the determination of the effective decay widths has been employed successfully so far, it presents two disadvantages. First, as the statistical precision improves, modelling the time distribution of the decays with an exponential function might not be a good approximation any longer, since *CP*-even corrections to the exponential decay rate quadratic in decay time and in the mixing parameters in Eq. (1.43) can be as large as the *CP*-odd first-order ones, see Eq. (1.44). On the other hand, measuring the effective lifetimes is very challenging, since it requires a precise knowledge of the selection efficiency as a function of decay time. While at B-factory experiments this task can be accomplished with relative ease, as the low background allows implementing a rather simple trigger selection that does not bias significantly the decay time distribution, and the angular acceptance is close to the full solid angle, this is not the case for experiments at hadron colliders like CDF and LHCb. In the latter ones, tight and complex requirements on decay-time related quantities, such as the flight distance of the D^0 meson, are needed to select a pure sample of decays from the near-overwhelming background of particles produced in the collision between the hadron bunches. Furthermore, the interactions between the colliding hadrons and the distribution of the particles produced in the collision are more difficult to simulate (the number and distribution of the particles produced in the collisions affect the detection efficiency of the signal decays). Finally, the geometrical acceptance of the experiment plays a more important role as well. For example, at LHCb the larger momentum of the D^0 mesons with respect to B-factories causes a decrease of their reconstruction efficiency at large decay times. In fact, a small but nonnegligible fraction of decays happening close to the boundary of the vertex tracker or between its silicon layers, which are likely to correspond to large decay times, are not reconstructed. All in all, the time-dependent efficiency is not reproduced by simulation with the required level of accuracy at hadron-collider experiments, and data-driven methods must be developed to perform the measurement.

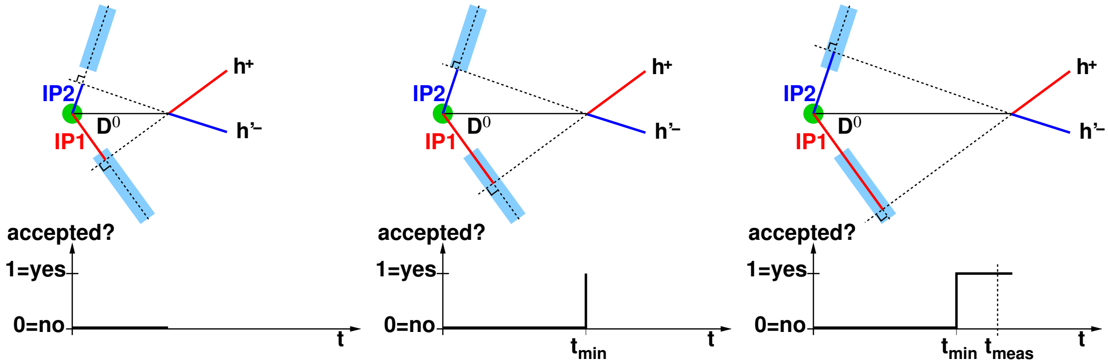

Figure 2.1: Variation of the decay-time acceptance for a $D^0 \to h^+h^-$ decay when moving the pp vertex along the D^0-meson momentum vector. The trigger requires the impact parameter of the hadron tracks with respect to the pp vertex to be larger than a fixed value. The shaded light-blue regions show the bands for accepting the tracks impact parameter. While the impact parameter of the negative track (IP2) is too low in the left plot, it reaches the accepted range in the central one. The actual measured decay time, t_{meas}, lies in the accepted region, which continues to larger decay times (right plot). Figure taken from Ref. [111].

At the LHCb experiment, the so-called *swimming* procedure [111, 113] was proposed and employed to analyse the data collected during 2011 [112]. It consists in calculating the per-candidate time acceptance by moving the proton–proton collision vertex in finite steps along the D^0 flight-distance direction, thus simulating smaller or larger decay times. For each step, the trigger selection algorithm is run, and the acceptance function is calculated as a step function, equal to unity or zero depending on the event being selected by the trigger or not, as shown in Fig. 2.1. However, while this procedure reproduces accurately the efficiency of the trigger requirements, it does not model the detector efficiency nor the geometrical acceptance. In fact, the pp vertex is shifted instead of the D^0 decay vertex. This approximation may play an important role, especially as far as the efficiency of the vertex detector is concerned. Furthermore, since the trigger selection needs to be repeated order of 100 times for each event in order to calculate the acceptance function with sufficient precision, this method requires significant computing power, and is likely to become unsustainable as the collected data increase. Already with the full data sample collected during 2011–2012, it has been used only as a cross-check of the baseline measurement [114], and even there it has been applied only to half of the decays of the control $D^0 \to K^-\pi^+$ channel, owing to computing constraints.

An alternative approach has thus been developed to overcome the intrinsic difficulties of measuring effective decay widths. This is based on the measurement of the time-dependent asymmetry of the decay rates of D^0 and $\overline{D}{}^0$ decays,

$$A_{CP}(f,t) \equiv \frac{\Gamma(D^0 \to f,t) - \Gamma(\overline{D}{}^0 \to f,t)}{\Gamma(D^0 \to f,t) + \Gamma(\overline{D}{}^0 \to f,t)}, \tag{2.4}$$

which is equal to

$$A_{CP}(f,t) \approx a_f^d + \frac{4|A_f|^2|\bar{A}_f|^2}{(|A_f|^2 + |\bar{A}_f|^2)^2} \times \Delta Y_f \frac{t}{\tau_{D^0}} \tag{2.5}$$

up to second order in the mixing parameters, where the coefficient in front of ΔY_f differs from unity by approximately $(a_f^d)^2/2 \le 10^{-6}$ [18, 30]. Therefore, ΔY_f is equal to the slope of $A_{CP}(f,t)$ up to negligible corrections. This approach has been employed in Refs. [114–118] where, however, slope of Eq. (2.5) is indicated as $-A_\Gamma^f$, neglecting y_{CP}^f in Eq. (2.3). This approach has two advantages over the method based on the measurement of the effective decay widths. First, the *CP*-even quadratic corrections to the exponential decay-time distribution in Eq. (1.43) cancel at numerator. Second, measuring the asymmetry does not require a precise knowledge of the selection efficiency of D^0 mesons as a function of time, since this cancels out in the ratio, but only of possible differences between the selection efficiencies of D^0 and $\overline{D}^0$ mesons.

2.1.2 $y_{CP}^{K^+K^-}$ and $y_{CP}^{\pi^+\pi^-}$

The parameter y_{CP}^f, where f is equal to K^+K^- or $\pi^+\pi^-$, has been measured by using either of the two strategies outlined in the previous section, with analogous experimental challenges and advantages. Until recently, it has mostly been measured from the effective decay widhts of $D^0 \to f$ and $D^0 \to K^-\pi^+$ decays [57, 59, 119–121], as

$$y_{CP}^f - y_{CP}^{K^-\pi^+} \approx \frac{\hat{\Gamma}_{D^0\to f} + \hat{\Gamma}_{\overline{D}^0\to f}}{\hat{\Gamma}_{D^0\to K^-\pi^+} + \hat{\Gamma}_{\overline{D}^0\to K^+\pi^-}} - 1. \tag{2.6}$$

whereas the approach based on the time-dependent ratio of the yields of $D^0 \to f$ and $D^0 \to K^-\pi^+$ decays has been employed only in the latest LHCb measurement [61], using

$$\frac{\Gamma(D^0\to f,t) + \Gamma(\overline{D}^0\to f,t)}{\Gamma(D^0\to K^-\pi^+,t) + \Gamma(\overline{D}^0\to K^+\pi^-,t)} \approx \text{const.} \times [1 - (y_{CP}^f - y_{CP}^{K^-\pi^+})\tau]. \tag{2.7}$$

The second approach is again more convenient from an experimental point of view, since it requires to know only the difference between the time-dependent efficiencies of reconstructing $D^0 \to f$ and $D^0 \to K^-\pi^+$ decays, and not the single efficiencies. However, in all of the references mentioned above, as well as in the world averages to the charm mixing and *CP* violation parameters [28, 47, 122, 123], the $y_{CP}^{K^-\pi^+}$ term has been neglected, assuming that the effective decay rate of RS decays is equal to unity. This approximation is no longer accurate at the current level of precision, and the linear terms in Eq. (1.51) need to be taken into account. In fact, the value of $y_{CP}^{K^-\pi^+}$ is smaller than that of y_{CP} approximately by a factor of $R_{K\pi} \approx (5.87\pm0.02)\%$ [47], *cf.* Eqs. (1.47) and (1.54), which is around 40% of the relative precision of the current world average of y_{CP}, approximately 16% (1.1×10^{-3} in absolute value). The impact of neglecting $y_{CP}^{K^-\pi^+}$ in the world average is shown in Appendix B.4. On the long term, also the quadratic terms $c_f'^{\pm}$ in Eqs. (1.44) and (1.52) might need to be taken into account in the determination of the effective decay widths. A similar argument applies to the quadratic term neglected within square brackets in Eq. (2.7), which is equal to $[\frac{1}{4}(x^2+y^2)(1-R_{K\pi}) + y_{CP}^{K^-\pi^+}(y_{CP}^{K^-\pi^+} - y_{CP}^f)]\tau^2$ and is currently negligible.

2.1.3 WS to RS ratio

The WS decays can be used to measure the mixing and *CP* violation parameters with good sensitivity. In fact, even though their branching fraction at zero decay time is suppressed with respect to that of CS decays by around $3\% \approx \lambda^2$ [36] (the decay amplitude is DCS), the number of WS decays following D^0 mixing is nearly as large as that of CS decays, since the decay amplitude that follows D^0-meson mixing is CF. Therefore, the interference contribution of WS decays with and without D^0 mixing is proportional to the product of a DCS and a CF decay amplitudes, whereas that of CS decays is proportional to the square of a CS decay amplitude, and are equal up to *U*-spin breaking effects.

The order of magnitude of all of the three terms in parenthesis in Eq. (1.55) is approximately the same, thus terms of second-order in mixing parameters contribute significantly to the time dependence of the decay rates and cannot be neglected. The time dependence is usually measured by analysing the time-dependent ratio of the WS to RS yields, separately for D^0 and $\overline{D}^0$ mesons,

$$\begin{aligned} \frac{\Gamma(D^0 \to \bar{f}, t)}{\Gamma(D^0 \to f, t)} &\approx R_f^+ + \sqrt{R_f^+} c_{\bar{f}}^+ \tau + c_{\bar{f}}'^+ \tau^2, \\ \frac{\Gamma(\overline{D}^0 \to f, t)}{\Gamma(\overline{D}^0 \to \bar{f}, t)} &\approx R_f^- + \sqrt{R_f^-} c_{\bar{f}}^- \tau + c_{\bar{f}}'^- \tau^2, \end{aligned} \tag{2.8}$$

where the ratios R_f and the coefficients $c_{\bar{f}}^{(\prime)\pm}$ are defined in Eqs. (1.49) and (1.56). The ratio with the RS yields allows to avoid modelling the time-dependent selection efficiency, as well to cancel out most of the biases from detection asymmetries and background that are shared by WS and RS decays. Differently from the numerator, the deviations of the time dependence of the denominator from an exponential function can be neglected. In fact, they cause corrections to the linear (quadratic) term in Eq. (2.8) which are suppressed by a factor of $R_f = (3.44 \pm 0.02) \times 10^{-3}$ [47] with respect to the $R_f^{\pm} c_{\bar{f}}^{\pm}$ ($c_{\bar{f}}'^{\pm}$) terms due to the time dependence of the numerator.

2.1.4 $\Delta Y_{K^-\pi^+}$ and $\Delta Y_{K\pi}$

The observable $\Delta Y_{K^-\pi^+}$ can be measured with the same methods described in Sect. 2.1.1 to measure $\Delta Y_{K^+K^-}$ and $\Delta Y_{\pi^+\pi^-}$. In particular, the Eqs. (2.2), (2.3), (2.4) and (2.5) are still valid, if one identifies f with $K^-\pi^+$ and substitutes $\overline{D}^0 \to f$ with $\overline{D}^0 \to \bar{f}$ and $\bar{A}_f$ with $\bar{A}_{\bar{f}}$. For example, the time-dependent *CP* asymmetry is defined, starting from Eq. (2.4), as

$$A_{CP}(f, t) \equiv \frac{\Gamma(D^0 \to f, t) - \Gamma(\overline{D}^0 \to \bar{f}, t)}{\Gamma(D^0 \to f, t) + \Gamma(\overline{D}^0 \to \bar{f}, t)}. \tag{2.9}$$

However, the sensitivity of $\Delta Y_{K^-\pi^+}$ to the *CP* violation parameters is smaller than that of ΔY for CS decays. In fact, even if the branching fraction of $D^0 \to K^-\pi^+$ decays is larger by about a factor of 10 than that of CS decays [36], implying an statistical uncertainty smaller by a factor of 3, the dependence of $\Delta Y_{K^-\pi^+}$ on the mixing and *CP* violation parameters is suppressed by a factor of $\sqrt{R_{K\pi}} \approx 6\%$ [47]. Therefore, this observable has never been employed as a test of mixing and *CP* violation.

An alternative observable that has not been employed so far, but that might guarantee better statistical precision, is the time dependent asymmetry of the sum of D^0 and $\overline{D}^0$ decay rates into $K^-\pi^+$ and $K^+\pi^-$ final states,

$$\begin{aligned} A_{CP}^{\text{untagged}}(K\pi, t) &\equiv \frac{[\Gamma(D^0 \to f, t) + \Gamma(\overline{D}^0 \to f, t)] - [\Gamma(\overline{D}^0 \to \bar{f}, t) + \Gamma(D^0 \to \bar{f}, t)]}{[\Gamma(D^0 \to f, t) + \Gamma(\overline{D}^0 \to f, t)] + [\Gamma(\overline{D}^0 \to \bar{f}, t) + \Gamma(D^0 \to \bar{f}, t)]} \\ &\approx a_{K\pi}^d + \Delta Y_{K\pi} \tau, \end{aligned} \tag{2.10}$$

where terms of order two or higher in the mixing parameters are neglected in the last passage. Here, the *CP* violation parameters $a_{K\pi}^d$ and $\Delta Y_{K\pi}$ are equal to

$$\begin{aligned} a_{K\pi}^d &\approx a_f^d - R_{K\pi} a_{\bar{f}}^d, \\ \Delta Y_{K\pi} &\approx \sqrt{R_{K\pi}} [2 y_{12} \sin \Delta_f \sin \phi_2^\Gamma - y_{12} \cos \Delta_f (a_f^d + a_{\bar{f}}^d)] \end{aligned} \tag{2.11}$$

up to corrections quadratic in a^d_f and $a^d_{\bar{f}}$. This observable could be measured with better statistical precision than $\Delta Y_{K^-\pi^+}$, since it does not require to determine the flavour of the D^0 meson at production (see Sect. 2.2 for a summary of the techniques that can be achieved for this aim). For example, at the LHCb experiment it could be measured by employing D^0 mesons produced in the *pp* collision instead of in the decay of $D^*(2010)^+$ mesons, whose production cross-section is smaller by around a factor of 3 [124]. The gain in precision would be even higher, since the π^+ meson from the $D^*(2010)^+ \to D^0\pi^+$ decay does not need to be reconstructed. This particle is usually characterised by lower momentum than the D^0-meson final-state particles, owing to the low Q-value of the $D^*(2010)^+$ decay, and thus by lower reconstruction efficiency. In fact, the magnetic field can deflect it out of the LHCb angular acceptance (see the next chapter for a description of the LHCb experiment). Unfortunately, the terms proportional to $x_{12}\cos\Delta_f\cos\phi^M_f$ in Eqs. (1.52) and (1.56) cancel in the sum of the contributions to $\Delta Y_{K\pi}$ from RS and WS decays, and only the term proportional to $y_{12}\sin\Delta_f\sin\phi^\Gamma_2$ can be measured (the *CP* asymmetries of the decay amplitudes are completely negligible in the SM for WS and RS decays). This term provides lower sensitivity to the mixing weak phases, since the angle Δ_f, which vanishes in the limit of U-spin invariance, is measured to be small, $\Delta_f = -0.28^{+0.18}_{-0.14}\,\text{rad}$.

2.1.5 Charm factories and multibody decays

Strong phases like $\Delta_{K\pi}$ cannot be measured directly at B Factories or hadron colliders. However, this angle is essential to interpret the results of the WS to the RS ratio in terms of the mixing and *CP* violation parameters. Experiments like CLEO and BESIII, which operate at charm factories producing D^0–$\overline{D}{}^0$ coherent pairs from $\psi(3770)$ decays, are crucial to perform this kind of measurements [125,126]. In fact, even if the produced number of D^0 decays is considerably lower than that of the B Factories and hadron colliders, the coherent state allows to take advantage of the entanglement of the two mesons if both are reconstructed. In particular, the phase $\Delta_{K\pi}$ can be determined based on the asymmetry of the number of decays into the final state $K^-\pi^+$ when the other meson decays into a *CP*-even or *CP*-odd final state.

Analogous measurements can be performed also to determine the strong phases of $D^0 \to K^0_S\pi^+\pi^-$ [127,128] and $D^0 \to K^\pm\pi^\mp\pi^+\pi^-$ decays. These multibody decays, which have comparable or greater branching fractions with respect to two-body decays and receive contributions both from CF and DCS amplitudes, provide very good sensitivity to both mixing and *CP* violation parameters. In fact, the formulas describing their decay rates as a function of time are very similar to those of the WS and RS two-body decays $D^0 \to K^\pm\pi^\mp$. However, for the latter decays the phase $\Delta_{K\pi}$ is fixed and approximately equal to zero, so that only the y parameter can be measured precisely starting from the linear term in Eq. (2.8). On the contrary, for multibody decays the linear term provides sensitivity to both x and y parameters, as well to both of the *CP*-violating phases ϕ^M_2 and ϕ^Γ_2, since the strong phase varies considerably across the multidimensional phase space of the final-state particles. The downside of these measurements is that the analysis of a three-body, and especially four-body final state, is particularly complicated and relies on the correct description of the decay amplitude across the phase space of the final-state particles, which is challenging both from the theoretical and experimental points of view. The impact of these uncertainties has been reduced for $D^0 \to K^0_S\pi^+\pi^-$ decays, at the cost of a slight decrease of the statistical precision, by the introduction of a model-independent method relying on the measurement of the strong phases as a function of phase space at charm factories [129]. On the contrary, measurements of four-body decays like $D^0 \to K^\pm\pi^\mp\pi^+\pi^-$ remain an open challenge and, despite some preliminary measurements [130,131] and the proposal

Table 2.1: Branching fractions and collected yields (in millions) of the main decays used to measure the parameters of mixing and time-dependent *CP* violation in charm decays. Values taken from Refs. [36, 56–59, 62, 114–116, 118, 133–138].

Decay	$\mathcal{B}$ $[10^{-3}]$	Collected yield $[10^6]$			
		Belle	BaBar	CDF	LHCb (2011–2018)
$D^0 \to K^+K^-$	4.08 ± 0.06	0.24	0.14	1.24	75.8
$D^0 \to \pi^+\pi^-$	1.455 ± 0.024	0.11	0.07	0.59	25.2
$D^0 \to K^+\pi^-$	0.150 ± 0.007	0.01	0.01	0.03	1.9
$D^0 \to K^0_S\pi^+\pi^-$	28.0 ± 1.8	1.2	0.7	0.32	41.0

of new measurement methods [132], have not been fully exploited so far.

2.2 Status of the art

During the last decade, four main experiments have contributed to a huge leap forward in the knowledge of mixing and *CP* violation in charm-quark decays. They are the BaBar and Belle experiments, installed at B Factories in the United States and in Japan, the CDF experiment at the Tevatron proton–antiproton collider at Fermilab laboratories (United States), and the LHCb experiment installed at the Large Hadron Collider (Switzerland). The first two experiments benefit from a cleaner experimental environment, due to the initial collision of elementary particles rather than hadrons, and allow a better control of systematic uncertainties and larger reconstruction efficiency, especially for neutral particles. However, the number of charm mesons produced and collected at the CDF and LHCb experiments is much larger, as shown in Table 2.1. Moreover, the LHCb detector benefits from a more efficient trigger and has much better particle identification capabilities than the CDF detector. Therefore, the precision of most of the parameters of mixing and *CP* violation is currently dominated by the measurements performed by the LHCb experiment, with the exception of decays involving neutral particles like the π^0 or K^0_L mesons, radiative decays, and measurements where the systematic uncertainty is comparable to the statistical one, like those of the parameter y_{CP}.

The most precise measurements of mixing and *CP* violation to date are listed in Table B.1 in Appendix B. The world average of the parameters are $x_{12} = (3.7 \pm 1.2) \times 10^{-3}$, $y_{12} = (6.0 \pm 0.6) \times 10^{-3}$, $\phi_2^M = (-0.01 \pm 0.03)$ rad and $\phi_2^\Gamma = (-0.03 \pm 0.10)$ rad [28]. The precision of the x_{12} parameter is driven by measurements of $D^0 \to K^0_S\pi^+\pi^-$ decays, while y_{12} is measured through the WS-to-RS ratio and the y_{CP} parameter, whose world average is $y_{CP} = (7.2 \pm 1.1) \times 10^{-3}$ [47].[1] The precision on ϕ_2^M is mostly determined by measurements of the ΔY parameter and that on ϕ_2^Γ, which is lower by around a factor of 3, mostly by measurements of $D^0 \to K^0_S\pi^+\pi^-$ decays. Measurements of *CP* violation in the WS-to-RS ratio provide further, but less precise, constraints on both of the *CP* violating weak angles. It is worth noting that, while the measurements of y_{CP} parameter allow to determine that the angle ϕ_2^Γ is approximately equal to zero rather than to π, they provide little sensitivity to the size of *CP* violation in charm-quark decays, since deviations of y_{CP} from y_{12} are second order in the *CP* violation parameters ϕ_2^M, ϕ_2^Γ and a_f^d, *cf.* Eqs. (1.44,1.47).

[1] Note, however, that this average neglects the term $y_{CP}^{K^-\pi^+}$ in Eqs. (2.6,2.7).

A summary of the most precise measurements of the ΔY observable is presented below. Before reviewing them, however, it is necessary to introduce the main methods employed to determine, or tag, the D^0 flavour at production. This is a required condition to measure all of the experimental observables described in the previous sections, with the only exceptions of y_{CP} and $A_{CP}^{\text{untagged}}(K\pi, t)$. In fact, the D^0 flavour cannot be inferred from its decay final state, since all final states under consideration are shared by D^0 and $\overline{D}{}^0$ mesons. Therefore, it has to be determined based on the D^0 production mechanism. This is usually achieved by considering only D^0 and $\overline{D}{}^0$ mesons that are produced in either of the two following decays:

1. the strong $D^*(2010)^+ \to D^0\pi^+$ decay;[2]
2. the weak $\overline{B} \to D^0\mu^- X$ decay, where $\overline{B}$ (B) stands for a generic meson containing a b quark and X for an arbitrary set of unreconstructed particles.

In the first case, the flavour-conserving strong-interaction decay allows to infer the flavour of the D^0 meson from the sign of the charge of the pion meson. The latter is often referenced to as tagging pion, π^+_{tag}, and is responsible of the naming of $D^0 \to K^\pm\pi^\mp$ decays as WS and RS. In the second case, the flavour is inferred from the sign of the charge of the muon, which coincides with the charge of the W boson that mediates the tree-level transition between the $\overline{b}$ and c quarks.

The first technique is generally more convenient for two reasons. On one hand, it guarantees higher yields. In fact, the production cross section of D^{*+} mesons at hadron colliders is larger than that of B mesons by around a factor of 10 [139, 140], while at they are comparable at B Factories [141]. However, the branching fraction $\mathcal{B}(D^{*+} \to D^0\pi^+) = (67.7 \pm 0.5)\%$ is much larger than $\mathcal{B}(\overline{B} \to D^0\mu^- X) = (6.83 \pm 0.35)\%$, where the last value is averaged over the typical mixture of b-hadrons that is produced at high-energy hadron colliders [36]. This disequilibrium in the production cross-sections is partly reduced at hadron colliders by the smaller reconstruction efficiency of D^{*+} decays, owing to the tighter trigger requirements on the D^0 flight distance that are needed to reject the background from associations of unrelated tracks produced in the collision of the initial hadrons. However, all in all the yield of D^{*+}-tagged decays is still larger by around a factor of three than that of μ^--tagged decays. On the other hand, even if at hadron colliders the number of pion mesons produced in the hadron collisions is much larger than that of muons, the background from random associations of true D^0 mesons with unrelated tracks is lower in D^{*+}-tagged decays. In fact, the low Q-value of the $D^{*+} \to D^0\pi^+$ decay imposes tight conditions on the direction and magnitude of the π^+_{tag} momentum, so that the invariant mass of the $D^0\pi^+_{\text{tag}}$ pair be close to that of the D^{*+} meson (see Sect. 5.1 for details).

The most precise measurements of the ΔY parameter until 2020 are summarised in Fig. 2.2, where possible differences between the K^+K^- and $\pi^+\pi^-$ final states are neglected. The LHCb measurements drive the current world average, $\Delta Y = (3.1 \pm 2.0 \pm 0.5) \times 10^{-4}$. They employ the data collected during 2011–2012, corresponding to $1(2)\,\text{fb}^{-1}$ of integrated luminosity of pp collisions at $\sqrt{s} = 7(8)\,\text{TeV}$, using both the D^{*+} or the μ^- tag, and during 2016–2018, corresponding to $5.4\,\text{fb}^{-1}$ at $\sqrt{s} = 13\,\text{TeV}$, but only using the μ^- tag. The parameter ΔY has been measured also in $D^0 \to K^0_S\pi^+\pi^-$ decays [62], where it is named $-\Delta y = (6 \pm 16 \pm 3) \times 10^{-4}$. However, this result is not included in the average above, since its uncertainty is considerably larger than those of the other measurements from LHCb, and its value is correlated with other measurements of D^0-meson observables which are used in the fits of the parameters of mixing and

[2] The inclusion of charge-conjugate processes is implied throughout, except in the discussion of asymmetries. Hereafter the $D^*(2010)^+$ meson is referred to as D^{*+} meson.

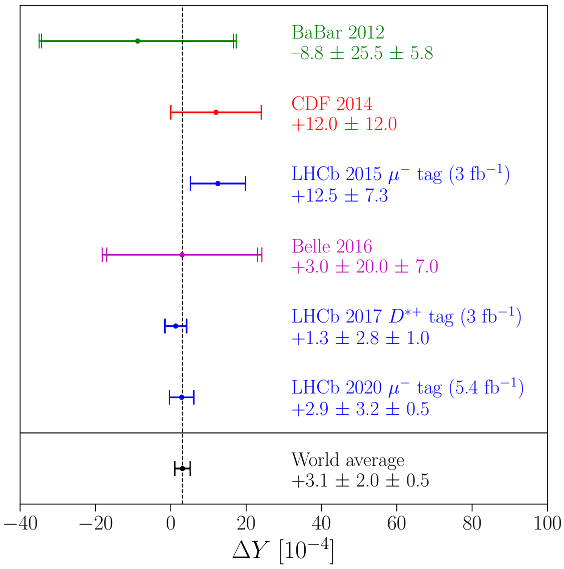

Figure 2.2: Summary of the most precise measurements of the parameter ΔY to date (final-state dependent contributions are neglected). Measurements references, from top to bottom: BaBar 2012 [57], CDF 2014 [115], LHCb 2015 μ^- tag [116], Belle 2016 [59], LHCb 2017 D^{*+} tag [114], LHCb 2020 μ^- tag [118]. The LHCb 2015 μ^- tag and LHCb 2017 D^{*+} tag measurements employ the data collected during 2011–2012, while the LHCb 2020 μ^- tag employs the data collected during 2016–2018. All of the other experiments employ the data sample collected during their whole lifetime.

CP violation of D^0 mesons. The measurement of ΔY presented in this thesis employs the D^{*+}-tagged data collected during 2015–2018, and represents the final and most precise measurement of the LHCb experiment on this subject until the next data-taking period, expected to take place during 2022–2024. In particular, it supersedes the preliminary measurement performed with the D^{*+}-tagged data collected during 2015–2016 [117].

Reducing the uncertainty on ΔY_f is essential, besides to test the SM predictions for time-dependent *CP* violation, also to determine the parameter $a^d_{K^+K^-}$ from measurements of the time-integrated asymmetry of $D^0 \to K^+K^-$ decays — which is the next step towards understanding the dynamical origin of the first observation of *CP* violation, reported by LHCb in 2019 [18]. In fact, using Eq. (2.5), the latter can be written as

$$A_{CP}(K^+K^-) \approx a^d_{K^+K^-} + \Delta Y_{K^+K^-} \frac{\langle t \rangle_{K^+K^-}}{\tau_{D^0}}, \tag{2.12}$$

where $\langle t \rangle_{K^+K^-}$ is the average measured decay time, and is equal to $1.7\tau_{D^0}$ at LHCb [30]. Since the expected precision of the measurement of $A_{CP}(K^+K^-)$ with the data collected by the LHCb experiment during 2015–2018 is around 5–6×10^{-4}, the current precision on $\Delta Y_{K^+K^-}$ would contribute significantly to the uncertainty on $a^d_{K^+K^-}$.

2.3 Measurement overview

Before any corrections are applied, the measured *raw* asymmetry between the number of D^0 and $\overline{D}^0$ decays into the final state f at time t,

$$A_{\rm raw}(f,t) \equiv \frac{N(D^{*+}\to D^0(f,t)\pi^+_{\rm tag}) - N(D^{*-}\to \overline{D}^0(f,t)\pi^-_{\rm tag})}{N(D^{*+}\to D^0(f,t)\pi^+_{\rm tag}) + N(D^{*-}\to \overline{D}^0(f,t)\pi^-_{\rm tag})}, \tag{2.13}$$

is equal to

$$A_{\rm raw}(f,t) \approx A_{CP}(f,t) + A_{\rm D}(\pi^+_{\rm tag}) + A_{\rm P}(D^{*+}) \tag{2.14}$$

up to third order in the asymmetries, where $A_{\rm D}(\pi^+_{\rm tag})$ is the detection asymmetry due to different reconstruction efficiencies of positively and negatively charged tagging pions and $A_{\rm P}(D^{*+})$ is the production asymmetry of $D^{*\pm}$ mesons in *pp* collisions. The measurement of ΔY_f from the slope of $A_{\rm raw}(f,t)$ is largely insensitive to time-independent asymmetries such as the detection and the production asymmetries, which depend only on the kinematics of the particles. However, the requirements used to select and reconstruct the D^0 decays introduce correlations between the kinematics and the measured decay time of the D^0 meson. This causes an indirect time dependence of both the production and the detection asymmetries which needs to be accounted for. These effects are controlled with a precision better than 0.5×10^{-4} by the equalisation of the kinematics of D^{*+} and D^{*-} candidates described in Chap. 5. A further time dependence of $A_{\rm P}(D^{*+})$ arises if the D^{*+} meson is produced in the decay of a B meson instead of the *pp* collision, since the production asymmetry of these *secondary* mesons is different than that of *primary* ones, and the measurement of their D^0 decay time is biased towards larger values. The size of this background is assessed based on the distribution of the D^0 impact parameter and its contribution to the asymmetry is subtracted as detailed in Chap. 6. Finally, ΔY is determined through a χ^2 fit of a linear function to the time-dependent asymmetry, as measured in 21 bins of decay time in the range $[0.45, 8]\,\tau_{D^0}$.

The analysis method is developed and validated using a sample of right-sign $D^0\to K^-\pi^+$ decays. This control sample has a kinematics and topology very similar to those of the signal channels, but its dynamical *CP* asymmetries are known to be smaller than the current experimental uncertainty (see Sect. 2.1.4 and Appendix B.3), and thus can be neglected. Therefore, the raw asymmetry between the number of reconstructed $D^0\to K^-\pi^+$ and $\overline{D}^0\to K^+\pi^-$ decays can be written as

$$A_{\rm raw}(K^-\pi^+,t) \approx A_{\rm D}(\pi^+_{\rm tag}) + A_{\rm D}(K^-\pi^+) + A_{\rm P}(D^{*+}), \tag{2.15}$$

where the right-hand side differs from that of Eq. (2.14), since it receives no contributions from dynamical *CP* asymmetries, but contains an additional detection asymmetry, $A_{\rm D}(K^-\pi^+)$, caused by the non-self-conjugate final state. However, this asymmetry is removed by the kinematic equalisation described in Chap. 5 as is the tagging asymmetry $A_{\rm D}(\pi^+_{\rm tag})$. The compatibility of the slope of the time-dependent asymmetry of $D^0\to K^-\pi^+$ decays, $\Delta Y_{K^-\pi^+}$, with zero is thus a useful cross-check of the effectiveness of the analysis method. In addition, the $D^0\to K^-\pi^+$ sample is used to estimate the size of the systematic uncertainties that are not expected to differ among the D^0-meson decay channels, allowing to achieve higher precision than what would be possible using the $D^0\to K^+K^-$ and $D^0\to \pi^+\pi^-$ samples.

During the development of the analysis method, the time-dependent asymmetries of the signal channels were shifted by a linear function whose intercept and slope were kept blind to avoid experimenter bias. Since a preliminary measurement using the 2015–2016 data sample, albeit with a different selection and analysis method, has been performed prior to this publication [117], two independent sets of blinding parameters were used for the 2015–2016 and 2017–2018 asymmetries. Only after the method was fixed based on the results of the $D^0 \to K^-\pi^+$ sample and all systematic uncertainties were estimated, the real values of $\Delta Y_{K^+K^-}$ and $\Delta Y_{\pi^+\pi^-}$ were measured.

Chapter 3

Experimental setup

This chapter briefly describes the Large Hadron Collider and the LHCb experiment, with a particular focus on the aspects that are most relevant to the measurement of the ΔY observable. The interested reader can find more detailed information in the references cited throughout the chapter.

3.1 Large Hadron Collider

The Large Hadron Collider (LHC) [142] is a superconducting circular hadron accelerator operating at the laboratories of CERN (*Conseil Européen pour la Recherche Nucléaire*), near Geneva. With a circumference of around 27 km, it is hosted in the same tunnel that previously housed the Large Electron Positron collider (LEP), about 100 m underground across the French–Swiss border.

Two proton beams, circulating in opposite directions along the ring, are bent by superconducting NbTi dipole magnets providing magnetic fields with intensities up to 8 T, and collide in four interaction points. Each of the points corresponds to one of the four large-scale experiments installed at CERN, which are managed by collaborations of order of one thousand scientists or more. The largest experiments, ATLAS and CMS, utilise general-purpose detectors and are mainly targeted at studies of the properties of the Higgs boson, of the vector bosons and of the quark top, as well as to searches for new interactions beyond the SM in collisions characterised by emitted particles of high transverse momentum. The ALICE experiment takes advantage of the capability of the LHC to collide also lead ions instead of protons to study the properties of QCD at high-density regimes, and in particular the phase transition to the quark–gluon plasma. Finally, the LHCb experiment was designed to perform high-precision measurements of b- and c-quark decays.

The distribution of the protons in the beams is not continuous, but organised in *bunches* of about 10^{11} protons each, whose length is approximately 8 cm. The time distance between two consecutive bunches is a multiple of 25 ns, corresponding to a nominal bunch-crossing rate of 40 MHz. However, larger gaps are present between some bunches, in order to allow the necessary time to switch the status of the dipole magnets responsible for the injection and for the dumping of the beams outside of the ring between the passage of two bunches. Therefore, the effective crossing rate is around 30 MHz.

The event rate of any process generated in the LHC proton–proton (pp) collisions is equal to

$$\frac{\mathrm{d}N}{\mathrm{d}t} = \mathcal{L}\,\sigma(\sqrt{s}), \tag{3.1}$$

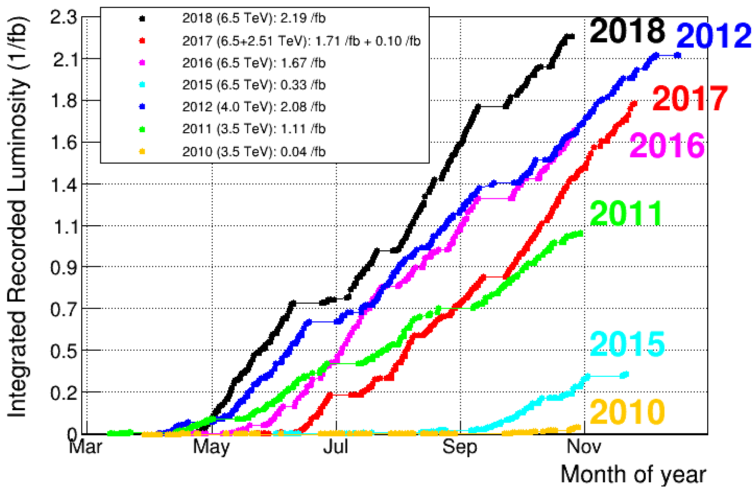

Figure 3.1: Integrated luminosity of pp collisions recorded by the LHCb experiment in each data-taking year. The beam energy, corresponding to half of the centre-of-mass energy $\sqrt{s}$, is reported as well.

where $\mathcal{L}$ is the instantaneous luminosity of the collider and $\sigma(\sqrt{s})$ is the cross-section of the process at centre-of-mass energy $\sqrt{s}$. The design specifications of the LHC targeted operations at the instantaneous luminosity of $10^{34}\,\mathrm{cm}^{-2}\,\mathrm{s}^{-1}$. However, the LHCb experiment is not limited by the number of $c\bar{c}$ and $b\bar{b}$ quark pairs produced in the pp interactions, but by the time needed to reconstruct the collision events and by the amount of data that can be recorded to be analysed. Therefore, the luminosity is limited to around $4 \times 10^{32}\,\mathrm{cm}^{-2}\,\mathrm{s}^{-1}$ by shifting the position of the colliding beams in the horizontal plane, thus reducing their overlap at the collision point. The instantaneous luminosity is kept constant during each data-taking, by reducing progressively the shift between the beams as time passes, and the number of protons in the bunches decreases owing to the collisions. The average number of pp interactions per bunch crossing is around 1.6. The reduced instantaneous luminosity is also needed to limit the radiation damage of the detectors, and in particular the innermost vertex detector that surrounds the collision region. In fact, this is much closer to the beam than its counterparts of the other LHC experiments.

The centre-of-mass energy of the pp collisions was 7 TeV during the 2010–2011 data taking, 8 TeV during 2012 and 13 TeV during 2015–2018. The integrated luminosity recorded by the LHCb experiment in each data-taking year is displayed, together with the beam energy, in Fig. 3.1. In each year, the recorded luminosity corresponds to a fraction between 87% and 94% of the total integrated luminosity delivered by the LHC.

3.2 LHCb detector

The LHCb experiment is mainly designed to perform precision measurements of the decays of hadrons containing b and c quarks, even though its experimental program encompasses also measurements of the electroweak sector of the SM, of interaction cross-sections of protons with gases and of heavy-ion collisions. In a high-energy pp collider like the LHC, the production cross-section of $b\bar{b}$ pairs is particularly large for small polar angles with respect to the direction of the beam axis, as shown in Fig. 3.2. Taking advantage of this feature, the LHCb detector is a single-arm spectrometer with angular coverage corresponding approximately to angles between

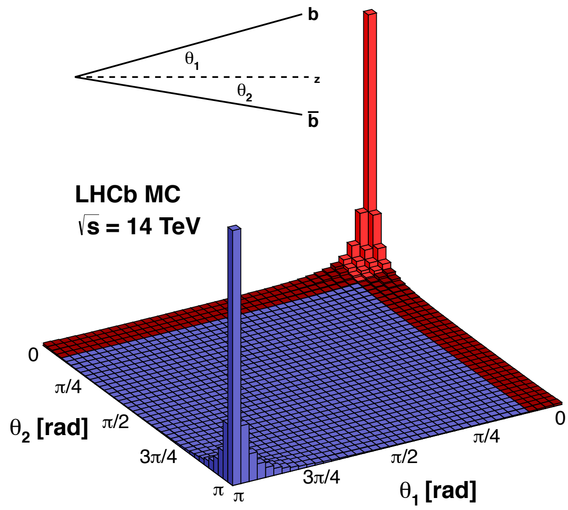

Figure 3.2: Production cross-section of $b\bar{b}$ pairs as a function of their polar angle with respect to the beam axis, for pp collisions simulated with PYTHIA [143] at a centre-of-mass energy of 14 TeV. The LHCb acceptance is displayed in red. The plot is taken from Ref. [144].

10 mrad and 300 (250) mrad in the horizontal (vertical) plane with respect to the beam axis [145]. This choice enables the detector to collect about 27% of the b quarks and 24% of the $b\bar{b}$ pairs produced in the pp collisions, to be compared to the corresponding geometrical efficiency of general-purpose detectors like CMS and ATLAS, which are around 49% and 41% for b quarks and $b\bar{b}$ pairs, respectively. However, the number of collected decays at equal instrumented solid angle is much larger, with significant cost benefits. The small solid angle covered also allows for a sequential arrangement of the detectors along the beam direction. This opens the possibility of installing RICH detectors that allow precise particle identification, and implies an easier design of the supporting structures and readout systems of the detectors, as well as the much easier access to the detectors after construction. In fact, most of the detector subsystem are assembled in two halves, which are mounted on rails and can be moved out separately for assembly and maintenance, as well to provide access to the beam-pipe, whenever necessary. Finally, the angular acceptance, which corresponds to the pseudorapidity range $1.8 < \eta < 4.9$, is complementary to that of the general purpose detectors like CMS and ATLAS, around $|\eta| < 2.4$.[1] This feature can be exploited to perform complementary studies of the parton distribution functions and of the electroweak sector of the SM.

The layout of the LHCb spectrometer is shown in Fig. 3.3. Its coordinate system is a right-handed system centred in the nominal pp interaction point, with the x axis pointing towards the centre of the LHC ring, the y axis pointing upwards and the z axis pointing along the beam. Its main components are, from left to right:

- the vertex locator (VELO), a silicon-strip vertex detector surrounding the pp interaction region, aimed at measuring the position of the vertices of the pp interactions and the decay vertices of heavy flavoured hadrons;
- a ring-imaging Cherenkov detector (RICH1) providing particle identification information (PID) for charged particles with momentum in the range 1–60 GeV/c;

[1] The pseudorapidity is defined as $\eta = -\log[\tan(\theta/2)]$, where θ is the polar angle with respect to the beam axis.

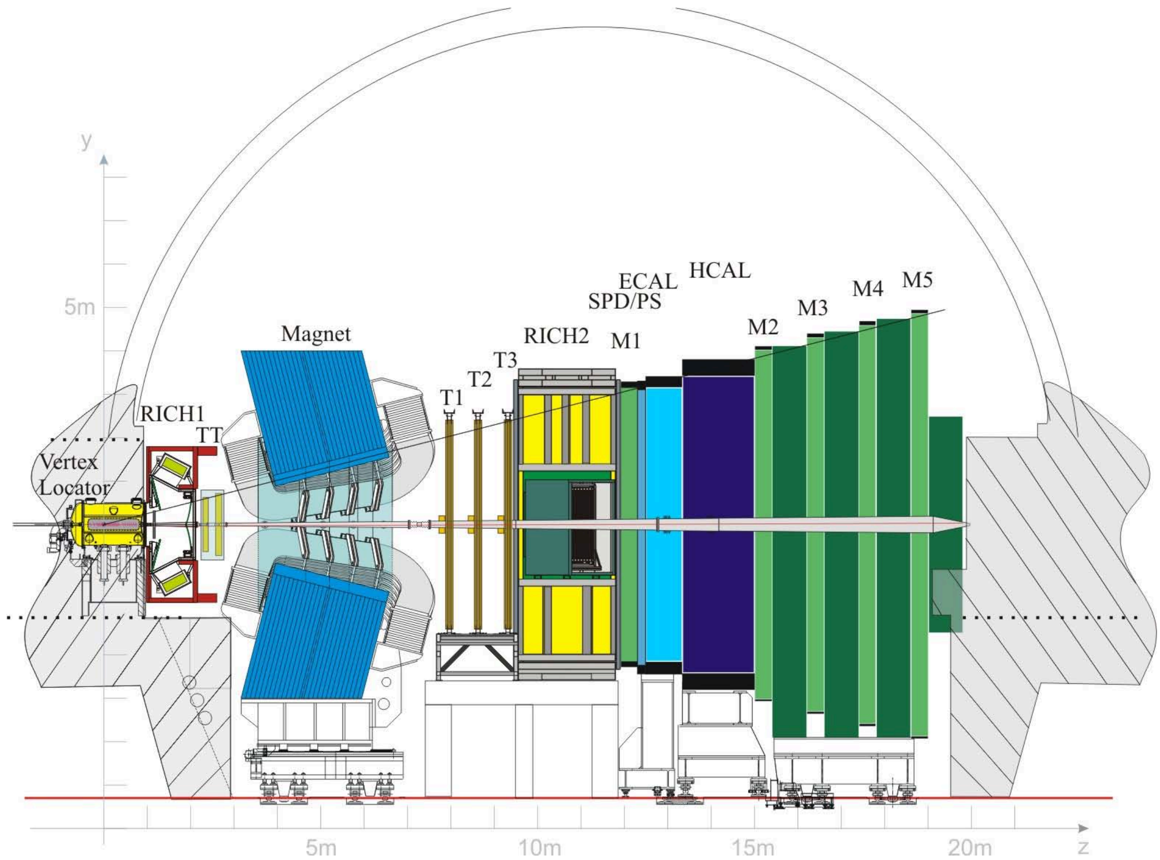

Figure 3.3: Side view of the LHCb spectrometer.

- the Tracker Turicensis (TT), a large-area silicon-strip tracking detector placed immediately upstream of the magnet;
- a nonsuperconducting magnet producing a vertical field with bending power 4 T m, needed to measure the momentum of charged particles;
- three tracking stations (T1, T2, T3) placed downstream of the magnet, to measure the momentum of charged particles. They are made up of silicon strips in the region closest to the beam pipe and of straw drift tubes in the outer one;
- a second ring-imaging Cherenkov detector (RICH2) providing PID information for charged particles with momenta from 15 GeV/c up to and beyond 100 GeV/c;
- the scintillating pad detector and the preshower detectors (SPD/PS), separated by a thin plate of lead, used to distinguish electrons from photons and from hadrons, respectively;
- an electromagnetic calorimeter (ECAL) to identify electrons and photons and to measure the energy of the latter ones;
- an hadronic calorimeter (HCAL) used at trigger level to obtain a rough estimate of the energy of hadrons;

- five muon stations (M1–M5), composed by alternating layers of iron and multiwire proportional chambers, used to identify muons particles.

The material budget between the pp interaction point and the end of the tracking system, just before the RICH2 detector, is 60% of a radiation length and 20% of an absorption length on average. All of the detectors are described in greater detail in the next sections.

3.2.1 Tracking system

Vertex locator

The vertex locator (VELO) is a silicon-strip vertex detector surrounding the pp interaction region. Its main purpose it to measure precisely the trajectories of charged particles, generally named "tracks", to measure precisely the position of both the primary vertices (PVs) of the pp collisions and the displaced secondary vertices, which are a distinctive feature of the decay of b- and c-hadrons, since their mean flight distance before decaying is order of 1 cm. Its role is crucial to discriminate the signal decays from the large background of particles produced in the pp collisions, as well as to measure precisely the decay time of the heavy flavoured hadrons.

It consists in 46 punched semicircular silicon modules arranged perpendicularly to the beam direction, on its left and right sides, as shown in Fig. 3.4. The arrangement ensures that every track produced in the nominal pp collision point and that is within the nominal LHCb acceptance intersects at least four sensors. Each module except the first four is composed of two overlapping radiation-resistant sensors, each one with a thickness of 300 μm, whose sensitive area starts at 8.2 mm radial distance from the beam and ends at 41.9 mm from it. Each pair of sensors consists of a R sensor, specialised to measure the radial distance from the beam with semicircular-shaped strips, and a ϕ sensor, specialised to measure the azimuthal angle with strips oriented approximately in the radial direction, as shown in Fig. 3.5. The first four modules contain only a R sensor, and are used to estimate the number of pp collisions in a given bunch crossing, to reject overcrowded events that correspond on average to lower reconstruction quality and require more time to be analysed. The R sensors are subdivided into four 45° regions to reduce the detector occupancy. Their pitch increases linearly with the radial distance, passing from 38 μm in the innermost region up to 102 μm at the outer radius, thus ensuring that the measurements along the track contribute to the precision on its impact parameter from the PV with roughly equal weight. The ϕ sensors are subdivided in two regions, inner and outer, whose border is located at 17.25 mm from the centre. In the inner region, the strip pitch increases linearly from 38 to 78 μm, whereas in the outer region the pitch increases from 39 to 97 μm. At the innermost radius, the inner strips have an angle of approximately 20° to the radial direction, whereas the outer strips have an angle of approximately 10°. The modules are installed so that adjacent ϕ sensors have opposite skew with respect to each other. This allows to remove possible ambiguities in the reconstruction of the tracks and to decrease the number of ghosts, defined as reconstructed tracks that do not correspond to the passage of any particles.

The minimum distance of the sensitive area of the VELO modules from the beam, 8.2 mm, is smaller than the safety distance from the beams required by the LHC during the beams injection. Therefore, the VELO sensors are mounted on a remote-controllable positioning system that allows to retract them by 3 cm along the x direction whenever the beams are not stable, in order to avoid damaging the sensors. This corresponds to the VELO *open* configuration, as opposed to the VELO *closed* configuration, and is shown in Fig. 3.4. Each half of the VELO detector is mounted inside a 300 μm thick AlMg3 box, with the double function of

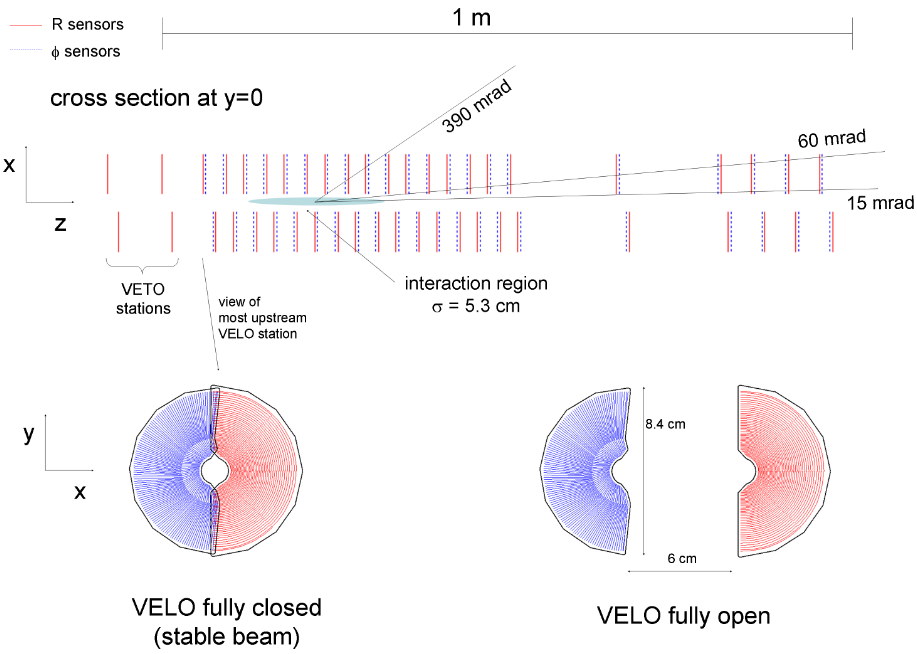

Figure 3.4: Top view of the VELO silicon sensors, with the detector in the open position. The front face of a pair of modules is shown in both the closed and open positions. Figure taken from Ref. [146].

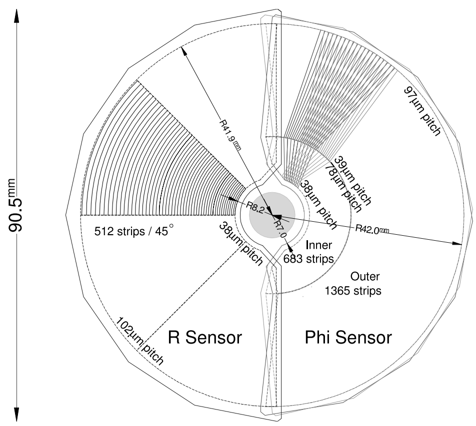

Figure 3.5: Geometrical scheme of the R and ϕ VELO sensors. For clarity, only a portion of the strips are illustrated. In the ϕ-sensor, the strips on two adjacent modules are indicated, to highlight the stereo angle. Figure taken from Ref. [146].

separating the LHC beam-pipe vacuum from that of the VELO detector, and to shield the VELO from electromagnetic effects induced by the high frequency beam structure, hence the name of radiofrequency (RF) box. The choice of its material, an Aluminium alloy with 3% Magnesium, was driven by the relatively small radiation length of the Aluminium, and is aimed at minimising the multiple scattering of the tracks before reaching the VELO, since this degrades significantly the resolution of the impact parameter. The two boxes present a highly corrugated shape to allow the two detector halves to overlap in the VELO *closed* configuration, as shown in Fig. 3.6.

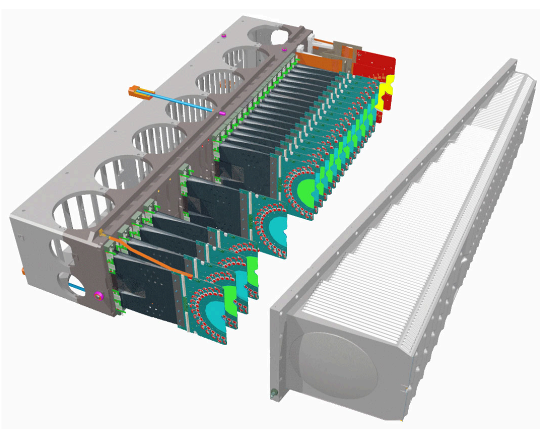
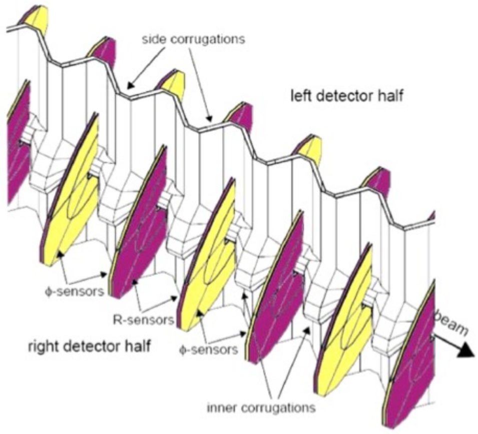

Figure 3.6: (Left) Exploded view of the module support and the modules (on the left), and of the RF box (on the right). The corrugated foil on the front face of the box, which forms a beam passage, can be seen. Its form allows the two halves to overlap when in the closed position. (Right) Inner view of the RF-boxes, with the detector halves in the fully closed position. The edges of the boxes are cut away to show the overlap between the sensors of the two halves. R- and ϕ-sensors are coloured in yellow and purple, respectively. Figures taken from Ref. [145].

Tracker turicensis

The tracker turicensis (TT) is a silicon microstrip detector placed approximately 2.4 m after the beam interaction region and immediately upstream of the dipole magnet. It allows to improve the precision of the measured momentum of charged particles, and to reduce the number of reconstructed ghost tracks with respect to using only the track segments in the VELO and in the T–stations. In addition, it permits reconstructing the trajectory upstream of the magnet of long-lived particles that are likely to decay outside of the VELO detector, such as the K^0_S meson and the Λ baryon, thus increasing their collection efficiency. Finally, it allows a rough measurement of the particles momenta without reconstructing the tracks segments downstream of the magnet, thanks to the tails of dipole magnetic field, which extend up to the region where it is installed. This feature is used to predict the rough expected trajectories of the tracks in the T–stations, thus reducing the number of upstream- and downstream-tracks combinations that have to be fitted during the collision-event reconstruction.

It covers a rectangular area about 150 cm wide and 130 cm high, corresponding to the full LHCb angular acceptance, and consists of four planar layers organised in two pairs, the TTa and TTb stations. These are separated by about 30 cm along the LHC beam axis, as displayed in Fig. 3.7. The first and last layers are organised in vertical strips measuring the x coordinate, whereas the second and third layer strips are rotated by $\pm 5^\circ$ with respect to the vertical. This small skew allows, similarly to that of the VELO ϕ sensors, to remove some ambiguities in the reconstruction of the tracks. All of the layers are modularly composed of 500 µm thick, 9.64 cm wide and 9.44 cm long silicon sensors, each carrying 512 readout strips with a strip pitch of 183 µm.

Magnet

A warm dipole magnet is placed between the TT and the T–stations, allowing for a measurement of the momentum of charged particles. The magnet is formed by two saddle-shaped coils that

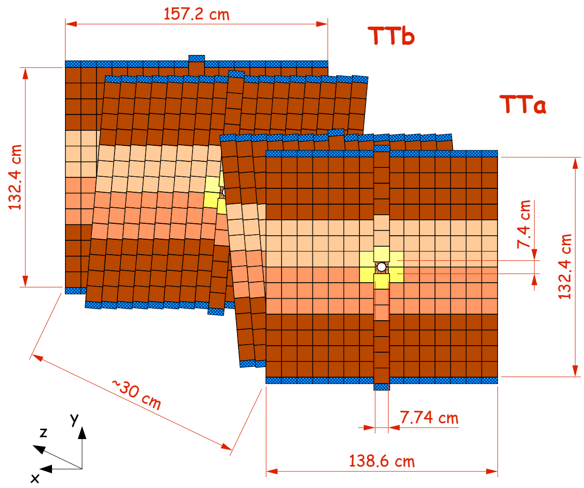

Figure 3.7: Scheme of the TT detector. Different readout sectors are indicated by different shadings. Figure taken from Ref. [147].

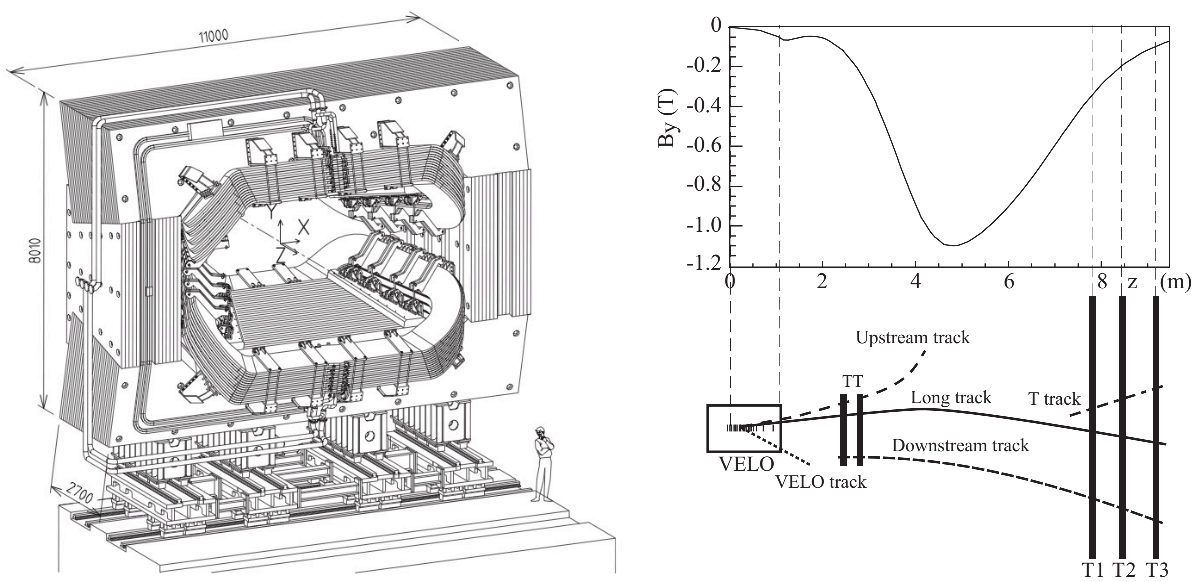

Figure 3.8: (Left) Perspective view of the LHCb dipole magnet (lengths are expressed in millimetres); the interaction point lies behind of the magnet. (Right) Vertical magnetic field measured on the z axis, as a function of the z coordinate. The z location of the tracking detectors is shown, as well as the names given to reconstructed tracks, depending on the detectors where they have left a detectable signal. Only long tracks, *i.e.* tracks with segments reconstructed in all of the three tracking detectors, are employed in the present measurement. Figures taken from Ref. [145].

are slightly inclined in order to match the detector angular acceptance, as shown in Fig. 3.8 (left). The produced magnetic field is approximatively vertical, has a total bending power of about 4 T m and reaches a maximum intensity of about 1.1 T. The profile of the magnetic-field intensity is displayed in Fig. 3.8 (right). Most of the detectors lie outside the magnetic field,

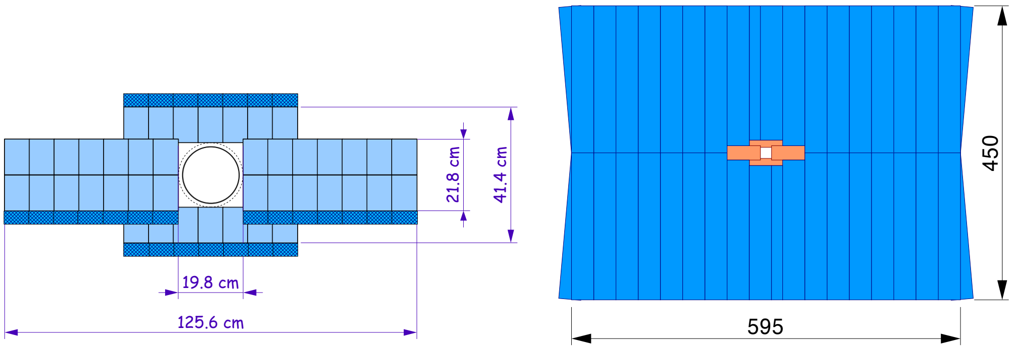

Figure 3.9: (Left) Front view of a layer of the inner tracker. (Right) Front view of one of the T–stations (lengths are expressed in centimetres). The inner tracker is drawn in orange and the outer tracker in blue. Figures taken from Ref. [147].

even if some residual field is present in the TT and, more importantly, in the T–stations. A precise magnetic-field map is determined with Hall probes before the data taking, to ensure excellent momentum resolution.

The magnetic field deflects the charged particles preferentially to the right or left side of the detector, depending on the sign of their charge. This effect is particularly important for low-momentum particles. For example, a pion mesons with a momentum equal to $5\,\mathrm{GeV}/c$ changes its direction, passing through the magnetic field, by about $250\,\mathrm{mrad}$. Therefore, it is not unlikely that it is deflected out of the LHCb angular acceptance, which is of similar size ($\pm 300\,\mathrm{mrad}$). This provokes large detection asymmetries for particles with opposite charge, which can bias the measurement of *CP* asymmetries. These asymmetries are partially mitigated by reversing the polarity of the magnet about every two weeks. The configuration with the magnetic field pointing upwards (downwards) is hereafter labelled *MagUp* (*MagDown*).

T–stations

The three tracking stations T1, T2 and T3, collectively named T–stations, are placed immediately downstream of the dipole magnet, and cover an area of approximatively $(6 \times 5)\,\mathrm{m}^2$. Each station is made up of four detection planes, with strip-like detectors oriented along the y direction for the first and fourth layers, and tilted by $\pm 5°$, like in the TT, for the inner two. In order to limit the costs, only a cross-shaped area close to the beam pipe, the "Inner Tracker", is covered with silicon micro-strip detectors, as shown in Fig. 3.9. On the contrary, the "Outer Tracker" (OT) covering larger polar angles consists of straw-tube detectors. The border between the inner and the outer trackers is determined by the requirement that the detector occupancy be lower than 10%. The single-hit detection efficiency in each layer is larger than 99%.

The Inner Tracker and employs the same technology and pitch as the TT, but with different width and length (the dimensions of each sensor are $7.6\,\mathrm{cm} \times 11\,\mathrm{cm}$). On the contrary, the straw tubes of the OT are a gaseous ionisation detector operating in the proportional-counter regime. Each of the four planes that form a T–station is made up of two rows of staggered drift tubes, as displayed in Fig. 3.10, in order to avoid dead regions between adjacent straws. The straw tubes are 2.4 m long, have 4.9 mm inner diameter and are filled with a gas mixture of $\mathrm{Ar/CO_2/O_2}$ (70%/28.5%/1.5%), which guarantees a drift time below 50 ns. The anode wire has a diameter of 25 μm, is made of golden-plated tungsten and is operated at 1550 V with

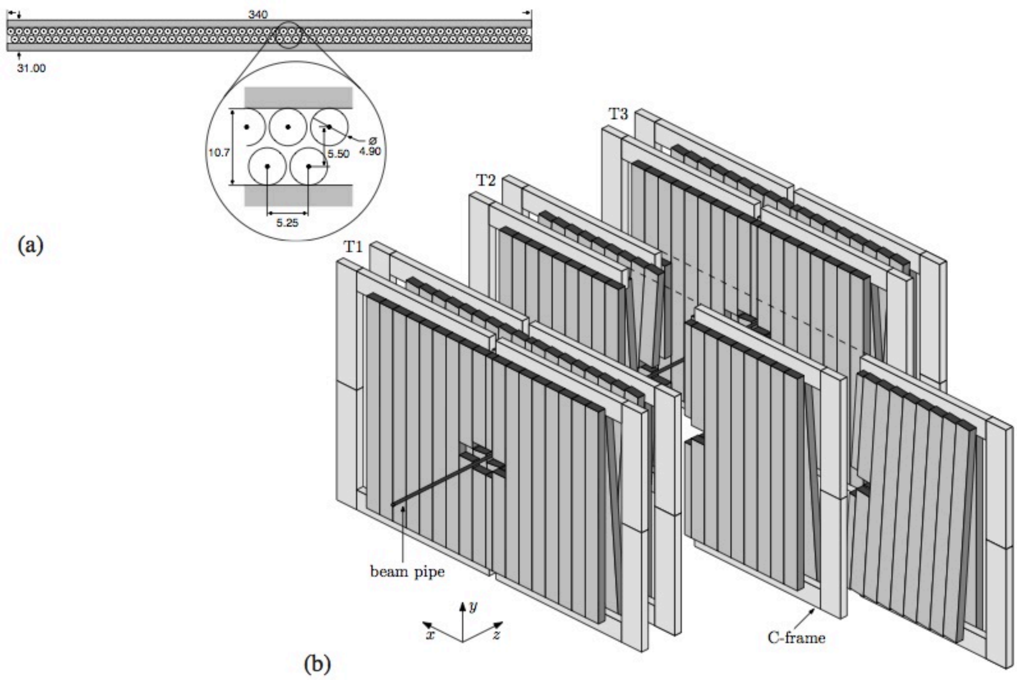

Figure 3.10: (a) Section of an OT detection plane. (b) Arrangement of OT straw-tubes modules in planes and stations. The second station is partially opened. Figures taken from Ref. [148].

respect to the tube of Kapton-XC coated with Aluminium. The straws wall is only 80 μm thick, ensuring that the total thickness of each T–station is just 3.2% of a radiation length. This is particularly important since, as the measurement of the drift time allows a spatial resolution of about 200 μm in each detection plane, the measurement of the momenta of charged particles is completely dominated by multiple scattering.

3.2.2 Particle identification and calorimetric systems

Cherenkov detectors

Two ring-imaging Cherenkov detectors (RICH) are used to discriminate among charged particles, and in particular among pion mesons, kaon mesons and protons [149]. The Cherenkov angle of a charged particle passing through a dielectric medium of refractive index n with a velocity greater than the phase velocity of light in the medium, is related to the mass and momentum of the particle as

$$\cos\theta_{\mathrm{C}} = \frac{1}{n}\sqrt{1+\left(\frac{mc}{p}\right)^{2}}. \tag{3.2}$$

To ensure good PID capabilities in a large momentum spectrum, 1–100 GeV/c, two distinct radiators are used. The RICH1 detector, placed right after the VELO and before the TT, uses fluorobutane (C_4F_{10}, $n = 1.0014$) as gas radiator and covers the momentum range 1–60 GeV/c and the full LHCb angular acceptance. On the contrary, the RICH2 detector is placed downstream of the T–stations since it covers the momentum range from approximately 15 to more than 100 GeV/c, corresponding to particles that in most cases are not deflected out of the LHCb acceptance by the magnetic field, and uses tetrafluoromethane (CF_4, $n = 1.0005$) as gas

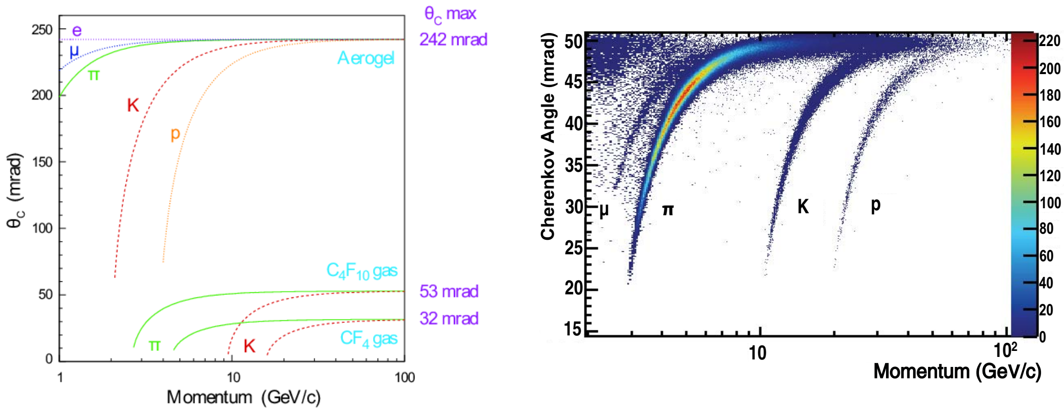

Figure 3.11: Cherenkov angle as a function of particle momentum (left) for the RICH radiators and for different particle masses and (right) for isolated tracks, defined as tracks whose Cherenkov ring does not overlap with any other ring, in the C_4F_{10} radiator. Figures taken from Refs. [145, 150].

radiator. Its acceptance is limited with respect to that of RICH1 detector, and corresponds to around $[15, 120]$ mrad in the horizontal plane and up to 100 mrad in the vertical plane. The characteristic curves of the radiators are shown for the most common particles detected within the LHCb acceptance in Fig. 3.11.

For both detectors, the Cherenkov photons are read by a lattice of hybrid photon detectors (HPDs) which are able to detect photons in the 200–600 nm spectrum.[2] The HPDs must be placed outside of the detector acceptance both to reduce the material budget of the RICH detectors, and owing to space constraints related to their shielding against the magnetic field. Therefore, a complex system of spherical and flat mirrors is needed to redirect the Cherenkov photons outside of the LHCb acceptance towards the HPDs, as shown in Fig. 3.12.

Calorimetric system

The calorimetric system is essential both to distinguish electrons and photons from hadrons, and for the implementation of the hardware trigger, as explained in Sect. 3.3.1. It consists of various detectors.

- The first calorimetric module consists of two polystyrene-based scintillating planes separated by a lead converter whose thickness is equal to 2.5 radiation lengths (X_0). These are named the Scintillator Pad Detector (SPD), used to distinguish photons from charged particles, and the PreShower detector (PS), which contributes to distinguish electromagnetic showers from hadrons. The thickness of each of the two detectors is equal to $2X_0$ and to 0.1 nuclear interaction lengths (λ_{int}).

- The electromagnetic calorimeter (ECAL), based on shashlik technology, consists of 66 2 mm-thick lead layers thickness alternated with 4 mm-thick scintillator tiles. Its total thickness corresponds to $25\,X_0$ and $1.2\,\lambda_{\text{int}}$, and allows to measure the energy of electromagnetic showers with a resolution $\sigma(E)/E = 1\% \oplus 10\%/\sqrt{E/\,\text{GeV}}$ [151];

[2] The HPD implements a technology similar to that of photomultipliers, but uses a silicon avalanche diode instead of multiple dynodes as electron multiplier.

Figure 3.12: Side-view schematic layout of the (left) RICH1 and (right) RICH2 detectors. Figures taken from Ref. [145].

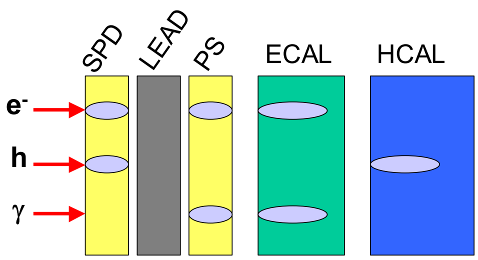

Figure 3.13: Energy deposited in the different detectors of the calorimetric system by electrons, hadrons and photons. Figure taken from Ref. [152].

- The hadronic calorimeter (HCAL), consisting of alternating layers of iron and scintillator tiles, whose thickness ($5.6\,\lambda_{\rm int}$) is limited by the space available in the LHCb cavern. As a consequence, the HCAL is only used to estimate the hadron energy in the hardware trigger, but is not used in most offline analyses, because it is not able to contain the full hadronic showers. Therefore, its resolution is limited to $\sigma(E)/E = 9\% \oplus 69\%/\sqrt{E/\,\mathrm{GeV}}$ [151].

All these detectors are read through photomultipliers placed above and below the LHCb acceptance, to which the scintillating light is transmitted through wave-shifting fibres. The energy deposits in the various detectors from different types of particles are shown in Fig. 3.13.

Three different segmentations are used for the scintillator tiles in the SPD, PS and ECAL detectors, corresponding to about $4 \times 4\,$cm, $6 \times 6\,$cm or $12 \times 12\,$cm, increasing passing from the innermost region closest to the beam pipe, which is characterised by the highest occupancy, to the outer one, as shown in Fig. 3.14. The tiles of the HCAL, instead, are divided only in two types: $13 \times 13\,$cm or $26 \times 26\,$cm. The geometry of the tiles of the first three detectors is

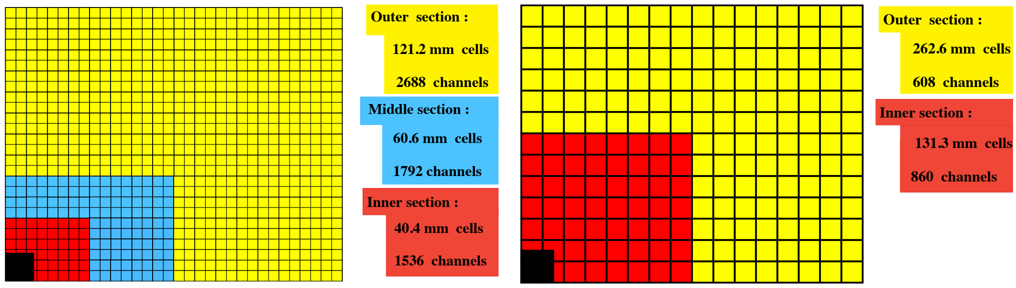

Figure 3.14: Segmentation of one quadrant (left) of the SPD, PS and ECAL and (right) of the HCAL. The black sector, corresponding to the beam pipe, is outside of the LHCb acceptance. Figure taken from Ref. [145].

projective with respect to the interaction point, that is corresponding tiles in different layers of the detectors cover the same solid angle with respect to the interaction point. This allows a fast estimate of the transverse energy of electromagnetic particles by the hardware trigger. An analogous design holds also for the HCAL.

Muon detectors

Five rectangular muon stations are designed to distinguish muon particles from hadrons, and to provide a quick measurement of the muon transverse momentum in the hardware trigger, with 20% resolution [153]. The angular acceptance of the detectors is $[20, 306]$ mrad ($[16, 258]$ mrad) in the horizontal (vertical) planes. The stations M2–5 are placed downstream of the HCAL and are interleaved with 80 cm-thick iron absorbers, to stop hadrons that manage to cross the HCAL. The total length of the absorbers, including the calorimeters, is approximately $20\,\lambda_{\rm int}$. Therefore, only muons with momentum greater than $6\,\mathrm{GeV}/c$ cross all of the stations. The station M1, instead, is placed in front of the calorimeters, where effects of multiple scattering are less important, and is used to improve the measurement of the transverse momentum in the hardware trigger.

The layout of the stations is displayed in Fig. 3.15. Each station is divided into four concentric regions, named R1–R4 starting from the beam pipe, arranged with a projective geometry for different stations. The dimension of the regions and their segmentations scale in the ratio 1:2:4:8., so as that the particles flux and channel occupancy are expected to be roughly the same over the four regions of a given station. The spacial resolution in the horizontal plane is higher in the first three chambers, to improve the resolution on the estimate of the momentum. Nearly all of the detectors are multiwire proportional chambers filled with a (40:55:5) $Ar/CO_2/CF_4$ gas mixture. The only exception is the R1 region of the M1 station, which has to cope with the higher particle rate before the HCAL and the iron absorbers, which is particularly high close to the beam pipe. This employs triple-GEM detectors with (45:15:40) $Ar/CO_2/CF_4$ gas mixture, which are considerably more radiation-resistant than multiwire proportional chambers. For both types of detectors, the detection efficiency is over 95%.

3.3 LHCb trigger

The LHCb trigger is designed to select the events containing decays of hadrons with b or c quarks, and to reject the more abundant background of events containing only light-quark particles. In

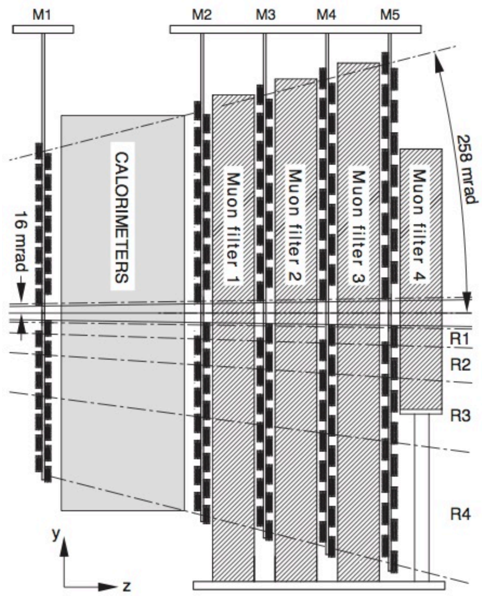

Figure 3.15: Side view of the muon system. Figure taken from Ref. [145].

order to achieve its purpose, it takes advantage of the long flight distance of b- and c-hadrons before they decay, order of one centimetre, and of their relatively high momentum in the plane transverse to the beam. The presence of muons, which are often produced in weak decays, or of electromagnetic showers, which can be a sign either to electrons from weak decays or of radiative decays, is employed for this aim as well.

The trigger scheme employed starting from 2015, which is sketched in Fig. 3.16, is divided in three stages. The first stage, known as Level-0 trigger (L0), is implemented in hardware with custom electronics. It is executed synchronously with the bunch crossing rate of the LHC (40 MHz) and reduces the event rate to 1 MHz. The events passing this selection are processed by the software-based trigger, which is run on a dedicated computer farm and is divided in two stages. The High Level Trigger 1 (HLT1) filters the events based on inclusive selections, and reduces their rate to around 140 kHz. Its output is processed by the High Level Trigger 2 (HLT2), which performs a more precise event reconstruction and selects the events based either on inclusive or exclusive requirements. The output rate of the events that are saved to permanent storage is 12.5 kHz. The three stages are described in greater detail in the next sections.

3.3.1 Hardware trigger

The purpose of the L0 trigger is to reduce the input collision rate of about 30 MHz to 1 MHz, which is the maximum rate at which the detector signals can be read out by design. This selection is performed synchronously with the LHC bunch-crossing rate, and has to be completed within a fixed latency of 4 μs. Therefore, it is fully implemented on FPGAs and processes only basic information from the calorimeters and muon chambers to provide a rough estimate of the greatest transverse momentum of muons, electrons, photons and hadrons of the event.

Calorimeter trigger The calorimetric system is designed projectively, so that corresponding cells in different layers of a calorimeter (and of different calorimetric detectors) cover the same

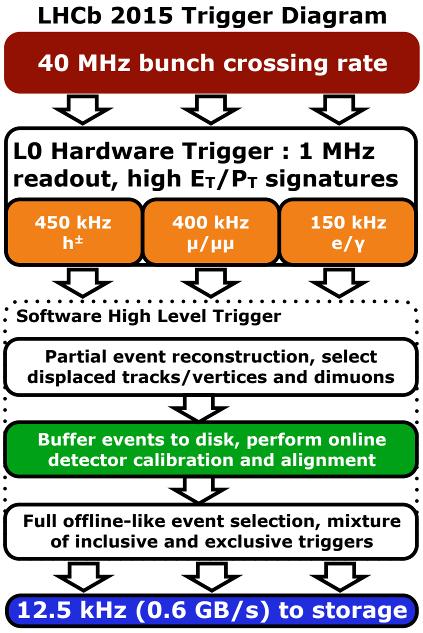

Figure 3.16: Trigger scheme of the LHCb experiment during 2015–2018.

solid angle with respect to the nominal collision point. This feature allows for a quick estimate of the transverse energy of the hadrons, photons and electrons as follows. The whole calorimeter is divided into clusters of 2×2 cells, which on average contain most of the energy released by a single particle, but are generally small enough to avoid to receive energy deposits from different particles. The transverse energy associated to a cluster is estimated as

$$E_{\mathrm{T}} = \sum_{i=0}^{4} E_i \sin\theta_i, \tag{3.3}$$

where E_i is the energy deposited in the i^{th} cell and θ_i is the angle between the beam axis and the straight line connecting the nominal collision point to the centre of the cell. Then, the energies are summed projectively along the different layers of the detector, yielding the total estimated transverse energy. The energy of electrons and photons is estimated using the information coming from the ECAL only. Furthermore, a cluster can fire the trigger only if there are at most 2 (4 in the inner region) PS hits in front of it. Electrons and photons are distinguished based on the presence of hits in the SPD cells aligned with the PS ones that fired the trigger. On the contrary, the hadron trigger selects the cluster candidate of highest energy in the HCAL. If the cluster of highest E_{T} in the ECAL is matched projectively to it, its energy is summed to that of the HCAL cluster. For all electrons, photons and hadrons, only the information about the most energetic particle of each type is considered. If it exceeds a fixed value, which is typically 3.7, 2.4 and 2.8 GeV for hadrons, electrons and photons, respectively, the event is retained.

Muon trigger The trigger reconstruction starts from the hits detected in the M3 chamber, and extrapolates the direction of the corresponding tracks starting from the collision point. For each muon station M1–5, an area denominated *field of interest* is considered around the extrapolated hit, taking into account trajectory variations due to the magnetic field or multiple scattering, under the hypothesis that its momentum in the x direction be larger than 0.6 GeV/c. If at least one hit is found in the *field of interest* of each station, the signals in the stations M1 and M2 are employed to estimate the transverse momentum of the muon with look-up tables, achieving 20% precision. The event is retained only if at least one of the two following conditions is met. The first is that the largest transverse momentum of a muon is greater than a threshold, which is typically 1.5 GeV/c. The second is that the square root of the product of the two greatest transverse momenta, $\sqrt{p_{\mathrm{T}}(\mu_1)\, p_{\mathrm{T}}(\mu_2)}$, is larger than a threshold, which is typically 1.3 GeV/c.

3.3.2 Software trigger

The complete set of detector signals of the events that fired the L0 trigger is written to the disk of a dedicated computer cluster, the Event Filter Farm (EFF). This consists of about 1,700 nodes with 27,000 physical cores and 10 PB of data storage, and is responsible for the execution of the high-level trigger. This divided in two steps, each implemented as a C++ executable, which are described in the next paragraphs.

HLT1 The first-stage software trigger performs a complete reconstruction of the tracks in the VELO to find the primary vertices (PV) produced in the collision between the proton bunches. The tracks having large impact parameter (IP) with respect to all of the PVs are extrapolated to the TT detector and matched with its track segments. This allows a rough estimate of the particles momentum. If this is larger than a preset threshold, which is typically $3\,\mathrm{GeV}/c$, the track is extrapolated through the magnetic field and the connected with the signal deposited in the T–stations. Then, it is fitted using a Kalman filter [154], which takes into account multiple scattering and corrects for energy losses due to the passage of the track through the detector material. Then, different selection algorithms are run, possible combining pairs of selected tracks or connecting them with the signals measured in the muon chambers. Each set of reconstruction and selection algorithms is named a *trigger line*. The event is selected to be processed by the HLT2 only if at least one of the trigger lines was fired. These require the presence of at least one track with good-quality reconstruction, large p_{T} and large IP with respect to all PVs or, alternatively, a muon-identity assignment.

HLT2 The second-stage software trigger performs a full reconstruction of the event, using the tracking and the PID information coming from all the detectors. Events of interest are categorised in few-hundreds trigger lines, each implementing selections based on the kinematics and PID information of the candidate particles and on the topology of the decays. Both inclusive and exclusive trigger lines, corresponding to particle decays that are only partially or completely reconstructed, are implemented.

The upgrade of the computing power and memory space of the EFF during 2013–2014 allowed the introduction of a new data-taking paradigm for a collider-based experiment, which permitted to increase significantly the number of events saved for offline analysis. In fact, the total buffer space of the EFF, around 10 PB, is sufficient to store the information of all the events selected by the L0 trigger during about ten days of continuous data-taking. Taking into account the LHC duty cycle, this leaves approximately 50 ms and 800 ms to execute the HLT1 and HLT2 triggers on each event, at a HLT1 output rate of 140 kHz. For comparison, during 2011–2012 the computing time available to the HLT2 was approximately 30 ms, even at the reduced HLT1 output rate of 100 kHz. As a consequence, the trigger reconstruction at HLT2

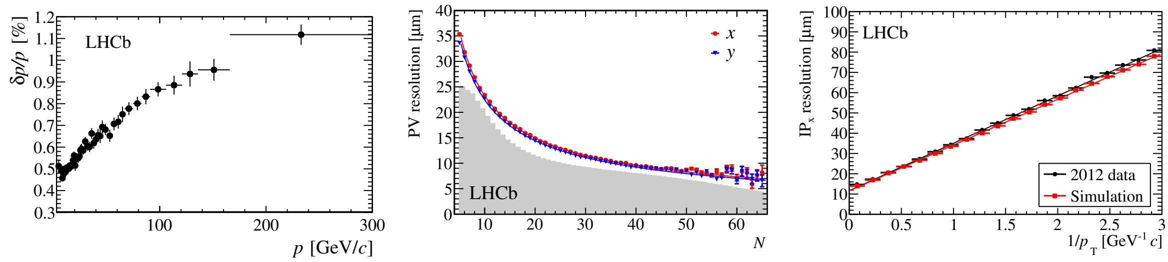

Figure 3.17: Performance of the tracking system of the LHCb detector. (Left) Relative momentum resolution as a function of momentum, for long tracks from the decay of J/ψ particles. (Centre) Primary vertex resolution in the x and y directions, for events with one reconstructed PV, as a function of tracks multiplicity, whose distribution is reported in grey in arbitrary units. (Right) Resolution of the x projection of the impact parameter with respect to the primary vertex, as a function of $1/p_{\mathrm{T}}$. Figures taken from Ref. [146].

level can be performed since 2015 with the same accuracy that was previously achievable only offline. Furthermore, the possibility of deferring the processing of the data for a significant amount of time before executing the HLT2 trigger allows to perform an alignment and calibration of the detector in between the execution of HLT1 and HLT2 triggers [155]. The consequent excellent performance of the online reconstruction offers the opportunity to perform physics analyses directly using candidates reconstructed at the trigger level for exclusive selections like those employed in the present thesis. The storage of only the triggered candidates, discarding the information of the rest of the event, enables a reduction in the event size by nearly one order of magnitude. The set of trigger lines employing this feature, the so-called *Turbo stream* [156, 157], accounts for about 5 kHz of the HLT2 output rate, and allows to increase significantly the rate of events saved to disk, achieving a total of 12.5 kHz. This paradigm was employed for nearly all of the charm exclusive lines, whose rate is limited by the available disk space and not by the signal production rate, and will become the standard for the whole experiment starting from 2022.

3.4 LHCb detector performance

A detailed description of the performance of the LHCb detector can be found in Ref. [146]. The following paragraphs review only the aspects that are most relevant to the measurement described in the present thesis.

Tracking

The relative uncertainty on the momentum of the charged particles passing through all of the three tracking detectors, which are named *long tracks*, varies from 0.5% for momenta below 20 GeV/c to 1.0% at 100 GeV/c. This corresponds to a relative mass resolution of about 5 per mil up for hadrons containing c and b quarks. The resolution on the PV position depends strongly on the number of tracks used to reconstruct the vertex. For the average number of 25 tracks, it equals 13 μm for both the x and y coordinates and 71 μm for the z coordinate. Finally, the impact parameter of a track with respect to a PV is measured with a resolution of $(15 + 29/p_{\mathrm{T}})$ μm, where p_{T} is measured in GeV/c. The resolutions plots are displayed in Fig. 3.17.

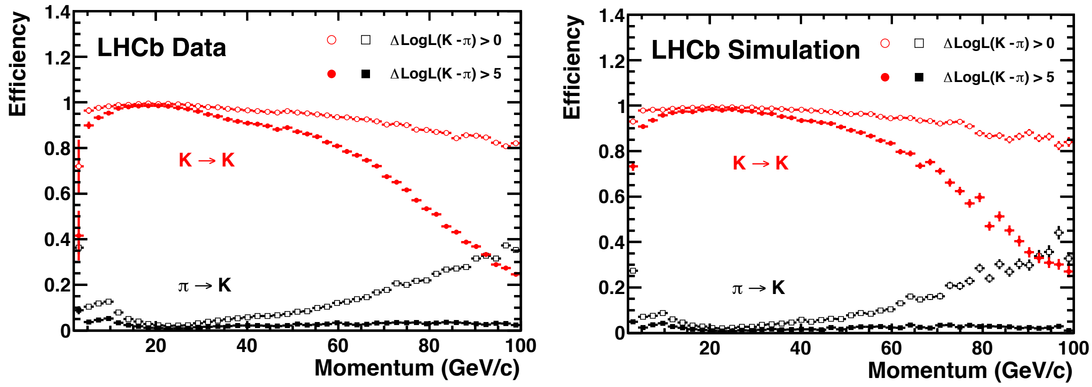

Figure 3.18: Kaon identification efficiency and pion misidentification rate as a function of track momentum for two different requirements on $\mathrm{DLL}_{K\pi}$. The left and right figures correspond to data and to the expectations from simulation, respectively. Figures taken from Ref. [146].

Particle identification

The particle identification of each track is performed by combining the information gathered by all PID detectors. Two main methods are used for this aim.

The first consists in calculating for each PID detector the likelihood of measuring the observed signal, assuming a pion identity for the track and employing as inputs its direction and measured momentum. The likelihood of different detectors is then multiplied, and is compared with its analogue under a difference identity hypothesis X, where X can equal K, p, μ or e. The logarithm of the likelihood ratio is used as a discriminant variable, and is named $\mathrm{DLL}_{X\pi} \equiv \log \mathcal{L}(X) - \log \mathcal{L}(\pi)$. For some detectors, like the RICH1 and RICH2, where the reconstruction of overlapping Cherenkov angles is particularly challenging, the interplay among different particles cannot be neglected. Therefore, a global likelihood, calculated based on all tracks and all detected signals, is maximised as a function of the tracks identities and used in the $\mathrm{DLL}_{X\pi}$ variable. When the particle identity is changed to X (or to π), the global likelihood is minimised again as a function of the mass assignment of the other particles. The minimisation algorithm is described in detail in Ref. [150]. The performance of the $\mathrm{DLL}_{K\pi}$ variable in distinguishing kaon from pion mesons is displayed in Fig. 3.18 for the two requirements that are most widely used in the trigger.

The second method relies neural networks trained on simulated events, implemented using the TMVA toolkit [158]. One neural network is trained for each particle identity X, including $X = \pi$, providing as output a real number between zero and unity, which is named `ProbNNx`. All of the variables used in the calculation of the $\mathrm{DLL}_{X\pi}$ variable are used in the network training, plus additional variables related to the occupancy and geometrical acceptance of each detector, as well as the quality of the track fitting and the number of energy deposits shared with other tracks. This approach, which is used mostly in offline analyses but not in the trigger, allows to take better into account correlations between different variables, and employs more information than the $\mathrm{DLL}_{X\pi}$ method. Therefore, its performance is significantly better, especially for muons and electrons, which are not well distinguished by the RICH detectors. On the contrary, the performance improvement for the discrimination between pion and kaon mesons is limited.

Chapter 4

Candidates selection

This chapter describes the trigger and offline requirements used to select the signal candidates. The simulation employed to study secondary decays and the kinematic weighting used to reduce discrepancies between data and simulation are detailed as well.

The measurement is performed using pp collision data collected at a centre-of-mass energy of 13 TeV during 2015, 2016, 2017 and 2018, corresponding to integrated luminosities of 0.3, 1.6, 1.7 and 2.1 fb^{-1}, respectively. The $D^{*+} \to D^0\pi^+_{\text{tag}}$ decay, where the D^0 meson subsequently decays into one of the following h^+h^- combinations, $K^-\pi^+$, K^+K^-, or $\pi^+\pi^-$, is reconstructed at the trigger level. The details of the selection are provided in the next sections.

4.1 Trigger selection

4.1.1 Hardware trigger

The thresholds of the requirements of the main hardware-trigger lines during 2015–2018 are summarised in Table 4.1. The natural choice to select $D^0 \to h^+h^-$ decays would be to use the `L0Hadron` line, which relies on the transverse energy measured in the hadronic calorimeter. However, its energy threshold, $E_{\text{T}} \gtrsim 3.7\,\text{GeV}$, is much larger than the software-trigger requirement on the D^0 transverse momentum, $p_{\text{T}}(D^0) \gtrsim 2\,\text{GeV}/c$. Moreover, owing to the approximated procedure employed to evaluate the transverse energy in the hardware trigger (see Sect. 3.3.1 for details), a sizeable fraction of D^0 mesons with transverse energy greater than the hardware-trigger threshold are not selected by the `L0Hadron` line, as displayed in Fig. 4.1. All in all, approximately 60% of the $D^0 \to h^+h^-$ decays reconstructed by the software trigger did not fire the `L0Hadron` line. These candidates correspond mostly to events where the hardware trigger was fired by other particles. In fact, charmed hadrons are produced in pairs in pp collisions, so that there is a high probability that the other charmed hadron fires the hardware trigger, also thanks to nonhadronic lines with lower thresholds. Finally, few per cents of the candidates correspond to events where one of the two mesons from the D^0-meson decay has decayed in flight into a muon or the D^0 meson has fired the electron trigger.

Therefore, no requirements on the type of hardware-trigger decision are applied in order not to lose a significant fraction of the decays yield. Even if this choice introduces different momentum thresholds and event topologies in the data sample, it does not bias the final measurement, as confirmed by the cross-checks in Sect. 8.1. For the purpose of comparison, it was checked that the requirement that the D^0 meson fired the hadron trigger or that the hardware trigger

Table 4.1: Summary of the thresholds of the requirements of the main L0-trigger lines, which are described in Sect. 3.3.1. Each configuration of the thresholds is identified by a *Trigger Configuration Key* (TCK), where the first two figures are equal to "00" during 2015 and to the last two figures of the year during 2016–2018. Each TCK is represented as a column, where the selected fraction of signal candidates with respect to the whole sample is reported in the last row. An additional requirement on the maximum number of hits in the SPD detector is employed to avoid events with large number of tracks, which correspond to a large ghost rate. This requirement is $n_{\mathrm{SPD}} < 900$ for the `L0DiMuon` line and $n_{\mathrm{SPD}} < 450$ for the others. Finally, the requirement on `SumEtPrev`, defined as the sum of the transverse energy of all of the clusters in the HCAL in the previous bunch crossing, is applied to all lines other than `L0DiMuon`, to reduce the probability that signals produced in the previous collision which last longer than 25 ns influence the trigger decision.

TCK	0x00a2	0x00a3	0x00a8	0x1603	0x1604	0x1605	0x1609	0x160e
`L0Hadron` E_{T} [MeV]	3600	3096	4008	3216	3552	3696	3696	3696
`L0Photon` E_{T} [MeV]	2688	2280	2688	2304	2784	2976	2832	2976
`L0Electron` E_{T} [MeV]	2688	2280	2688	2112	2256	2592	2352	2592
`L0Muon` p_{T} [MeV/c]	2800	2400	2800	1100	1300	1500	1300	1500
`L0DiMuon` $\sqrt{p_{\mathrm{T}1}p_{\mathrm{T}2}}$ [MeV/c]	1300	1300	1300	1000	1200	1300	1300	1300
`SumEtPrev` E_{T} [GeV]	–	–	–	–	–	–	–	–
Fraction of events [%]	2.5	1.3	1.1	0.8	0.5	1.4	12.2	0.9

TCK	0x160f	0x1611	0x1612	0x1702	0x1703	0x1704	0x1705	0x1706
`L0Hadron` E_{T} [MeV]	3744	3888	3888	2976	3216	3552	3696	3888
`L0Photon` E_{T} [MeV]	2784	2976	2976	2112	2304	2784	2976	3072
`L0Electron` E_{T} [MeV]	2400	2616	2616	1872	2112	2256	2592	2688
`L0Muon` p_{T} [MeV/c]	1800	1500	1600	700	1100	1300	1500	1900
`L0DiMuon` $\sqrt{p_{\mathrm{T}1}p_{\mathrm{T}2}}$ [MeV/c]	1500	1400	1500	900	1000	1200	1300	1800
`SumEtPrev` E_{T} [GeV]	–	–	–	24	24	24	24	24
Fraction of events [%]	10.0	0.7	1.5	0.1	0.6	0.5	2.1	0.4

TCK	0x1707	0x1708	0x1709	0x17a7	0x1801	0x18a1	0x18a2	0x18a4
`L0Hadron` E_{T} [MeV]	3720	3216	3456	3720	3792	3792	3792	3792
`L0Photon` E_{T} [MeV]	2712	2304	2472	2712	2952	2952	2952	2952
`L0Electron` E_{T} [MeV]	2304	2112	2112	2304	2376	2376	2376	2376
`L0Muon` p_{T} [MeV/c]	1700	1100	1400	1700	1750	1750	1750	1750
`L0DiMuon` $\sqrt{p_{\mathrm{T}1}p_{\mathrm{T}2}}$ [MeV/c]	1800	1000	1300	1800	1800	1800	1800	1800
`SumEtPrev` E_{T} [GeV]	24	24	24	24	24	24	24	24
Fraction of events [%]	10.8	5.5	11.6	0.0	14.8	0.0	14.3	6.4

was fired by a particle other than the D^{*+} meson, which is used in many other D^{*+}-tagged measurements like that of Ref. [18], would select about 96% of the candidates.

4.1.2 First-stage software trigger

One or both of the tracks from the D^0-meson decay are required to have been responsible for the decision of the first-stage software trigger. This can be based either on the single- or two-tracks lines, which are designed select a sample with enhanced heavy-flavour hadron content. These lines employed four sets of thresholds during 2015–2018, each one labelled with a letter and corresponding to:

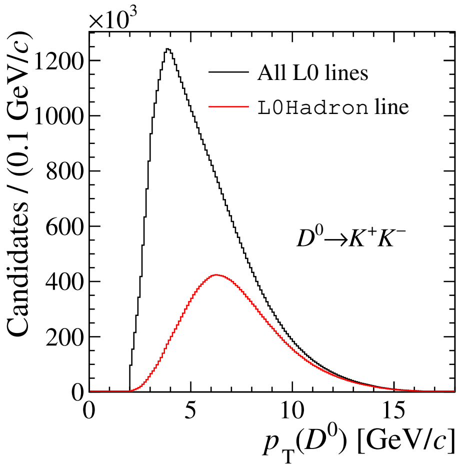

Figure 4.1: Distribution of the D^0 transverse momentum, for all selected signal candidates and for those where the D^0 meson fired the `L0Hadron` hardware-trigger line.

(a) the 9.4% of the sample (whole 2015 sample and 16.4% of the 2016 sample);

(b) the 2.1% of the sample (7.6% of the 2016 sample);

(c) the 8.4% of the sample (29.8% of the 2016 sample);

(d) the 80.1% of the sample (46.2% of the 2016 sample and full 2017–2018 sample).

The single-track line requires the presence of at least one track with high p_{T} and large χ^2_{IP} with respect to all PVs, where the χ^2_{IP} is defined as the difference in the vertex-fit χ^2 of a given PV reconstructed with and without the particle being considered. This is ensured by requiring that the following condition is satisfied by the track,

$$\begin{aligned}&\left\{(p_{\mathrm{T}} > 25) \wedge (\chi^2_{\mathrm{IP}} > 7.4)\right\} \vee \\ &\qquad\left\{[1 < p_{\mathrm{T}} < 25] \wedge \left[\ln \chi^2_{\mathrm{IP}} > \ln(7.4) + \frac{1}{(p_{\mathrm{T}}-1)^2} + \alpha_0\left(1 - \frac{p_{\mathrm{T}}}{25}\right)\right]\right\}, \end{aligned} \tag{4.1}$$

where p_{T} is expressed in GeV$/c$ and α_0 is a constant equal to 1.1, 1.6 and 2.3 for the (a,d), (b) and (c) samples. The boundary of the condition in Eq. (4.1) is plotted in Fig. 4.2 for all values of the α_0 parameter.

On the other hand, the two-track line requires the presence of two tracks of high p_{T} forming a good-quality vertex that is significantly displaced from their associated PV, defined as the PV to which the IP of the two-track combination is the smallest. The selection in this case is based on a bonsai boosted decision tree [159] that takes as inputs the χ^2 of the two-track vertex fit, the number of tracks with $\chi^2_{\mathrm{IP}} > 16$, the sum of the p_{T} of the two tracks and their χ^2_{FD} with respect to the associated PV, where the χ^2_{FD} is the flight-distance (FD) significance. This is defined as the difference in the vertex-fit χ^2 of the PV reconstructed including the two tracks, and the sum of the PV vertex-fit χ^2 (without including the two tracks) and of the two-track vertex-fit χ^2. The additional background rejection allowed by the identification of the tracks vertex allows for looser requirements on the transverse momentum and the χ^2_{IP} of the tracks with respect to the single-track line. Also for the two-tracks line, the requirement employed for the sample (c) is tighter with respect to the other samples. All the requirements of the first-stage trigger lines are listed in Table 4.2.

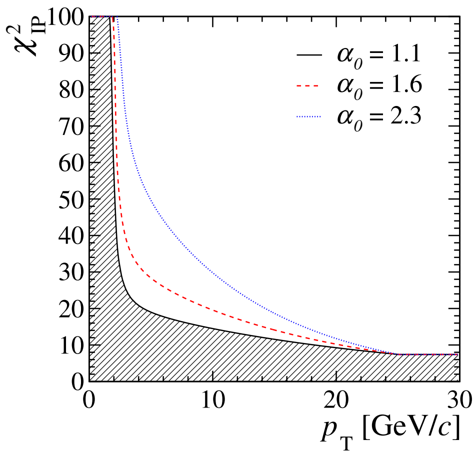

Figure 4.2: Requirement of the single-track line of the first-stage software trigger in the $\chi^2_{\rm IP}$ *vs.* $p_{\rm T}$ plane, for the three values of the parameter α_0.

4.1.3 Second-stage software trigger

The second-stage software trigger combines all pairs of oppositely charged tracks with distance of closest approach (DOCA) less than 0.1 mm to form D^0-meson candidates. Both tracks are required to be of high quality based on the χ^2 per degree of freedom (χ^2/ndf) of their track fit and on the output of a multivariate classifier trained to identify fake tracks, which combines information from all of the tracking detectors. The two tracks are required to have $p > 5\,\mathrm{GeV}/c$ and to have a $\chi^2_{\rm IP}$ with respect to all PVs in the event greater than 4. Finally, the tracks are given a pion or kaon mass assignment, depending if their $\mathrm{DLL}_{K\pi}$ is less or greater than 5, respectively. The χ^2/ndf of the two-track vertex fit is required to be less than 10 and the D^0 candidate is required to satisfy $p_{\rm T} > 2\,\mathrm{GeV}/c$ and to have a reconstructed mass within $\pm 150\,\mathrm{MeV}/c^2$ of its known value. The angle between the D^0 momentum and the vector connecting the D^0-meson PV and decay vertex (DV), $\theta_{\rm DIRA}$, is required to be less than 17.3 mrad, where the D^0-meson PV is defined as the PV to which the D^0-meson $\chi^2_{\rm IP}$ is the smallest. The $\chi^2_{\rm FD}$ of the D^0 meson with respect to its PV is required to be greater than 25. Finally, all remaining good-quality tracks of the event, as described above, which satisfy $p > 1\,\mathrm{GeV}/c$ and $p_{\rm T} > 200\,\mathrm{MeV}/c$, are assigned a pion mass hypothesis and are combined with the D^0 meson to form a D^{*+}-meson candidate. The χ^2/ndf of the D^{*+} vertex fit is required to be less than 25, and the value of $\Delta m \equiv m(h^+h^-\pi^+_{\rm tag}) - m(h^+h^-)$ is required to lie in the range $[130, 160]\,\mathrm{MeV}/c^2$. This variable is preferred over the invariant D^{*+}-meson mass, $m(h^+h^-\pi^+_{\rm tag})$, since it is measured with better resolution. In fact, the error on the reconstructed D^0-meson mass, $m(h^+h^-)$, cancels to large extent in the difference $m(h^+h^-\pi^+_{\rm tag}) - m(h^+h^-)$. All the requirements of the second-stage software trigger are summarised in Table 4.2.

4.2 Offline selection

In the offline selection, the particle identification criteria for the $\pi^\pm$-meson candidates from the D^0 decay are strengthened, requiring $\mathrm{DLL}_{K\pi}(\pi^\pm) < -5$. This allows to reduce the background of misidentified $D^0 \to K^-\pi^+$ decays in the sample of the $\pi^+\pi^-$ decay channel, as detailed in Appendix E.1. In addition, to suppress the $D^0 \to K^-e^+\nu_e$ background, the $K^\pm$ mesons from

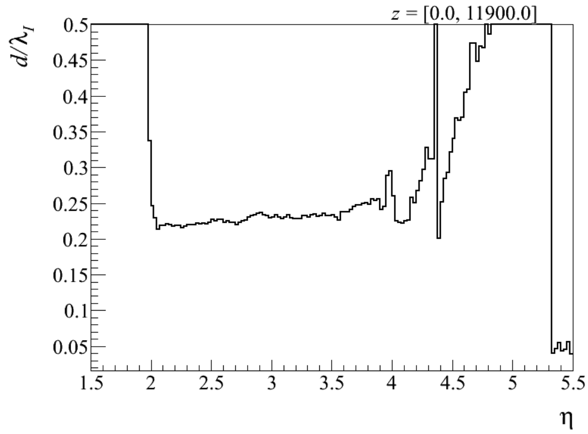

Figure 4.3: Material thickness of the LHCb detector until the end of the RICH2 detector as a function of pseudorapidity, for a particle produced in the nominal pp interaction point and unbent by the magnetic field. The thickness is quantified in interaction-lengths units and is averaged over the azimuthal angle ϕ. The peak at $\eta = 4.38$, corresponding to a polar angle of 25 mrad, is due to the conical beam pipe inside the RICH1 detector [161]. Figure taken from Ref. [160].

the $D^0 \to K^+K^-$ decay are required not to be identified as electrons or positrons, based on the output of the `ProbNNe` neural network. This requirement is applied to both particles to avoid introducing different efficiencies for D^0 and $\overline{D}^0$ decays. Its efficiency in rejecting the background is detailed in Appendix E.1. In addition, the pseudorapidity of the h^+, h^- and $\pi^+_{\rm tag}$ tracks is required to lie in the range $[2, 4.2]$ to exclude candidates that traversed detector material corresponding to more than 0.3 interaction lengths between the pp interaction point and the end of the tracking system, as these candidates are affected by large detection asymmetries [160], as shown in Fig. 4.3. The scarcely populated tails of the momentum distributions of all particles are removed by upper requirements on its value, thus rejecting candidates characterised by a poor performance of the particle identification, as shown in Fig. 3.18. The D^0 flight distance in the plane transverse to the beam,

$$R_{xy} \equiv \sqrt{(x_{\rm DV} - x_{\rm PV})^2 + (y_{\rm DV} - y_{\rm PV})^2}, \tag{4.2}$$

is required to be less than 4 mm to remove D^{*+} candidates produced by hadronic interactions with the detector material, and the z coordinate of the D^0 decay vertex is required to lie within 200 mm from the nominal pp interaction point to reject D^0 candidates that are not produced in the pp collision region. These include D^0 mesons produced in the interaction of other hadrons with the RF foil that protects the VELO or with the VELO sensors, and which decayed soon thereafter, as well as the D^0 candidates that originated in the two ovoid regions on the right and on the left of the nominal collision point of the proton bunches in Fig. 4.4. Finally, the h^+h^- invariant mass, $m(h^+h^-)$, is required to lie in the range $[1847.8, 1882.6]$, $[1850.6, 1879.9]$ and $[1846.2, 1884.2]\,\mathrm{MeV}/c^2$ for the $D^0 \to K^-\pi^+$, $D^0 \to K^+K^-$ and $D^0 \to \pi^+\pi^-$ candidates, respectively, corresponding to ± 2 times the mass resolution around the known D^0-meson mass.

Since the Q-value of the $D^{*+} \to D^0\pi^+_{\rm tag}$ decay, about $6\,\mathrm{MeV}/c^2$, is low with respect to the π^+-meson mass, the momenta of the D^0 and of the $\pi^+_{\rm tag}$ mesons are nearly aligned in the laboratory frame. As a consequence, the resolution on the position of the D^{*+}-meson decay vertex along its momentum direction, approximately 1.5 cm, is of the same order of the average flight distance of the D^0 meson, approximately 1 cm. Moreover, the uncertainty on the angle between the pion

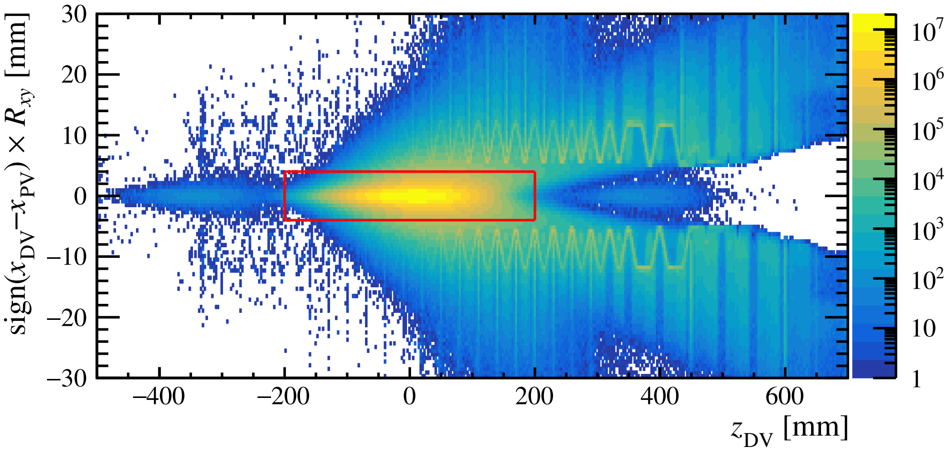

Figure 4.4: Signed radial distance of the DV of the D^0 meson with respect to its PV, as defined in Eq. (4.2), *vs.* its z coordinate. Vertical lines corresponding to VELO sensors and the wavy shape of the shielding RF foil are visible in the region $R_{xy} > 5\,\text{mm}$. Only the candidates within the red rectangle ($R_{xy} < 4\,\text{mm} \wedge |z_{\rm DV}| < 200\,\text{mm}$) are selected for further analysis.

and D^0 mesons dominates the uncertainty on the invariant mass of the $m(D^0\pi^+_{\rm tag})$ meson. In order to improve the resolution on the D^0 decay time and on the $m(D^0\pi^+_{\rm tag})$ invariant mass, a kinematic fit is performed in which the D^{*+} meson is required to originate from the PV [162]. In particular, this improves the resolution on the $m(D^0\pi^+_{\rm tag})$ mass by around a factor of 2. However, the measured decay time of D^0 mesons coming from secondary D^{*+} mesons, that is that originate from B-meson decays, is biased towards higher values. The IP of secondary D^0 mesons in general differs from zero, whereas that of primary candidates is equal to zero within the experimental uncertainty. The background of secondary decays is suppressed by requiring that the D^0-meson IP be less than 60 µm and that its decay time be less than $8\,\tau_{D^0}$. Finally, the D^0 decay time is required to be greater than $0.45\,\tau_{D^0}$ to exclude events with reconstruction efficiency much less than unity, since their simulated reconstruction efficiency is very sensitive to possible discrepancies between simulation and data.

Clone tracks are removed by relying on a discriminating variable based on the Kullback–Liebler distance [163]. A tiny fraction of tracks that share the same VELO-track segment and are reconstructed both as a kaon and as a $\pi^+_{\rm tag}$ meson is found in the plane of the asymmetry of their momenta *vs.* the angle between their directions, as shown in Fig. 4.5. These tracks are rejected by the following requirement,

$$0.026\,\frac{p(\pi^+_{\rm tag}) - p(K^\pm)}{p(\pi^+_{\rm tag}) + p(K^\pm)} < -0.01976 + \theta[\vec{p}(\pi^+_{\rm tag}), \vec{p}(K^\pm)], \tag{4.3}$$

which rejects about 0.0012% and 0.023% of the $D^0 \to K^-\pi^+$ and $D^0 \to K^+K^-$ candidates, respectively. All offline requirements are summarised in Table 4.2.

4.3 Removal of the $m(D^0\pi^+_{\rm tag})$ background

After these requirements, around 2.5%, 4.7% and 4.9% of the $D^0 \to K^-\pi^+$, $D^0 \to K^+K^-$ and $D^0 \to \pi^+\pi^-$ candidates, respectively, can be combined with more than one $\pi^+_{\rm tag}$ candidate to form a D^{*+} candidate. When this happens, one D^{*+} candidate is selected at random. The distribution

Table 4.2: Summary of the selection requirements. The definition of the variables that were not defined in the text is given in Appendix C. The labels "15,16" and "17,18" refer to different thresholds during 2015–2016 and 2017–2018, respectively. The hardware-trigger requirements are described in Sect. 4.1.1.

Candidate	Variable	HLT1		HLT2	Offline	Unit
		Single-track	Two-track			
	track $\chi^2/\text{ndf}(h^\pm)$	< 2.5	< 2.5	< 3	< 2.5	–
	track-based ghost probability$(h^\pm)$	$< 0.4^{(a)}, 0.2^{(b,c,d)}$	$< 0.4^{(a)}, 0.2^{(b,c,d)}$	–	< 0.2	–
	`TRACK_CloneDist`$(h^\pm)$	–	–	–	$== -1$	–
	$p(h^\pm)$	$> 3^{(a,b)}, 5^{(c,d)}$	$> 3^{(a,b)}, 5^{(c,d)}$	> 5	< 120	GeV/c
$h^\pm$	$p_{\text{T}}(h^\pm)$	–	$> 0.5^{(a,b)}, 0.6^{(c,d)}$	> 0.8	< 12	GeV/c
	$\eta(h^\pm)$	–	–	–	$\in [2, 4.2]$	–
	$p_{\text{T}} - \chi^2_{\text{IP}}(h^\pm)$	see Eq. (4.1)	–	–	–	–
	$\chi^2_{\text{IP}}(h^\pm)$	–	> 4	> 4	–	–
	$\text{DLL}_{K\pi}(K^\pm)$	–	–	> 5	–	–
	$\text{DLL}_{K\pi}(\pi^\pm)$	–	–	< 5	< -5	–
	`ProbNNe`($K^\pm$ from $D^0 \to K^+K^-$)	–	–	–	< 0.2	–
	$\eta(h^+h^-$ DV, PV)	–	$\in [2, 5]$	–	–	–
	$m_{\text{corr}}(h^+h^-)$	–	> 1	–	–	GeV/c
	output of the classifier	–	$> 0.95^{(a,b,d)}, 0.97^{(c)}$	–	–	–
	$\max\{p_{\text{T}}(h^+), p_{\text{T}}(h^-)\}$	–	–	> 1	–	GeV/c
	$p_{\text{T}}(D^0)$	–	> 2	> 1	$\in [2, 18]$	GeV/c
	$p(D^0)$	–	–	–	< 180	GeV/c
	$m(h^+h^-)$	–	–	$\in [1715, 2015]$	–	MeV/c^2
	$m(K^-\pi^+)$	–	–	–	$\in [1847.8, 1882.6]$	MeV/c^2
	$m(K^+K^-)$	–	–	–	$\in [1850.6, 1879.8]$	MeV/c^2
	$m(\pi^+\pi^-)$	–	–	–	$\in [1846.2, 1884.2]$	MeV/c^2
	DOCA(h^+, h^-)	–	–	< 0.1	–	mm
D^0	D^0 vertex-fit χ^2/ndf	–	< 10	< 10	–	–
	$\theta_{\text{DIRA}}(D^0)$	–	$< \pi/2$	< 17.3	–	mrad
	$\chi^2_{\text{FD}}(D^0)$	–	–	> 25	–	–
	R_{xy}	–	–	–	< 4	mm
	$\lvert z(\text{DV})\rvert$	–	–	–	< 200	mm
	D^0 proper decay time	–	–	–	$\in [0.45, 8]$	τ_{D^0}
	IP(D^0)	–	–	–	< 60	μm
	track $\chi^2/\text{ndf}(\pi^+_{\text{tag}})$	–	–	< 3	–	–
	track-based ghost probability(π^+_{tag})	–	–	$< 0.4^{15,16}, 0.25^{17,18}$	< 0.15	–
π^+_{tag}	`TRACK_CloneDist`(π^+_{tag})	–	–	–	$== -1$	–
	$p_{\text{T}}(\pi^+_{\text{tag}})$	–	–	$> 0.1^{15,16}, 0.2^{17,18}$	$\in [0.2, 1.4]$	GeV/c
	$p(\pi^+_{\text{tag}})$	–	–	> 1	< 16	GeV/c
	$\eta(\pi^+_{\text{tag}})$	–	–	–	$\in [2, 4.2]$	–
D^{*+}	D^{*+} vertex-fit χ^2/ndf	–	–	< 25	–	–
	$\Delta m = m(h^+h^-\pi^+_{\text{tag}}) - m(h^+h^-)$	–	–	$\in [130, 160]$	–	MeV/c^2
	$m(D^0\pi^+_{\text{tag}})$	–	–	–	< 2020	MeV/c^2

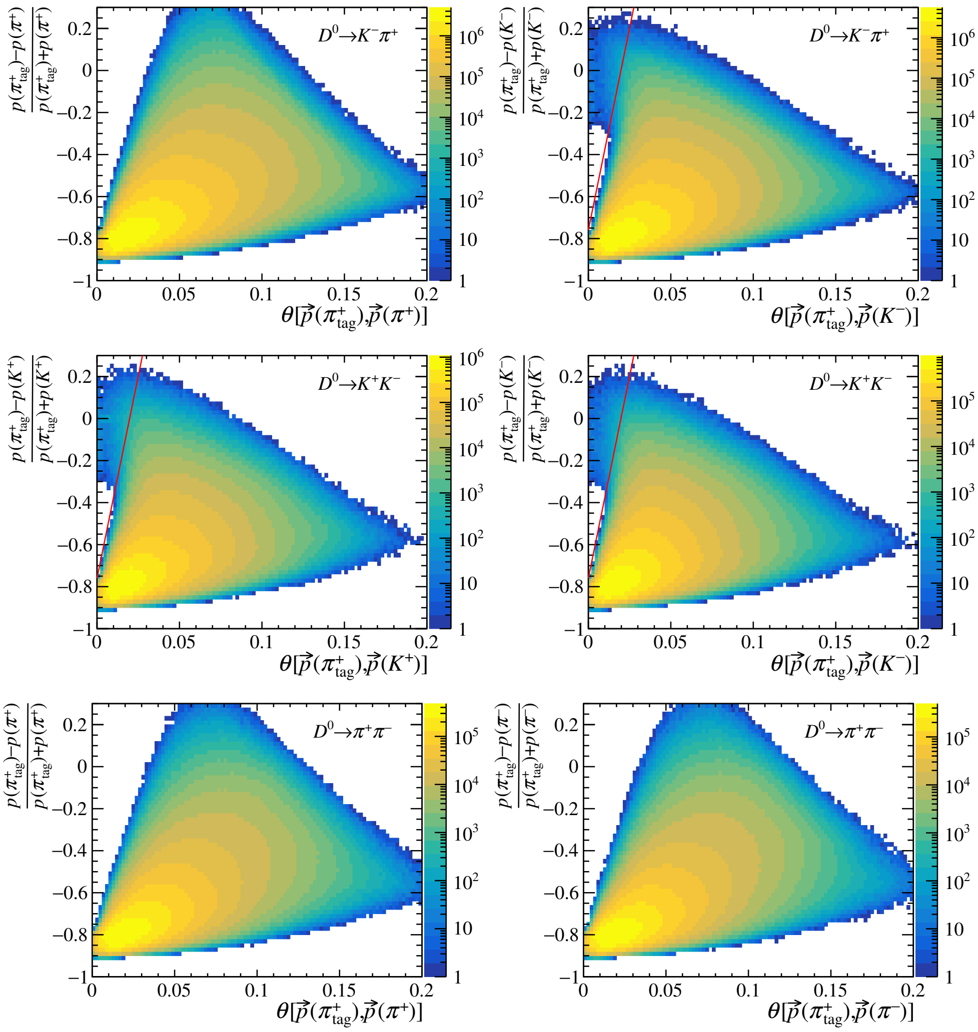

Figure 4.5: Asymmetry and angle between the momenta of one of the D^0-meson final-state hadrons and the $\pi^+_{\rm tag}$ meson for (top) $D^0 \to K^-\pi^+$, (centre) $D^0 \to K^+K^-$ and (bottom) $D^0 \to \pi^+\pi^-$ decays. The requirement of Eq. (4.3), which rejects the clones concentrated near the point $(0, 0)$, is displayed wherever applied.

of the invariant mass of the D^{*+} candidates, $m(D^0\pi^+_{\rm tag})$, is displayed for the three decay channels in Fig. 4.6. This quantity is calculated using the known D^0 mass in the determination of the D^0-meson energy. This choice ensures that the relatively large resolution with which the invariant mass of the D^0 meson, $m(h^+h^-)$, is known does not contribute to the uncertainty on the D^{*+} invariant mass, and that possible differences in the D^{*+} resolution for different D^0-meson decay channels are greatly mitigated. The $m(D^0\pi^+_{\rm tag})$ signal window is defined as $[2009.2, 2011.3]\,\mathrm{MeV}/c^2$ and retains about 96.9% of the D^{*+} mesons. The purity within this window is 97.7%, 95.5% and 94.1% for the $D^0 \to K^-\pi^+$, $D^0 \to K^+K^-$ and $D^0 \to \pi^+\pi^-$ samples, respectively. The residual background is dominated by combinations of real D^0 decays or, to lesser extent, by pairs of unrelated h^+h^- tracks, with unrelated particles. The percentage of $D^0 \to K^-\pi^+$ events with multiple candidates is therefore around half of the percentage of the K^+K^- or $\pi^+\pi^-$ decay channels since, whenever a $D^0 \to K^-\pi^+$ decay is associated with

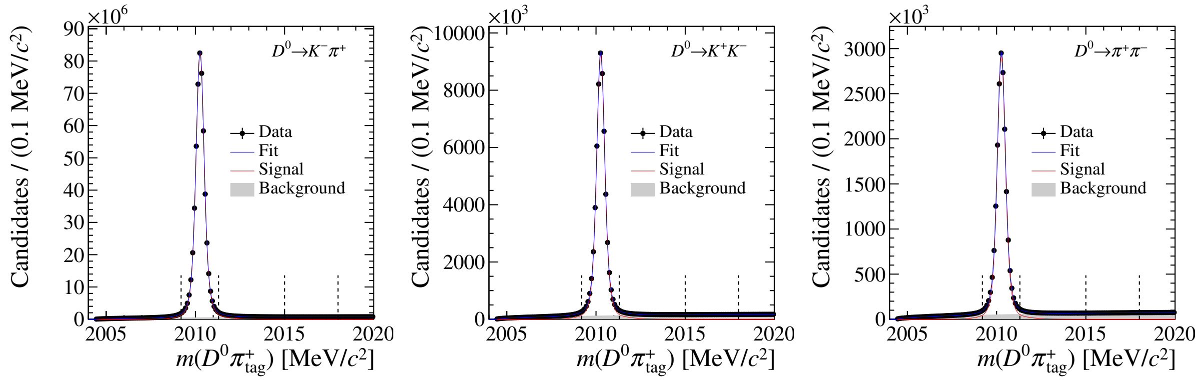

Figure 4.6: Distribution of $m(D^0\pi^+_{\rm tag})$ for the (left) $K^-\pi^+$, (centre) K^+K^- and (right) $\pi^+\pi^-$ decay channels. The signal window and the lateral window employed to remove the combinatorial background (grey filled area) are delimited by the vertical dashed lines.

a $\pi^-_{\rm tag}$ meson, it is classified as a wrong-sign $\overline{D}^0 \to K^-\pi^+$ decay. The small difference in the percentages of multiple candidates for the $D^0 \to K^+K^-$ and $D^0 \to \pi^+\pi^-$ samples is due to the slightly different kinematics of these decays, owing to the different masses of the kaon and pion mesons and to the PID requirements. The residual background is subtracted by using background candidates in the lateral mass window $[2015, 2018]$ MeV/c^2, weighted with a suitable negative coefficient. This coefficient is determined based on a binned maximum-likelihood fit to the $m(D^0\pi^+_{\rm tag})$ distribution, which relies on an empirical model. The signal probability density function (PDF) is described by the sum of two Gaussian functions and a Johnson S_U distribution [164], which has a Gaussian-like core but allows for asymmetric tails,

$$S_U(x;\mu,\sigma,\delta,\gamma) \propto \left[1+\left(\frac{x-\mu}{\sigma}\right)^2\right]^{-\frac{1}{2}} \times \exp\left\{-\frac{1}{2}\left[\gamma+\delta\sinh^{-1}\left(\frac{x-\mu}{\sigma}\right)\right]\right\}, \tag{4.4}$$

where the μ and σ parameters are correlated with the mean and standard deviation of the distribution, and the δ and γ parameters describe the asymmetric tails. The background PDF, instead, is modelled by the function $\sqrt{m(D^0\pi^+_{\rm tag}) - m_0} \times \{1 + \alpha[m(D^0\pi^+_{\rm tag}) - m_0] + \beta[m(D^0\pi^+_{\rm tag}) - m_0]^2\}$, where m_0 is defined as the sum of the D^0 and π^+ masses and the small parameters α and β quantify the deviations from a square-root function. The background subtraction is performed without distinguishing between D^{*+} and D^{*-} candidates, but separately in each decay-time bin, since the background PDF changes slightly as a function of decay time. The 21 bins of decay time, which span the range $[0.45, 8]\tau_{D^0}$, are chosen to be equally populated, except the last two bins, which contain half the number of candidates. An example of the fits for the three decay channels is reported in Fig. 4.7. The magnitude of the coefficient used to weight the background candidates in the $m(D^0\pi^+_{\rm tag})$ lateral window is displayed in Fig. 4.8 for the fit to the D^{*+} and D^{*-} candidates as well as for the fit to their sum. The coefficients obtained from the first two fits agree within the statistical uncertainty. The background subtraction is expected to be effective only if the kinematics and the asymmetry of the background in the signal and lateral windows are equal. Deviations from this assumption, as well as the impact of the uncertainty of the value of the coefficients and of possible variations of their value between D^{*+} and D^{*-} candidates, are assessed among systematic uncertainties in Sect. 7.1.

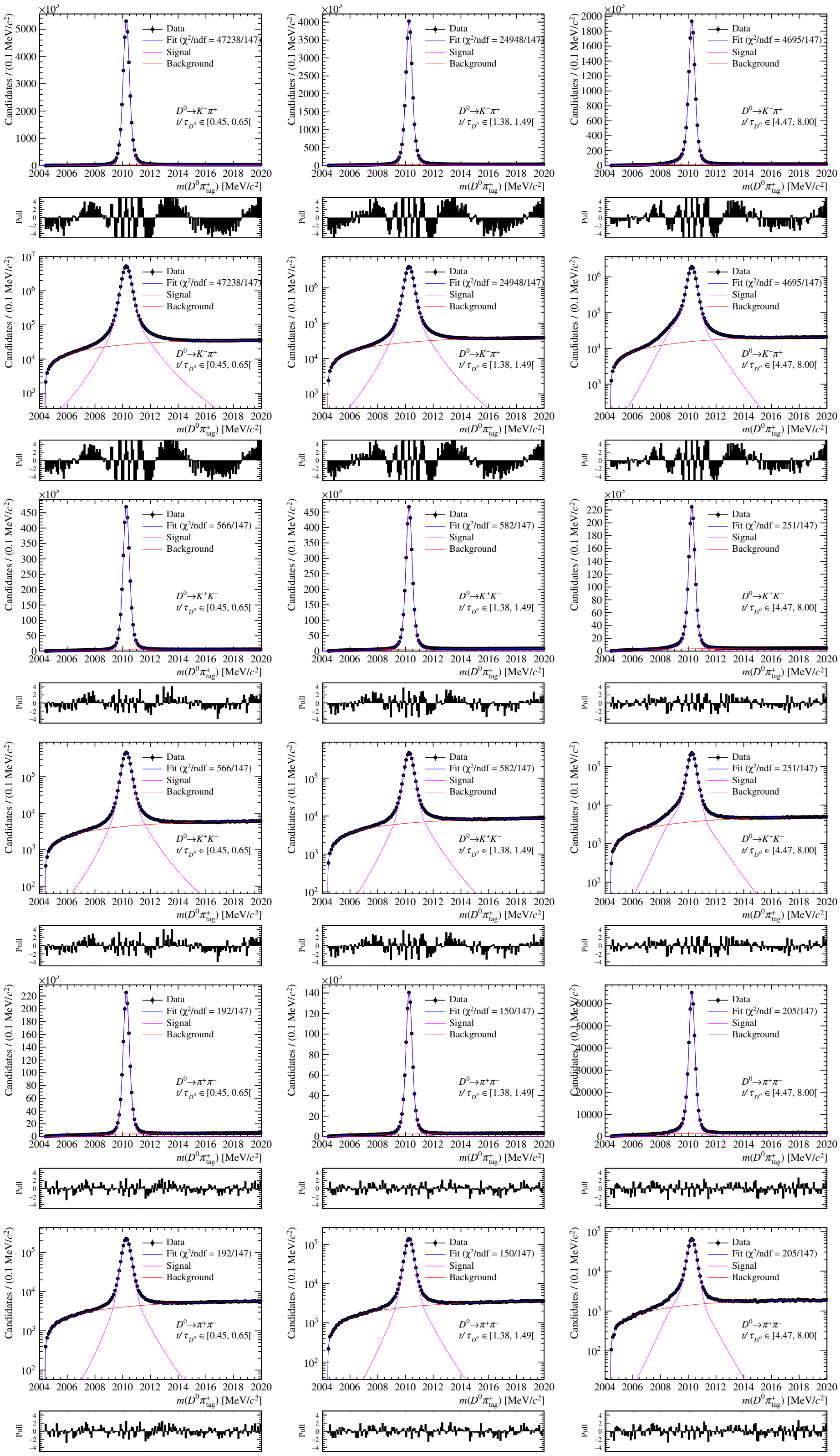

Figure 4.7: Distribution of $m(D^0\pi^+_{\rm tag})$, with fits superimposed, for the (top) $K^-\pi^+$, (centre) K^+K^- and (bottom) $\pi^+\pi^-$ decay channels, both in linear and in logarithmic scales. Left, central and right plots correspond to the first, tenth and last bin of decay time, respectively.

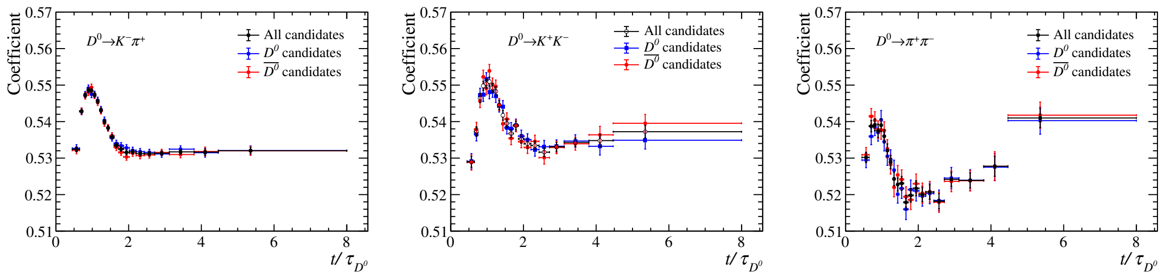

Figure 4.8: Magnitude of the coefficient used to remove the $m(D^0\pi^+_{\rm tag})$ background as a function of decay time, as calculated from the results of the fits to the $m(D^0\pi^+_{\rm tag})$ distributions.

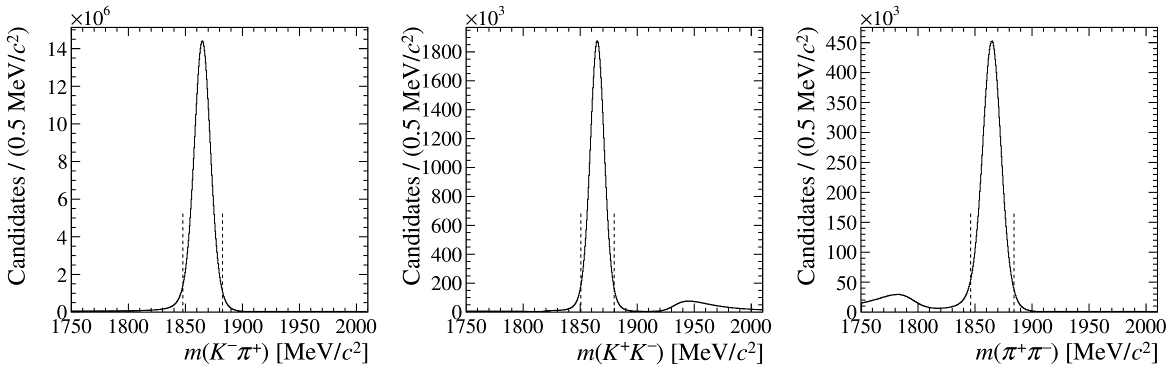

Figure 4.9: Distribution of $m(h^+h^-)$ after the subtraction of the $m(D^0\pi^+_{\rm tag})$ background for the (left) $D^0 \to K^-\pi^+$, (centre) $D^0 \to K^+K^-$ and (right) $D^0 \to \pi^+\pi^-$ samples. The signal window is delimited by the vertical dashed lines.

4.4 Signal yield

The $m(h^+h^-)$ distributions after the removal of the $m(D^0\pi^+_{\rm tag})$ background are plotted in Fig. 4.9. The number of D^0 candidates in the signal region for each year, magnet polarity and decay channel in reported in Table 4.3. The total yield is equal to 519, 58 and 18 millions for the $K^-\pi^+$, K^+K^- and $\pi^+\pi^-$ decay channels, respectively. The number of candidates per integrated luminosity is larger by a factor of 3.4 than that of the measurement with the data collected during 2011 and 2012 at centre-of-mass energies of 7 TeV and 8 TeV [114]. This is ascribable to several factors. Firstly, the production cross section of charm quarks in pp collisions at $\sqrt{s} = 13$ TeV is larger by a factor of approximately 1.8 [124, 165]. Secondly, about one third of the candidates is selected only by the two-track line of the first-stage software trigger, which was introduced in 2015, and not by the single-track line. In particular, the acceptance at small decay times is considerably increased by the two-track line, as shown in Fig. 4.10. Finally, the real-time reconstruction of the events since 2015 [156, 157] allowed to increase the trigger rate, and to loosen some of the software-trigger requirements, such as the requirement on $\chi^2_{\rm FD}(D^0)$ of the second-stage software trigger. All in all, the total number of candidates selected for the present measurement is about 6.1 times that of the 2011–2012 measurement.

However, the precision on ΔY does not improve as the ratio of the square root of the number of collected events in 2015–2018 and in 2011–2012. In fact, its precision strongly depends on the time distribution of the events. In particular, it is very sensitive to the number of events at smallest decay times (more numerous) and at largest decay times (much rarer). In fact, thanks

Table 4.3: Number of signal candidates after the subtraction of the $m(D^0\pi^+_{\text{tag}})$ background, in millions. The number of candidates selected in the measurement with 2011–2012 data [114] is reported for comparison.

Data sample	$\int \mathcal{L}\,\mathrm{d}t$ [fb^{-1}]	$D^0 \to K^-\pi^+$	$D^0 \to K^+K^-$	$D^0 \to \pi^+\pi^-$
2015 *MagUp*	0.3	9.9	1.1	0.4
2015 *MagDown*		15.5	1.7	0.6
2016 *MagUp*	1.6	70.8	7.7	2.6
2016 *MagDown*		77.0	8.5	2.8
2017 *MagUp*	1.7	80.1	8.9	2.8
2017 *MagDown*		83.3	9.4	2.9
2018 *MagUp*	2.1	94.9	10.7	3.4
2018 *MagDown*		87.6	9.9	3.1
Total 2015–2018	5.7	519.1	57.9	18.4
Total 2011–2012	3.2	87.5	9.6	3.0

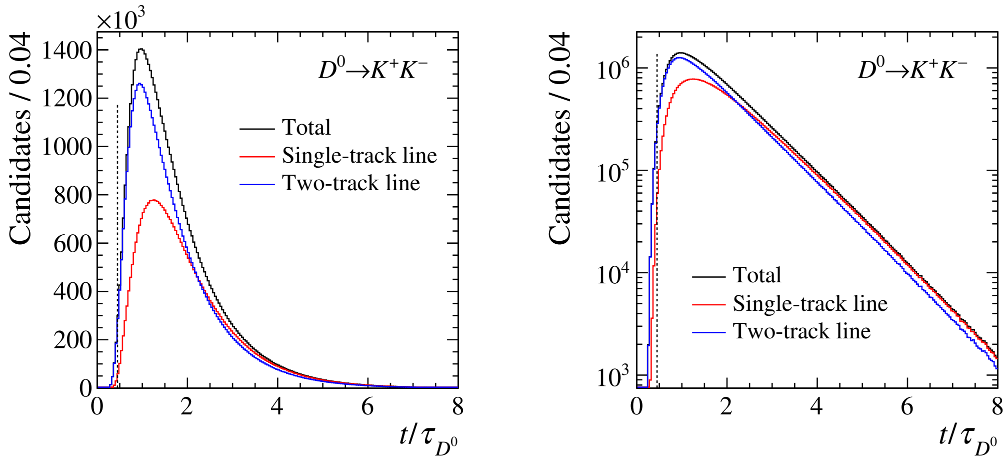

Figure 4.10: Distribution of the D^0 decay time, separately for different HLT1 lines, in (left) linear and (right) logarithmic scale. The vertical dashed line represents the lower requirement on decay time ($0.45\,\tau_{D^0}$), while the upper requirement is at $8\,\tau_{D^0}$.

to its larger lever arm, a large asymmetry at small or large decay times modifies the slope of the fitted time-dependent asymmetry much more than an asymmetry of equal size at intermediate decay times. Most of the additional events that were collected in 2015–2018 thanks to the two-track line are concentrated at small decay times, which were already abundantly populated by candidates selected by the single-track line. On the contrary, nearly all of the candidates at large decay times — where the number of candidates is much lower — were already collected by the single-track line, as displayed in Fig. 4.10. As a consequence, the increase in precision of the measurement with 2015–2018 data with respect to that with 2011–2012 data is lower than what would be naively expected with a simple scaling based on the square root of the number of events.

Table 4.4: Selection requirements of the secondary decays obtained by combining a D^{*+} meson with a μ^- particle.

Candidate	Variable	Requirement	Unit
μ^-	track-based ghost probability (μ^-)	< 0.4	–
	track $\chi^2/\mathrm{ndf}(\mu^-)$	< 5	–
	$p_\mathrm{T}(\mu^-)$	> 2	GeV/c
	$p(\mu^-)$	> 3	GeV/c
	$\chi^2_\mathrm{IP}(\mu^-)$	> 4	–
$D^{*+}\mu^-$	$m(D^{*+}\mu^-)$	$\in [3, 5]$	GeV/c^2
	$\theta_\mathrm{DIRA}(D^{*+}\mu^-)$	< 44.7	mrad
	$(D^{*+}\mu^-)$ vertex χ^2/ndf	< 6	–

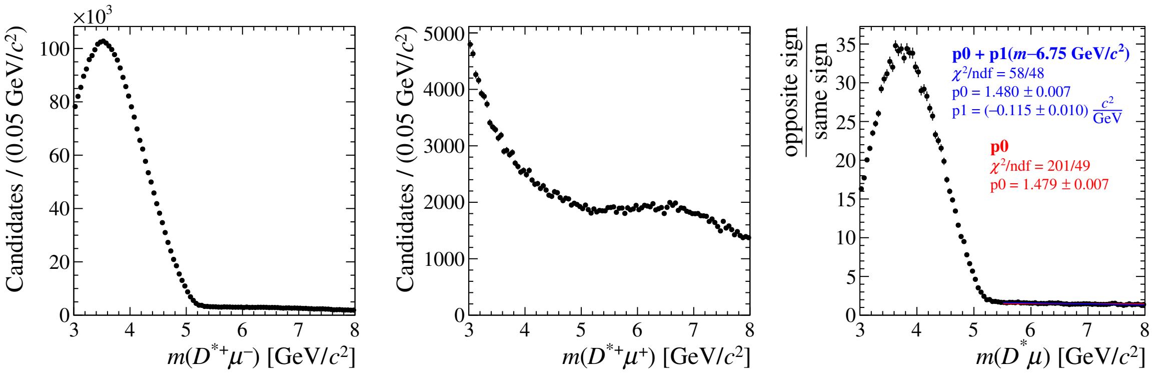

Figure 4.11: Invariant-mass distribution of the combination of the D^{*+} meson with a muon with (left) opposite and (centre) equal charge. The ratio of the two distributions is shown in the right plot, together with the χ^2 fits of a constant and a linear function in the range $[5.5, 8]$ GeV/c^2.

4.5 $(D^{*+}\mu^-)$ sample

A pure sample of secondary decays, obtained by combining a D^{*+} meson with a muon with opposite charge (opposite-sign pair), is used to check the agreement of simulated secondary decays with real data. The selection requirements employed in addition to those detailed in the previous sections are listed in Table 4.4. The residual combinatorial background of D^{*+} mesons combined with unrelated μ^- particles, or other misidentified particles, is removed based on the distribution of the invariant mass of the combinations of D^{*+} mesons with muons with the same charge (same-sign pairs), $m(D^{*+}\mu^+)$, which is shown in Fig. 4.11. The ratio of the $m(D^{*+}\mu^\pm)$ distribution of opposite-sign pairs to that of same-sign pairs is fitted in the region $[5.5, 8]$ GeV/c^2 with a linear function. The function is then extrapolated to the signal region and the same-sign pairs in the signal region are assigned a weight equal to the negative of its value to remove the background.

Table 4.5: List of the decays used to generate the simulated sample of inclusive $B^0 \to D^{*\pm}X$ decays. The values of the branching fractions are taken from Ref. [36].

Decay channel	$\mathcal{B}$ $[10^{-3}]$		EvtGen model
$B^0 \to D^{*-}e^+\nu_e$	50.5	$\pm\,1.4$	HQET2 1.205 0.908 1.404 0.854
$B^0 \to D^{*-}\mu^+\nu_\mu$	50.5	$\pm\,1.4$	HQET2 1.205 0.908 1.404 0.854
$B^0 \to D^{*-}D_s^{*+}$	17.7	$\pm\,1.4$	SVV_HELAMP 0.4904 0. 0.7204 0. 0.4904 0.
$B^0 \to D^{*-}2\pi^+\pi^-\pi^0$	17.6	$\pm\,2.7$	PHSP
$B^0 \to D^{*-}\tau^+\nu_\tau$	15.7	$\pm\,1.0$	ISGW2
$B^0 \to D^{*-}\pi^+\pi^0$	15	$\pm\,5$	PHSP
$B^0 \to D^{*-}D^*(2007)^0K^+$	10.6	$\pm\,0.9$	PHSP
$B^0 \to D^{*-}D^{*+}K^0$	8.1	$\pm\,0.7$	PHSP
$B^0 \to D^{*-}D_s^+$	8.0	$\pm\,1.1$	SVS
$B^0 \to D^{*-}3\pi^+$	7.21	$\pm\,0.29$	PHSP
$B^0 \to D^{*-}D^+K^0 + D^{*+}D^-K^0$	6.4	$\pm\,0.5$	PHSP
$B^0 \to D^{*-}\pi^+$	2.74	$\pm\,0.13$	SVS
$B^0 \to D^{*-}\rho^+$	6.8	$\pm\,0.9$	SVV_HELAMP 0.317 0.19 0.936 0. 0.152 1.47
$B^0 \to D^{*-}D^0K^+$	2.47	$\pm\,0.21$	PHSP
$B^0 \to D^{*-}\omega\pi^+$	2.46	$\pm\,0.18$	PHSP
$B^0 \to D^{*-}K^+K^{*0}$	1.29	$\pm\,0.33$	PHSP
$B^0 \to D^{*+}D^{*-}$	0.80	$\pm\,0.06$	SVV_HELAMP 0.56 0. 0.96 0. 0.47 0.
$B^0 \to D^{*+}D^-$	0.61	$\pm\,0.16$	SVS
$B^0 \to D^{*-}K^0\pi^+$	0.30	$\pm\,0.08$	PHSP
$B^0 \to D^{*-}K^{*+}$	0.33	$\pm\,0.6$	SVV_HELAMP 0.283 0. 0.932 0. 0.228 0.
$B^0 \to D^{*-}K^+$	0.212	$\pm\,0.015$	SVS
$B^0 \to D^{*-}K^+\pi^-\pi^+$	0.47	$\pm\,0.04$	PHSP

4.6 Simulation

Simulation is used to estimate the size of the background components of secondary decays in Chap. 6. In the simulation, pp collisions are generated using Pythia [143] with a specific LHCb configuration [166]. Decays of unstable particles are described by EvtGen [167], in which final-state radiation is generated using Photos [168]. The interaction of the generated particles with the detector, and its response, are implemented using the Geant4 toolkit [169] as described in Ref. [170]. In order to speed-up the simulation, only the decay of the primary and secondary signal decays is simulated, whereas all of the other particles produced in the pp collision are discarded.

The decay channels, branching fractions and EvtGen decay models used in the simulation of B^0 and B^+ inclusive decays into $D^{*\pm}$ mesons are listed in Tables 4.5 and 4.6, respectively. The simulation of the D^{*+}-meson decay always employs the VSS model, while the D^0-meson decay employs a phase-space model, and forces the decay into the $K^-\pi^+$ final state. Primary decays are studied by using a simulation generated at $\sqrt{s} = 8\,\text{TeV}$ instead of 13 TeV to minimise the usage of computing resources, since the former was already available at the time that this measurement was started. The kinematic weighting employed to reduce the discrepancies between simulation and data is described later on. After the application of the selection requirements described in the previous sections, the number of simulated candidates selected is about 450k, 380k and 390k for primary decays and for B^0 and B^+ secondary decays, respectively. Around

Table 4.6: List of the decays used to generate the simulated sample of inclusive $B^+ \to D^{*\pm}X$ decays. The values of the branching ratios are taken from Ref. [36].

Decay channel	$\mathcal{B}$ $[10^{-3}]$		EvtGen model
$B^+ \to D^{*-}2\pi^+\pi^0$	15	$\pm\,7$	PHSP
$B^+ \to D^{*+}\overline{D}^*(2007)^0K^0$	9.2	$\pm\,1.2$	PHSP
$B^+ \to D^{*+}\overline{D}^0K^0$	3.8	$\pm\,0.4$	PHSP
$B^+ \to D^{*-}3\pi^+\pi^-$	2.6	$\pm\,0.4$	PHSP
$B^+ \to D^{*-}2\pi^+$	1.35	$\pm\,0.22$	PHSP
$B^+ \to D^{*-}D^{*+}K^+$	1.32	$\pm\,0.00$	PHSP
$B^+ \to D^{*+}\overline{D}^*(2007)^0$	0.81	$\pm\,0.17$	SVV_HELAMP 0.56 0. 0.96 0. 0.47 0.
$B^+ \to D^{*+}D^-K^+$	0.63	$\pm\,0.13$	PHSP
$B^+ \to D^{*-}D^+K^+$	0.60	$\pm\,0.13$	PHSP
$B^+ \to D^{*+}\overline{D}^0$	0.39	$\pm\,0.05$	SVS

Table 4.7: Parameters used to set the relative abundance of B^+ and B^0 events in the simulated sample. The sums of the branching fractions are taken from Tables 4.5 and 4.6. The B^+-meson production cross-section is taken from Ref. [171]; since no measurements of the B^0-meson cross-section at $\sqrt{s} = 13\,\text{TeV}$ are available to date, it is assumed to be equal to that of the B^+ meson, similarly to what is measured at $\sqrt{s} = 7\,\text{TeV}$ [139]. The ratio of the product of the factors listed in the three columns for the B^+ meson to that for the B^0 meson is equal to 0.15 ± 0.03, where the uncertainty is dominated by the knowledge of the B^+ inclusive branching ratio into $D^{*\mp}$ mesons.

Decay-head particle	Cross section [μb]	$\mathcal{B}(B \to D^{*\mp}X)$	Generator-level efficiency
B^+	86.6 ± 6.4	0.036 ± 0.007	0.2604 ± 0.0001
B^0	(same)	0.226 ± 0.007	0.2773 ± 0.0001

107k B^0-meson decays are reconstructed also as $(D^{*+}\mu^-)$ candidates, employing the requirements of Sect. 4.5.

The same number of B^+- and B^0-meson decays into D^{*+} mesons was simulated by Geant4. This number is calculated after the implementation of the generator-level requirements. These are a set of minimal requirements (looser than those of the trigger and of the offline selection) on the momenta of the generated particles, which are applied right after the Pythia 8 simulation and EvtGen are run. Only the events that satisfy these requirements, whose fraction with respect to the total number of generated decays is named “generator-level efficiency”, are transmitted to Geant4 to continue the simulation. The samples of B^+ and B^0 decays are eventually merged, but weighting the B^+ events with a factor of 0.15 to account for different generator-level efficiencies and branching ratios (Table 4.7).

To reduce the discrepancies between simulation and data, the three-dimensional distribution of the D^0-meson transverse momentum, pseudorapidity and azimuthal angle, ϕ, in simulation is weighted to that of data. This is particularly relevant for primary decays, where the Pythia 8 simulation was run at $\sqrt{s} = 8\,\text{TeV}$ instead of 13 TeV. The weighting is performed separately for the samples of primary D^{*+} decays, secondary D^{*+} decays and secondary decays reconstructed as $(D^{*+}\mu^-)$ pairs. Data where the D^0-meson IP is less than 60 μm and lies in the range $[100, 200]$ μm are used as weighting targets for primary and secondary simulated events, respectively, while for

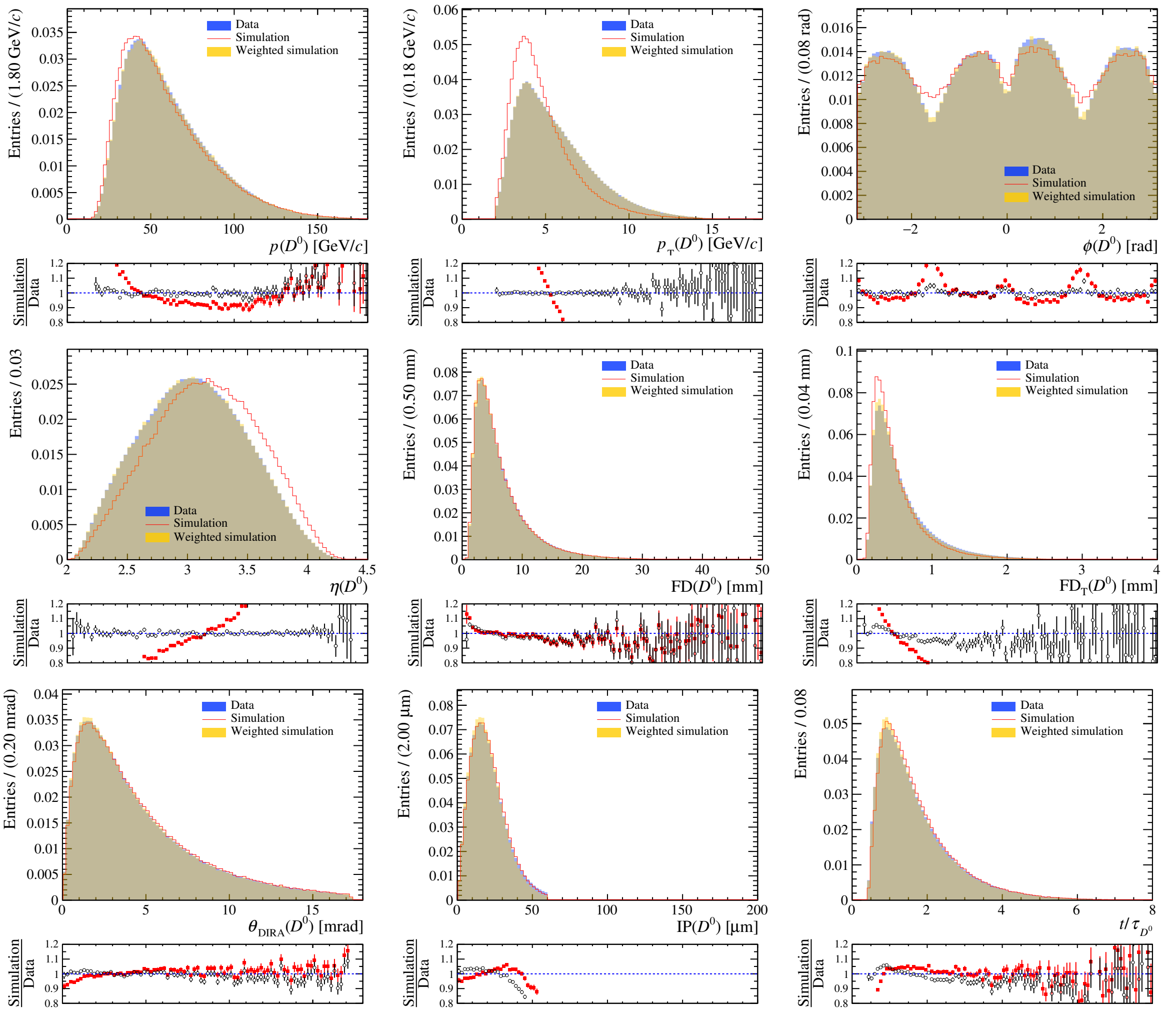

Figure 4.12: Comparison between the kinematic distributions of $D^0 \to K^-\pi^+$ primary decays in data and simulation, both before and after the three-dimensional $(p_{\rm T}, \eta, \phi)$ weighting of the D^0-meson momentum. The data sample of primary decays is selected using 1/150 of the candidates satisfying the requirement IP$(D^0) < 60\,\mu$m. In the plots displaying the ratio of simulated to real data, full red squares (open black circles) correspond to simulated data before (after) the weighting.

$(D^{*+}\mu^-)$ candidates all data with IP less than 200 μm are employed. The weighting is performed using the `GBReweighter` class of the `hep_ml` package [172], with 2-folding.

The distributions of the main kinematic variables of data and simulation are compared (before and after the weighting) in Figs. 4.12, 4.13 and 4.14 for primary and secondary decays and for the $(D^{*+}\mu^-)$ sample, respectively. While for the $(D^{*+}\mu^-)$ sample the data agrees with the weighted simulation typically within 5% (with slightly larger disagreements for small values of the direction angle, IP and decay time), the agreement for primary decays and for the full sample of secondary decays is worse. As far as primary decays are concerned, the discrepancies are mainly due to the residual contamination of secondary decays in the data satisfying IP$(D^0) < 60\,\mu$m. This contamination is estimated to be around 4.0% in Chap. 6, and possesses larger momenta and consequently larger FD and IP on average with respect to primary decays. On the other hand, the discrepancies are slightly larger for secondary decays. Again, the

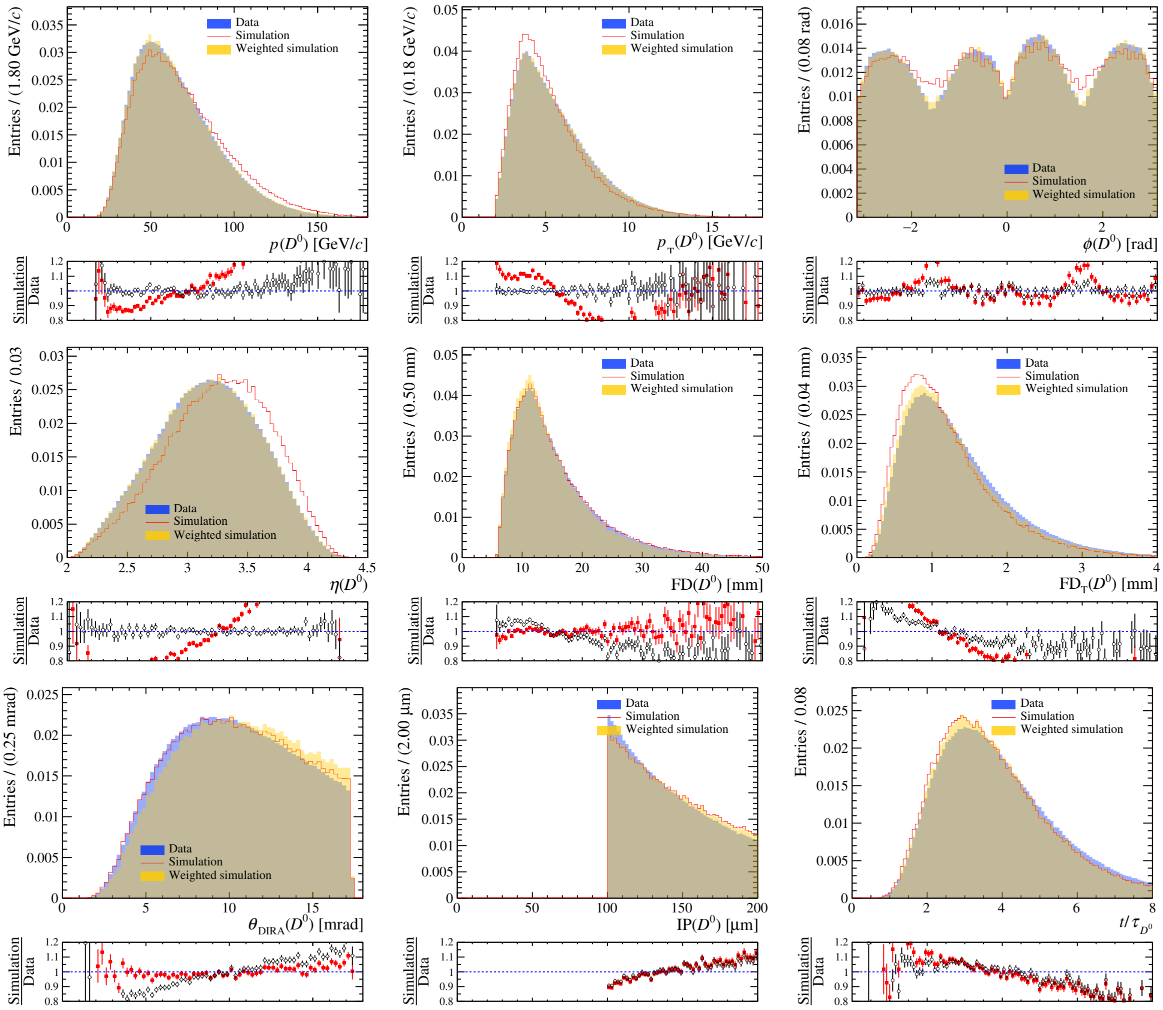

Figure 4.13: Comparison between the kinematic distributions of $D^0 \to K^-\pi^+$ secondary decays in data and simulation, both before and after the three-dimensional $(p_\mathrm{T}, \eta, \phi)$ weighting of the D^0-meson momentum. The data sample of secondary decays is selected using 1/6 of the candidates satisfying the requirement $100 < \mathrm{IP}(D^0) < 200\,\mu\mathrm{m}$. In the plots displaying the ratio of simulated to real data, full red squares (open black circles) correspond to simulated data before (after) the weighting.

contamination of primary decays in the data with IP $> 100\,\mu$m, which is approximately equal to 5.3%, biases the distributions of the IP and of the direction angle towards lower values. Another source of disagreement is traced back to the absence, which was noticed only after the simulation had been finalised, of the decays $B^0 \to D\overline{D}K^*$, where at least one of the D and $\overline{D}$ mesons is a $D^{*\pm}$ meson and K^* is a kaon-meson resonance. Although these decays are not reported by the PDG collaboration [36], they are predicted by the hadronisation of Pythia 8 and they are taken into account into the baseline model of EvtGen [167]. Their predicted branching fractions make up around 10% of the inclusive branching fraction of B^0 mesons into $D^{*\pm}$ mesons. Preliminary studies show that these decays correspond on average to higher decay times and flight distances with respect to semileptonic B^0 decays, and might explain the discrepancies observed for these two variables between data and simulation. In any case, independently of what is the origin of the discrepancies in all of the samples, their impact on the measurement is estimated among systematic uncertainties in Sect. 7.3.

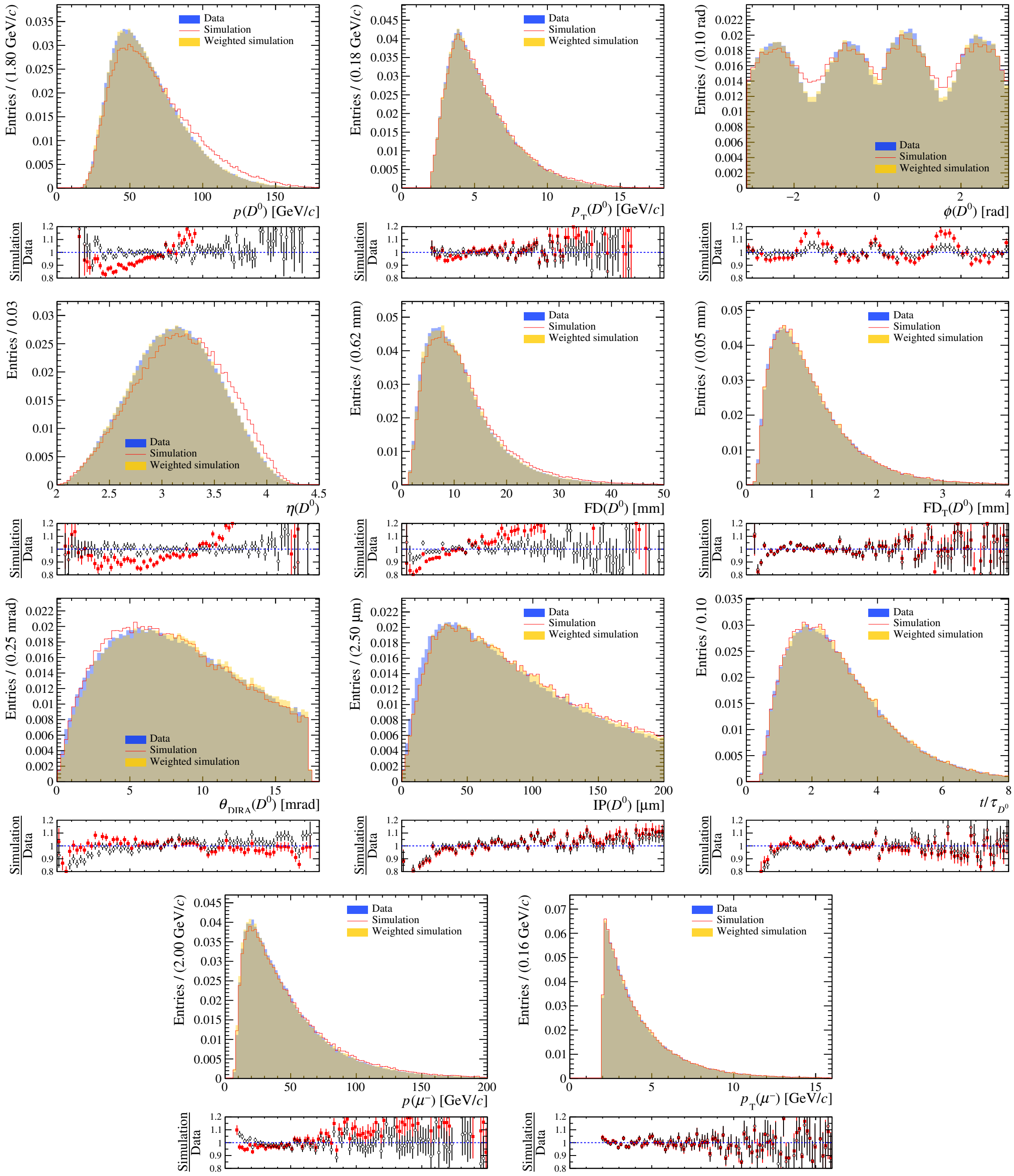

Figure 4.14: Comparison between the kinematic distributions of $(D^{*+}\mu^-)$ secondary candidates in data and simulation, both before and after the three-dimensional $(p_{\mathrm{T}}, \eta, \phi)$ weighting of the D^0-meson momentum. The data sample of secondary decays is selected using 1/6 of the candidates satisfying the requirement $\mathrm{IP}(D^0) < 200\,\mu\mathrm{m}$. In the plots displaying the ratio of simulated to real data, full red squares (open black circles) correspond to simulated data before (after) the weighting.

Chapter 5

Nuisance asymmetries

This chapter describes the production mechanism of momentum-dependent nuisance asymmetries in signal decays, and the kinematic weighting employed to remove them. Finally, minor biases caused by the kinematic weighting on the measurement of ΔY are evaluated.

Throughout this chapter, all the studies are performed by employing the $D^0 \to K^-\pi^+$ sample, where the slope $\Delta Y_{K^-\pi^+}$ is known to be less than 0.3×10^{-4} in magnitude at 90% CL based on experimental results, as shown in Appendix B.3. The raw asymmetry of this decay channel, *cf.* Eq. (2.15), is affected by the same nuisance asymmetries as the K^+K^- and $\pi^+\pi^-$ channels, plus by an additional detection asymmetry from the non-self-conjugate $K^-\pi^+$ final state, $A_{\mathrm{D}}^{K^-\pi^+}(t)$. In order to avoid experimenter's bias, the optimal configuration of the kinematic weighting is decided based on its effectiveness in removing the kinematics-dependent asymmetries of the $K^-\pi^+$ decay channel, and only once it is fixed it is applied — unvaried — to the signal channels. The fact that the kinematic weighting is able to remove all of the nuisance asymmetries in the $D^0 \to K^-\pi^+$ sample, which is affected by the largest detection asymmetries, is a persuasive cross-check of the validity of the method, which is expected to be effective *a fortiori* in the $D^0 \to K^+K^-$ and $D^0 \to \pi^+\pi^-$ samples.

5.1 Production mechanism

Before any corrections are applied, the data sample contains momentum-dependent detection asymmetries. The largest ones arise from the π^+_{tag} meson and are caused by the vertical dipole magnetic field, which bends oppositely charged particles in opposite directions. The configuration with the magnetic field pointing upwards (downwards), *MagUp* (*MagDown*), bends positively (negatively) charged particles in the horizontal plane towards negative values of x. For a given magnet polarity, low-momentum particles of one charge at large or small emission angles in the horizontal plane may be deflected out of the detector or into the uninstrumented LHC beam pipe before passing through the T-stations, whereas particles with the opposite charge are more likely to remain within the acceptance. This is shown in Fig. 5.1, where the vector momentum of the π^+_{tag} meson is parametrised using its emission angles in the bending and vertical planes, $\theta_{x(y)} \equiv \arctan(p_{x(y)}/p_z)$, and its curvature in the magnetic field, $k \equiv 1/\sqrt{p_x^2 + p_z^2}$. The large areas with asymmetries greater than 20% in magnitude in the top plots are due to the fact that negative (positive) values of θ_x can be measured for positively (negatively) charged tagging pions only if their curvature is small enough — that is if their momentum is large enough —,

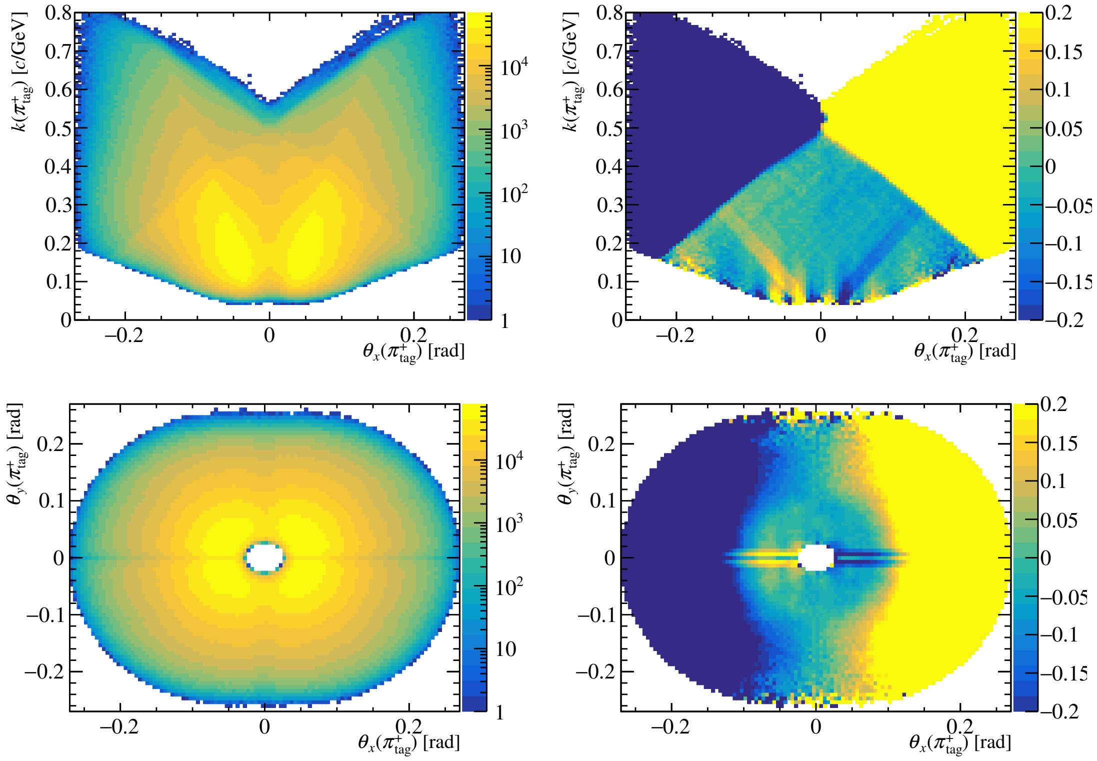

Figure 5.1: (Left) sum and (right) asymmetry of the distributions of $\pi^+_{\rm tag}$ and $\pi^-_{\rm tag}$ candidates, in the (top) θ_x *versus* k and (bottom) θ_x *versus* θ_y planes, for the $D^0 \to K^-\pi^+$ sample recorded during 2017 with the *MagUp* polarity. The angle $\theta_{x(y)} \equiv \arctan(p_{x(y)}/p_z)$ is the emission angle of the $\pi^+_{\rm tag}$ meson in the bending (vertical) plane, and $k \equiv 1/\sqrt{p_x^2 + p_z^2}$ is proportional to its curvature in the magnetic field. The asymmetries during other data-taking years are similar, and opposite in sign for the data collected with the *MagDown* polarity. Regions of the distributions with asymmetries larger than 20% in magnitude are discarded from the sample.

otherwise they are bent outside of the T-stations acceptance. On the other hand, the diagonal bands in Fig. 5.1 (top-right) correspond to candidates with emission angle θ_y close to zero, *cf.* Fig. 5.1 (centre-right), which are bent into the beam pipe. Further sources of asymmetries are the left–right asymmetric shape of the VELO detector (*cf.* Fig. 3.4), the left–right asymmetry of the material budget of the detector (owing to the cabling and to the asymmetric support structure of the inner tracker of the T-stations), dead channels and inhomogeneities of the detection efficiency among different detector regions. Even if these asymmetries cancel to large extent in the average between the samples collected with *MagUp* and *MagDown* polarities, smaller residual asymmetries survive also after averaging. Such residual asymmetries receive contributions from variations of the detection efficiency over time, and by the combination of right–left misalignment of detector elements and of the nonzero x coordinate of the pp collision point (this differs from zero by around 1 mm). Another source of asymmetry is the different crossing angle between the proton beams for the *MagUp* and *MagDown* polarities. The crossing angle, which lies on the x–z plane and is approximately equal to $-0.10(-0.40)$ mrad for the *MagUp* (*MagDown*) polarity, provokes a boost of the momentum distribution of D^{*+} mesons along the x direction up to around $30\,\text{MeV}/c$. Additional momentum-dependent asymmetries that are independent of the magnet polarity are the D^{*+} production asymmetry and the tracking-efficiency asymmetry. The

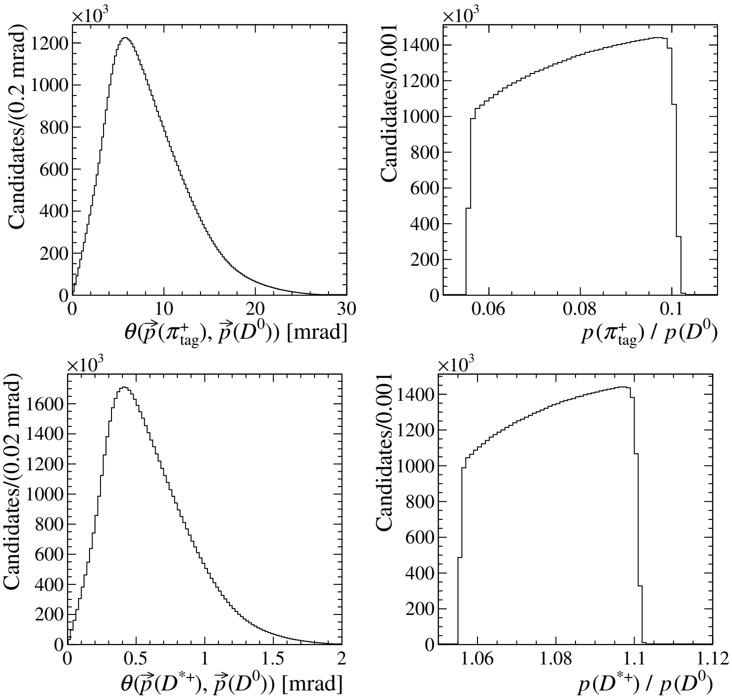

Figure 5.2: Distributions of the (left) angle and (right) ratio between the momenta of the (top) $\pi^+_{\rm tag}$ and D^0 mesons and (bottom) D^{*+} and D^0 mesons.

latter is caused by the higher occupancy of the detector half downstream of the magnet towards which the negatively charged particles are bent. In fact, the number of negatively charged tracks is larger with respect to positively charged tracks, owing to secondary electrons produced in the interaction of the particles with the detector material. Since the tracking efficiency decreases as a function of the detector occupancy, a positive tracking asymmetry is observed, especially at large momenta. A detailed study of all of the aforementioned asymmetries is provided in Ref. [173]. Finally, for the $D^0 \to K^-\pi^+$ decay channel, the asymmetry due to the different cross-section with matter of positively and negatively charged kaon mesons is independent of the magnet polarity. A similar, but much smaller effect is expected also from the different cross-section of positively and negatively charged pions, which affects both the $K^-\pi^+$ final state and the tagging pion. It is worth noting that, even if the phase-space regions with acceptance asymmetries larger than few tens per cent are removed from the data sample — for example by applying the fiducial requirements employed in Ref. [18] —, residual asymmetries of the order of few per cent remain in other regions. Moreover, the contribution of these asymmetries to the total asymmetry is even more important, since they often correspond to more populated regions of the distributions.

Since the Q-value of the D^{*+} decay is small with respect to the pion mass, both the magnitude and the direction of the momenta of the D^{*+}, $\pi^+_{\rm tag}$ and D^0 mesons are highly correlated. In particular, the momenta of the $\pi^+_{\rm tag}$ and D^{*+} mesons form an angle less than 20 mrad with the momentum of the D^0 meson, and their ratios over the D^0 momentum are nearly constant in the LHCb rest frame, as shown in Fig. 5.2. As a consequence, all aforementioned asymmetries reflect into momentum-dependent asymmetries of the D^0 meson, with all being of similar size. These asymmetries would not bias the measurement of ΔY if they did not depend on the D^0-meson decay time. However, even if the momentum of the D^0 meson is uncorrelated with its decay time, the selection requirements introduce correlations between their measured values. For example, owing to the second-stage software-trigger requirement on the χ^2_{FD} of the D^0 meson, low decay times are measured only if the D^0 momentum is sufficiently large. The correlation of the flight distance of the D^0 meson, and of the momentum of the D^0 and π^+_{tag} mesons, with the D^0-meson decay time is shown in Fig. 5.3, where their normalised distributions are plotted in different colours for each decay time bin. Smaller decay times correspond to smaller flight distances and larger momenta on average.

The largest correlations concern the transverse momentum of the D^0 meson. Therefore, the asymmetry of the D^0-meson transverse-momentum distribution is the most important factor causing nondynamical time-dependent asymmetries. The raw asymmetry of the samples collected with the *MagUp* polarity, of order of 1%, increases as a function of transverse momentum, and correspondingly decreases as a function of decay time, as shown in Fig. 5.4 (centre) and in Fig. 5.6 (left) with red points. This corresponds to negative measured values of $\Delta Y_{K^-\pi^+}$, even if the dependence of the asymmetry on decay time, which is shown in Fig. 5.6, is not actually linear. The nonlinearity is confirmed by the large χ^2/ndf of the linear fits to the asymmetry, which are displayed in Fig. 5.7.

Among the samples collected with *MagUp* polarity, that collected during 2016 presents a much larger slope, even if its momentum-dependent asymmetries are similar to those collected during different years. In fact, owing to the different requirements of the first-stage software trigger during 2016, particularly during the data-taking with the *MagUp* polarity, the correlations are larger during 2016, as shown in Fig. 5.4 (top). The impact of the first-stage software-trigger requirements on the correlations is displayed in further detail in Appendix D.1. The raw-asymmetry slopes for the samples collected with *MagDown* polarity are smaller in magnitude and opposite in sign, owing to smaller momentum-dependent asymmetries which present the opposite dependence on the D^0-meson transverse momentum with respect to the *MagUp*-polarity data (they increase as a function of transverse momentum).

5.2 Kinematic weighting

Both the correlations between the momenta of the particles and decay time and the dependence of the asymmetry on these momenta are essential ingredients to produce time-dependent nuisance asymmetries. Therefore, eliminating either or them is sufficient to remove the nuisance asymmetries. The two corresponding strategies that can be followed are:

1. to weight the momentum distribution of the D^0 and π^+_{tag} mesons in each decay time bin to a reference distribution, thus removing the correlation between decay time and momentum;
2. to remove the momentum-dependent asymmetries through a time-integrated equalisation of the kinematics of the events containing D^0 and $\overline{D}^0$ candidates.

The second method is adopted since, in the context of the current trigger selections, it allows for a better statistical precision. In fact, the momentum distribution of the D^0 and of the π^+_{tag} meson shifts significantly as a function of decay time, as shown in Fig. 5.3. Therefore, since the reference momentum distribution used as weighting target should be zero wherever any of the distributions of the various decay time bins is zero, this procedure requires to discard a large fraction of candidates (or to assign to them weights very different from unity) both in the lower and upper tails of the distributions.

The nuisance asymmetries are removed by weighting the kinematic distributions of π^+_{tag} and π^-_{tag} candidates and of D^0 and $\overline{D}^0$ candidates to match their average. This equalises their kinematics and makes their asymmetries equal to zero by construction. Many weighting schemes,

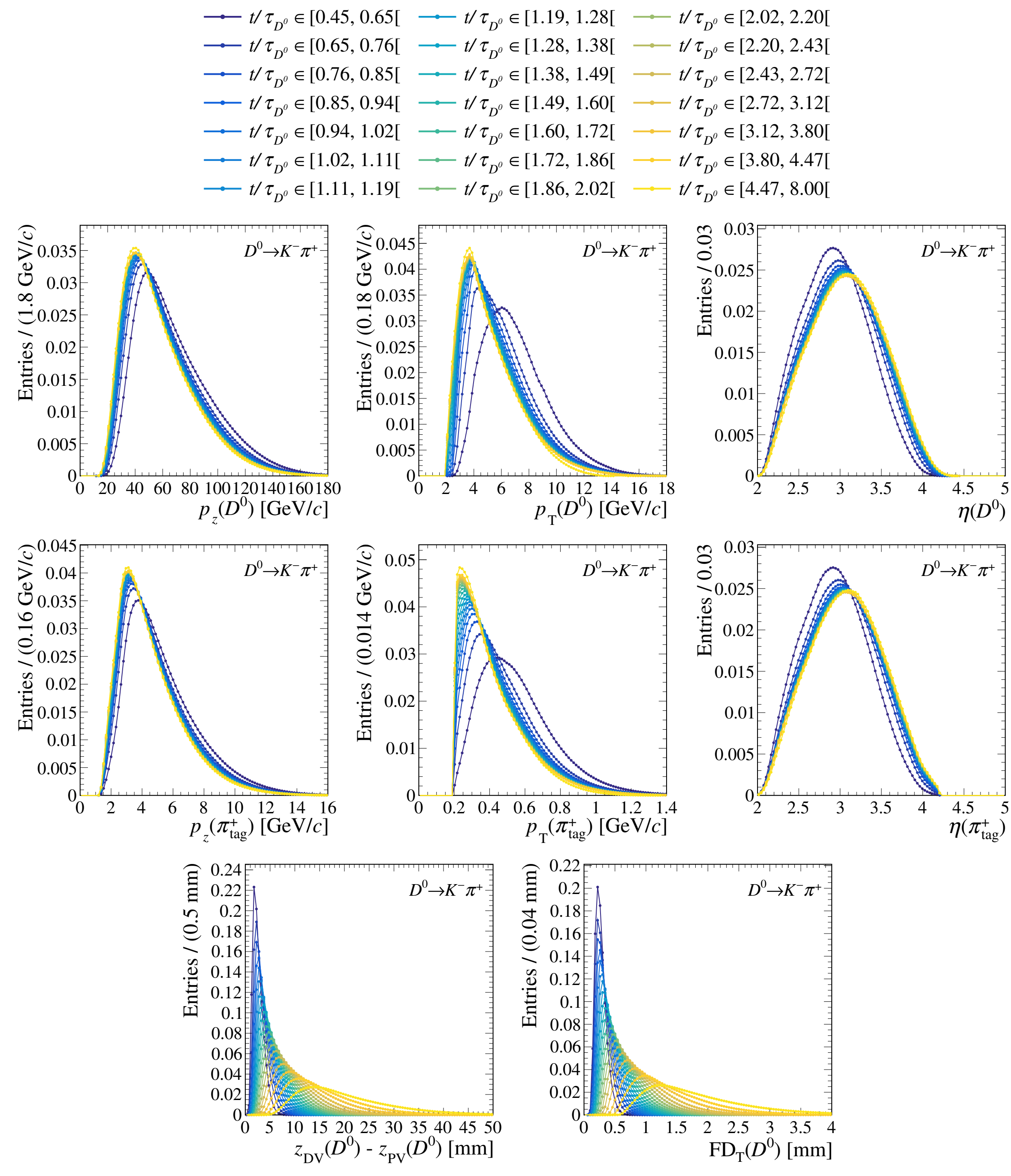

Figure 5.3: Normalised distributions of the z and transverse components and of the pseudorapidity of the D^0- and $\pi^+_{\rm tag}$-meson momentum, and of the z and transverse components of the D^0-meson flight distance, in different colours for different decay-time bins.

acting on different kinematic variables, have been considered. The configuration described below is chosen since it minimises the residual asymmetries, due to the finite precision of the weighting, of all of the kinematic variables of the D^0 and $\pi^+_{\rm tag}$ mesons. Alternative schemes, less effective in removing the asymmetries, are discussed in Appendix D.3.

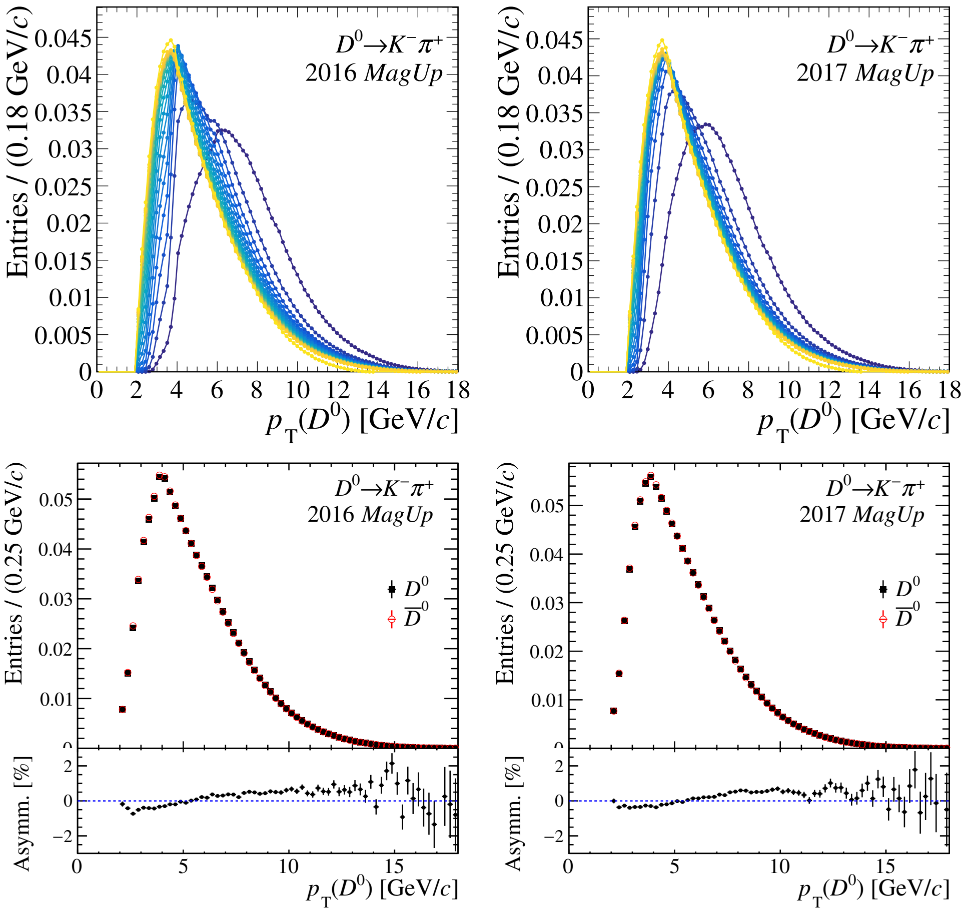

Figure 5.4: (Top) Normalised distributions of the D^0 transverse momentum, in different colours for each decay time bin. Blue (yellow) colours correspond to lower (higher) decay times. (Bottom) Asymmetry of the normalised p_{T} distributions of D^0 and $\overline{D}^0$ mesons. All plots correspond to the $D^0 \to K^-\pi^+$ sample, collected during (left) 2016 and (right) 2017 with the *MagUp* polarity.

The weighting is performed with a binned approach in two successive steps. The first step equalises the (θ_x, θ_y, k) distributions of π^+_{tag} and π^-_{tag} candidates to remove the largest acceptance and detection asymmetries, and employs 36 bins in the range $[-0.27, 0.27]$ rad for θ_x, 27 bins in the range $[-0.27, 0.27]$ rad for θ_y, and 40 bins in the range $[0, 0.8]\,c$/GeV for k. For each variable, all bins have the same width. In addition, bins with fewer than 40 π^+_{tag} or π^-_{tag} candidates, or where the raw asymmetry between the number of π^+_{tag} and π^-_{tag} candidates is greater than 20% in magnitude, are removed by setting the corresponding weights equal to zero. This avoids weights whose value would be prone to large statistical fluctuations or very different from unity. The effect of these requirements is very similar to the application of the fiducial requirements used to remove phase-space regions characterised by large detection asymmetries in Ref. [18], as shown in Fig. D.3 in Appendix D.2, but removes fewer candidates from the data sample. In each bin, the π^+_{tag} (π^-_{tag}) candidates are assigned a weight equal to $\sqrt{N_\mp/N_\pm}$, where $N_\pm$ is equal to the number of π^+_{tag} (π^-_{tag}) candidates in the bin. As a consequence, the number of both π^+_{tag} and π^-_{tag} candidates in the bin after the weighting equals the geometric average of their raw numbers. Employing the arithmetic average instead of the geometrical one is verified not to

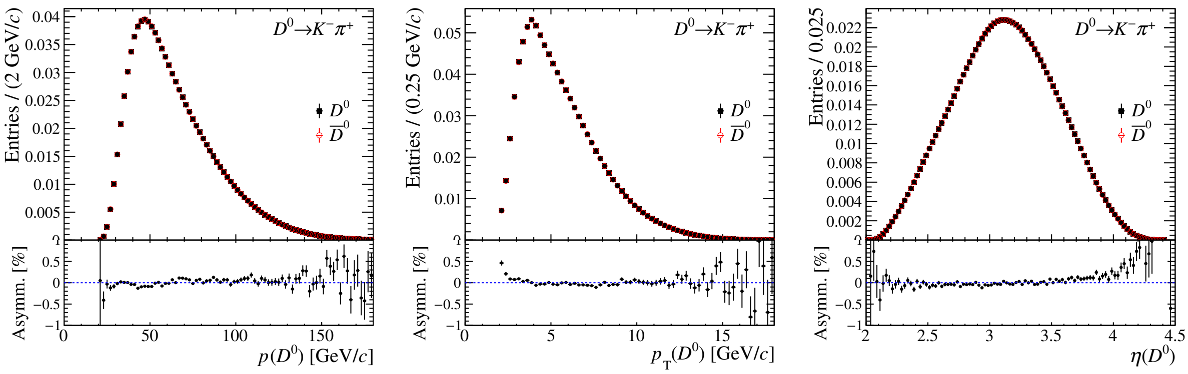

Figure 5.5: Residual asymmetries of the D^0-meson momentum, transverse momentum and pseudorapidity, after the weighting of the vector-momentum distribution of the $\pi^{\pm}_{\rm tag}$ mesons.

change the results noticeably. On the contrary, assigning a weight only to $\pi^+_{\rm tag}$ candidates to equalise their distribution to that of $\pi^-_{\rm tag}$ candidates, or *vice versa*, has been shown to cause a significant bias [174].

Even after the weighting of the $\pi^+_{\rm tag}$-meson kinematics, residual asymmetries dependent on the D^0-meson momentum and pseudorapidity of order of 0.5% are observed in the sample, as displayed in Fig. 5.5. These asymmetries are removed by performing a second weighting, this time considering the three-dimensional distribution of $(p_{\rm T}(D^0), \eta(D^0), \eta(\pi^+_{\rm tag}))$. The first two variables are the ones most correlated with decay time, while $\eta(\pi^+_{\rm tag})$ is included to avoid that the weighting of the D^0-meson kinematics interferes with that of the $\pi^+_{\rm tag}$ meson, introducing new asymmetries in its kinematic distributions. The binning of this second weighting employs 32 bins in the range $[2, 18]$ GeV/c for $p_{\rm T}(D^0)$, 25 bins in the range $[2, 4.5]$ for $\eta(D^0)$ and 22 bins in the range $[2, 4.2]$ for $\eta(\pi^+_{\rm tag})$. All bins of each variable have the same width, and the same limits on the minimum number of candidates and on the maximum asymmetry per bin as in the first weighting are applied.

Since both the detection asymmetries and the correlations induced by the trigger depend on the data-taking conditions and on the magnet polarity, the weighting is performed separately in eight subsamples, divided according to the year and the magnet polarity. In fact, the change of the correlations between the *MagUp* and *MagDown* polarities during 2016 makes it impossible to take advantage in a simple way of the partial cancellation of the asymmetry in the average between the two polarities. The agreement among the measured values of $\Delta Y_{K^-\pi^+}$ in the eight subsamples is used as a cross-check of the validity of the method. Furthermore, since the asymmetries are different between the $K^-\pi^+$ and the signal decay channels, owing to the asymmetric $K^-\pi^+$ final state, the weighting is performed independently for different D^0 decay channels.

The weighting slightly modifies the flavour-integrated momentum distribution and, consequently, also the $m(D^0\pi^+_{\rm tag})$ distribution — the weights are calculated from the signal candidates, but are applied to the background candidates as well. Therefore, the fits to the $m(D^0\pi^+_{\rm tag})$ distributions that are used to calculate the coefficients to subtract the background are repeated after each step of the weighting, and the coefficients are updated accordingly. The values of the coefficients are displayed, before and after each of the two steps of the kinematic weighting, in Fig. D.4 of Appendix D.2.

The fits to the time-dependent asymmetry of $D^0 \to K^-\pi^+$ candidates for all of the eight subsamples are displayed in Fig. 5.6 in red for raw data, in black after the first step of the kinematic weighting and in azure after the second step. The summary of the numerical results of $\Delta Y_{K^-\pi^+}$ and their weighted average are reported in Fig. 5.7. For raw data, the time-dependent asymmetry does not display a linear behaviour for many of the subsamples, and the eight measured values of $\Delta Y_{K^-\pi^+}$ are inconsistent with each other ($\chi^2/\text{ndf} = 124/7$). On the other hand, the average of $\Delta Y_{K^-\pi^+}$ itself is incompatible with zero at a level greater than 3σ. Part of this incompatibility is due to the momentum-dependent detection asymmetry of the $K^-\pi^+$ final state, which receives a polarity-independent contribution from the asymmetric cross-sections of positively and negatively charged kaon mesons with matter. However, also the χ^2/ndf of the average of the four subsamples collected with the *MagUp* (*MagDown*) polarity has a low p-value, equal to 0.025% (2.15%). This fact indicates the presence of significant asymmetries that vary as a function of data-taking time, in addition to the time-independent asymmetries from the $K^-\pi^+$ final state and from the dipole magnetic field. The tight configuration of the first-stage software-trigger requirements during 2016 is largely responsible for the anomalously large magnitude of the slope of the raw asymmetry and for the low p-value of the average of the subsamples collected with the *MagUp* polarity, but it is not the only factor into play. In fact, the 2018 samples display larger momentum-dependent asymmetries with respect to the previous years for both magnet polarities, corresponding to larger magnitudes of the asymmetry slope. In particular, the sample collected during 2018 with the *MagDown* polarity is the main responsible for the low p-value of the average of the values of $\Delta Y_{K^-\pi^+}$ measured with the *MagDown* polarity. The increase of the asymmetries during 2018 is likely due to the radiation damage of the detector after six years of operations, and in particular of the VELO detector, which is the closest to the collision point.

On the contrary, after each step of the kinematic weighting, the time dependence of the asymmetry is well described by a linear function in all subsamples, as confirmed by the compatibility of the χ^2/ndf of the linear fits with unity. In addition, the measurements of $\Delta Y_{K^-\pi^+}$ are compatible among different years and magnet polarities. This is an important result to confirm the reliability of the method. In fact, the working assumption of the kinematic weighting is that, for each subsample, at least one between the kinematics-dependent asymmetry and the correlation between kinematics and decay time is constant during the data-taking.[1] The breaking of this assumption might lead to inconsistencies among the results of the eight subsamples even after the weighting. Finally, a significant shift of the value of $\Delta Y_{K^-\pi^+}$, -0.7×10^{-4}, is observed between the first and second steps of the weighting. This corresponds to about 1.5 times the statistical uncertainty on $\Delta Y_{K^-\pi^+}$, and is traced back to the residual asymmetries of Fig. 5.5, which are not removed by the first step of the weighting. The linear fit to the time-dependent asymmetry of the full weighted data sample is shown in Fig. 5.8. The fitted value of $\Delta Y_{K^-\pi^+}$, which coincides with the average of the results of the eight subsamples divided according to the year and magnet polarity, is

$$\Delta Y_{K^-\pi^+} = (-0.1 \pm 0.5) \times 10^{-4},$$

[1] This is the reason why the kinematic weighting cannot be applied directly to the whole data sample. For example, let assume that the asymmetries of the samples collected with opposite magnet polarities are equal in magnitude and opposite in sign. Therefore, they would cancel out in the sum of the samples collected with *MagUp* and *MagDown* polarities, and the kinematic weighting applied to the whole sample would have no effect, the weights being all equal to unity. However, since the correlations during the data-taking performed with the *MagUp* polarity are larger — owing to the tighter trigger requirements during 2016 for the *MagUp* polarity —, kinematics asymmetries of equal magnitude for the *MagUp* and *MagDown* polarities would reflect into larger time-dependent asymmetries for the *MagUp* polarity. Therefore, the slopes of the time-dependent asymmetries measured in the samples collected with opposite magnet polarities would be opposite in sign but would differ in magnitude, and the slope of the asymmetry of the total sample would differ from zero.

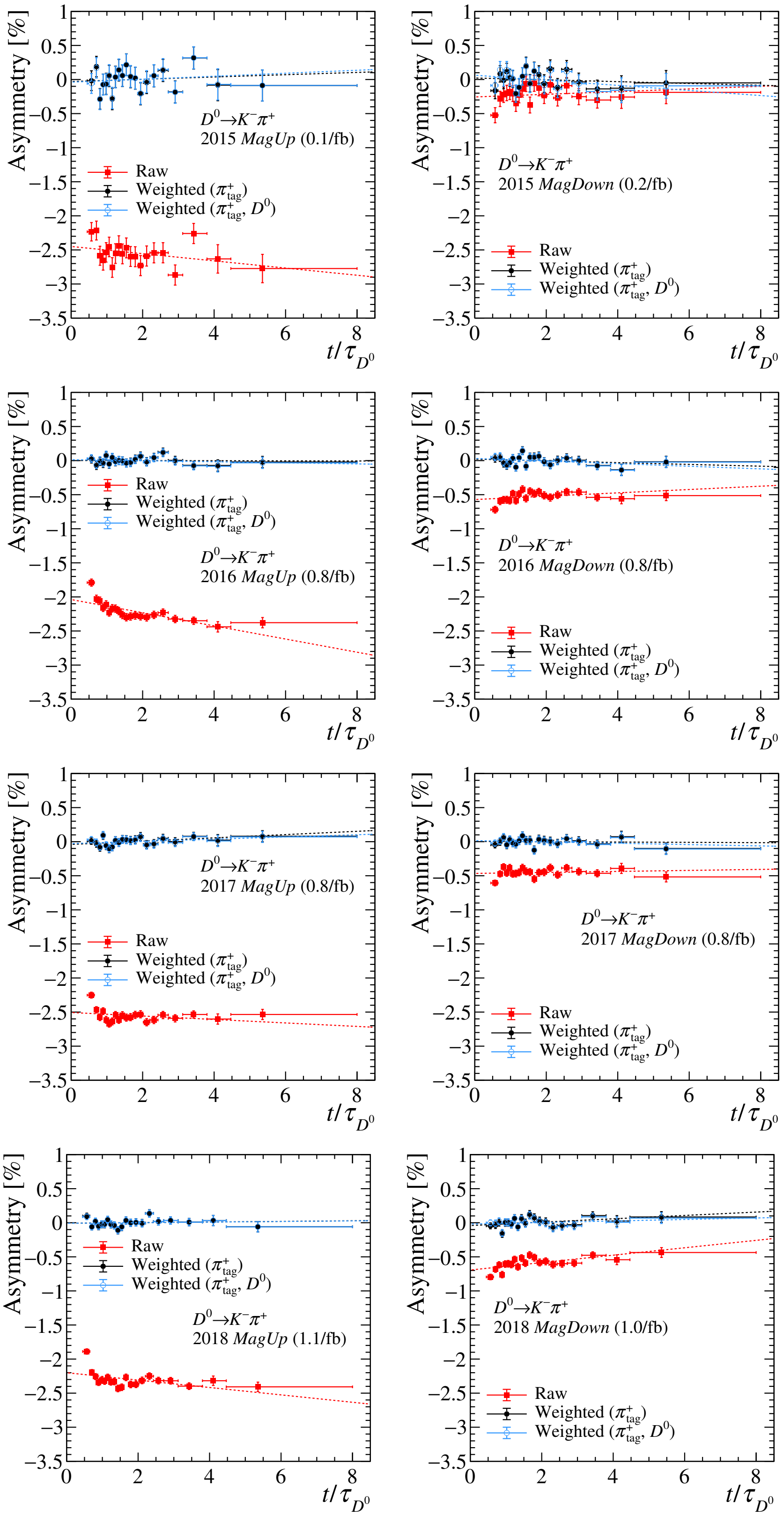

Figure 5.6: Linear fit to the time-dependent asymmetry of $D^0 \to K^- \pi^+$ decays (red) for raw data, (black) after the first kinematic weighting and (azure) after the second kinematic weighting.

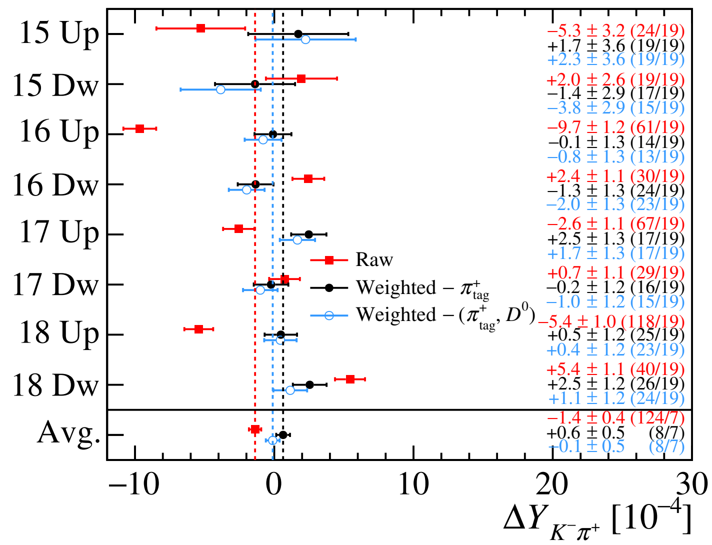

Figure 5.7: Summary of the fitted values of $\Delta Y_{K^-\pi^+}$ in the eight subsamples divided according to the year and magnet polarity, together with their average. The numerical values of $\Delta Y_{K^-\pi^+}$ and the χ^2/ndf of the fits are reported on the right. The global p-values of the eight linear fits to the time-dependent asymmetry are 7×10^{-23}, 45% and 64% for raw data and after the first and second step of the kinematic weighting, respectively, whereas the p-values of the average of $\Delta Y_{K^-\pi^+}$ are 1×10^{-21}, 30% and 31%, respectively.

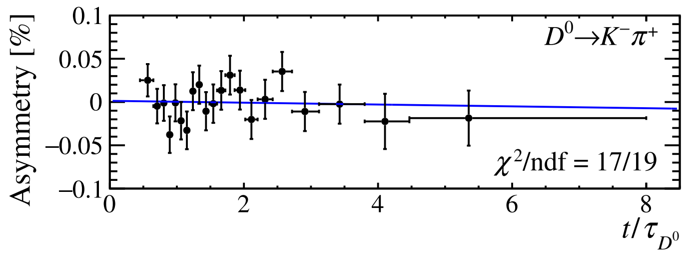

Figure 5.8: Linear fit to the time-dependent asymmetry of the full $D^0 \to K^-\pi^+$ sample after the kinematic weighting.

where only the statistical uncertainty is reported.

The compatibility of this measurement of $\Delta Y_{K^-\pi^+}$ with zero is not a good indicator of the effectiveness of the kinematic weighting. In fact, secondary decays, whose contribution to the asymmetry is subtracted in Chap. 6, bias the results by around $+0.25 \times 10^{-4}$ even after the kinematic weighting. Thus, the optimal configuration of the kinematic weighting is chosen only based on its effectiveness in removing the kinematics-dependent asymmetries from the distributions of all the main kinematic variables of the event. In particular, alternative weighting configurations would have provided values of $\Delta Y_{K^-\pi^+}$ closer to zero after the subtraction of secondary decays, as detailed of Appendix D.3. The residual asymmetries after the kinematic weighting are shown both for the $K^-\pi^+$ control channel and for the signal channels in Appendix D.4. Note that the total time-integrated asymmetry after the kinematic weighting is equal to zero by construction. Therefore, the asymmetry of weighted data cannot be used to measure the CP asymmetry in the decay, a^d.

Further details on the kinematic weighting, such as the distribution of the weights, are provided in Appendix D.2, while possible biases caused by the weighting to the measurement of $\Delta Y_{(K^-\pi^+)}$ are evaluated in Sect. 5.4. Limitations of the effectiveness of the weighting in removing the asymmetries owing to the discrete, binned procedure adopted are evaluated among systematic uncertainties in Sect. 7.4. As robustness checks of the kinematic weighting, a possible dependence of the asymmetry on hidden variables is checked by controlling that the measurement of $\Delta Y_{(K^-\pi^+)}$ remains stable when performed on different data subsamples, divided according to the value of the main variables on which the asymmetry might depend, as detailed in Sect. 8.1. Finally, the stability of the measurement as a function of the minimum number of candidates in the three-dimensional bins and of the maximum value of the asymmetry between the number of D^0 and $\overline{D}^0$ candidates in the bins is checked in Sect. 8.2.

5.3 Kinematic weighting of the signal samples

Once the analysis method has been fixed based on the studies on the $K^-\pi^+$ decay channel, it is applied also to the K^+K^- and $\pi^+\pi^-$ ones to measure the value of ΔY. Before then, the time-dependent asymmetry of the signal samples, $A(t)$, was kept unknown by adding to all the measured asymmetries a term that is constant and one that is linear in decay time,

$$A(t) \to A(t) + A_0 + \Delta Y_0 \frac{t}{\tau_{D^0}}, \tag{5.1}$$

where the parameters A_0 and ΔY_0 are random numbers generated in the ranges $[-0.1, 0.1]$ and $[-0.02, 0.02]$, respectively. The limits of the last range correspond to about ± 100 times the statistical uncertainty on the world average of ΔY, excluding the measurement presented in this thesis [47]. The constant shift A_0 was essential to keep unknown the value of ΔY, since the time-integrated asymmetry after the kinematic weighting is zero by construction. Therefore, if the constant shift had not been applied, a negative value of the intercept of the asymmetry with the y axis would have signalled a positive value of the real slope of the asymmetry, and *vice versa*. The shifting parameters were the same for the K^+K^- and $\pi^+\pi^-$ decay channels, so that the compatibility between the measurements of $\Delta Y_{K^+K^-}$ and $\Delta Y_{\pi^+\pi^-}$ could be cross-checked even if their values were blinded. Finally, two different sets of random parameters A_0 and ΔY_0 were employed for the data collected during 2015–2016 and 2017–2018, since a preliminary measurement of the ΔY parameter, although employing a different analysis method and only a subsample of the 2015–2016 data analysed in this thesis, had already been performed in 2019 [117].

As for the $K^-\pi^+$ decay channel, the kinematic weighting is essential to ensure the removal of the kinematics-dependent asymmetries and the compatibility of the results of the different subsamples. The results of the linear fit to the asymmetry are displayed, for all eight subsamples, in Figs. 5.9 and 5.10 for the K^+K^- and the $\pi^+\pi^-$ decay channels, respectively. The global p-values of the eight fits are equal to 5.5% and 31%, respectively; the numerical results, the χ^2/ndf of the fits and the average of the eight subsamples are summarised in Figs. 5.11 and 5.12. The relatively low p-value of the K^+K^- final state is mainly due to the linear fit to the asymmetry of the sample collected during 2016 with the *MagDown* polarity, and is attributed to a statistical fluctuation. In fact, the large χ^2/ndf of this fit is mainly caused by the values of the asymmetry in the two highest bins of decay time, which fluctuate in opposite directions with respect to the fitted line. The absence of anomalous asymmetries in any of the kinematics distributions of this subsample strengthens this hypothesis.

The linear fit to the time-dependent asymmetry for the full weighted data samples is shown in Fig. 5.13. The fitted values of ΔY, which coincide with the average of the results of the eight subsamples divided according to the year and magnet polarity, are

$$\begin{aligned}\Delta Y_{K^+K^-} &= (-2.0 \pm 1.5) \times 10^{-4},\\ \Delta Y_{\pi^+\pi^-} &= (-3.6 \pm 2.7) \times 10^{-4},\end{aligned}$$

where only the statistical uncertainties are reported. The two measurements agree with each other within 0.5σ.

5.4 Dilution of the measured value of ΔY

Owing to the correlation between the decay time and momentum of the D^0 and π^+_{tag} mesons, a possible time-dependent asymmetry due to a nonzero value of ΔY would reflect into momentum-dependent asymmetries and would be partially cancelled by the kinematic weighting. This would cause a dilution of the measured value of ΔY. However, such possible asymmetries are expected to be distributed smoothly in the three-dimensional phase space of the D^0-meson (or π^+_{tag}-meson) momentum. Therefore, the size of the dilution is expected to be moderate. In particular, it is measured with a data-driven method as follows:

1. an artificial value of ΔY_f is injected in the raw sample, filtering the data according to an efficiency that changes linearly with decay time, with opposite slopes for positively and negatively charged D^{*+} candidates,

   $$\epsilon^{\pm}(t) = \frac{1 \pm \Delta Y_f{}^{\text{inj}}\, t/\tau_{D^0}}{\alpha},$$

   where α is a normalisation factor shared by $\epsilon^+(t)$ and $\epsilon^-(t)$. In this way, the slope of the time-dependent asymmetry is artificially increased by a quantity $\Delta Y_f{}^{\text{inj}}$ (the "injected" value of ΔY_f), which is indistinguishable from a dynamical *CP*-violating time-dependent asymmetry;[2]

2. the measurement of ΔY_f is performed using the baseline procedure by (i) calculating new coefficients to subtract the $m(D^0\pi^+_{\text{tag}})$ background from the filtered sample, (ii) calculating new kinematic weights based on the $m(D^0\pi^+_{\text{tag}})$-background-subtracted momenta distributions and (iii) fitting the time-dependent asymmetry of the weighted sample with a linear function. The steps (i) to (iii) are performed for both the first and second step of the kinematic weighting.

This test is repeated 11 times for injected values of $\Delta Y_f{}^{\text{inj}}$ equally spaced between -5×10^{-3} and 5×10^{-3}, which correspond to about 100 times the experimental precision on $\Delta Y_{K^-\pi^+}$, for each D^0-meson decay channel. The results for the measured value of ΔY_f as a function of the injected one are displayed in Fig. 5.14. Here, since all measurements are highly correlated — they share most of the $D^{*\pm}$ candidates —, the value of the baseline result with $\Delta Y_f{}^{\text{inj}} = 0$ is subtracted from all the other results, and the uncertainties are calculated accordingly as the

[2] If one indicates the original time-dependent asymmetry in raw data with $A(t)$, the total asymmetry after the filtering with the $\epsilon^{\pm}(t)$ efficiencies is equal to $\left[A(t) + \Delta Y_f{}^{\text{inj}} t/\tau_{D^0}\right] \times \left[1 + \mathcal{O}\big(A(t)\Delta Y_f{}^{\text{inj}} t/\tau_{D^0}\big)\right]$. The size of the last term is estimated to be $|A(t)\Delta Y_f{}^{\text{inj}} t/\tau_{D^0}| \leq (2\%) \times (5 \times 10^{-3}) \times 5.5 = 5.5 \times 10^{-4}$, where 5×10^{-3} is the maximum size of $\Delta Y_f{}^{\text{inj}}$ used in the test and 5.5 is the average decay time in the last decay-time bin.

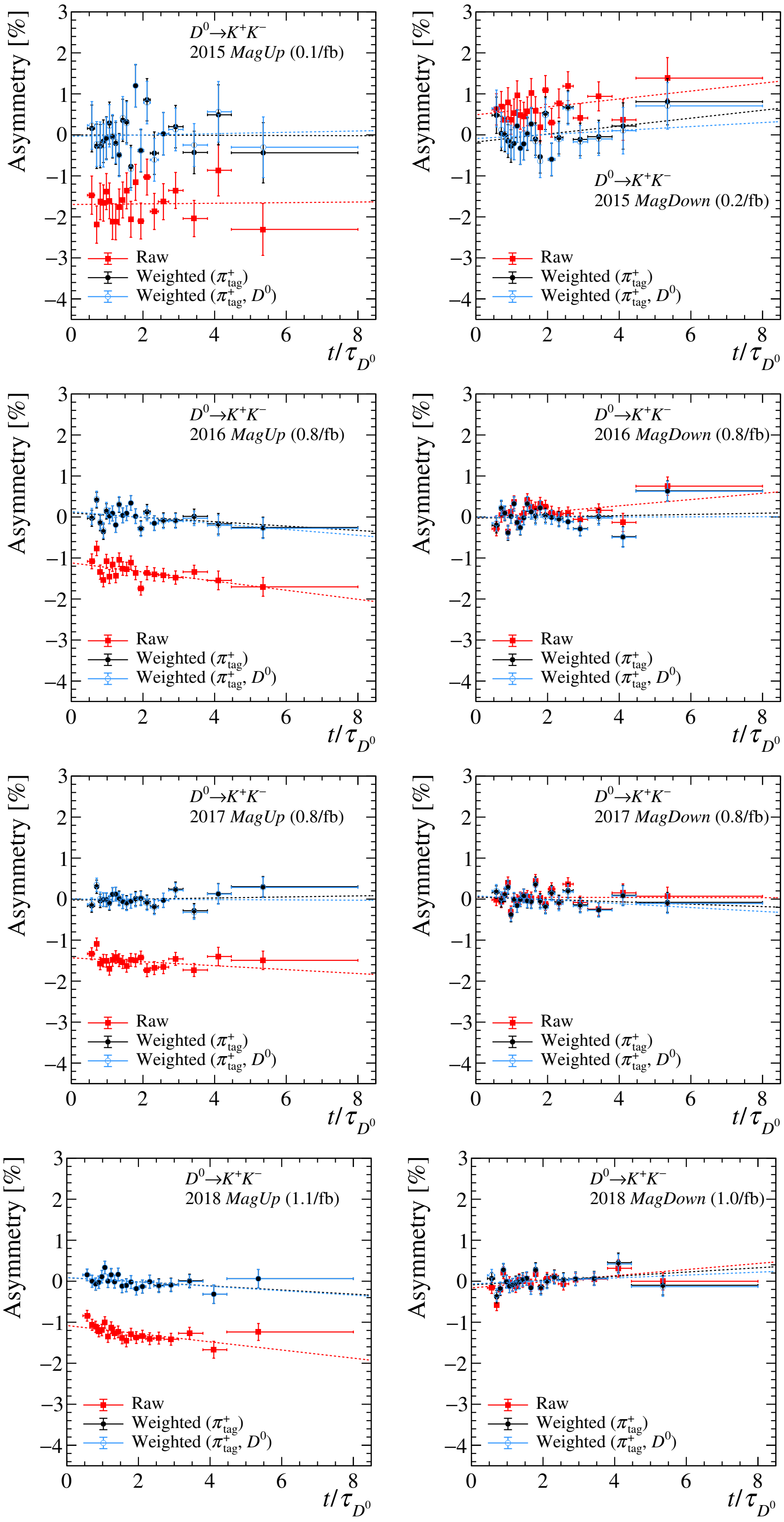

Figure 5.9: Linear fit to the time-dependent asymmetry of the $D^0 \to K^+K^-$ sample (red) for raw data, (black) after the first kinematic weighting and (azure) after the second kinematic weighting.

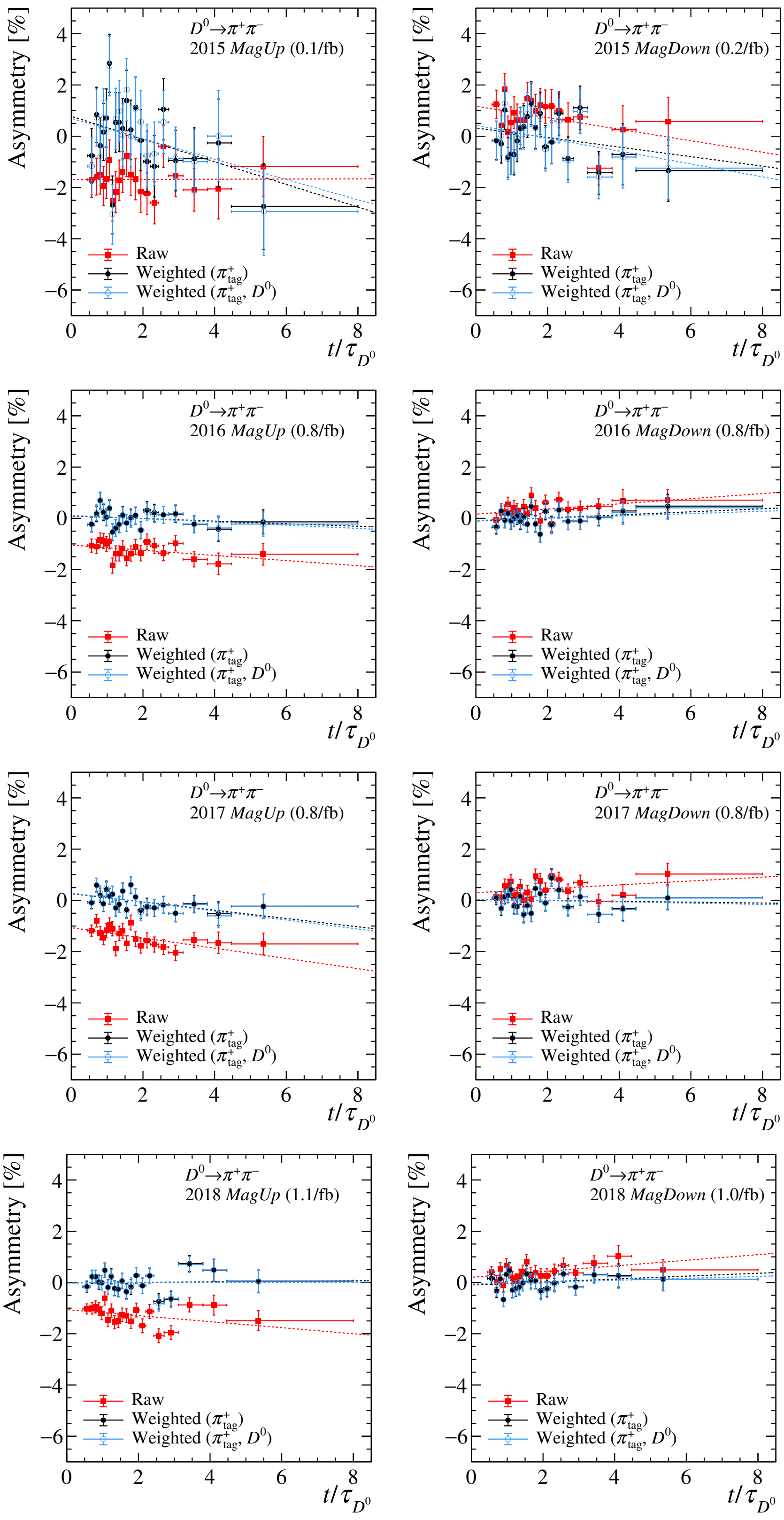

Figure 5.10: Linear fit to the time-dependent asymmetry of the $D^0 \to \pi^+\pi^-$ sample (red) for raw data, (black) after the first kinematic weighting and (azure) after the second kinematic weighting.

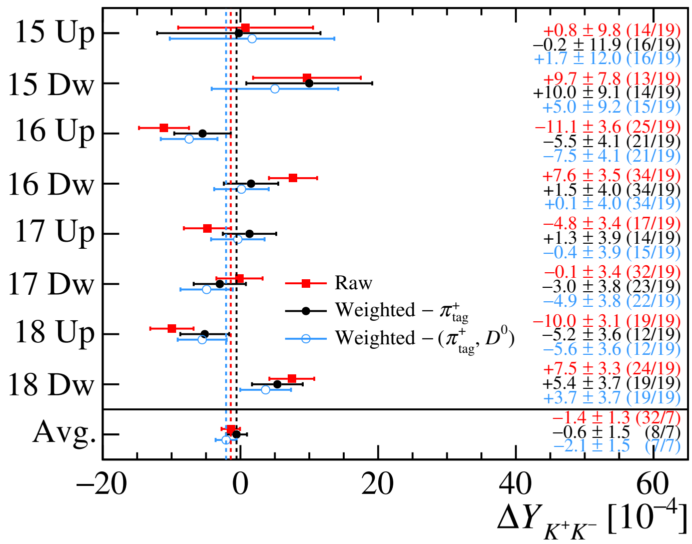

Figure 5.11: Summary of the fitted values of $\Delta Y_{K^+K^-}$ in the eight subsamples divided according to the year and magnet polarity, together with their average. The numerical values of $\Delta Y_{K^+K^-}$ and the χ^2/ndf of the fits are reported on the right. The global p-values of the eight linear fits to the time-dependent asymmetry are 7.4%, 42% and 41% for raw data and after the first and second steps of the kinematic weighting, respectively, whereas the p-values of the average of $\Delta Y_{K^+K^-}$ are 4×10^{-5}, 33% and 45%, respectively.

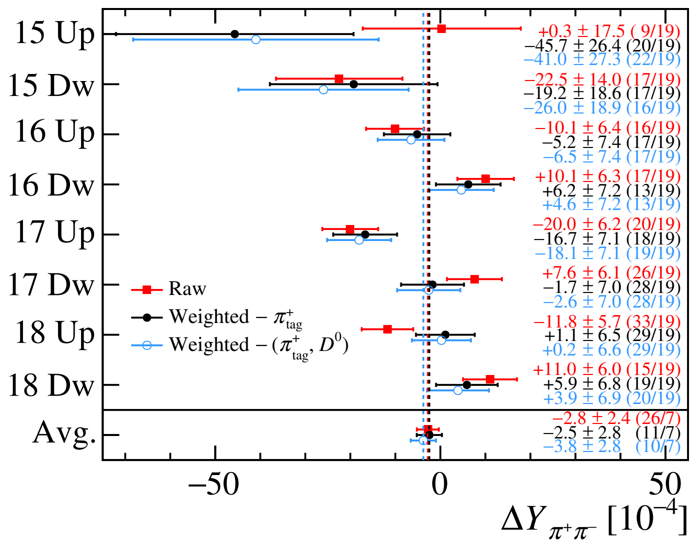

Figure 5.12: Summary of the fitted values of $\Delta Y_{\pi^+\pi^-}$ in the eight subsamples divided according to the year and magnet polarity, together with their average. The numerical values of $\Delta Y_{\pi^+\pi^-}$ and the χ^2/ndf of the fits are reported on the right. The global p-values of the eight linear fits to the time-dependent asymmetry are 40%, 37% and 31% for raw data and after the first and second steps of the kinematic weighting, respectively, whereas the p-values of the average of $\Delta Y_{\pi^+\pi^-}$ are 0.05%, 14% and 17%, respectively.

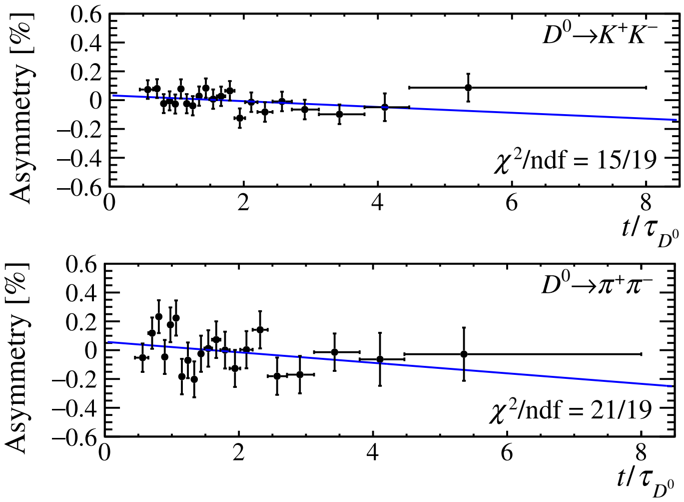

Figure 5.13: Linear fit to the time-dependent asymmetry of the full $D^0 \to K^-\pi^+$ data sample after the kinematic weighting.

difference in quadrature of the uncertainty minus the uncertainty of the result with $\Delta Y_f{}^{\text{inj}} = 0$. The results are fitted with a linear function both before and after the kinematic weighting. The P-values of all the fits are larger than 5%.

For the most abundant $K^-\pi^+$ decay channel, the fit to raw data shows an intercept equal to zero within an uncertainty of 0.02×10^{-4}, as expected, and a slope equal to unity within 3×10^{-3}. The deviation of the measured slope from unity, 3.1×10^{-3}, amounts to around 4.4 times its uncertainty. This discrepancy may be due to various causes, including the approximate procedure used to filter the data and to calculate the uncertainties, and the nonlinear dependence on decay time of the raw asymmetry. In any case, its absolute size is negligible for the aim of the measurement (and is smaller by an order of magnitude than the dilution measured in weighted data). For weighted data, the intercept is again compatible with zero within 2σ with an uncertainty of 0.02×10^{-4}, while the slope differs from unity by $(3.08 \pm 0.08)\%$. In other words, the bias on the measurement of $\Delta Y_{K^-\pi^+}$ after the kinematic weighting increases linearly with its value and corresponds to a dilution of the measured value amounting to $(3.1 \pm 0.3)\%$, where the uncertainty is conservatively estimated as the deviation from unity of the slope of the fit to raw data. The value and uncertainty of $\Delta Y_{K^-\pi^+}$ measured in Sect. 5.2 are multiplied by the reciprocal of unity minus the dilution value, 1.032, to correct for this effect. The result is identical with the one shown previously up to the first significant figure,

$$\Delta Y_{K^-\pi^+} = (-0.1 \pm 0.5) \times 10^{-4},$$

where only the statistical uncertainty is displayed.

The results of the tests for the less abundant K^+K^- and $\pi^+\pi^-$ decay channels are consistent with those of the $K^-\pi^+$ one, but less precise. In particular, the dilutions (the offsets) after the second weighting are equal to $(3.5 \pm 0.2)\%$ and $(2.9 \pm 0.5)\%$ $((+0.02 \pm 0.06) \times 10^{-4}$ and $(+0.20 \pm 0.12) \times 10^{-4})$ for the K^+K^- and $\pi^+\pi^-$ decay channels, respectively. Since the kinematic correlations are nearly indistinguishable for the three decay channels, the size nearly indistinguishable obtained with the $K^-\pi^+$ decay channel is assumed to be the same also for the K^+K^- and $\pi^+\pi^-$ ones. From here on out, the value of ΔY and the statistical and systematic uncertainties are multiplied by a factor of 1.032 to account for this dilution effect. In particular,

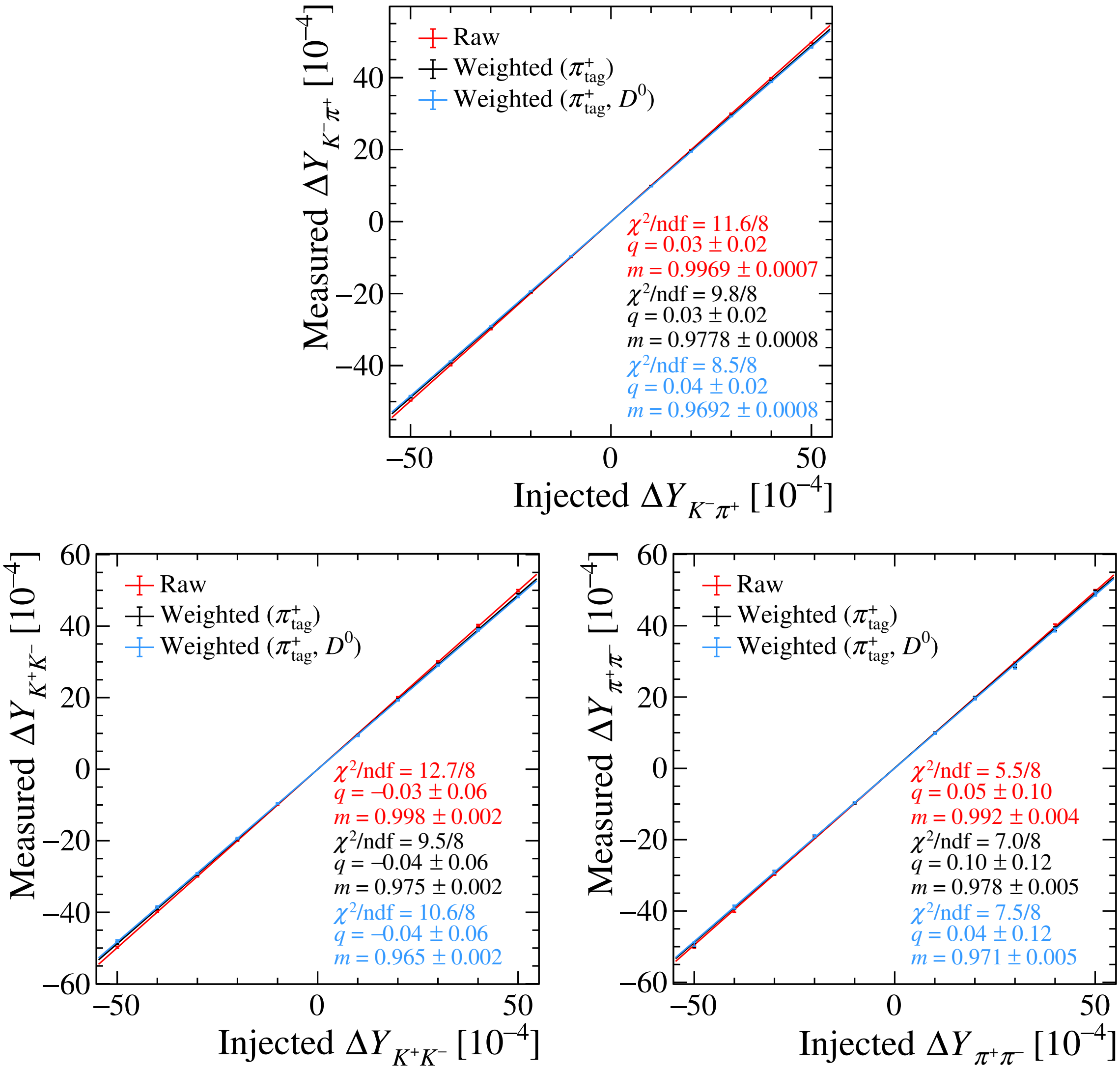

Figure 5.14: Measured value of (top) $\Delta Y_{K^-\pi^+}$ (bottom left) $\Delta Y_{K^+K^-}$ and (bottom right) $\Delta Y_{\pi^+\pi^-}$ as a function of the time-dependent asymmetry ${\Delta Y_f}^{\rm inj}$ injected into the data sample. In each plot, the result obtained for ${\Delta Y_f}^{\rm inj} = 0$ is subtracted from all the other points.

the results in Sect. 5.3 become

$$\begin{aligned} \Delta Y_{K^+K^-} &= (-2.1 \pm 1.5) \times 10^{-4}, \\ \Delta Y_{\pi^+\pi^-} &= (-3.8 \pm 2.8) \times 10^{-4}, \end{aligned}$$

where only the statistical uncertainty is displayed.

Chapter 6

Secondary decays

This chapter describes the subtraction of the contribution to the asymmetry from secondary decays which, corresponding to around 4% of the signal candidates, are the largest background of the measurement.

The largest source of background after the $m(D^0\pi^+_{\rm tag})$ background has been subtracted is that of secondary decays, where the D^{*+} meson is not produced in the primary vertex of the pp collision (PV), but in the decay of a B meson, as shown in Fig. 6.1. The total asymmetry measured in the previous chapter is equal to

$$A_{\rm tot}(t) = A_{\rm prim}(t) + f_{\rm sec}(t)[A_{\rm sec}(t) - A_{\rm prim}(t)], \tag{6.1}$$

where $f_{\rm sec}(t) \equiv N_{\rm sec}(t)/[N_{\rm prim}(t) + N_{\rm sec}(t)]$ is the fraction of secondary decays, $N_{\rm prim}(t) \equiv N^+_{\rm prim}(t) + N^-_{\rm prim}(t)$ is the sum of the number of D^0 and $\overline{D}^0$ primary decays, $N_{\rm sec}(t) \equiv N^+_{\rm sec}(t) + N^-_{\rm sec}(t)$ is its analogue for secondary decays, the asymmetries of primary and secondary decays are defined as

$$A_{\rm prim}(t) \equiv \frac{N^+_{\rm prim}(t) - N^-_{\rm prim}(t)}{N^+_{\rm prim}(t) + N^-_{\rm prim}(t)}, \qquad A_{\rm sec}(t) \equiv \frac{N^+_{\rm sec}(t) - N^-_{\rm sec}(t)}{N^+_{\rm sec}(t) + N^-_{\rm sec}(t)}, \tag{6.2}$$

and t is the measured decay time of the D^0 meson. Thus, the bias on the measurement of the time-dependent asymmetry in Eq. (6.1) is proportional to the fraction of secondary decays and to the difference of the asymmetry of secondary and primary decays. These quantities are measured in Sects. 6.1 and 6.2, respectively.

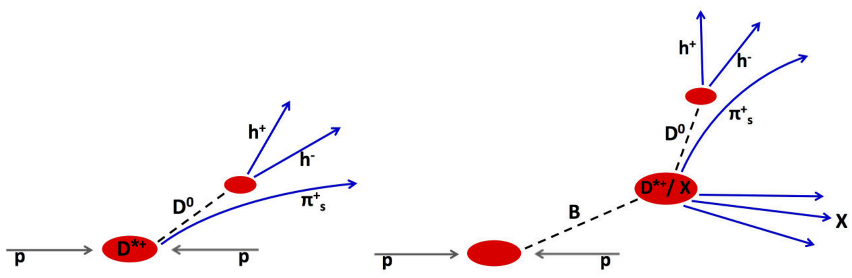

Figure 6.1: Topologies of (left) primary and (right) secondary decays. In the right figure, X stays for all particles other than the D^{*+} meson which are produced in the decay of the B meson.

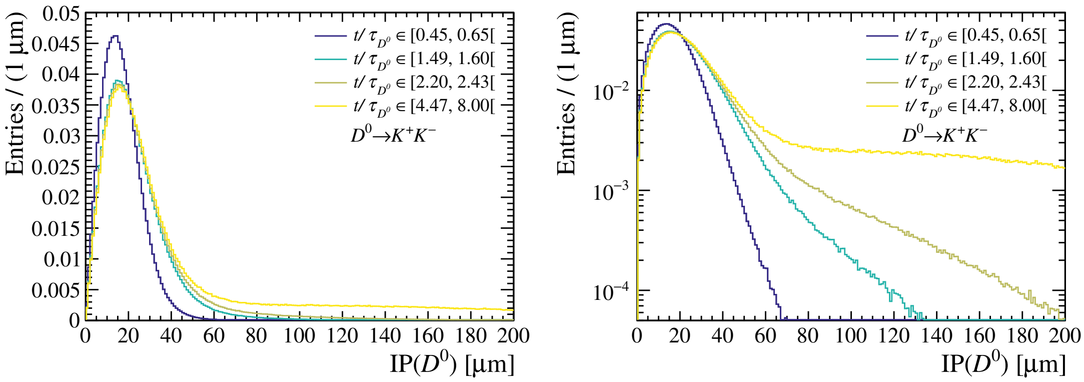

Figure 6.2: Distributions of the D^0-meson IP in (left) linear and (right) logarithmic scale, for the 0^{th}, 10^{th}, 15^{th} and 20^{th} bins of decay time. The long tails of the distributions at high decay times are due to secondary decays.

In both sections, secondary decays are distinguished from primary decays based on the distribution of the impact parameter (IP) of the D^0 meson with respect to its PV. While for primary decays the momentum of the D^0 meson points back to its PV and its IP is zero within experimental resolution, the momentum of secondary D^0 mesons does not necessarily point back to the PV, as shown in Fig. 6.1. As a result, the IP distribution of secondary decays is broader than that of primary decays, as displayed in Fig. 6.2, especially at large decay times, which correspond on average to large flight distances. Therefore, at large decay times the long tail of the IP distribution can be used to disentangle secondary from primary decays and to measure their fraction. On the contrary, at small decay times the distributions of primary and secondary decays are nearly indistinguishable and relying on simulation is necessary.

The invariant mass $m(D^0\pi^+_{\text{tag}})$, when calculated with the constraint that the D^{*+} meson is produced in the PV [162], also provides discriminating power between primary and secondary decays. In fact, it is equal to

$$\begin{aligned} m(D^0\pi^+_{\text{tag}}) &= \sqrt{m(D^0)^2 + m(\pi^+_{\text{tag}})^2 + 2\left[E(D^0)E(\pi^+_{\text{tag}}) - p(D^0)p(\pi^+_{\text{tag}})\cos\theta\right]} \\ &\approx \sqrt{m(D^0)^2\left[1 + \frac{p(\pi^+_{\text{tag}})}{p(D^0)}\right] + m(\pi^+_{\text{tag}})^2\left[1 + \frac{p(D^0)}{p(\pi^+_{\text{tag}})}\right] + p(D^0)p(\pi^+_{\text{tag}})\theta^2}, \end{aligned}$$

where the three terms depending on the momenta are of similar size, and the resolution is dominated by that on the tiny angle θ between the momenta of the D^0 and π^+_{tag} mesons. Such resolution is improved by around a factor of two by the constraint that the D^{*+} meson is produced in the PV. However, for secondary decays this constraint biases the measured angle to smaller values and, consequently, reduces the measured value of $m(D^0\pi^+_{\text{tag}})$. The size of this effect increases with the flight distance of the B meson, which is correlated with the D^0-meson measured decay time. This effect is displayed in Fig. 6.3, where a long tail appears on the left of the $m(D^{*+})$ peak for large decay times. While the effect is more clearly visible when loosening the IP requirement to $\text{IP}(D^0) < 200\,\mu\text{m}$, it cannot be neglected even with the baseline requirement $\text{IP}(D^0) < 60\,\mu\text{m}$. All the studies in this chapter employ an enlarged signal window $m(D^0\pi^+_{\text{tag}}) \in [2007.5, 2011.3]\,\text{MeV}/c^2$, which covers most of the left tail of the $m(D^0\pi^+_{\text{tag}})$ distribution of secondary decays, in order to maximise the discriminating power between primary and secondary decays.

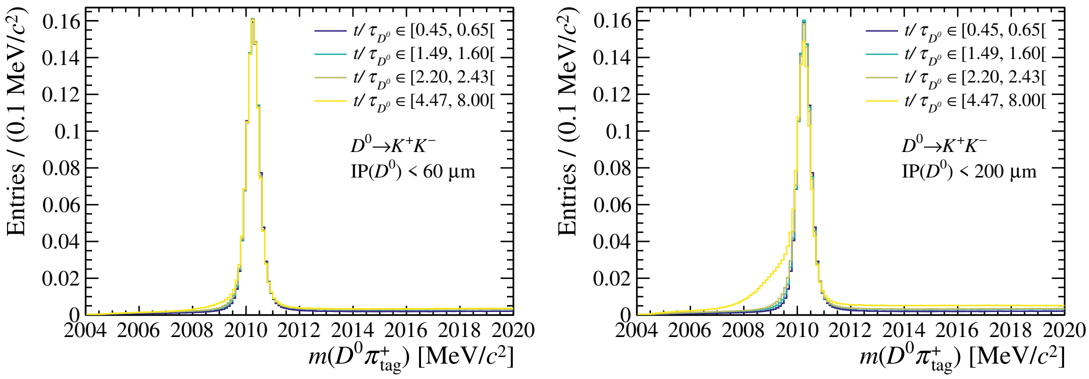

Figure 6.3: Distributions of $m(D^0\pi^+_{\rm tag})$ with (left) the baseline and (right) a looser requirement on the IP(D^0), for the 0$^{\rm th}$, 10$^{\rm th}$, 15$^{\rm th}$ and 20$^{\rm th}$ bins of decay time. The tail on the left of the $m(D^{*+})$ peak at large decay times is due to secondary decays.

6.1 Background size

The D^0-meson decay time is measured with respect to its PV. Since the average lifetime of the mixture of B^0 and B^+ mesons (1.52 and 1.64 ps, respectively [36]) is greater than the lifetime of the D^0 meson (0.41 ps) by approximately a factor of 4, the measured decay time of secondary decays is biased towards larger values. As a consequence, the fraction of secondary decays increases as a function of decay time. This implies that even a time-independent difference between the asymmetry of primary and secondary decays can introduce a spurious time-dependent asymmetry in the data sample and bias the measurement of ΔY, *cf.* Eq. (6.1). In particular, this effect causes the greatest bias to the measurement since, indeed, the most important causes of asymmetry difference between secondary and primary decays are nearly time-independent, as discussed in Sect. 6.2.

The fraction of secondary decays is determined through a maximum-likelihood binned template fit to the IP(D^0) *versus* $t(D^0)$ two-dimensional distribution, for D^0 and $\overline{D}^0$ samples combined. For this aim, the IP(D^0) range is extended from $[0, 60]$ to $[0, 200]$ μm to increase the discriminating power between primary and secondary decays. The two-dimensional templates of primary and secondary decays, as well as the fraction of B^+ mesons in the template of secondary decays, which is shown in Fig. 6.4, are fixed to the results of the simulation, and only the time-integrated fraction of secondary decays is left free to vary in the fit. The projections of the fit results are shown for all decay-time bins in Figs. 6.5 and 6.6. The results of the fit, where the time-integrated fraction of secondary decays is the only parameter left free to vary, agree with data typically within 10%. Slightly larger discrepancies, always below the 20% level, are observed mainly in the first decay-time bins, and are probably due to a poor reproduction of the trigger requirements in simulation, which has the largest impact at low decay times, where the selection efficiency is the smallest. These discrepancies, whose impact on the measurement is assessed among systematic uncertainties in Sect. 7.3, affect similarly primary and secondary decays and cancel to good extent in the calculation of the fraction of secondary decays. The systematic uncertainty on the finite size of the simulated sample used to prepare the two-dimensional templates is discussed in Sect. 7.3 as well.

The fitted fraction of secondary decays is displayed in Fig. 6.7 (left) both for the loose requirement IP(D^0) < 200 μm and for the baseline one, IP(D^0) < 60 μm. In both cases, the

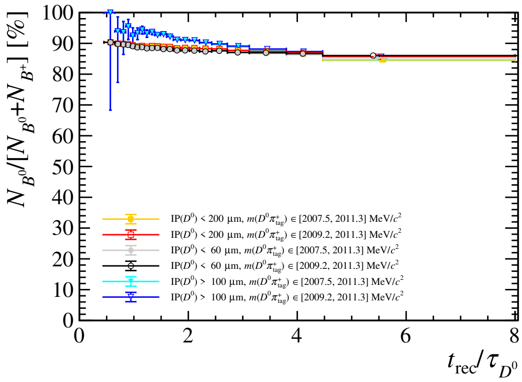

Figure 6.4: Fraction of B^0 mesons with respect to the total number of B mesons as a function of the measured decay time of secondary decays in simulation.

fractions are displayed both for the enlarged $m(D^0\pi^+_{\rm tag})$ signal window, $[2007.5, 2011.3]$ MeV/c^2, and for the baseline one. The values for the baseline window are calculated from the fit results and from the fraction of primary and secondary decays that fall into the baseline $m(D^0\pi^+_{\rm tag})$ signal window with respect to their total number in the enlarged window, as measured in simulation and shown in Fig. 6.8. While tightening the IP and $m(D^0\pi^+_{\rm tag})$ signal windows reduces substantially the fraction of secondary decays at large decay times, the impact at low decay times is limited. For the baseline selection employed for the ΔY measurement, the fraction increases from around 2% at low decay times to around 7% at large decay times, as shown in Fig. 6.7 (right). Thus, the fraction of secondary decays in the first decay-time bins is not negligible as it was assumed in previous LHCb measurements relying on data-driven methods [114, 175].

6.2 Background asymmetry

A measurement of the difference of the asymmetry of secondary and primary decays, entering Eq. (6.1), is needed in addition to that of $f_{\rm sec}(t)$ to subtract the contribution of secondary decays to the asymmetry. The main source of such asymmetry difference is given by the different production asymmetries and by the different asymmetries of the hardware-trigger efficiency for D^{*+} and B mesons. The former ones are due to different hadronisation probabilities of c and $\bar{c}$ quarks into D^{*+} and D^{*-} mesons, and of b and $\bar{b}$ quarks into $\overline{B}^0/B^-$ and B^0/B^+ mesons, owing to the initial non-self-conjugate pp state. The latter are caused by the combination of two factors. The first is the different efficiency asymmetry of the various hardware-trigger lines, caused by different momentum thresholds, different geometrical acceptances of the detectors involved and different interactions of the relevant particles with the detector material. For example, muons are the only particles that need to pass through the whole detector to fire their dedicated hardware-trigger line, and are thus the only particles sensitive to left-right asymmetric defects of the muon chambers. On the other hand, differently from the kaon mesons and thus from the hadronic trigger, they are not affected by an asymmetric interaction cross-section with matter. The second factor is the different probability that a primary or secondary decay fires a given hardware-trigger line. For example, the probability that a secondary decay fires the muon line is larger than that of a primary decay. In fact, semileptonic $\overline{B}^0$-meson decays represent the largest contribution to the inclusive branching fraction of $\overline{B}^0$ mesons into D^{*+} mesons, whereas primary D^{*+} decays are less frequently associated with the production of muons (the most frequent cases

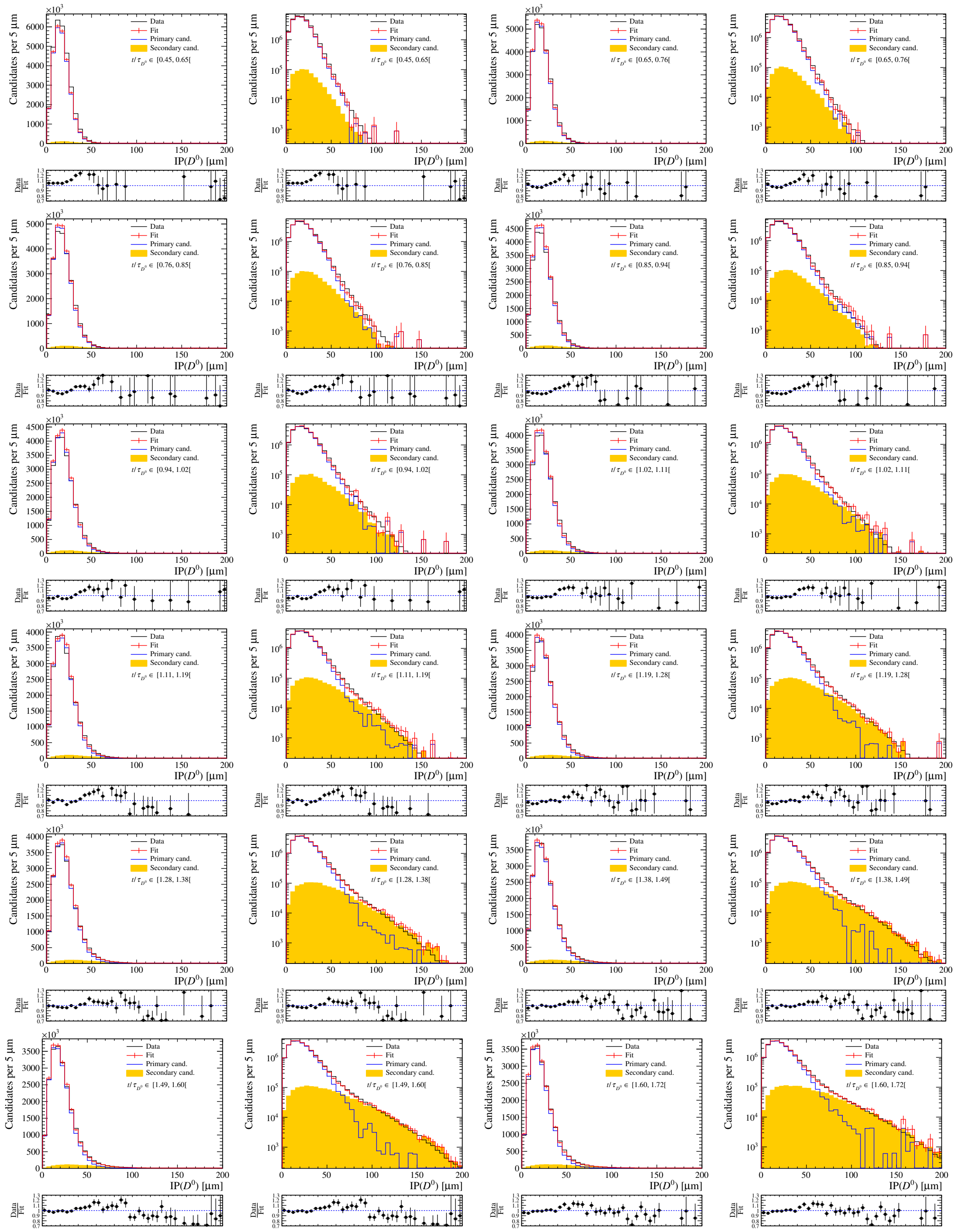

Figure 6.5: Projections of the template fit to the IP(D^0) *versus* $t(D^0)$ distribution of $D^0 \to K^-\pi^+$ and $\overline{D}^0 \to K^+\pi^-$ decays combined, for the time bins from 1 to 12. A looser requirement $m(D^0\pi^+_{\rm tag}) \in [2007.5, 2011.3]\,{\rm MeV}/c^2$ is applied with respect to the baseline selection of Sect. 4.3. The templates are taken from simulation for both primary and secondary decays and only the relative time-integrated abundance is left free to vary in the fit.

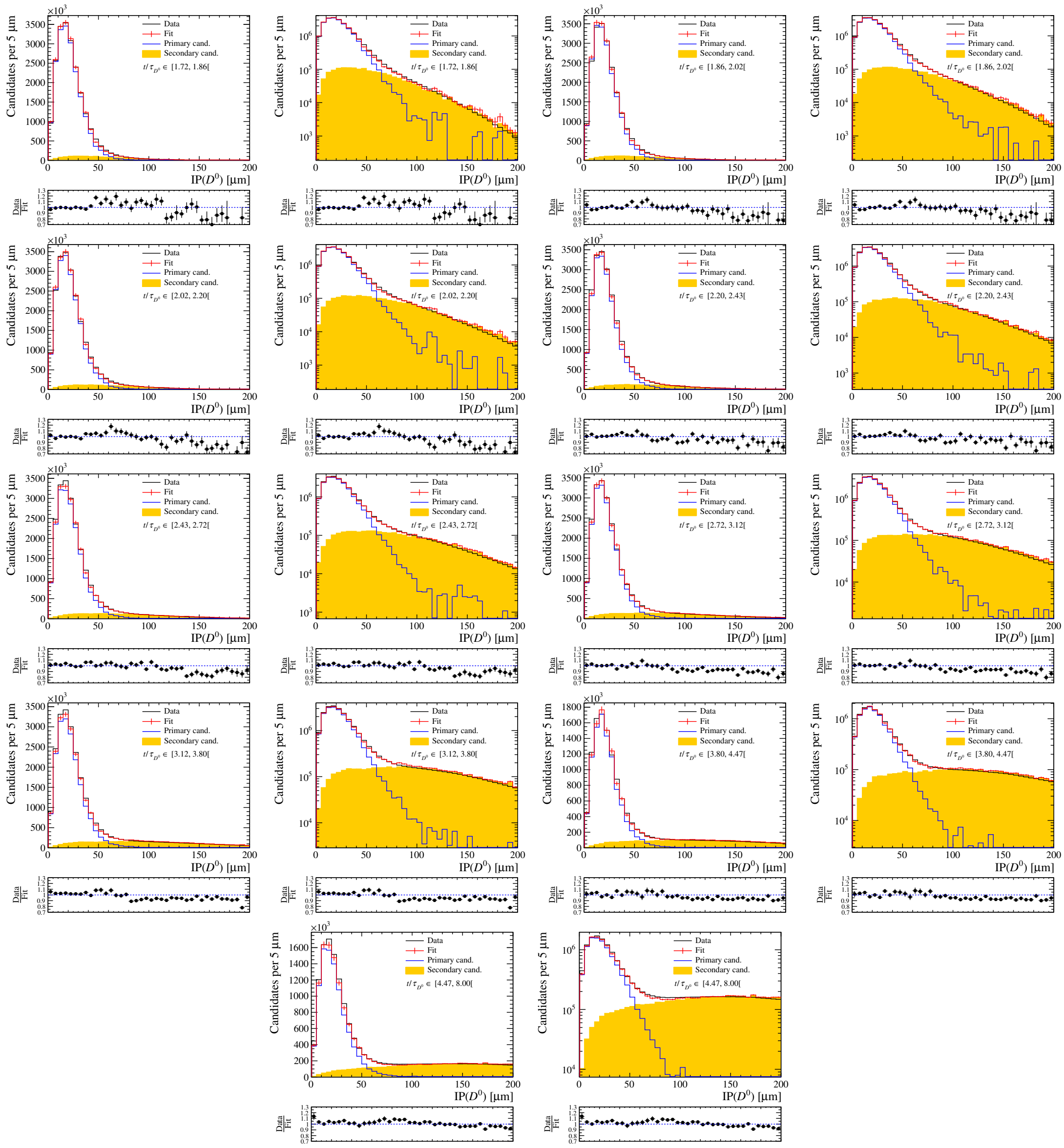

Figure 6.6: Projections of the template fit to the IP(D^0) *versus* $t(D^0)$ distribution of $D^0 \to K^-\pi^+$ and $\overline{D}^0 \to K^+\pi^-$ decays combined, for the time bins from 13 to 21. A looser requirement $m(D^0\pi^+_{\rm tag}) \in [2007.5, 2011.3]\,\mathrm{MeV}/c^2$ is applied with respect to the baseline selection of Sect. 4.3. The templates are taken from simulation for both primary and secondary decays and only the relative time-integrated abundance is left free to vary in the fit.

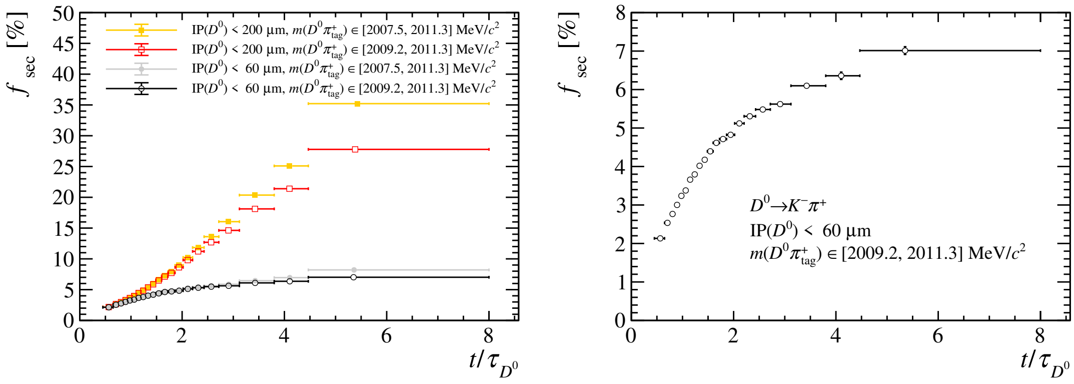

Figure 6.7: (Left) Fraction of secondary decays obtained in the template fit to the IP(D^0) *versus* $t(D^0)$ two-dimensional distributions of $D^0 \to K^-\pi^+$ decays. (Right) Magnification of the left plot for the data with the baseline IP and $m(D^0\pi^+_{\rm tag})$ requirements. Only the statistical uncertainty is reported.

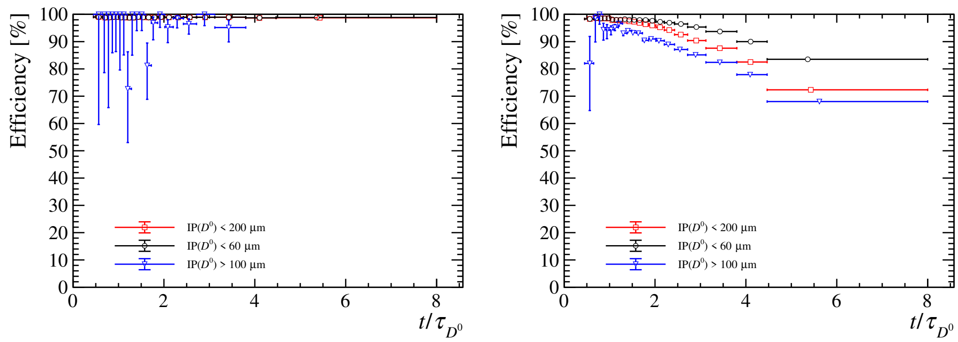

Figure 6.8: Fraction of simulated decays whose $m(D^0\pi^+_{\rm tag})$ lies in the baseline signal window with respect to those in the enlarged one, $[2007.5, 2011.3]\,\mathrm{MeV}/c^2$, for (left) primary and (right) secondary decays.

being the semileptonic decay of the other anti-charm hadron from the hadronisation of the $c\bar{c}$ pair produced in the pp collision, the decay in flight of one of the D^0-meson daughters into a muon, or a decay involving muons that is completely uncorrelated with that of the D^{*+} meson). Therefore, the asymmetric efficiency of the muon trigger line contributes more to the asymmetry of secondary than of primary decays. As opposed to production and trigger asymmetries, the momentum-dependent asymmetries in the detection of the D^{*+} decay, which are discussed in the previous chapter, are expected to cancel in the asymmetry difference, since the kinematics of primary and secondary decays is very similar (*cf.* Figs. 4.12 and 4.13 in Sect. 4.6). Furthermore, detection asymmetries are removed for both categories at once by the kinematic weighting.

Both the production and the trigger asymmetries are expected to depend weakly on momenta. In particular, the difference of the trigger asymmetries is mainly due to particles other than the D^{*+} meson which are produced in the $\overline{B}$-meson decay or in the hadronisation of the other $\bar{c}$ or b quark, and are only loosely correlated with the D^0-meson kinematics. Since the momenta are in turn only weakly correlated with decay time, the difference of the production and trigger asymmetries is assumed to be independent of decay time. However, a significant time dependence of the secondary asymmetry might arise owing to B^0-meson mixing. In fact, the production asymmetry of D^{*+} mesons from B^0-meson decays depends, in addition to the B^0-meson production asymmetry and to the asymmetry of its inclusive branching fractions into

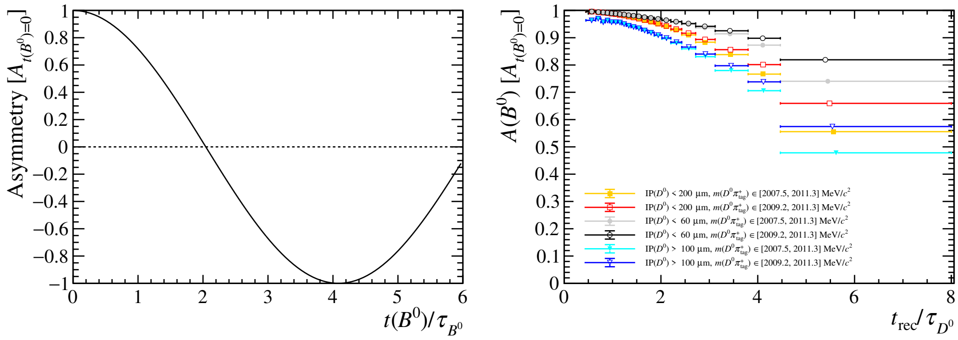

Figure 6.9: Impact of B^0 mixing on the time variation of the asymmetry of the number of D^{*+} mesons from B^0-meson decays, as a function of the (left) B^0 true decay time and (right) D^0 measured decay time. The asymmetry is zero after half of the B^0 mesons have oscillated, at $t = \pi\tau_{B^0}/2x \approx 2.04\,\tau_{B^0}$. The second plot is produced using the approximate estimated value of the B^0 decay time (see the text for details); its shape reproduces closely that of the left plot in the range $[0, 1.4]\tau_{B^0}$. The unit of measurement of the y axis is the production asymmetry of D^{*+} mesons coming from B^0 mesons that decayed at zero decay time, denoted as A_{B^0} in Eq. (6.3).

D^{*+} and D^{*-} mesons, on the fraction of B^0 mesons that oscillate before decaying — the total asymmetry is zero after half of the B^0 mesons has oscillated —, and the B^0-meson decay time is correlated with the measured decay time of the D^0 meson. Consequently, the asymmetry difference is parametrised as

$$A_{\text{sec}}(t) - A_{\text{prim}}(t) = f_{B^0}(t) A_{B^0} A_{B^0}^{\text{no mix}}(t) + f_{B^+}(t) A_{B^+} - A_{D^{*+}}, \tag{6.3}$$

where t is the measured decay time of the D^0 meson, $f_{B^0}(t)$ ($f_{B^+}(t) = 1 - f_{B^0}(t)$) is the fraction of secondary decays originating from B^0 (B^+) decays, $A_{B^0}^{\text{no mix}}(t)$ is the asymmetry between the number of B^0 mesons that have not oscillated into $\overline{B}^0$ mesons before decaying and those that have oscillated, A_{B^0} (A_{B^+}) is the product of the sum of the B^0 (B^+) production and trigger asymmetries with the asymmetry of its inclusive branching fraction into D^{*+} and D^{*-} mesons, and $A_{D^{*+}}$ is the sum of the production and trigger asymmetries of D^{*+} mesons. The asymmetry $A_{B^0}^{\text{no mix}}$ is plotted both as a function of B^0 decay time and of the measured decay time of the D^0 meson in Fig. 6.9. The dependence on the D^0-meson decay time is different for different requirements on the values of IP(D^0) and of $m(D^0\pi^+_{\text{tag}})$, since these variables are correlated with the B^0-meson flight distance and hence with its decay time. Finally, the fraction $f_{B^0}(t)$ measured in simulated data is plotted in Fig. 6.4. Its dependence on decay time is neglected in the following, since it is much smaller than the asymmetry dependence on time due to B^0 mixing.

The kinematic weighting of Sect. 5.2 does not modify Eq. (6.3) since, even if it removes by construction the time-integrated asymmetry of the sum of primary and secondary decays satisfying IP(D^0) $< 60\,\mu$m, it does not modify the asymmetry difference to first order. This analytical result is confirmed by the experimental cross-check in Appendix D.3. It is not possible to rely on previous measurements to estimate the size of the asymmetries in Eq. (6.3), since neither the production nor the triggering asymmetries have been measured with sufficient precision, below 10^{-3}, to date. Therefore, the asymmetry difference between secondary and primary decays is measured from data satisfying IP(D^0) $> 100\,\mu$m in the enlarged signal window $m(D^0\pi^+_{\text{tag}}) \in [2007.5, 2011.3]\,\text{MeV}/c^2$, where the fraction of secondary decays is larger than 80%, as shown in Fig. 6.10. This asymmetry is plotted for kinematically weighted data in Fig. 6.11,

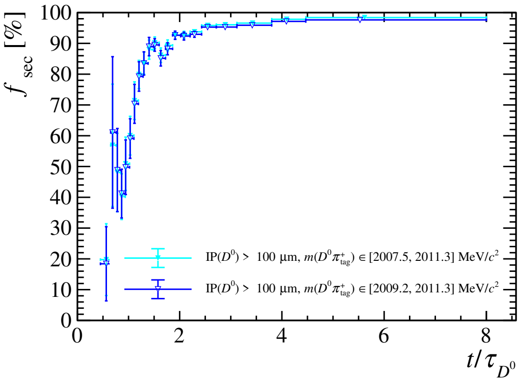

Figure 6.10: Fraction of secondary decays in data satisfying $\mathrm{IP}(D^0) > 100\,\mu\mathrm{m}$ and $m(D^0\pi^+_{\mathrm{tag}}) \in [2007.5, 2011.3]\,\mathrm{MeV}/c^2$, as calculated from the results of the template fit to the IP *versus* t distribution of D^0 mesons.

and nearly coincides with the sum of the production and trigger asymmetries of secondary decays. In turn, this is nearly indistinguishable from the asymmetry difference of secondary and primary decays, up to a dilution of around 4%. In fact, the kinematic weighting removes by construction the time-integrated asymmetry of primary and secondary decays satisfying $\mathrm{IP}(D^0) < 60\,\mu\mathrm{m}$, which consists of around 96% primary and 4% secondary decays. In the first bins of decay time, where the IP distributions of primary and secondary decays are very similar, the fraction of primary decays can contribute significantly to the total asymmetry, *cf.* Fig. 6.10. However, the statistical precision of the asymmetry in these bins is very low, and the contribution from primary decays is verified to have a negligible impact on the results below.

The asymmetry of Fig. 6.11 is fitted under two different hypothesis. The first fit, represented with a red line, models the asymmetry with a constant function, thus neglecting a possible time dependence from B^0 mixing. This approximation has been the working assumption of all of the previous D^{*+}-tagged measurements of mixing and *CP* violation at LHCb [114, 117, 175]. The second fit, represented with a blue line, models the asymmetry with the sum of a constant function and of the cyan curve in Fig. 6.9 (right) multiplied by a normalisation factor, and accounts for the effect of B^0 mixing according to Eq. (6.3) (under the assumption that f_{B^0} and f_{B^+} are independent of time). The numerical results of the fits are displayed in Fig. 6.11. The contribution of B^0 mixing to the time dependence of the asymmetry might be significant, but cannot be disentangled unambiguously from the constant hypothesis, as confirmed by the large uncertainties of the fitted parameters and by their large correlation. This ambiguity is mainly due to the large uncertainty on the asymmetry difference at low decay times. The precision with which it is known might be improved by performing a simultaneous fit to the $(\mathrm{IP}(D^0), t(D^0))$ distributions of D^0 an $\overline{D}^0$ candidates instead of adopting the present method. However, the dependence of the asymmetry on $\mathrm{IP}(D^0)$, which is shown in Fig. 6.9 (right), implies that the templates (or PDFs) used in the fit should be different for D^0 and $\overline{D}^0$ decays, and their shape would depend on the exact value of A_{B^0}, which is not known *a priori*. Given the small size of the total contribution to the asymmetry from secondary decays, the current, less precise approach is preferred to avoid unnecessary complications.

The models corresponding to the best points of the two fits in Fig. 6.11 nearly coincide. Therefore, in the following section a constant dependence of the asymmetry on decay time is assumed. The asymmetry difference $A_{\mathrm{sec}} - A_{\mathrm{prim}}$ is equal to $(2.2 \pm 0.4) \times 10^{-3}$. The correction

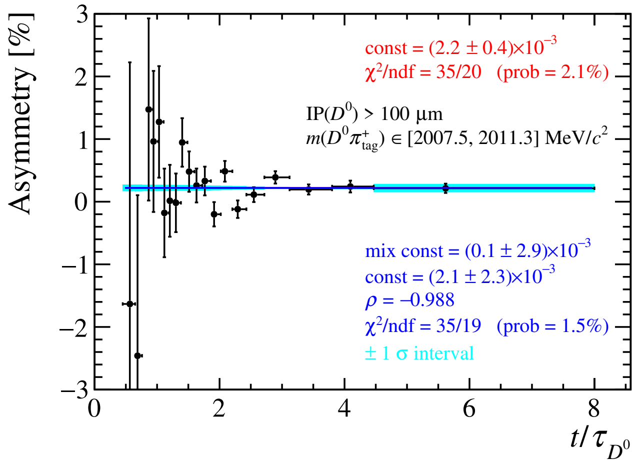

Figure 6.11: Asymmetry of $D^0 \to K^-\pi^+$ candidates with $\mathrm{IP}(D^0) > 100\,\mu\mathrm{m}$ in the enlarged signal region $m(D^0\pi^+_{\mathrm{tag}}) \in [2007.5, 2011.3]\,\mathrm{MeV}/c^2$, after the kinematic weighting of Sect. 5.2. The fits with a constant function and a constant plus the cyan template from Fig. 6.9 (right), which overlap nearly perfectly, are superimposed. The cyan band represents the 1σ confidence interval of the results of the fit modelling the B^0-meson mixing.

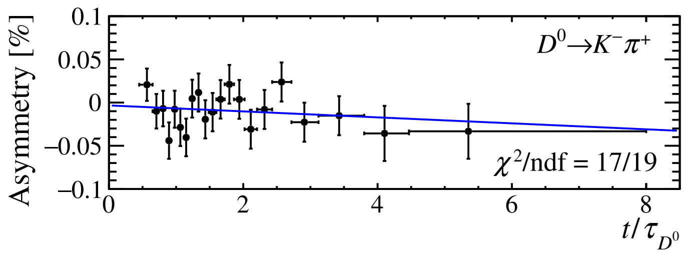

Figure 6.12: Linear fit to the time-dependent asymmetry of the full $D^0 \to K^-\pi^+$ sample after the kinematic weighting and the subtraction of the contribution of secondary decays to the asymmetry.

for the 4% dilution owing to the 4% fraction of secondary decays satisfying $\mathrm{IP}(D^0) < 60\,\mu\mathrm{m}$ that enter the vector-momentum distributions used to calculate the weights for the kinematic weighting of Sect. 5.2 is much smaller than the statistical uncertainty, and is neglected. The possible impact of B^0-meson mixing on the measurement is accounted for in the systematic uncertainty in Sect. 7.3.

6.3 Removal of the bias

In each bin of decay time, the asymmetry of primary decays is calculated from the measured asymmetry, $A(t)$, according to Eq. (6.1), by subtracting the term $f_{\mathrm{sec}}(t)(A_{\mathrm{sec}} - A_{\mathrm{prim}})$ from it. In the subtraction, the values of $f_{\mathrm{sec}}(t)$ measured in Sect. 6.1 and shown as black open circles in Fig. 6.7 are used, as well as the time-independent asymmetry difference represented by the red line in Fig. 6.11. The uncertainties of $f_{\mathrm{sec}}(t)$ and of $A_{\mathrm{sec}} - A_{\mathrm{prim}}$ are set to zero, while their possible impact on the measurement is taken into consideration by the systematic uncertainty in Sect. 7.3. The linear fit to $A_{\mathrm{prim}}(t)$ is displayed in Fig. 6.12. The fitted slope is

$$\Delta Y_{K^-\pi^+} = (-0.4 \pm 0.5) \times 10^{-4},$$

and corresponds to a shift of -0.25×10^{-4} with respect to the result without subtraction of the contribution of secondary decays to the asymmetry that is shown in Sect. 5.4. The size of the shift is roughly equal to the following approximate expression, which follows from Eq. (6.1) under the approximation that the time-dependence of the fraction of secondary decays on decay time is linear,

$$\begin{aligned}\Delta(\Delta Y) &\approx -\frac{f_{\mathrm{sec}}(t_{\mathrm{max}}) - f_{\mathrm{sec}}(t_{\mathrm{min}})}{(t_{\mathrm{max}} - t_{\mathrm{min}})/\tau_{D^0}} \times (A_{\mathrm{sec}} - A_{\mathrm{prim}}) \\ &\approx -\frac{7.0\% - 2.1\%}{5.4 - 0.6}(2.2 \times 10^{-3}) \approx -0.22 \times 10^{-4},\end{aligned} \tag{6.4}$$

where $t_{\mathrm{min(max)}}$ is the average decay time of the candidates in the first (last) decay-time bin. This estimate is in keeping with the result based on the subtraction of the contribution of secondary decays to the asymmetry performed separately in each decay-time bin, from which it differs by only 0.03×10^{-4}.

No differences are expected in $f_{\mathrm{sec}}(t)$ and in the asymmetry difference among different D^0 decay channels. In fact, the production mechanism and triggering efficiency of secondary decays, as well as their asymmetry, are expected to be the same for different D^0 decay channels, whereas the detection asymmetry of the D^0-meson final state, which is different, cancels out in the difference between secondary and primary decays and in addition is removed by the kinematic weighting. The only asymmetry that might not cancel out is that from a possible nonzero value of ΔY in the K^+K^- and $\pi^+\pi^-$ decay channels. In fact, the measured decay time of secondary decays is systematically larger than the true one, and might provoke a decrease of the slope of the dynamical time-dependent asymmetry for secondary decays. Thus, the difference between the secondary and primary asymmetries can receive a time-dependent contribution from dynamical asymmetries, which is not accounted for in Eq. (6.3). However, this effect is expected to be small. In fact, the parameter ΔY is known to be less than 2.1×10^{-4}, *cf.* Sect. 2.2, and the decay time range analysed corresponds to a maximum of $5.4\,\tau_{D^0}$, implying that the maximum dynamical asymmetry is less than 1.1×10^{-3}, a factor of 2 below the fitted value of the asymmetry difference in Fig. 6.11. In addition, it is expected to cancel out to good approximation in the asymmetry difference, since the measured decay time of secondary decays with $\mathrm{IP}(D^0) < 60\,\mu\mathrm{m}$ in the $m(D^0\pi^+_{\mathrm{tag}})$ signal region is about 70% of the true one, as shown in Fig. 6.13. Therefore, this effect is neglected. The related bias is estimated to be smaller than $50\% \times 30\% = 15\%$ of the total contribution of secondary decays to the asymmetry, where 50% is due to the maximum size of the asymmetry and 30% to the relative difference of the true and measured decay times of secondary decays. Its maximum size is 0.04×10^{-4} in absolute value, and is accounted for in the systematic uncertainty of Sect. 7.3.

The hypothesis that the asymmetry difference between secondary and primary decays of the K^+K^- and $\pi^+\pi^-$ channels is equal to that of $K^-\pi^+$ decays is verified in data where, however, the precision of the results for the former ones is less precise by nearly a factor of three than that for the $K^-\pi^+$ channel. Therefore, the results obtained with the $D^0 \to K^-\pi^+$ sample are employed to correct the $D^0 \to K^+K^-$ and $D^0 \to \pi^+\pi^-$ samples as well, to minimise the statistical fluctuations on the correction values. The results and the analogues of Fig. 6.12 for the signal channels are reported in Chap. 9. The shift of the value of ΔY after the subtraction of the contribution of secondary decays is equal to -0.24×10^{-4} and -0.25×10^{-4} for the K^+K^- and $\pi^+\pi^-$ decay channels, respectively.

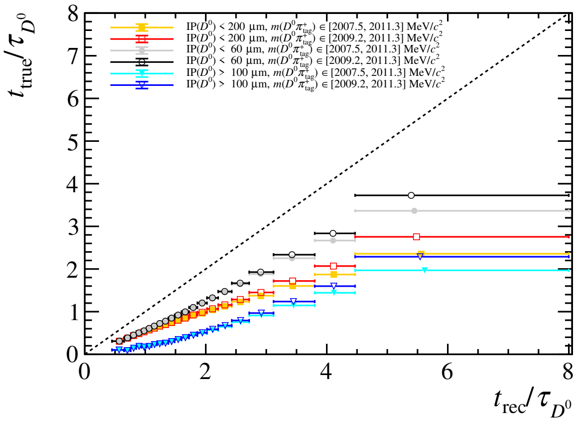

Figure 6.13: True decay time of secondary D^0 mesons as a function of their measured decay time.

Chapter 7

Systematic uncertainties

This chapter discusses the systematic uncertainties of the measurement. Whenever they are not expected to depend on the D^0-meson decay channel, they are calculated relying on the $K^-\pi^+$ final state to reduce the statistical uncertainty on their estimated value. The values of all of the systematic uncertainties are summarised in Sect. 7.7.

The main systematic uncertainties are due to the subtraction of the $m(D^0\pi^+_{\text{tag}})$ background under the D^{*+}-meson mass peak, to the asymmetry of the time-dependent shifts of its position for D^{*+} and D^{*-} mesons, and to uncertainties in the subtraction of the contribution of secondary decays to the asymmetry. Minor contributions are related to limitations of the kinematic weighting of Sect. 5.2, as well as to the background of misidentified D-meson decays under the D^0-meson mass peak. Each of these sources of uncertainty is discussed in detail in one of the following sections.

7.1 Removal of the background under the D^{*+} mass peak

The effectiveness of the removal of the $m(D^0\pi^+_{\text{tag}})$ background under the D^{*+}-meson mass peak, as described in Sect. 4.3, rests on two assumptions, namely:

1. the background properties, and in particular its asymmetry, are the same in the signal and in the lateral window;
2. the coefficient to weight the candidates in the lateral window, *i.e.* the opposite of the ratio of the integral of the background PDF in the lateral to that in the signal window, is measured precisely.

The first assumption is tested by changing the $m(D^0\pi^+_{\text{tag}})$ window used to subtract the background. Two windows closer to the signal region ($[2004.5, 2008.5]$ and $[2013, 2015]\,\text{MeV}/c^2$) and one farther from the signal window ($[2018, 2020]\,\text{MeV}/c^2$) with respect to the standard one, $[2015, 2018]\,\text{MeV}/c^2$, are used for this aim. The results of the measurement of $\Delta Y_{(K^-\pi^+)}$ for the three decay channels and for the four lateral windows, including the standard one, are summarised in the first four rows of Table 7.1. The deviations of the values of $\Delta Y_{(K^-\pi^+)}$ measured with the alternative windows with respect to the baseline one are affected by statistical fluctuations in addition to a possible systematic bias. In particular, the largest deviations happen for the $[2013, 2015]$ ($[2018, 2020]$) MeV/c^2 window for the $K^-\pi^+$ decay channel (for the K^+K^- and $\pi^+\pi^-$ decay channels), and not for the $[2004.5, 2008.5]\,\text{MeV}/c^2$ window, which is the farthest with

Table 7.1: Summary of the results of the cross-checks on the removal of the $m(D^0\pi^+_{\rm tag})$ background — the baseline measurement is highlighted in grey. The second (third) column indicates whether the fits to the $m(D^0\pi^+_{\rm tag})$ distribution are performed separately for samples relative to different years and magnet polarities (for the samples of D^{*+} and D^{*-} candidates) or not. All the values in the table are provided before the subtraction of the contribution to the asymmetry of secondary decays, which is assumed to be equal for all of the cross-checks.

Sideband [MeV/c^2]	Sum over samples	Sum over D^{*+} flavours	Bkg. model	$\Delta Y_{K^-\pi^+}$ [10^{-4}]	$\Delta Y_{K^+K^-}$ [10^{-4}]	$\Delta Y_{\pi^+\pi^-}$ [10^{-4}]
$[2004.5, 2008.5]$	Yes	Yes	Nominal	0.11 ± 0.49	-2.01 ± 1.50	-0.36 ± 2.78
$[2015.0, 2018.0]$	Yes	Yes	Nominal	0.11 ± 0.48	-2.22 ± 1.47	-0.69 ± 2.73
$[2013.0, 2015.0]$	Yes	Yes	Nominal	0.28 ± 0.48	-2.43 ± 1.49	-0.82 ± 2.76
$[2018.0, 2020.0]$	Yes	Yes	Nominal	0.11 ± 0.48	-1.98 ± 1.48	-1.91 ± 2.75
$[2015.0, 2018.0]$	Yes	Yes	A_Γ 2011–2012	0.11 ± 0.48	-2.26 ± 1.46	-0.68 ± 2.70
$[2015.0, 2018.0]$	Yes	Yes	ΔA_{CP}	0.11 ± 0.48	-2.20 ± 1.48	-0.64 ± 2.73
$[2015.0, 2018.0]$	No	Yes	Nominal	0.11 ± 0.48	-2.22 ± 1.48	-0.68 ± 2.73
$[2015.0, 2018.0]$	No	No	Nominal	0.18 ± 0.48	-2.38 ± 1.48	-0.51 ± 2.73

respect to the baseline one. The values of the maximum deviations are $+0.18\times10^{-4}$, $+0.24\times10^{-4}$ and -1.23×10^{-4} for the $K^-\pi^+$, K^+K^- and $\pi^+\pi^-$ sample, respectively, corresponding to $+0.37$, $+0.16$ and -0.45 of the statistical uncertainty of the baseline measurements. For the $K^-\pi^+$ sample, since no systematic trends are pinpointed in the results, the size of a possible bias is estimated as the root mean square (RMS) of the deviations of $\Delta Y_{K^-\pi^+}$ measured with the three alternative lateral windows with respect to the baseline one, 0.10×10^{-4}. This number is an upper limit and likely overestimates the size of the bias, since it encloses a large statistical component. The analogue RMSs for the K^+K^- and $\pi^+\pi^-$ samples are 0.22×10^{-4} and 0.74×10^{-4}, respectively. However, these value are likely to enclose even larger statistical fluctuations, owing to the smaller size of the samples with respect to the $K^-\pi^+$ one. The features of the $m(D^0\pi^+_{\rm tag})$ background are expected to be the same in all three decay channels — the only difference being the different signal-to-background (S/B) ratio in the $m(D^0\pi^+_{\rm tag})$ signal window, and the different kinds of background candidates under the $m(D^0)$ mass peak, which possess different $m(D^0\pi^+_{\rm tag})$ distribution. However, the systematic uncertainty on the latter category is already taken into account in Sect. 7.5, and should not be double counted. Therefore, the value of the systematic uncertainty of the $K^-\pi^+$ sample, multiplied by the ratio of the S/B ratio of the $K^-\pi^+$ final state to that of the signal sample under consideration, is conservatively taken as systematic uncertainty for the K^+K^- and the $\pi^+\pi^-$ samples. Using the values S/B $= 44.6,\ 22.2,\ 16.2$ for the $K^-\pi^+$, K^+K^- and $\pi^+\pi^-$ samples, respectively, the uncertainty is estimated to be 0.20×10^{-4} (0.28×10^{-4}) for the K^+K^- ($\pi^+\pi^-$) decay channel. Explicit checks for the presence of correlations between the $m(D^0\pi^+_{\rm tag})$ variable and the kinematic variables used in the weighting of Sect. 5.2 are reported in Appendix D.5. The results support the hypothesis that possible biases to the measurement due to variations of the background features as a function of $m(D^0\pi^+_{\rm tag})$ are smaller than the systematic uncertainties above, which are probably overestimated.

Various tests are performed to test the second assumption. First, the alternative PDFs adopted in Refs. [18, 114] are used to model the background,

$$\mathcal{P}_{\rm bkg}(m; m_0, \alpha, \beta) \equiv \frac{\theta_{\rm H}(m - m_0)}{I_B}\left[1 + e^{-\alpha(m-m_0)} + \beta(m - m_0)\right], \qquad (A_\Gamma\ 2011\text{–}2012)$$

$$\mathcal{P}_{\rm bkg}(m; m_0, \alpha, \beta) \equiv \frac{\theta_{\rm H}(m - m_0)}{I_B}(m - m_0)^{\alpha} e^{-\beta(m-m_0)}, \qquad (\Delta A_{CP})$$

where $m \equiv m(D^0\pi^+_{\rm tag})$, $m_0 \equiv m(D^0) + m(\pi^+)$, $\theta_{\rm H}$ is the Heaviside step function and I_B is the appropriate normalisation factor in the range $[2004, 2020]\,{\rm MeV}/c^2$. The deviations of the value of ΔY from the baseline result when using these alternative parametrisations are listed in Table 7.1 and amount to 0.00×10^{-4}, 0.04×10^{-4} and 0.05×10^{-4} at most for the $K^-\pi^+$, K^+K^- and $\pi^+\pi^-$ decay channels, respectively. Second, since the shape of the background PDF might change over the data-taking time as a consequence of changes in the operations of the detector and of the trigger, the fits to the $m(D^0\pi^+_{\rm tag})$ distribution are performed separately for each year and magnet polarity. The corresponding results are listed in the next-to-last line of Table 7.1 and amount to 0.00×10^{-4}, 0.00×10^{-4} and 0.01×10^{-4} for the $K^-\pi^+$, K^+K^- and $\pi^+\pi^-$ decay channels, respectively. Finally, the shape of the background PDF might depend also on the charge of the $\pi^+_{\rm tag}$ meson, since the kinematics of oppositely charged pions produced in a *pp* collision can differ, and this difference can be further increased by detection asymmetries. This hypothesis is tested by repeating the fits separately not only for each year and magnet polarity, but also for the distributions of D^{*+} and D^{*-} candidates. The deviations from the baseline result are listed in the last line of Table 7.1 and amount to 0.07×10^{-4}, -0.16×10^{-4} and 0.18×10^{-4} for the $K^-\pi^+$, K^+K^- and $\pi^+\pi^-$ decay channels, respectively. Since the effect is expected to be of the same size for the three decay modes, but the deviations contain a statistical fluctuation in addition to the possible bias, the deviation observed in the $K^-\pi^+$ sample (properly multiplied by the ratio of the S/B ratios) is taken to estimate an upper bound to the effect, obtaining the values 0.14×10^{-4} and 0.19×10^{-4} for the K^+K^- and the $\pi^+\pi^-$ decay channels, respectively.

The systematic uncertainties that account for possible deviations from the assumptions listed at the beginning of this section are summed in quadrature to estimate the total systematic uncertainty on the removal of the $m(D^0\pi^+_{\rm tag})$ background, which is equal to 0.12×10^{-4}, 0.24×10^{-4} and 0.34×10^{-4} for the $K^-\pi^+$, K^+K^- and $\pi^+\pi^-$ decay channels, respectively. Finally, a cross-check is performed by repeating the measurement without subtracting the $m(D^0\pi^+_{\rm tag})$ background, to make sure that possible contributions to the asymmetry from the $m(D^0\pi^+_{\rm tag})$ background (which are in any case subtracted with good precision thanks to the background removal) are moderate in size. The results are $\Delta Y_{K^-\pi^+} = (0.20 \pm 0.47) \times 10^{-4}$, $\Delta Y_{K^+K^-} = (-2.41 \pm 1.39) \times 10^{-4}$ and $\Delta Y_{\pi^+\pi^-} = (-1.01 \pm 2.52) \times 10^{-4}$, corresponding to shifts of $\Delta\Delta Y_{RS} = 0.09 \times 10^{-4}$, $\Delta\Delta Y_{KK} = -0.20 \times 10^{-4}$ and $\Delta\Delta Y_{\pi^+\pi^-} = -0.32 \times 10^{-4}$ from the baseline results. The size of the shifts is less than that of the estimated systematic uncertainty, thus confirming that the uncertainty covers very conservatively any possible effects related to a imperfect removal of the $m(D^0\pi^+_{\rm tag})$ background.

7.2 Time and flavour dependent shift of the D^{*+} mass peak

The $m(D^0\pi^+_{\rm tag})$ signal window is fixed to $[2009.2, 2011.3]\,{\rm MeV}/c^2$ and does not depend on the D^{*+}-meson flavour nor on the D^0-meson decay time. This can potentially give rise to nuisance time-dependent asymmetries. In fact, if the $m(D^0\pi^+_{\rm tag})$ signal distributions of D^{*+} and D^{*-} mesons are shifted with respect to each other, for example because of biases of opposite sign

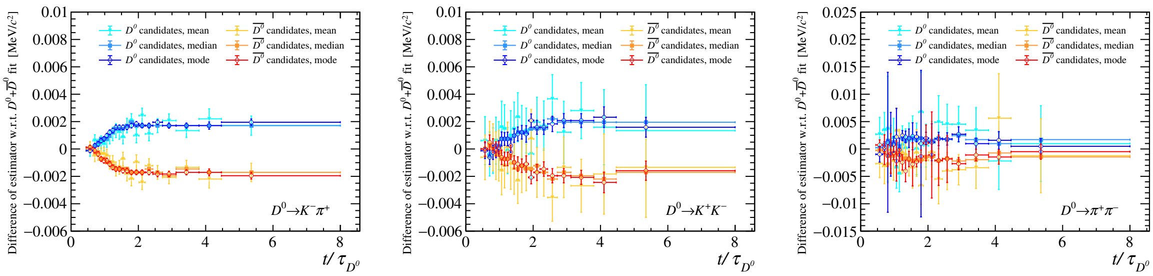

Figure 7.1: Shift of the $m(D^0\pi^+_{\rm tag})$ signal distribution of D^{*+} and D^{*-} candidates as a function of D^0 decay time for the (left) $K^-\pi^+$, (centre) K^+K^- and (right) $\pi^+\pi^-$ decay channels. The shift is estimated as the difference of the mean, median and mode of the D^{*+} (D^{*-}) signal PDF, as obtained in the fits described in Sect. 4.3, and the corresponding values obtained in the fit to the D^{*+} and D^{*-} candidates combined. In both fits the whole, kinematically weighted data sample is employed. Note that the range of the y axis for the $\pi^+\pi^-$ decay channel is different from the others.

in the measured momentum of $\pi^+_{\rm tag}$ and $\pi^-_{\rm tag}$ mesons, this would provoke different selection efficiencies for D^{*+} and D^{*-} candidates. Moreover, since the momentum is correlated with the D^0-meson decay time, and the bias on the $\pi^+_{\rm tag}$-meson momentum can depend on the value of the momentum itself, it is possible that the relative shift changes as a function of decay time. This would result in a time-dependent asymmetry of the selection efficiencies of D^{*+} and D^{*-} candidates that would contribute as an additional term in the raw asymmetry in Eq. (2.14) of Sect. 2.3.

The size of the shift between the D^{*+} and D^{*-} distributions is estimated by comparing the difference of the mean, median and mode of the $m(D^0\pi^+_{\rm tag})$ signal PDF for the D^{*+} and D^{*-} mesons in the fits of Sect. 4.3, with respect to those of the fit to the $m(D^0\pi^+_{\rm tag})$ distribution of D^{*+} and D^{*-} candidates combined. These estimators are preferred with respect to other options, such as the fraction of signal candidates in the signal window, since they are less influenced by statistical fluctuations of the shape of the small tails of the signal PDF, which can be difficult to disentangle from background. The results are shown in Fig. 7.1 for the candidates kinematically weighted according to the procedure in Sect. 5.2, but are the same within uncertainty also for raw data and after the first step of the kinematic weighting. The results for the three estimators agree within the uncertainty and among different decay channels. For the $K^-\pi^+$ final state, which provides the best precision, the relative shift between D^{*+} and D^{*-} mesons, which is compatible with zero at low decay times, is found to increase up to $4\,\mathrm{keV}/c^2$ at large decay times.

The impact of the shift on the measurement of ΔY is estimated by repeating the measurement of $\Delta Y_{K^-\pi^+}$ using a time-dependent and flavour-dependent $m(D^0\pi^+_{\rm tag})$ signal window. For each decay-time bin and flavour, the baseline signal window is shifted by the corresponding shift of the mode in Fig. 7.1. This procedure is applied to raw data and to data after the first step of the kinematic weighting, as well to the fully kinematically weighted data where the measurement is eventually performed. The measured value of $\Delta Y_{K^-\pi^+}$ is shifted by -0.14×10^{-4} with respect to its baseline value. The magnitude of this shift is taken as a systematic uncertainty for all decay channels. The corresponding shifts for the K^+K^- and $\pi^+\pi^-$ channels, where statistical fluctuations are expected to play a larger role, are $+0.15\times10^{-4}$ and -0.37×10^{-4}, respectively.

As a further cross-check, the asymmetry between the fraction of D^{*+} and D^{*-} events that fall in the $m(D^0\pi^+_{\rm tag})$ signal window is plotted in Fig. 7.2. The time-dependent slope of this asymmetry, whose value corresponds to the bias on the measurement of ΔY under the hypothesis

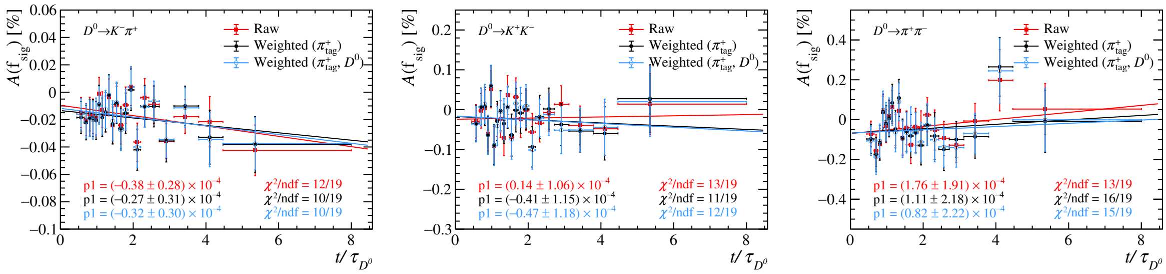

Figure 7.2: Asymmetry of the fraction of D^{*+} and D^{*-} candidates selected by the baseline $m(D^0\pi^+_{\text{tag}})$ signal window as a function of the D^0-meson decay time, for the (left) $K^-\pi^+$, (centre) K^+K^- and (right) $\pi^+\pi^-$ decay channels. The fractions are taken from the fits described in Sect. 4.3, which employ the whole data sample. Note that the range of the y axis depends on the decay channel.

that the dependence of the fraction asymmetry on decay time is linear, are consistent with zero, although within larger statistical uncertainties of 0.30×10^{-4}, 1.2×10^{-4} and 2.2×10^{-4} for the $K^-\pi^+$, K^+K^- and $\pi^+\pi^-$ decay channels, respectively. The larger statistical uncertainties are due to the larger fluctuations that affect the determination of the shape of the tails of the signal PDF with respect to their modes.

7.3 Secondary decays

The bias on ΔY due to the contribution of secondary decays to the asymmetry results from the product of their fraction and of the asymmetry difference between secondary and primary decays, as quantified in Eq. (6.1). Its size can be roughly estimated under the approximation that the fraction of secondary decays increases linearly with decay time and that the asymmetry difference is constant, yielding Eq. (6.4). Under this approximation, the relative uncertainty on the measurement of $(A_{\text{sec}} - A_{\text{prim}})$, 16%, reflects into an equal relative uncertainty on the subtracted bias, corresponding to an absolute value of 0.04×10^{-4}. As a cross check, possible nonlinear variations of the measured value of ΔY with the value of the asymmetry difference are tested by repeating 1000 times the subtraction of the contribution to the asymmetry from secondary decays with the baseline procedure of Sect. 6.3, each time drawing the value of the asymmetry difference from a Gaussian distribution whose mean and sigma are fixed to the values obtained in the fit to the data with $\text{IP}(D^0) > 100\,\mu\text{m}$ in Fig. 6.11 (left). The residuals of the measured value of ΔY with respect to the baseline one are plotted in Fig. 7.3. The average of the residual distribution is compatible with zero within 0.01×10^{-4} for all decay channels and thus is neglected. On the other hand, its RMS is equal to 0.04×10^{-4}, 0.04×10^{-4} and 0.03×10^{-4} for $K^-\pi^+$, K^+K^- and $\pi^+\pi^-$ decay channels, respectively, and confirms the linear estimate above.

The impact of the uncertainty on the contribution of B^0 mixing to the secondary asymmetry is estimated as follows. The values of the constant term of the asymmetry and of the normalisation factor that multiplies the black template in Fig. 6.9 (right), which models the impact of B^0 mixing on the time dependence of the asymmetry, are sampled randomly 1000 times from a bivariate Gaussian PDF whose parameters are fixed to those obtained in the fit to the asymmetry of data with $\text{IP}(D^0) > 100\,\mu\text{m}$ in Fig. 6.11 (left). The time-dependent asymmetry difference, $A_{\text{sec}}(t) - A_{\text{prim}}(t)$, is thus modelled as in Eq. (6.3), with $f_{B^+}(t)$ assumed to be independent of

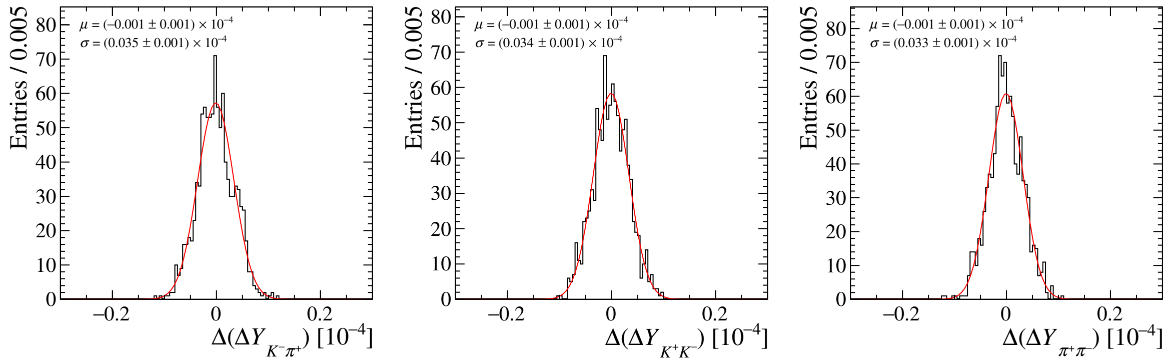

Figure 7.3: Difference between the fitted value of ΔY obtained in 1000 pseudoexperiments where the constant asymmetry difference of secondary and primary decays is varied within its uncertainty, and the baseline one.

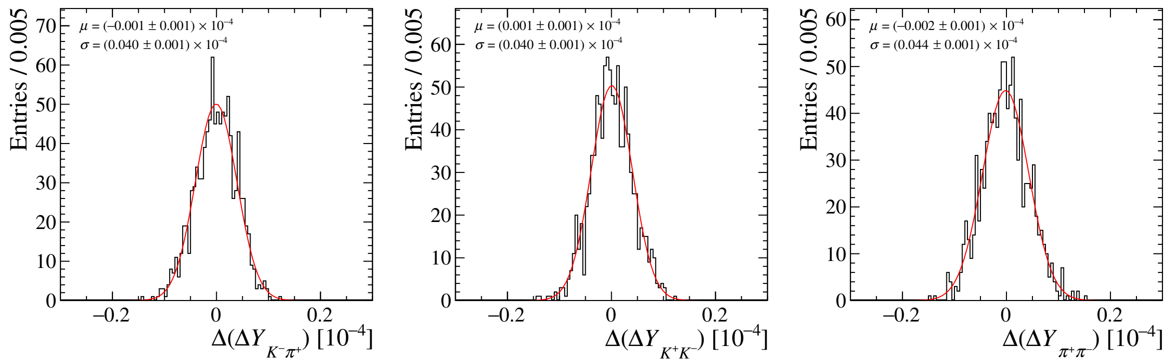

Figure 7.4: Difference between the fitted value of ΔY obtained in 1000 pseudoexperiments that take into account the impact of B^0 mixing on the secondary asymmetry, within the uncertainty of its fitted value, and that of the baseline model that assumes a time-independent asymmetry.

decay time.[1] Then, the so-obtained contribution of secondary decays to the total asymmetry is subtracted using Eq. (6.1), taking the values of $f_{\text{sec}}(t)$ from the baseline measurement. The residuals of the measured value of ΔY with respect to the baseline one are plotted in Fig. 7.4. The average of the residuals distribution is compatible with zero within 0.01×10^{-4} for all decay channels and is neglected. On the other hand, its RMS, which is equal to 0.04×10^{-4} for all decay channels, is compatible with the uncertainty due to the measurement of the asymmetry difference in the hypothesis of time independence. Therefore, a systematic uncertainty of 0.04×10^{-4} is assigned to account for the uncertainty on the asymmetry difference of secondary and primary decays in the subtraction of the bias from secondary decays.

[1]This approximation is justified by the observation that the value of f_{B^+} is less than 15%, as shown in Fig. 6.4. Therefore, the contribution of the time-dependence of the asymmetry from B^+ mesons is expected to be smaller that that due to B^0 mixing, even if the relative variation of $f_{B^+}(t)$ as a function of decay time for data satisfying $\text{IP}(D^0) > 100\,\mu\text{m}$ is as large as 50% (the relative variation of f_{B^+} as a function of decay time for data satisfying the baseline requirement $\text{IP}(D^0) < 60\,\mu\text{m}$ is much smaller). In fact, the relative variation of the asymmetry due to the mixing of B^0 mesons, which make up more than 85% of the secondary decays, can be as large as 50%, as shown in Fig. 6.9 (right). This 50% variation is also much larger than the relative variation of $f_{B^0}(t) = 1 - f_{B^+}(t)$ as a function of decay time is less than 5% both in the $\text{IP}(D^0) > 100\,\mu\text{m}$ ad in the $\text{IP}(D^0) < 60\,\mu\text{m}$ regions, and is negligible with respect to the

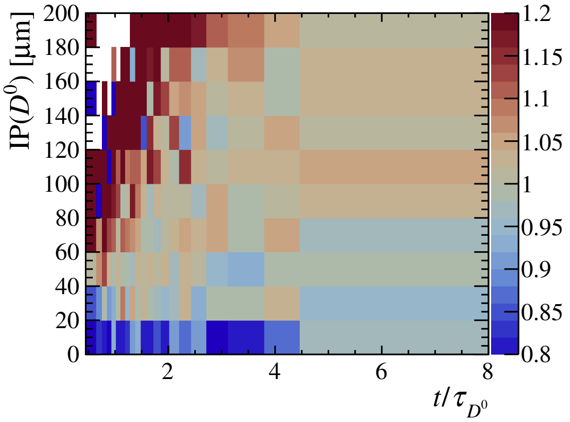

Figure 7.5: Ratio between the IP(D^0)-*versus*-t(D^0) normalised distributions of simulation to data of ($D^{*+}\mu^-$) pairs.

The second factor contributing to the uncertainty on the subtracted bias is the uncertainty on the variation of the fraction of secondary decays as a function of decay time. This can be caused by discrepancies between simulation and data in the distributions of either decay time or IP(D^0). The size of the discrepancies is estimated using the ($D^{*+}\mu^-$) sample of secondary decays described in Sect. 4.5, which allows a fair comparison between data and simulation thanks to its high purity. The ratio of the IP(D^0)-*versus*-t(D^0) distribution of simulation and data for this sample is plotted in Fig. 7.5. The simulation presents fewer (more) candidates at low (large) values of IP(D^0), but this behaviour is not significantly correlated with decay time. The relative normalisation between primary and secondary decays in the template fit of Sect. 6.1 is essentially determined by secondary decays with large values of IP(D^0) — let us say IP(D^0) $> 100\,\mu\text{m}$ —, where they can be unambiguously disentangled from primary decays. The shape of the template is then used to infer the amount of secondary decays in the signal region, IP(D^0) $< 60\,\mu\text{m}$. Since the ratio of ($D^{*+}\mu^-$) simulation and data in the interval IP(D^0) $\in [100, 200]\,\mu\text{m}$ (IP(D^0) $< 60\,\mu\text{m}$) is equal to 1.04 (0.95), the fraction of secondary decays with IP(D^0) $< 60\,\mu\text{m}$ is underestimated by about $1 - (0.95/1.04) = 8\%$ owing to imperfections in the IP(D^0) template of secondary decays. Another error might arise from an imperfect decay-time distribution of simulated secondary decays. In particular, the simulation underestimates the number of secondary decays at $0.6\tau_{D^0}$ by around 20%, as shown in Fig. 4.14, with the size of the underestimation progressively decreasing until reaching zero at around $1\,\tau_{D^0}$. Therefore, the fraction of secondary decays in the first bins of decay time might be further underestimated by up to 20% in addition to the underestimation due to wrong IP(D^0) templates that affect the time-integrated fraction. Taking both effects into account, $f_{\text{sec}}(t_{\text{max}})$ might be underestimated by 8% (0.6% in absolute value) and $f_{\text{sec}}(t_{\text{min}})$ up to $1 - (1 - 8\%)(1 - 20\%) = 26\%$ (0.6% in absolute value). The two errors tend to cancel in the difference $f_{\text{sec}}(t_{\text{max}}) - f_{\text{sec}}(t_{\text{min}})$ in Eq. (6.4). However, it is assumed conservatively that they are uncorrelated. The fractional uncertainty on $f_{\text{sec}}(t_{\text{max}}) - f_{\text{sec}}(t_{\text{min}})$ due to each of two effects is 11%, and it translates into an equal relative uncertainty on the subtracted bias, corresponding to an absolute value of 0.03×10^{-4}.

The estimated size of the discrepancies between the fraction of secondary decays in simulation and data is roughly in agreement with what is observed in the results of the template fit whose projections are plotted in Figs. 6.5 and 6.6, where the ratio of the fit results to data differs from unity by less than 15%. In particular, in the last decay-time bins the normalisation of secondary decays seems too large by around 8%. This would partially compensate the underestimation of the time-integrated fraction of secondary decays discussed in the previous paragraph.

Finally, the statistical uncertainty on the templates owing to the limited size of the simulated sample is not taken into account in the fit. On the contrary, the minimum content of every bin is set artificially to 0.01. This approach might bias the results, in particular owing to statistical fluctuations in the poorly populated upper tails of the IP distributions. Possible biases related to this choice are checked by setting the minimum population of each bin to 10 instead of 0.01. The normalisation of the template of secondary decays decreases by 6%, corresponding to a variation of the subtracted bias of 0.02×10^{-4}. This value is summed linearly to the bias due to the underestimation of the fraction of $f_{\rm sec}(t_{\rm max})$ calculated previously (the absolute value of the effect on $f_{\rm sec}(t_{\rm min})$ is negligible), and the result is summed in quadrature with the bias on $f_{\rm sec}(t_{\rm min})$ and with the uncertainty on the asymmetry difference to yield the total systematic uncertainty on the subtraction of secondary decays, which is equal to 0.07×10^{-4}. This number is smaller by a factor of 10 than the corresponding uncertainty of the ΔY measurement with D^{*+}-tagged data collected during 2011–2012 [114, 174].

7.4 Discrete implementation of the kinematic weighting

The kinematic weighting employed in Sect. 5.2 to remove the nuisance time-dependent asymmetries equalises the vector momentum distributions of the $\pi^+_{\rm tag}$ and D^0 mesons through a binned approach. However, the weighting functions are, in principle, continuous functions of the momenta. Therefore, the discrete method used to calculate the weights intrinsically degrades its accuracy, even in the limit of large number of events per bin. On the other hand, the bins cannot be too fine owing to the limited number of candidates, especially in the $\pi^+\pi^-$ decay channel.

The possible bias due to the finite size of the bins is estimated by increasing and decreasing the width of the bins of the $K^-\pi^+$ sample, as shown in Table 7.2, and by observing the impact of this change on the measured value of $\Delta Y_{K^-\pi^+}$. In order to make the comparison among the various binnings fair, only the events that are selected with the finest binning are considered when calculating $\Delta Y_{K^-\pi^+}$ with coarser binnings. In fact, only the bins containing more than 40 events and whose asymmetry is less than 20% in magnitude are used for the measurement, whereas the candidates in the other bins are discarded, as explained in Sect. 5.2. Therefore, increasing the binning intrinsically reduces the size of the sample and introduces statistical fluctuations in the results.

The results are plotted in Fig. 7.6. It is interesting to note that they are much more stable after the second than after the first step of the kinematic weighting. The measured value of $\Delta Y_{K^-\pi^+}$ reaches a *plateau* for a number of bins between 10^4 and 10^5. The systematic uncertainty on the choice of the binning is estimated as the absolute value of the difference between the value of $\Delta Y_{K^-\pi^+}$ measured with the two finest binnings, which is taken as a proxy of the *plateau* value, and the baseline one, and amounts to 0.05×10^{-4}.

7.5 Background under the D^0 mass peak

As a side effect, the removal of the $m(D^0\pi^+_{\rm tag})$ background removes also the $m(h^+h^-)$ background from random associations of two charged tracks, whose $m(D^0\pi^+_{\rm tag})$ distribution is equal to that of random combinations of D^0 mesons with unrelated pion mesons. This effect can be appreciated in Fig. 7.7 (bottom-right), where the tail on the right of the D^0-meson mass peak disappears

Table 7.2: Binning schemes used to calculate the systematic uncertainty on the discrete implementation of the kinematic weighting. All binning schemes employ the ranges $[-0.27, 0.27]$ rad, $[-0.27, 0.27]$ rad and $[0, 0.08]c$/GeV for the variables θ_x, θ_y and k, respectively, in the first step of the weighting and $[2, 18]$ GeV/c, $[2, 4.2]$ and $[2, 4.2]$ for the variable $p_T(D^0)$, $\eta(D^0)$ and $\eta(\pi^+_{tag})$, respectively, in the second step of the weighting. The baseline binning scheme is highlighted in grey.

N_{bins}								$\Delta Y_{K^-\pi^+}$ $[10^{-4}]$	
$\theta_x(\pi^+_{tag})$	$\theta_y(\pi^+_{tag})$	$k(\pi^+_{tag})$	tot$_1$ $[10^3]$	$p_T(D^0)$	$\eta(D^0)$	$\eta(\pi^+_{tag})$	tot$_2$ $[10^3]$	π^+_{tag} weighting	(π^+_{tag}, D^0) weighting
18	14	20	5	16	12	11	2	-1.09 ± 0.52	-0.02 ± 0.52
25	19	28	13	23	18	16	7	-0.42 ± 0.52	0.24 ± 0.52
36	27	40	39	32	25	22	18	-0.63 ± 0.52	0.20 ± 0.52
51	38	57	110	45	35	31	49	-0.71 ± 0.52	0.21 ± 0.52
72	54	80	311	64	50	44	141	-0.90 ± 0.52	0.13 ± 0.52
102	76	113	876	91	71	62	401	-0.74 ± 0.52	0.18 ± 0.52
144	108	160	2488	120	100	88	1056	-0.84 ± 0.52	0.12 ± 0.52

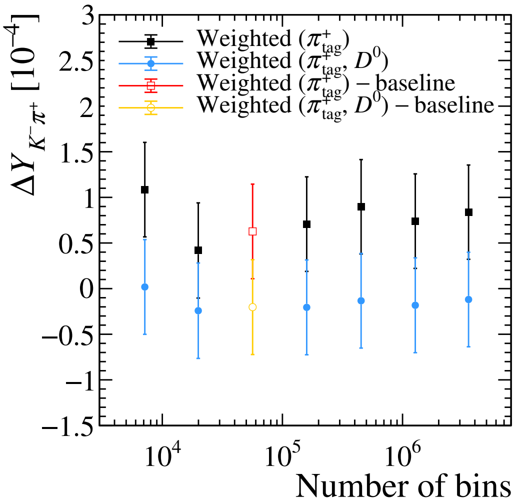

Figure 7.6: Measurements of $\Delta Y_{K^-\pi^+}$ as a function of the number of bins employed in the kinematic weighting. The definition of the binnings is provided in Table 7.2.

after the removal of the $m(D^0\pi^+_{tag})$ background. However, misreconstructed charm-hadron decays are not removed and contaminate the dataset in the $m(h^+h^-)$ signal window. Their number and asymmetry must be assessed to estimate how much they bias the measurement.

The most important backgrounds in the range $m(h^+h^-) \in [1750, 2010]$ MeV/c^2 are listed in Table 7.3. Their $m(h^+h^-)$ distributions are studied using the RapidSim application [176]. This is a fast-simulation package which employs as input the heavy-quarks momentum distributions from the FONLL program [177], decays the heavy hadrons using EvtGen [167], and simulates the final state radiation (FSR) with Photos [168]. Finally, it applies geometrical-acceptance requirements and smears parametrically the momenta, vertex position and IPs of the particles based on the performance of the LHCb experiment. The EvtGen models used in generation are listed in Table 7.3, while the requirements used to emulate the trigger are listed in Table 7.4.

The selection efficiency of the PID requirements on the two D^0-meson final-state particles is not simulated by RapidSim. On the contrary, it is calculated as a function of momentum and of pseudorapidity with the data-driven approach described in Ref. [178], which relies on large calibration data with self-tagged decays (like $J/\psi \to \mu^+\mu^-$ for muons). These PID efficiencies are displayed for all relevant particle types in Appendix E.2.

The $m(D^0\pi^+_{\rm tag})$ and $m(h^+h^-)$ distributions of all decays listed in Table 7.3 are plotted, together with their expected relative normalisations, in Fig. 7.8. Since for $D_s^+ \to K^-K^+\pi^+$ and $D_s^+ \to \pi^+\pi^-\pi^+$ decays the values of the invariant masses $m(h^+h^-)$ and $m(D^0\pi^+_{\rm tag})$ are linearly anticorrelated, as shown in Fig. 7.9, the mean of the $m(h^+h^-)$ Gaussian peak shifts as a function of the value of $m(D^0\pi^+_{\rm tag})$ and the removal of the $m(D^0\pi^+_{\rm tag})$ background introduces a negative peak on the left of the one corresponding to the $m(D^0\pi^+_{\rm tag})$ signal window in Fig. 7.8 (bottom). The most important backgrounds in the $m(h^+h^-)$ signal window are three-body decays of D mesons, where one particle is not reconstructed, but the misidentification of another particle with one of larger mass compensates for the loss of invariant mass due to the unreconstructed particle. Typical cases are those of an unreconstructed neutrino or π^0 meson, and the identification of a pion as a kaon meson, or of a lepton as a pion or kaon meson.

The fraction of background decays in the $m(h^+h^-)$ signal window is measured with a template fit to the time-integrated $m(h^+h^-)$ distributions. Describing the signal PDF with high accuracy is fundamental to guarantee the reliability of the results, since signal candidates are much more numerous than most background components also outside of the $m(h^+h^-)$ signal window. Therefore, the resolution tails of the signal and signal events with FSR cannot be parametrised by using data-driven models, but must be estimated based on simulation.

The signal PDF is modelled as follows. The RapidSim simulation is used to determine the

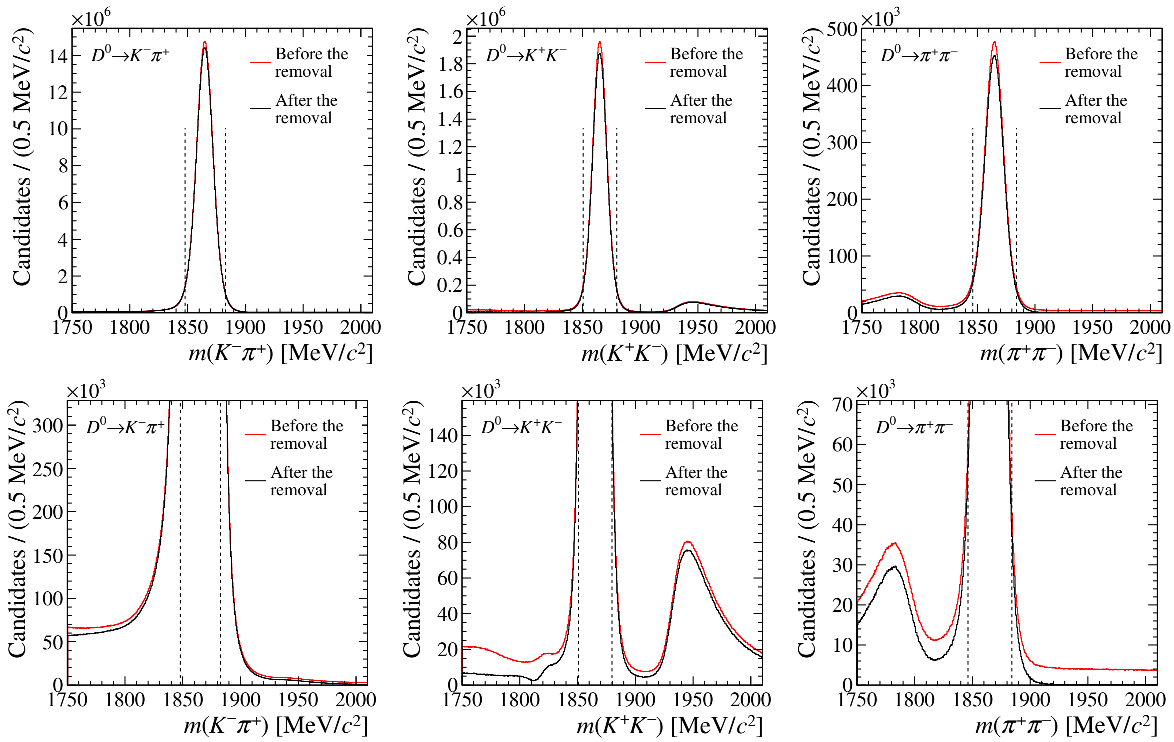

Figure 7.7: (Top): distribution of the invariant mass $m(h^+h^-)$ of the final-state particles of the D^0-meson candidate (red) before and (black) after the removal of the $m(D^0\pi^+_{\rm tag})$ background. The vertical dashed lines delimit the signal window. (Bottom): Magnification to put in evidence the shape of the residual background under the $m(D^0)$ peak.

Table 7.3: Decays of charmed hadrons whose $m(h^+h^-)$ distribution overlaps with the $[1750, 2010]\,\mathrm{MeV}/c^2$ range, when reconstructed as (top) $D^0 \to K^-\pi^+$, (centre) $D^0 \to K^+K^-$ and (bottom) $D^0 \to \pi^+\pi^-$ decays. The main origin of the candidates is either the $D^{*+} \to D^0\pi^+_{\mathrm{tag}}$ decay ($\mathcal{B} = 68\%$), or the pp collision. The EvtGen model used to generate the decays and the number of generated events are displayed in the fourth and fifth column (D^{*+} decays are always simulated using the `VSS` model). In the last column, $p_1 \to p_2$ indicates that the particle p_1 is reconstructed with the particle identity p_2, possible causing a suppression of the selection efficiency owing to the PID requirements ("PID-suppr."). Both unreconstructed particles ("not rec.") or the wrong identification of the D_s^+ as a D^{*+} meson produce a suppression of the selection efficiency due to kinematic selection requirements ("kin.-suppr.").

Decay	$\mathcal{B}$ (%)	Origin	Model	N_{gen}	Notes
$D^0 \to K^-\pi^+$	3.9	D^{*+}	`PHSP`	130M	–
$D^0 \to K^-\mu^+\nu_\mu$	3.4	D^{*+}	`ISGW2`	500M	$\mu^+ \to \pi^+$, ν_μ not rec. (kin.-suppr.)
$D^0 \to K^-e^+\nu_e$	3.5	D^{*+}	`ISGW2`	500M	$e^+ \to \pi^+$, ν_e not rec. (kin.-suppr.)
$D^0 \to K^+K^-$	0.41	D^{*+}	`PHSP`	100M	$K^+ \to \pi^+$ (PID-suppr.)
$D^0 \to \pi^+\pi^-$	0.15	D^{*+}	`PHSP`	100M	$\pi^- \to K^-$ (PID-suppr.)
$D^0 \to \pi^-\pi^+\pi^0$	1.5	D^{*+}	`D_DALITZ`	300M	$\pi^- \to K^-$ (PID-suppr.), π^0 not rec. (kin.-suppr.)
$D^0 \to K^+K^-$	0.41	D^{*+}	`PHSP`	100M	–
$D^0 \to K^-\pi^+$	3.9	D^{*+}	`PHSP`	130M	$\pi^+ \to K^+$ (PID-suppr.)
$D^0 \to K^-\pi^+\pi^0$	14.4	D^{*+}	`D_DALITZ`	300M	$\pi^+ \to K^+$ (PID-suppr.), π^0 not rec. (kin.-suppr.)
$D_s^+ \to K^-K^+\pi^+$	5.4	pp	`D_DALITZ`	300M	D_s^+ rec. as D^{*+} (kin.-suppr.)
$D^0 \to K^-\mu^+\nu_\mu$	3.3	D^{*+}	`ISGW2`	500M	$\mu^+ \to K^+$ (PID-suppr.), ν_μ not rec. (kin.-suppr.)
$D^0 \to K^-e^+\nu_e$	3.5	D^{*+}	`ISGW2`	500M	$e^+ \to K^+$ (PID-suppr.), ν_e not rec. (kin.-suppr.)
$D^0 \to \pi^+\pi^-$	0.15	D^{*+}	`PHSP`	100M	–
$D^0 \to K^-\pi^+$	3.9	D^{*+}	`PHSP`	130M	$K^- \to \pi^-$ (PID-suppr.)
$D^0 \to \pi^-\mu^+\nu_\mu$	0.27	D^{*+}	`ISGW2`	800M	$\mu^+ \to \pi^+$, ν_μ not rec. (kin.-suppr.)
$D^0 \to \pi^-e^+\nu_e$	0.29	D^{*+}	`ISGW2`	800M	$e^+ \to \pi^+$, ν_e not rec. (kin.-suppr.)
$D_s^+ \to \pi^+\pi^-\pi^+$	1.8	pp	`D_DALITZ`	300M	D_s^+ rec. as D^{*+} (kin.-suppr.)

FSR distribution by selecting only events satisfying $m_{\mathrm{true}}(h^+h^-) < m(D^0) - 0.5\,\mathrm{MeV}/c^2$ and by fitting them with an empirical function, as shown in Fig. 7.10 (left). Then, the fitted shape is

Table 7.4: Selection requirements for the data simulated with the RapidSim application.

Variable	Requirement	Unit
$p(h^\pm)$	$\in [5, 120]$	GeV/c
$p_{\mathrm{T}}(h^\pm)$	$\in [0.8, 12]$	GeV/c
$\eta(h^\pm)$	$\in [2, 4.2]$	–
$\mathrm{IP}(h^\pm)$	> 30	µm
$p_{\mathrm{T}}(D^0)$	> 2	GeV/c
$\mathrm{FD}(D^0)$	> 0.8	mm
$\theta_{\mathrm{DIRA}}(D^0)$	< 17.3	mrad
$\mathrm{IP}(D^0)$	< 200	µm
$R_{xy}(D^0)$	< 4	mm
$p(\pi^+_{\mathrm{tag}})$	$\in [1, 16]$	GeV/c
$p_{\mathrm{T}}(\pi^+_{\mathrm{tag}})$	$\in [0.2, 1.4]$	GeV/c
$\eta(\pi^+_{\mathrm{tag}})$	$\in [2, 4.2]$	–

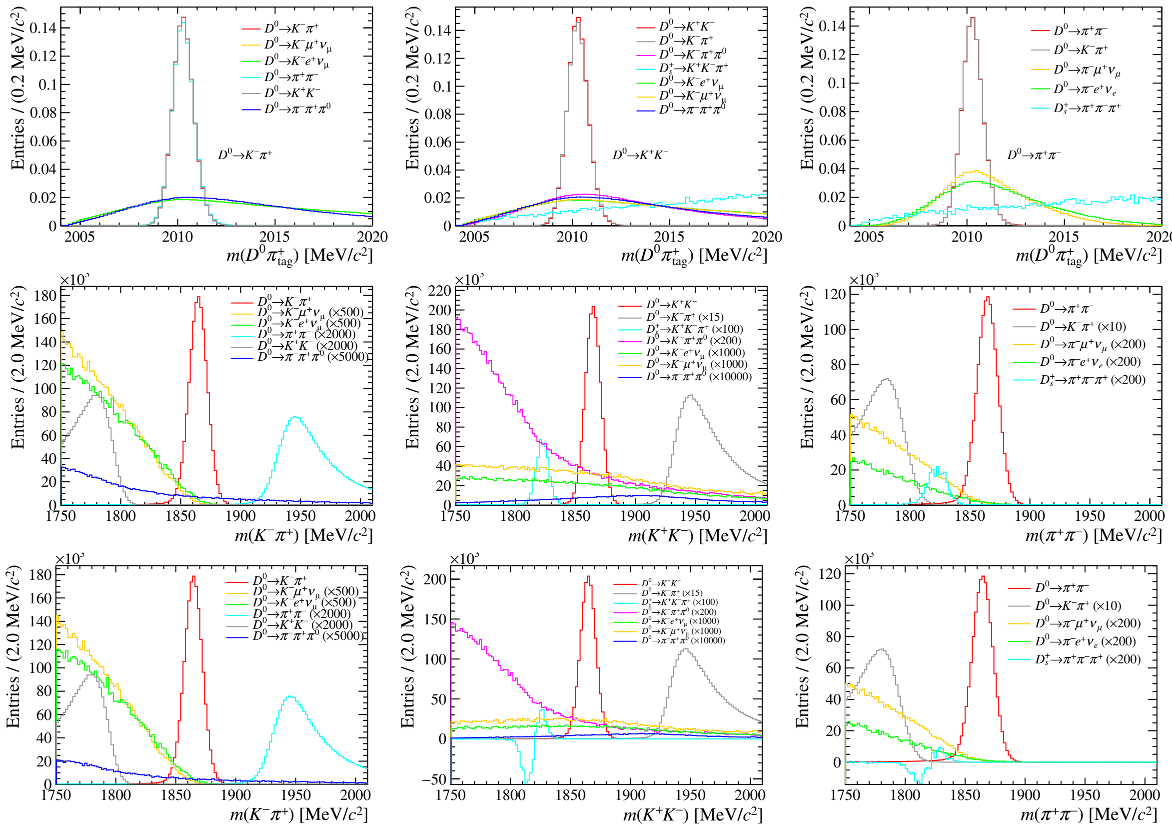

Figure 7.8: RapidSim distributions of (top) $m(D^0\pi^+_{\rm tag})$, (centre) $m(h^+h^-)$ of the candidates in the $m(D^0\pi^+_{\rm tag})$ signal window and (bottom) $m(h^+h^-)$ of the selected candidates after the removal of the $m(D^0\pi^+_{\rm tag})$ background, for all signal and background decays listed in Table 7.3. For the $m(h^+h^-)$ plots, the normalisations relative to the signal component are shown in the legend, using the D_s^+–to–D^{*+} cross-section ratio from Ref. [124]. Left, centre and right plots correspond to the $K^-\pi^+$, K^+K^- and $\pi^+\pi^-$ decay channels.

convolved with a resolution function composed by four Gaussian functions with shared mean. The resulting PDF for the $K^-\pi^+$ decay channel is fitted to the simulated sample of primary decays described in Sect. 4.6, filtered by requiring that neither of the D^0-meson final-state particles is identified as a muon (the decay in flight of the hadrons into muons is taken into account later). This sample comprises a lower number of candidates with respect to the RapidSim one, but reproduces the experimental resolution much more accurately. The results of the fit are shown in Fig. 7.11. The resolution function is then fixed to the results of this fit for all D^0-meson signal decay channels, apart from the mean and a global scale factor shared by all of the four Gaussian functions, which are left free to vary. These free parameters take into account both possible biases on the $m(h^+h^-)$ mass, since the Kalman filter used in the tracking parametrises the loss of energy due to the interactions of particles with the detector by using a pion hypothesis for both pion and kaon mesons, and for different resolutions for the three decay channels, owing to different emission angles and momenta of the D^0-meson final-state particles which are caused by different PID requirements and decay Q-values.

Additional resolution tails are due to candidates for which either of the D^0 daughter hadrons decayed in flight into a muon before exiting the magnetic field. The $m(h^+h^-)$ distribution of

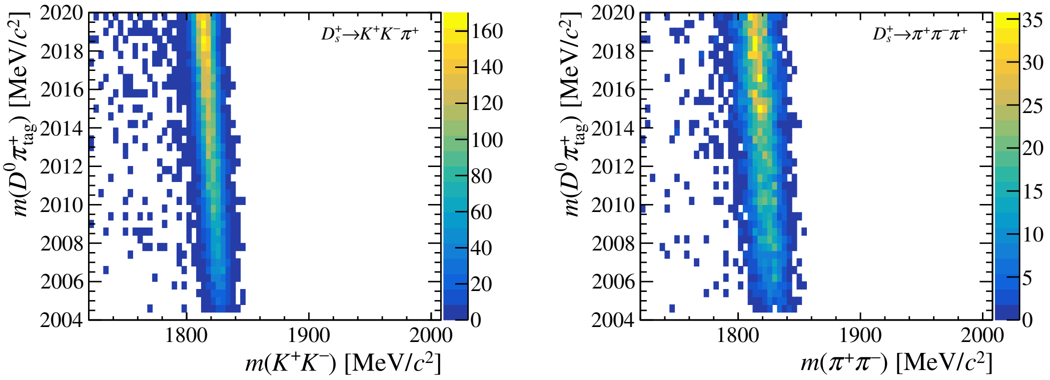

Figure 7.9: (Left) Distribution of $D_s^+ \to K^+K^-\pi^+$ decays in the $m(D^0\pi^+_{\rm tag})$-*versus*-$m(K^+K^-)$ plane, when they are reconstructed as $D^0 \to K^+K^-$ candidates coming from a $D^{*+} \to D^0\pi^+_{\rm tag}$ decay. (Right) Distribution of $D_s^+ \to \pi^+\pi^-\pi^+$ decays in the $m(D^0\pi^+_{\rm tag})$-*versus*-$m(\pi^+\pi^-)$ plane, when they are reconstructed as $D^0 \to \pi^+\pi^-$ candidates coming from a $D^{*+} \to D^0\pi^+_{\rm tag}$ decay.

these candidates is estimated based on the simulation of $D^0 \to K^-\pi^+$ decays, by analysing only candidates where the π^+ or K^- meson has passed through all of the muon stations and is

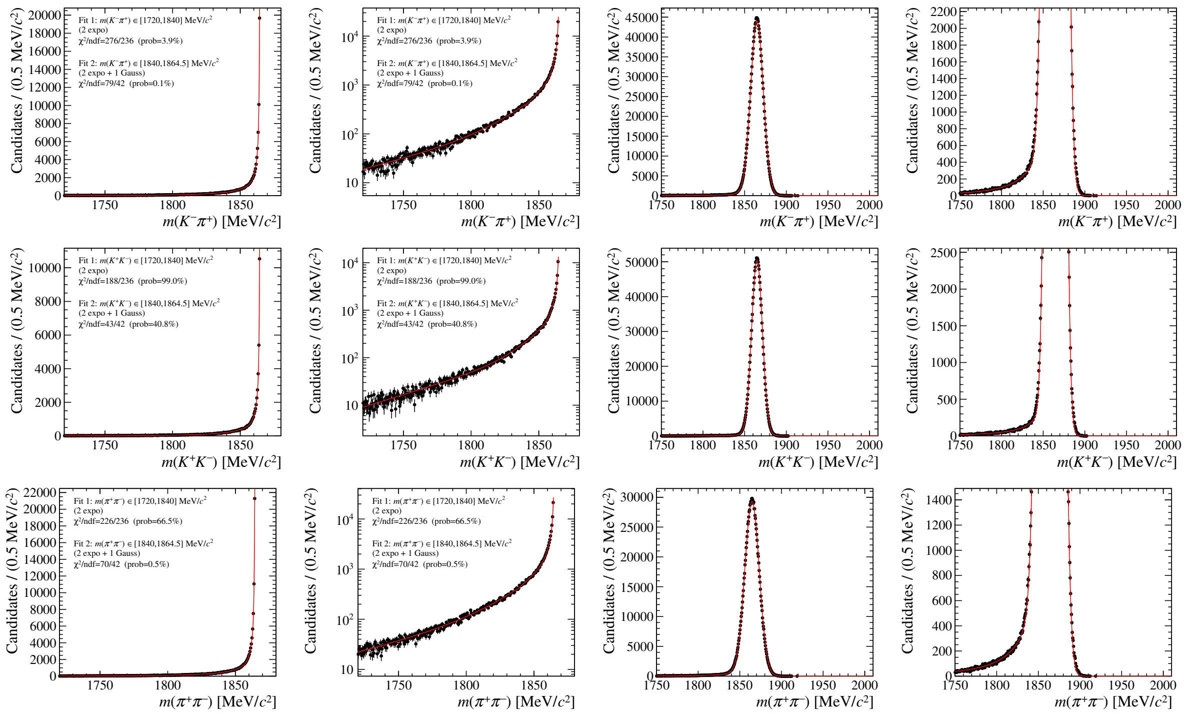

Figure 7.10: Fits to the RapidSim $m(h^+h^-)$ signal distribution for events with FSR, in (left) linear and (centre-left) logarithmic scale. The true values of the momenta are used and only events more distant than 0.5 MeV/c^2 from the D^0-meson mass peak are taken into account. Centre-right and right plots display the cross-check fit where the FSR distributions is fixed to that obtained in the left plot, is convolved with a Gaussian resolution function and is compared with the RapidSim distribution (calculated using smeared momenta) of all data, including candidates without FSR. Top, centre and bottom plots correspond to the $K^-\pi^+$, K^+K^- and $\pi^+\pi^-$ decay channels.

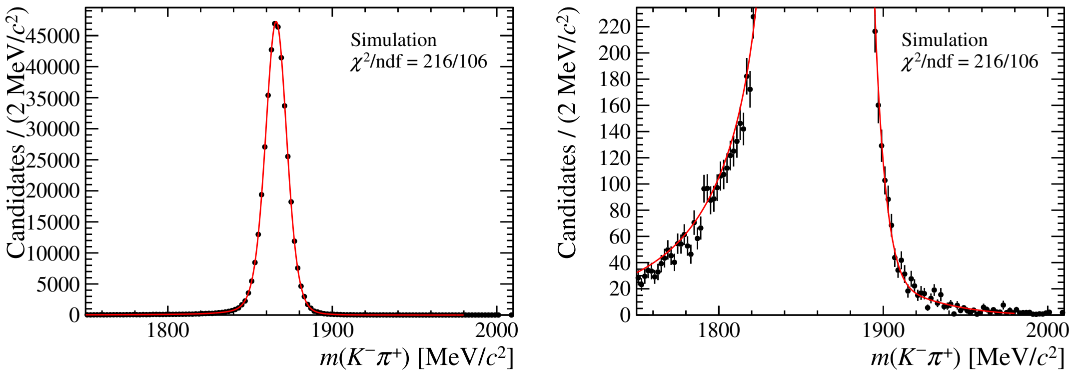

Figure 7.11: (Left) Result of the fit of the resolution to the distribution of simulated $m(K^-\pi^+)$ decays, where both K^- and π^+ candidates are required not to pass through all of the muon chambers. The shape of the FSR is fixed to that obtained in the fit to the RapidSim simulation in Fig. 7.10, and only the resolution function, parametrised as the sum of four Gaussian functions with shared mean, is left free to vary. (Right) Magnification of the left plot.

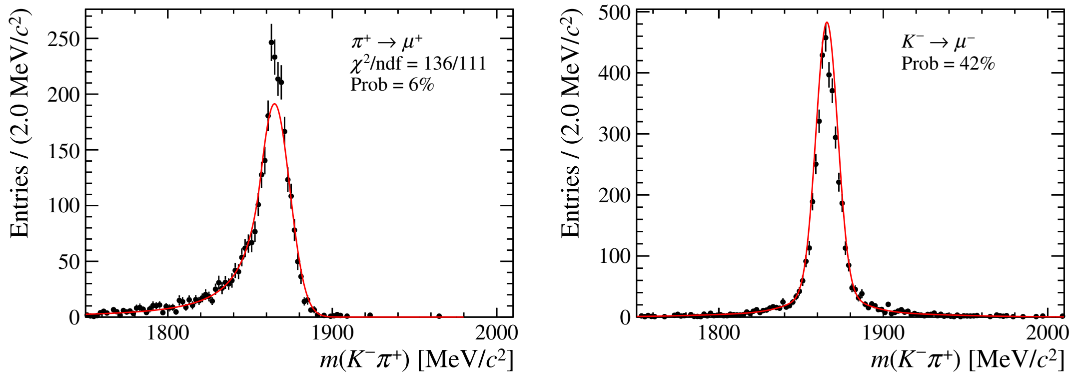

Figure 7.12: Fits to the mass distribution of simulated $D^0 \to K^-\pi^+$ decays, where the (left) π^+ meson and (right) K^- meson pass through all of the muon stations and are thus identified as muons.

thus identified as a muon, which are around 0.72% and 1.04% of the total, respectively. The corresponding $m(h^+h^-)$ distributions are plotted in Fig. 7.12. Owing to the low Q-value of the $\pi^+ \to \mu^+\nu_\mu$ decay, the direction of the μ^+ lepton essentially coincides with that of the π^+ meson and its momentum is dominated by the boost factor of the π^+ meson in the laboratory frame. Therefore, the measured momentum of the π^+ meson is typically smaller than the true one, resulting in a long left tail of the $m(h^+h^-)$ distribution. This distribution is fitted with a Crystal ball function [179] as shown in Fig. 7.12 (left). On the other hand, the $K^- \to \mu^-\overline{\nu}_\mu$ decay has a much higher Q-value and the momentum of the μ^- meson can differ significantly from that of the K^- meson. As a consequence, the measured momentum of the K^- meson can be both larger or smaller than the true one, corresponding to tails on both sides of the D^0-meson mass peak.Therefore, the mass distribution of these candidates is fitted with the sum of two Gaussian functions with shared mean, as shown in Fig. 7.12 (right). In the template fit to the data, the shapes of both decay-in-flight components and the fraction of the signal PDF described by them are fixed to those obtained in the fits to simulated $D^0 \to K^-\pi^+$ decays.

As far as the PDFs of the background components are concerned, they are fixed to the templates obtained with RAPIDSIM. Since the $m(h^+h^-)$ templates of the background channels with a μ^+ and a e^+ lepton in the final state are nearly degenerate, their ratio is always fixed to expectations from simulation. Finally, the $D_s^+ \to \pi^+\pi^-\pi^+$ decay is not included in the $D^0 \to \pi^+\pi^-$ fit, and the $D^0 \to \pi^-\pi^+\pi^0$ background is not included in the $D^0 \to K^-\pi^+$ nor in the $D^0 \to K^+K^-$ fit, since they are negligible with respect to all other backgrounds, as shown in Fig. 7.8 (bottom). The overall agreement between the expected normalisations of the background components and data is reported in Fig. E.4, corresponding to a fit where the relative normalisation of all backgrounds with respect to the signal are fixed to the expectations and only the mean and width of the signal resolution and the overall normalisation of the total PDF are fitted to data. In the baseline fits used to estimate the systematic uncertainty, few more parameters are left free to vary in order to improve the agreement.

For the $D^0 \to K^-\pi^+$ sample, while the relative normalisation of the $D^0 \to K^+K^-$ background with respect to the signal is fixed to expectations given its smallness and the complexity of extracting its normalisation from the fit, the normalisations of the $D^0 \to \pi^+\pi^-$ background and of the sum of $D^0 \to K^-e^+\nu_e$ and $D^0 \to K^-\mu^+\nu_\mu$ decays are left free to vary. The projections of the fit are shown in Fig. 7.13 (left). The fitted normalisation of the $D^0 \to K^-\ell^+\nu_\ell$ ($D^0 \to \pi^+\pi^-$) templates is larger by a factor of 1.06 (1.12) with respect to expectations. The largest contamination in the signal region is due to $D^0 \to K^-\ell^+\nu_\ell$ decays and is equal to $(2.5 \pm 0.1) \times 10^{-4}$, where only the statistical uncertainties of the templates and of the fitted normalisation are considered.

In the fit to the K^+K^- sample, whose projection is shown in Fig. 7.13 (centre), the normalisation of the $D^0 \to K^-\ell^+\nu_\ell$ backgrounds is fixed to expectations, while the normalisations of all other backgrounds are left free to vary. This ensures that the normalisation of $D^0 \to K^-\ell^+\nu_\ell$ backgrounds is not artificially increased to improve the agreement of the fit with data in the range $m(K^+K^-) \in [1910, 1925]\,\mathrm{MeV}/c^2$, where the discrepancies are likely due to a poor reproduction of the $D^0 \to K^-\pi^+$ left tail (a fit where this constraint is removed is shown in Fig. E.5 in Appendix E.3). The fitted normalisation of the $D^0 \to K^-\pi^+\pi^0$, $D_s^+ \to K^+K^-\pi^+$ and $D^0 \to K^-\pi^+$ templates are equal to 0.84, 0.65, and 1.19 times the expectations, respectively. The largest contaminations in the signal region are due to $D^0 \to K^-\pi^+\pi^0$, $D^0 \to K^-\ell^+\nu_\ell$ and $D^0 \to K^-\pi^+$ decays and amount to $(8.2 \pm 0.1) \times 10^{-4}$, $(3.7 \pm 0.1) \times 10^{-4}$ and $(2.3 \pm 0.1) \times 10^{-4}$, respectively, where only the statistical uncertainties of the templates and of the fitted normalisations are considered.

Finally, in the fit to the $\pi^+\pi^-$ sample, whose results are shown in Fig. 7.13 (right), the normalisation of the $D^0 \to K^-\pi^+$ backgrounds is free to vary, while that of $D^0 \to \pi^-\ell^+\nu_\ell$ background events is fixed to expectations. This ensures that the normalisation of $D^0 \to \pi^-\ell^+\nu_\ell$ backgrounds is not artificially increased to improve the agreement of the fit with data in the range $m(\pi^+\pi^-) \in [1800, 1825]\,\mathrm{MeV}/c^2$, where the discrepancies are likely due to a poor reproduction of the $D^0 \to K^-\pi^+$ right tail (a fit where this constraint is removed is shown in Fig. E.5 in Appendix E.3). The fitted normalisation of the $D^0 \to K^-\pi^+$ background is equal to 1.02 times its expectations. The only background contamination in the signal region is due to $D^0 \to \pi^-\ell^+\nu_\ell$ decays and amounts to $(2.6 \pm 0.1) \times 10^{-4}$, where only the statistical uncertainties of the templates and of the fitted normalisation are considered.

The contribution of the background decays to the total time-dependent asymmetry in the

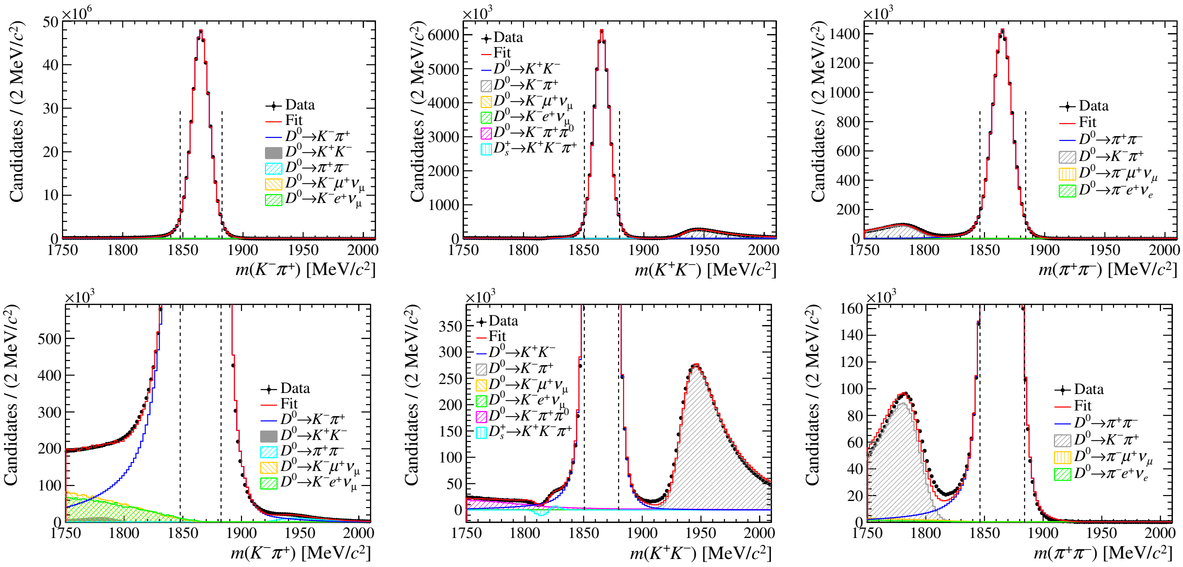

Figure 7.13: Nominal template fit to the time and flavour integrated $m(h^+h^-)$ distributions of (left) $K^-\pi^+$, (centre) K^+K^- and (right) $\pi^+\pi^-$ decays. Bottom plots are magnified to put the background components in evidence.

$m(h^+h^-)$ signal window is equal to

$$\begin{aligned} A_{\text{tot}}(t) &= A_{\text{sig}}(t) + \sum_{\text{bkg}} f_{\text{bkg}}(t)[A_{\text{bkg}}(t) - A_{\text{sig}}(t)] \\ &\approx A_{\text{sig}}(t) + \sum_{\text{bkg}} f_{\text{bkg}}(t) A_{\text{bkg}}(t) \end{aligned} \tag{7.1}$$

where the sum runs over all background components, $A_{\text{sig}}(t)$ ($A_{\text{bkg}}(t)$) is the asymmetry of the signal (of the background component "bkg") in the signal window, $f_{\text{bkg}}(t)$ is the fraction of background decays in the signal window, and in the last passage the signal asymmetry is neglected since all background fractions are less than 1×10^{-3} and the signal asymmetry is much smaller than 1% after the kinematic weighting (*cf.* Figs. 6.12 and 9.1). Expanding both the background asymmetries and fractions to linear order in decay time,

$$A_{\text{bkg}}(t) \approx A^0_{\text{bkg}} + A^1_{\text{bkg}} \frac{t}{\tau_{D^0}}, \qquad f_{\text{bkg}}(t) \approx f^0_{\text{bkg}} + f^1_{\text{bkg}} \frac{t}{\tau_{D^0}}, \tag{7.2}$$

the total asymmetry can be written as

$$A_{\text{tot}}(t) \approx A_{\text{sig}}(t) + \sum_{\text{bkg}} f^0_{\text{bkg}} A^0_{\text{bkg}} + \sum_{\text{bkg}} [f^0_{\text{bkg}} A^1_{\text{bkg}} + f^1_{\text{bkg}} A^0_{\text{bkg}}] \frac{t}{\tau_{D^0}}, \tag{7.3}$$

and the corresponding bias on the measurement of ΔY is approximately equal to

$$\Delta(\Delta Y) \approx \sum_{\text{bkg}} [f^0_{\text{bkg}} A^1_{\text{bkg}} + f^1_{\text{bkg}} A^0_{\text{bkg}}]. \tag{7.4}$$

In order to estimate its size, the time-dependent fractions of all background components are calculated based on the RapidSim distributions of $m(h^+h^-)$ *vs.* $t(D^0)$, and on the time-integrated relative normalisation between the background and the signal decays obtained in the time-integrated fits to the $m(h^+h^-)$ distributions. The plots of the time-dependent fractions are shown in Appendix E.3, while the results of the linear fits are summarised in Table 7.5. Owing to the approximate emulation of the candidates selection in RapidSim, the time distributions of RapidSim signal candidates and data agree only within 20% both at low and high decay times, as shown in Fig. E.9 in Appendix E.3. Therefore, assuming conservatively that a relative uncertainty of similar size affects also the backgrounds, but the effects do not cancel completely in the ratio, the uncertainty on f_0 is set to the sum in quadrature of the fit uncertainty and $20\% \times \sqrt{2} \approx 28\%$ of the value of the time-integrated fraction $\langle f \rangle$, and the uncertainty on f_1 is set to the sum in quadrature of the fit uncertainty and $40\% \times \sqrt{2}/5.4 = 10\%$ of $\langle f \rangle$, where 40% is the difference of the bias on $f(t)$ at large and low decay times and 5.4 is the difference between the average decay time of the last and first decay-time bins.

The background asymmetries are calculated from $m(h^+h^-)$ data lateral windows. For each background, it is assumed that the value of the asymmetry does not depend on the value of $m(h^+h^-)$. Moreover, the asymmetry of semileptonic backgrounds is measured without distinguishing between them, that is making the assumption that the asymmetry of semimuonic or semipositronic decays are equal or, alternatively, that the ratio of their candidates number in the signal and lateral window is equal. Furthermore, the asymmetry of the signal decays is neglected, since its time-integrated asymmetry is equal to zero by construction due to the kinematic weighting and its slope is known to be less than the current world average of ΔY, which is compatible with zero within 0.02%. The plots of the time-dependent asymmetry in the lateral windows are displayed in Appendix E.3.

For the $K^-\pi^+$ sample, the asymmetry of the $D^0 \to K^-\ell^+\nu_\ell$ background is measured in the window $[1750, 1780]\,\mathrm{MeV}/c^2$, where the fraction of $D^0 \to K^-\ell^+\nu_\ell$ decays is about 69%. The contribution to the asymmetry from the $D^0 \to K^+K^-$ background component is neglected, since its fraction is less than 4%, and the asymmetry of the $D^0 \to K^-\ell^+\nu_\ell$ background is calculated as the measured asymmetry divided by the fraction of $D^0 \to K^-\ell^+\nu_\ell$ decays in each decay time bin. The fit to the measured asymmetry is shown in Fig. E.10 (Appendix E.3).

For the K^+K^- sample, the asymmetry of the $D^0 \to K^-\pi^+$ background component is measured in the window $[1920, 1970]\,\mathrm{MeV}/c^2$, where the fraction of $D^0 \to K^-\pi^+$ decays is around 99%. Therefore, no corrections are applied to take into account the contribution to the asymmetry from other negligible background decays. The asymmetry of the $D^0 \to K^-\pi^+\pi^0$ background component is measured in the sideband $[1750, 1780]\,\mathrm{MeV}/c^2$, where its fraction is 76%, while 20% of the events are given by $D^0 \to K^+K^-$ decays and only 4% by $D^0 \to K^-\ell^+\nu_\ell$ candidates. Therefore, it is measured as the total asymmetry in each decay time bin, divided by the corresponding measured fraction of $D^0 \to K^-\pi^+\pi^0$ decays — without corrections for the contributions to the asymmetry of other backgrounds. The fits to the measured asymmetries are shown in Fig. E.11 (Appendix E.3). Finally, the asymmetry of the $D^0 \to K^-\ell^+\nu_\ell$ background, whose fraction is subdominant over the whole the $m(K^+K^-)$ analysed range, is conservatively estimated to be $A^0_{K^-\ell^+\nu_\ell} < 2\%$ and $A^1_{K^-\ell^+\nu_\ell} < 1\%$, which are the maximum values of the asymmetries in all other decay channels. This conservative hypothesis is further motivated by the size of the measured asymmetry of the same background in the $D^0 \to K^-\pi^+$ decay channel (where, however, the ℓ^+ is reconstructed as a π^+ meson and not a K^+ meson), which is smaller.

Also in the $\pi^+\pi^-$ sample the asymmetry of the $D^0 \to \pi^-\ell^+\nu_\ell$ background component cannot be measured from data due to its tiny fraction over the whole $m(\pi^+\pi^-)$ analysed range, although it is probably equal to that of the $D^0 \to K^-\ell^+\nu_\ell$ decay channel in the $K^-\pi^+$ sample — the mis-ID for the two background decays is the same. The size of the systematic uncertainty is conservatively estimated using an upper bound on A^0 and A^1 equal to 2% and 1%, respectively,

Table 7.5: Intercept and slope of the linear fits to the fraction and asymmetry of the $m(h^+h^-)$ background components for the (top) $K^-\pi^+$, (centre) K^+K^- and (bottom) $\pi^+\pi^-$ decay channels. The last two columns display the two terms that cause the bias on ΔY.

Decay channel	f_0 [10^{-3}]	f_1 [10^{-3}]	A_0 [%]	A_1 [%]	f_0A_1 [10^{-4}]	f_1A_0 [10^{-4}]
$D^0 \to K^-\ell^+\nu_\ell$	0.24 ± 0.07	0.00 ± 0.06	0.37 ± 0.18	-0.06 ± 0.09	0.00 ± 0.00	0.00 ± 0.00
$D^0 \to K^-\pi^+\pi^0$	0.71 ± 0.23	0.05 ± 0.09	-1.8 ± 0.7	0.5 ± 0.4	0.04 ± 0.03	-0.01 ± 0.02
$D^0 \to K^-\pi^+$	0.21 ± 0.07	0.00 ± 0.03	-0.94 ± 0.09	0.02 ± 0.04	0.00 ± 0.00	0.00 ± 0.00
$D^0 \to K^-\ell^+\nu_\ell$	0.34 ± 0.11	0.01 ± 0.04	< 2	< 1	< 0.03	< 0.01
$D^0 \to \pi^-\ell^+\nu_\ell$	0.27 ± 0.08	-0.01 ± 0.03	< 2	< 1	< 0.03	< 0.01

in analogy to what is done in the $D^0 \to K^+K^-$ sample for the $D^0 \to K^-\ell^+\nu_\ell$ background component.

All estimated values of A^0 and A^1 are summarised in Table 7.5. The same table reports also the values of the estimated biases on ΔY. These are equal to $(0.00 \pm 0.00) \times 10^{-4}$, $(-0.05 \pm 0.04) \times 10^{-4}$ and $(0.00 \pm 0.03) \times 10^{-4}$ for the $K^-\pi^+$, K^+K^- and $\pi^+\pi^-$ decay channels, respectively. The systematic uncertainty is estimated as the sum in quadrature of the value and uncertainty of the bias, and amounts to 0.00×10^{-4}, 0.06×10^{-4} and 0.03×10^{-4} for the $K^-\pi^+$, K^+K^- and $\pi^+\pi^-$ decay channels, respectively. These uncertainties are smaller by around a factor of 10 than the conservative systematic uncertainty assigned to the same effect in the ΔY measurement with D^{*+}-tagged data collected during 2011–2012 [114, 174].

7.6 Decay time resolution

The decay time resolution measured in simulation is equal to $\sigma_t \approx 0.11\tau_{D^0} \approx 43\,\text{fs}$, as shown in Fig. 7.14 (left). In particular, it varies moderately as a function of decay time, increasing from $0.088\,\tau_{D^0}$ in the first decay-time bin to $0.113\,\tau_{D^0}$ in the last one. Owing to its small value with respect to the D^0-meson lifetime, it is expected to have a negligible impact on the measurement of ΔY, namely a slight dilution of its measured value (at least to first order). For comparison, in the measurement with the μ^--tagged sample collected during 2016–2018 by the LHCb experiment, where the decay-time resolution was larger by a factor of 2.5, the dilution was 5.7% [118].

The size of the dilution is estimated through 1000 simulated experiments where a sample of 80 million candidates, whose number is equal to the sum of the K^+K^- and $\pi^+\pi^-$ samples combined, is generated with a time-dependent asymmetry corresponding to ΔY^{inj} equal to $\{\pm 30,\ \pm 50\} \times 10^{-4}$. The decay time of each candidate is generated according to an exponential PDF convolved with a resolution function modelled by the sum of two Gaussian functions, which is fitted to the time-integrated resolution measured in simulation, as shown in Fig. 7.14 (left). Then, a time-dependent asymmetry is introduced with the same procedure used to estimate the dilution due to the kinematic weighting in Sect. 5.4. Finally, the candidates are filtered according to the decay-time acceptance, which is estimated based on the ratio of the observed decay-time distribution of $D^0 \to K^+K^-$ decays to an exponential function convolved with the decay time resolution. The resulting distribution is fitted through three `erf` functions plus the negative of an `erf` function, which models the decrease of the acceptance at large decay times, as shown in Fig. 7.14 (right). The distribution of the values of ΔY measured in the 1000 simulated

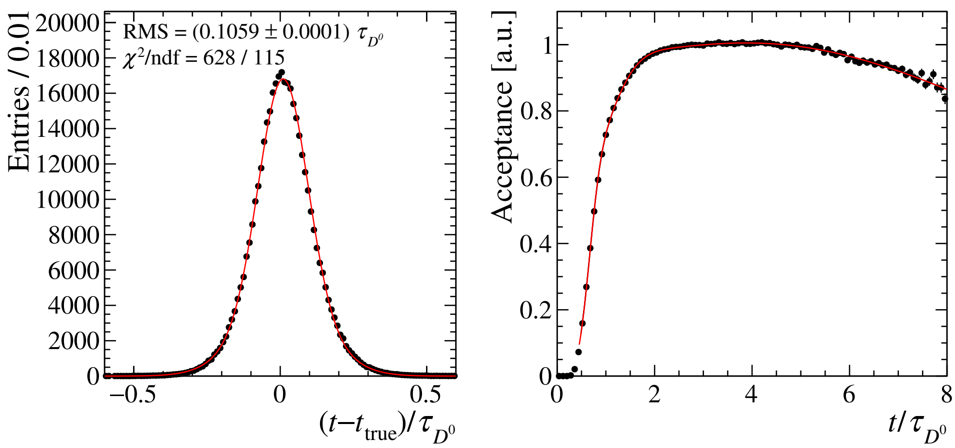

Figure 7.14: (Left) Decay-time resolution, as measured in the simulation of $D^0 \to K^-\pi^+$ decays. The result of a fit of the sum of two Gaussian functions is superimposed. (Right) Fit to the decay-time acceptance, defined as the ratio of the decay-time distribution of $D^0 \to K^+K^-$ data over an exponential function convolved with the resolution function fitted in the left plot.

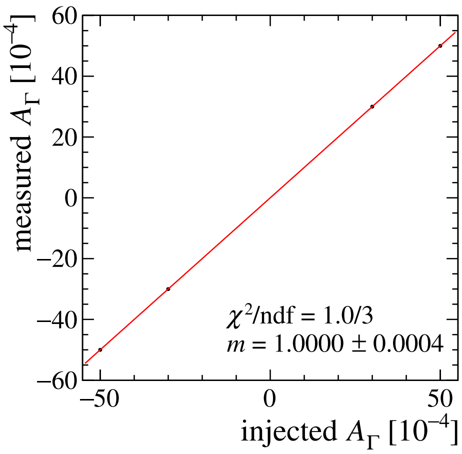

Figure 7.15: Average measured value of ΔY as a function of the injected one in 1000 simulated experiments set up to quantify the effect of the finite decay-time resolution on the measurement.

experiments produced at fixed injected asymmetry ΔY^{inj} is Gaussian, and its mean is used to estimate the size of the dilution.

The average measured value of ΔY is shown as a function of the injected one in Fig. 7.15. A linear fit is superimposed, where the intercept is fixed to zero and the slope is compatible with unity within 4×10^{-4}. Since the impact of the dilution on both the absolute value and the statistical uncertainty of ΔY are less than 0.01×10^{-4}, no correction is applied and no systematic uncertainty is assigned for this effect.

7.7 Summary

All systematic uncertainties discussed in the previous sections are summarised in Table 7.6. The total systematic uncertainty is equal to less than 20% of the statistical uncertainty for the signal channels, whereas it corresponds to around 45% of the statistical uncertainty for the $K^-\pi^+$ control channel.

Table 7.6: Summary of the systematic uncertainties. The statistical uncertainties are reported for comparison.

Systematic source	$\Delta Y_{K^-\pi^+}$ $[10^{-4}]$	$\Delta Y_{K^+K^-}$ $[10^{-4}]$	$\Delta Y_{\pi^+\pi^-}$ $[10^{-4}]$
Subtraction of the $m(D^0\pi^+_{\rm tag})$ background	0.12	0.24	0.34
Flavour dependent shift of $m(D^{*+})$ peak	0.14	0.14	0.14
Secondary decays	0.07	0.07	0.07
Kinematic weighting	0.05	0.05	0.05
$m(h^+h^-)$ background	0.00	0.06	0.03
Total systematic	0.2	0.3	0.4
Statistical	0.5	1.5	2.8

Chapter 8

Cross-checks

This chapter describes the cross-checks performed to confirm the reliability of the measurement. Since no significant trends are spotted in any of the cross-checks, no systematic uncertainties are assigned to the effects investigated.

8.1 Hidden variables

The nuisance asymmetries of Chap. 5 can depend on hidden variables in addition to those taken into account by the kinematic weighting of Sect. 5.2. Possible hidden variables are, for example, the L0 and first-stage software-trigger line and the position of the D^0 decay vertex in the VELO detector. If the nuisance asymmetries depend on these variables even after the kinematic weighting and these variables are correlated with the D^0 decay time, this might cause a bias to the measurement. In order to check the presence of possible large biases, the ΔY parameter is measured in data subsamples divided according to the value of the hidden variables that are expected to be most correlated with production or detection asymmetries, and to the value of the most important kinematic variables of the decay. In fact, it is possible that residual asymmetries become evident only for some particular values of such variables.

Each cross-check is performed as follows. First, the sample is subdivided into three bins based on the value of the hidden variable. The only exception regards the L0-trigger decision test, where two bins are employed, instead. Then, the samples are further divided according to the data-taking year and magnet polarity, since some detection asymmetries and the trigger configuration are known to depend on these variables as well. Finally, the time-dependent asymmetry is measured for each subsample by removing the $m(D^0\pi^+_{\text{tag}})$ background and by employing the kinematic weights taken from the baseline measurement, which does not divide the sample according to the value of the hidden variable.

The results of the tests for the kinematics of the D^0 and π^+_{tag} mesons and for the position of the D^0 decay vertex in the VELO are displayed in Figs. 8.1, 8.2 and 8.3 for the $K^-\pi^+$, K^+K^- and $\pi^+\pi^-$ decay channels, respectively. The results of the tests for the event occupancy, estimated through the number of reconstructed primary vertices or long tracks in the event, and for the L0 and first-stage software-trigger decisions, are displayed in Figs. 8.4, 8.5 and 8.6 for the $K^-\pi^+$, K^+K^- and $\pi^+\pi^-$ decay channels, respectively. For the $\pi^+\pi^-$ decay channel, the samples relative to some data-taking periods — in particular that corresponding to data collected during 2015 with the *MagUp* polarity — are extremely small, and for some values of the analysed variables some decay-time bins have no candidates. When this happens, these bins are not employed in the fits to the time-dependent asymmetry, resulting in large statistical uncertainties. In particular, in Fig. 8.3 the measurement performed with the data collected in 2015 with *MagUp* polarity and corresponding to the range $R_{xy} < 0.32\,\mathrm{mm}$ is not shown since its value, $(128 \pm 156) \times 10^{-4}$, lies outside of the y-axis range. However, it is used to calculate the p-value displayed on the same plot.

P-values less than 5% are obtained in the tests relative to the $\eta(D^0)$ and $\eta(\pi^+_{\rm tag})$ variables and to the L0 trigger decision for the $K^-\pi^+$ decay channel, and in the tests relative to the number of primary vertices and long tracks for the K^+K^- decay channel. The low p-value of the $\eta(D^0)$ test is attributed to residual asymmetries at $\eta(D^0) \geq 3.7$, which are not corrected for by the kinematic weighting. These asymmetries have opposite sign for opposite magnet polarities and cancel in the average between the two. In particular, the P-values of the χ^2/ndf of the average of $\Delta Y_{K^-\pi^+}$ in the three $\eta(D^0)$ bins are, from smaller to larger values of η, 77%, 17% and 0.03%, respectively. The average value in the bin $\eta(D^0) > 3.4$, which is responsible for the low global p-value, is $\Delta Y_{K^-\pi^+} = (0.32 \pm 0.92) \times 10^{-4}$. On the other hand, the p-value of the χ^2/ndf of the average of the three pseudorapidity bins is 83%, confirming the absence of significance trends as a function of $\eta(D^0)$ after the average between the samples collected with opposite magnet polarities. The conclusion for $\eta(\pi^+_{\rm tag})$, which is highly correlated with $\eta(D^0)$, is analogous.[1]

The low P-value in the L0-decision test is ascribed to different detection asymmetries related to different L0 requirements. The hadronic trigger efficiency might differ for the $K^-\pi^+$ and $K^+\pi^-$ final states, which are not self-conjugate. On the other hand, events where the D^0 did not fire the L0 hadron line — and in most cases particle other than the D^{*+}-meson final state particles are responsible of the L0 trigger decision or the D^0 meson fired a nonhadronic L0 line — are affected by detection asymmetries as well. In fact, the particles produced in the pp collision other than the D^{*+} meson contain a $\bar{c}$ quark which, for example, can decay into a μ^- but not into a μ^+ lepton. Analogously, also the D^0-meson trigger efficiency of nonhadronic trigger lines is expected to differ between the $K^-\pi^+$ and $K^+\pi^-$ final states. The hypothesis above is confirmed by the fact that the p-values of the averages of the sample where the D^0 meson fired the L0 hadron trigger line and of its complimentary are 30% and 42%, respectively,[2] whereas the p-value of their average is 0.005%. This incompatibility is a direct consequence of the fact that the kinematic weighting, whose weights are calculated based on the sum of the two samples, removes the asymmetries from the sum of the two samples, and not from each sample separately. However, since the measurement is performed by using the sum of the two samples, the observed incompatibility between them is not expected to bias the final measurement.

As a further check, the L0 cross-check test is repeated by calculating the kinematic weights separately for the two L0 requirements, to confirm that the kinematic weighting is able to remove the nuisance asymmetries when applied separately to the two samples. The results are in agreement with this assumption, as shown in Fig. 8.7.

Finally, the low P-values of the $D^0 \to K^+K^-$ tests as a function of the number of PVs and of long tracks, which are correlated and are equal to 3.1% and 3.5%, respectively, are attributed to a statistical fluctuation. The P-values of the χ^2/ndf of the dispersion of the results of the 8 subsamples with respect to the baseline one in the three bins of the variable under consideration are, from smaller to larger values of the variable, 8.4%, 9.0% and 40% (4.4%, 36% and 22%)

[1] The P-values of the χ^2/ndf of the averages of $\Delta Y_{K^-\pi^+}$ in the three $\eta(\pi^+_{\rm tag})$ bins are, from smaller to larger values of η, 75%, 24% and 0.1%, respectively. The average value in the bin $\eta(\pi^+_{\rm tag}) > 3.4$, which is responsible for the low global p-value, is $\Delta Y_{K^-\pi^+} = (-0.07 \pm 0.93) \times 10^{-4}$, and the p-value of the χ^2/ndf of the average of the three pseudorapidity bins is 99%.

[2] The corresponding values of $\Delta Y_{K^-\pi^+}$ are $(1.23 \pm 0.77) \times 10^{-4}$ and $(-2.77 \pm 0.62) \times 10^{-4}$.

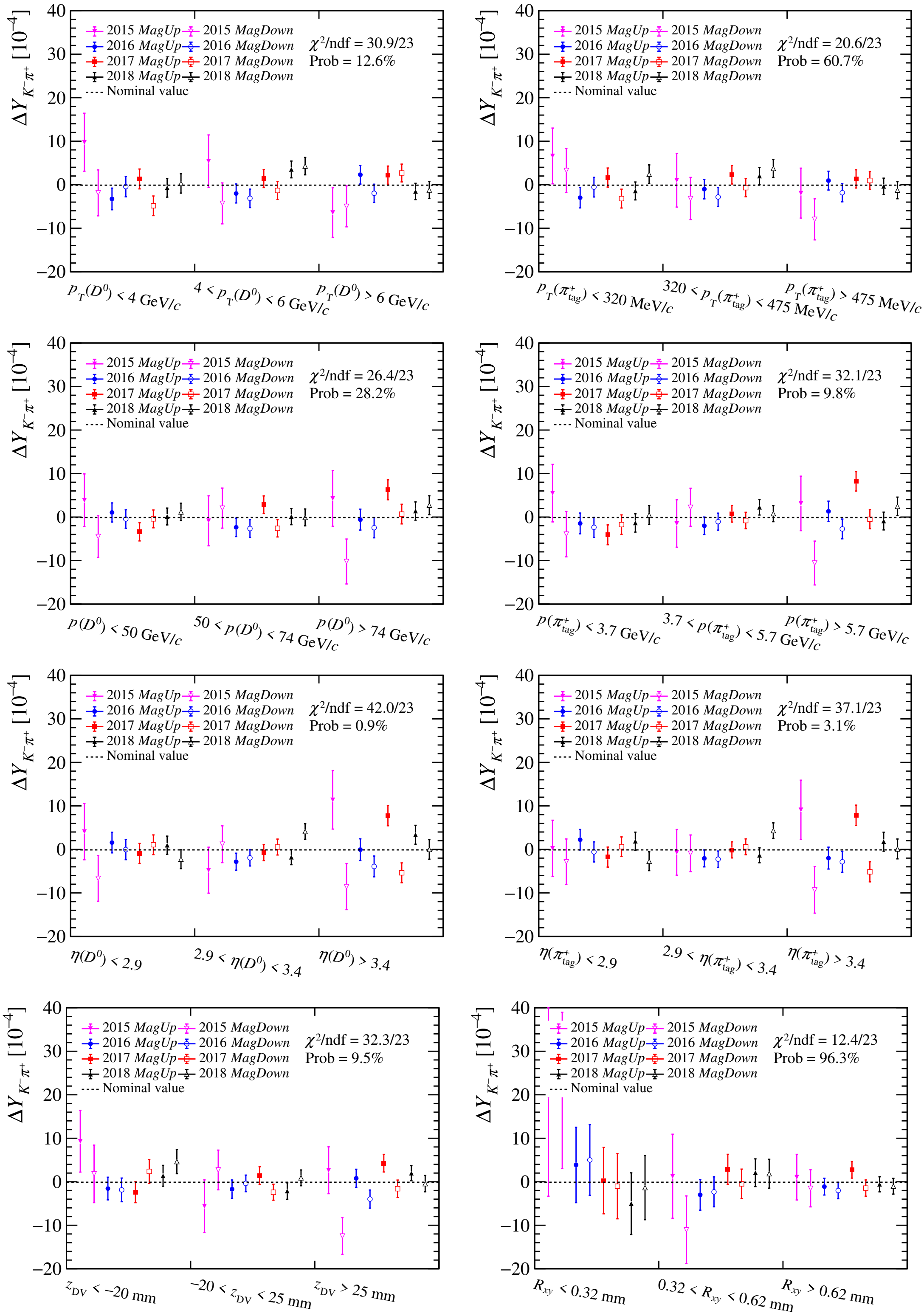

Figure 8.1: Measurements of $\Delta Y_{K^-\pi^+}$ performed separately in three bins of the momentum, transverse momentum and pseudorapidity of the D^0 and $\pi^+_{\rm tag}$ mesons and of the position of the D^0 decay vertex along the beam direction and in the plane transverse to it. Each of these bins is further divided in eight subsamples corresponding to different data-taking years and magnet polarities. The p-value of the dispersion of the measurements around the baseline one is displayed as well.

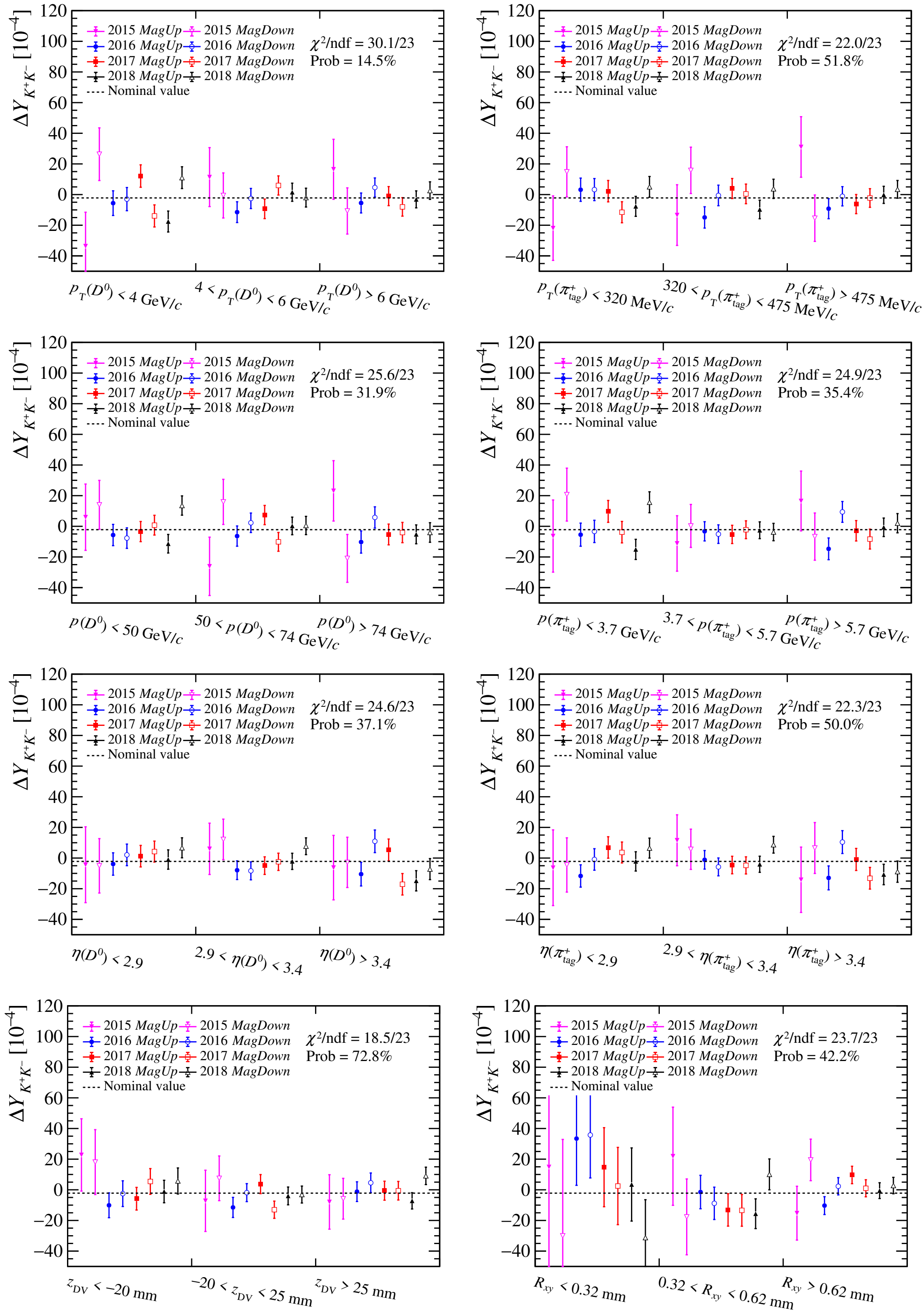

Figure 8.2: Measurements of $\Delta Y_{K^+K^-}$ performed separately in three bins of the momentum, transverse momentum and pseudorapidity of the D^0 and $\pi^+_{\rm tag}$ mesons and of the position of the D^0 decay vertex along the beam direction and in the plane transverse to it Each of these bins is further divided in eight subsamples corresponding to different data-taking years and magnet polarities. The p-value of the dispersion of the measurements around the baseline one is displayed as well.

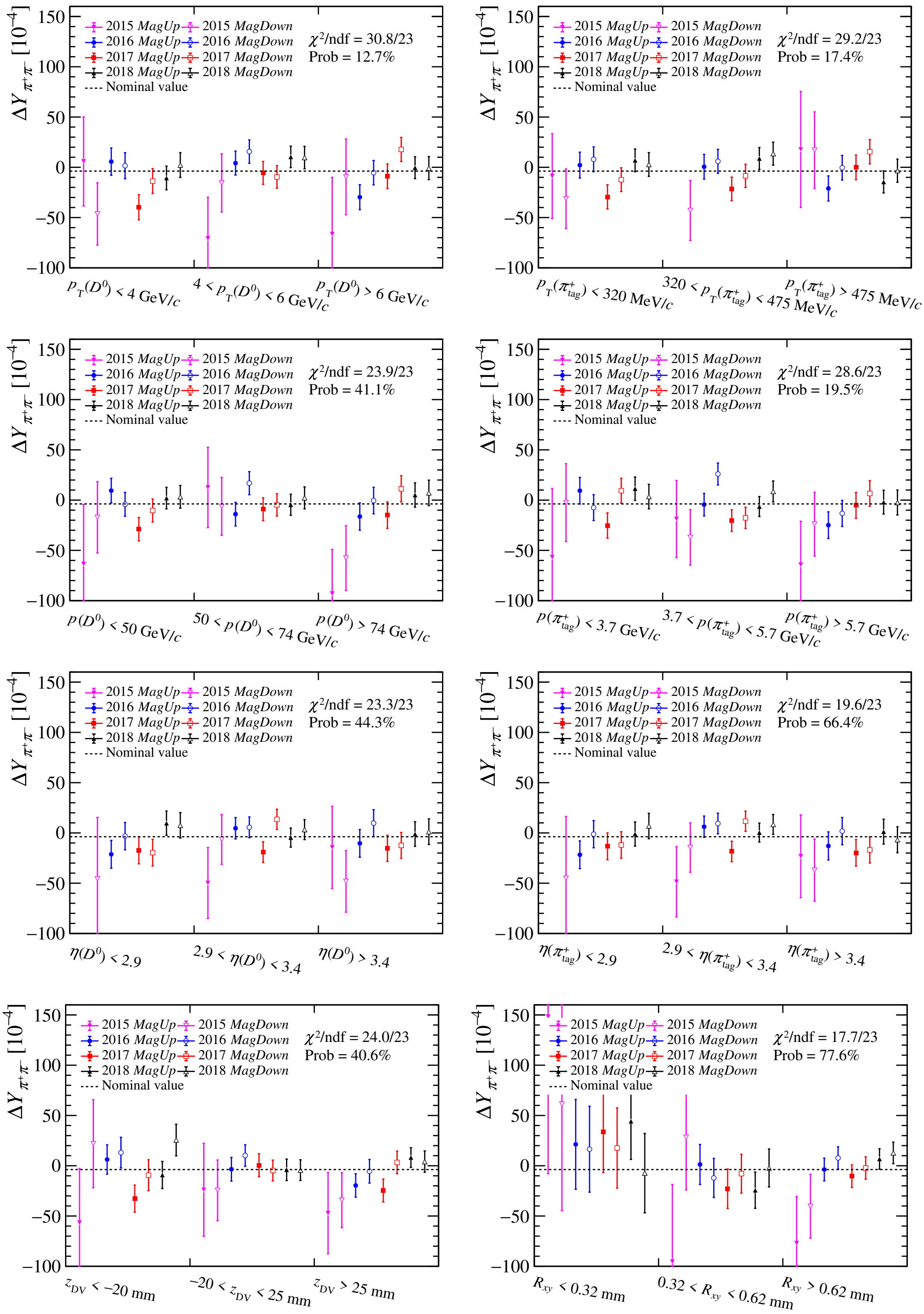

Figure 8.3: Measurements of $\Delta Y_{\pi^+\pi^-}$ performed separately in three bins of the momentum, transverse momentum and pseudorapidity of the D^0 and $\pi^+_{\rm tag}$ mesons and of the position of the D^0 decay vertex along the beam direction and in the plane transverse to it. Each of these bins is further divided in eight subsamples corresponding to different data-taking years and magnet polarities. The p-value of the dispersion of the measurements around the baseline one is displayed as well.

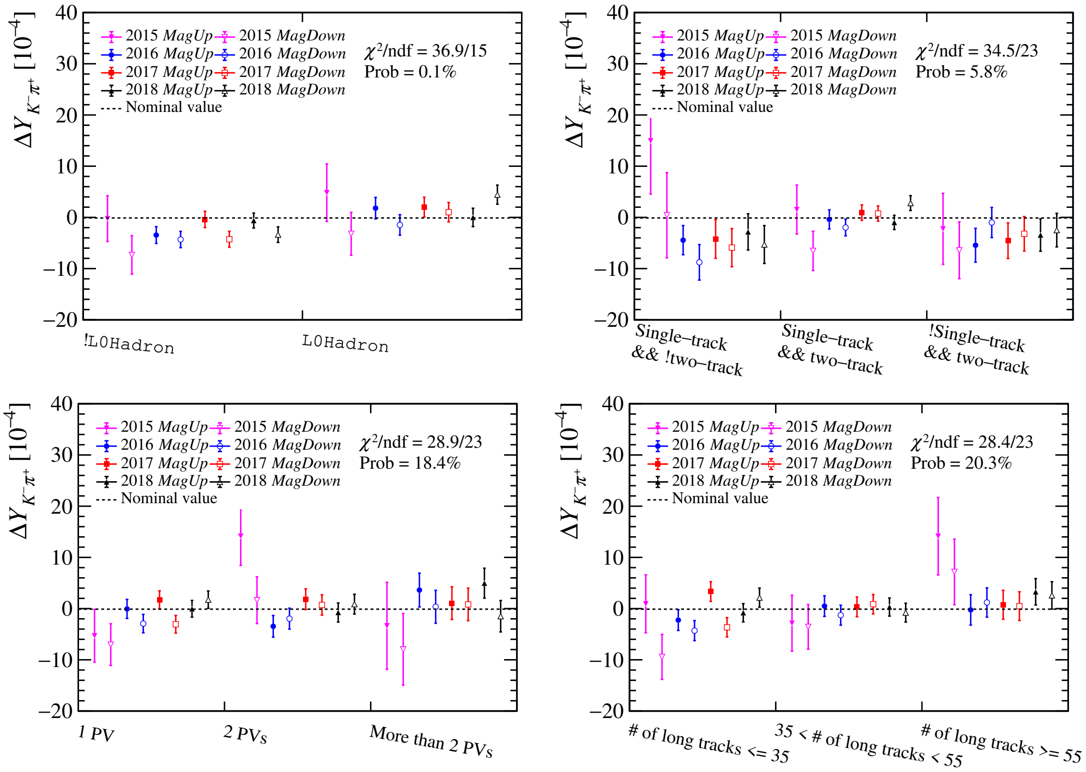

Figure 8.4: Measurements of $\Delta Y_{K^-\pi^+}$ performed separately in subsamples corresponding to different trigger requirements and detector occupancies (and, for each subsample, separately for different data-taking years and magnet polarities). The p-value of the dispersion of the measurements around the average of the baseline one is displayed as well.

for the test regarding the number of PVs (of long tracks). Thus, the low P-value is mainly due to the first bin (and, in particular, to the sample collected during 2017 with the *MagDown* polarity), but no significant trends are spotted[3] and no effects are observed in the more abundant $D^0 \to K^-\pi^+$ sample, strengthening the hypothesis of a statistical fluctuation.

8.2 Kinematic weighting

In the kinematic weighting of Sect. 5.2, only the events populating three-dimensional momentum bins with more than 40 candidates (for both the D^0 and $\overline{D}^0$ candidates) and an asymmetry less than 20% are assigned a nonzero weight. A possible concern is that a nonzero value of ΔY would modify the asymmetry in the single bins. In particular, it would cause both a global offset of the asymmetry, which is the effect expected if the correlations between the between the D^0-meson kinematics and decay time was zero, and a bin-dependent change responsible of the dilution of the measured value of ΔY described in Sect. 5.4. As a consequence, the choice to assign a zero weight to a bin is influenced by the actual value of ΔY, and by the sign of ΔY relative to that of the nuisance asymmetries in the given bin. This might bias the measurement of ΔY.

[3] The average of $\Delta Y_{K^+K^-}$ in the three bins is, from smaller to larger values of the two variables, $(-3.9\pm2.1)\times10^{-4}$, $(1.2\pm2.4)\times10^{-4}$ and $(-5.2\pm3.8)\times10^{-4}$ for test as a function of the number of PVs and $(-3.4\pm2.3)\times10^{-4}$, $(-0.4\pm2.3)\times10^{-4}$ and $(-3.5\pm3.4)\times10^{-4}$ for the test as a function of the number of long tracks, respectively.

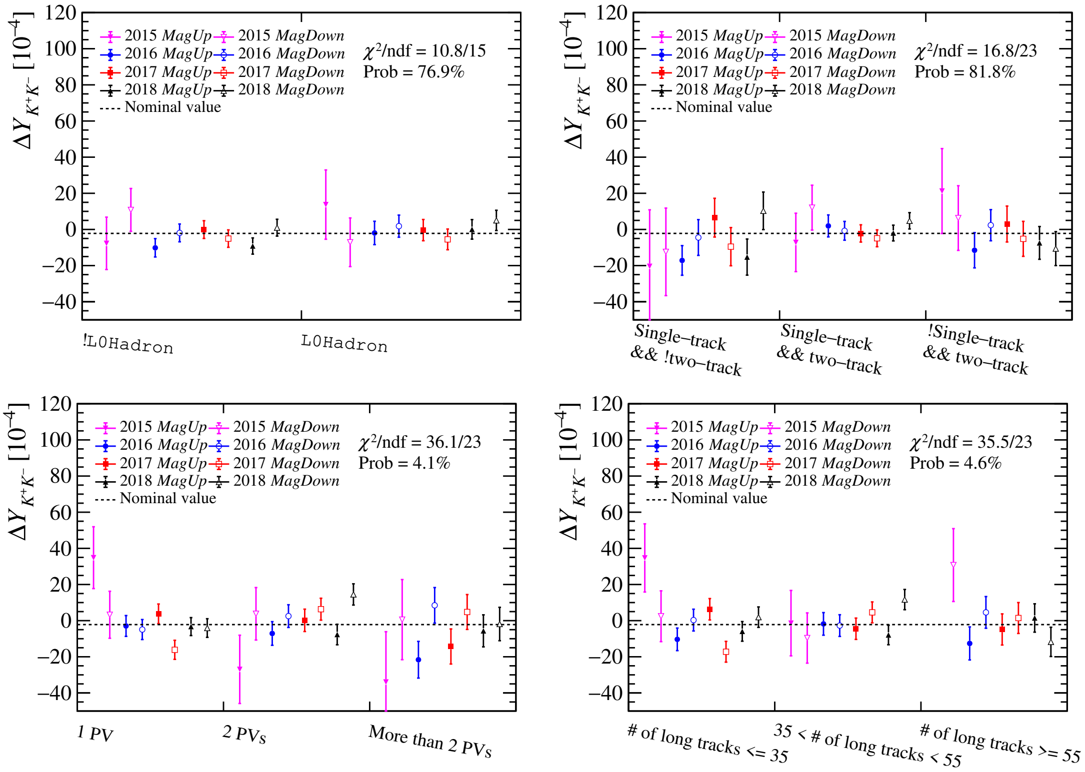

Figure 8.5: Measurements of $\Delta Y_{K^+K^-}$ performed separately in subsamples corresponding to different trigger requirements and detector occupancies (and, for each subsample, separately for different data-taking years and magnet polarities). The p-value of the dispersion of the measurements around the baseline one is displayed as well.

However, possible dilution (or enhancement) effects or constant biases on the measured value of ΔY have already been estimated in Sect. 5.4. The measurement results are corrected for the dilution effect, whereas the fitted value of the intercept q in Fig. 5.14 is less than 0.04×10^{-4} in magnitude and can be safely neglected. Therefore, no systematic uncertainties are assigned to these effects.

As an additional cross-check, the measurement of ΔY is performed again for both the K^+K^- and $\pi^+\pi^-$ decay channels, assigning a zero weight only to the bins for which the corresponding bin of the $D^0 \to K^-\pi^+$ sample has fewer than 40 candidates or an asymmetry greater than 20%. In this way, the choice of the zero weights is independent of the value of ΔY.[4] The results, $\Delta Y_{K^+K^-} = (-2.36 \pm 1.51) \times 10^{-4}$ and $\Delta Y_{\pi^+\pi^-} = (-2.96 \pm 2.74) \times 10^{-4}$, are shifted by -0.28×10^{-4} and -0.20×10^{-4} with respect to the baseline results, respectively. These values correspond to -0.19 and -0.08 times the statistical uncertainty. Finally, the stability of the measurement as a function of the threshold of the minimum number of candidates per bin (for the maximum asymmetry) is checked by performing the kinematic weighting using different thresholds between 5 and 200 (10% and 30%). The dispersion of the results with respect to the baseline one is compatible with being statistical fluctuations with a p-value of 11%.

[4] The residual dependence on ΔY due to bins which are populated only by D^0 candidates *aut* $\overline{D}^0$ candidates in the K^+K^- or $\pi^+\pi^-$ decay channels, but not for the $K^-\pi^+$ one, for which the weights cannot be calculated and are set to zero, can be safely neglected. In fact, these events correspond to the scarcely populated tails of the kinematic distributions.

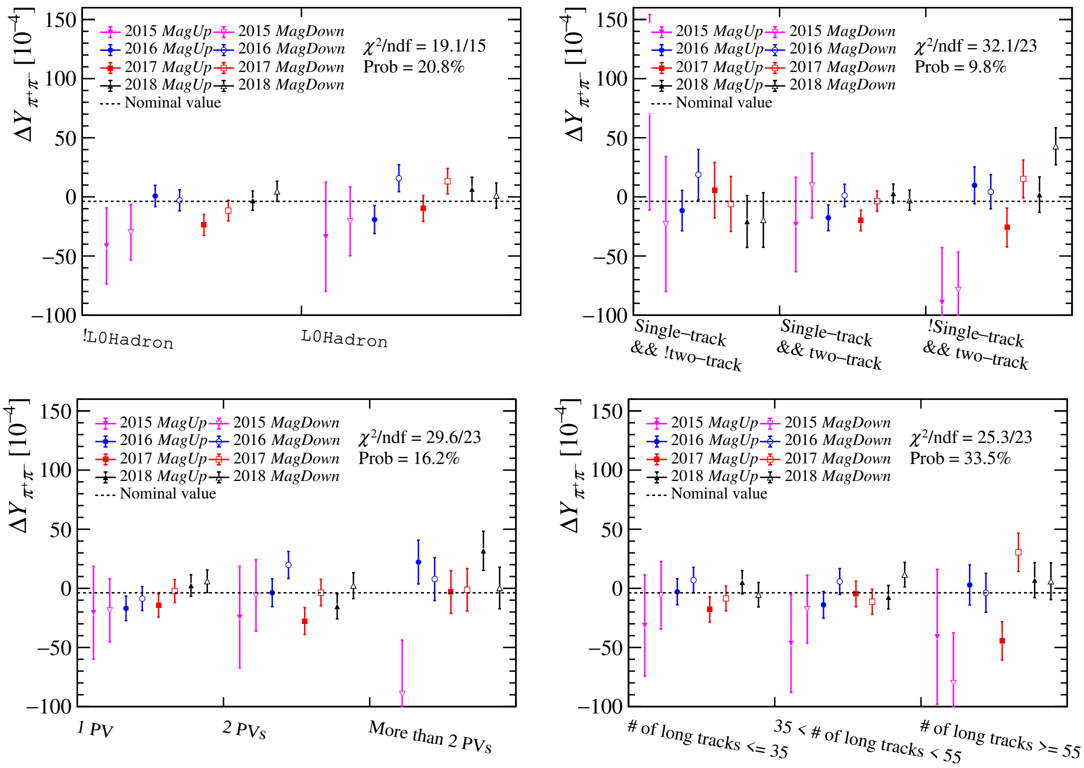

Figure 8.6: Measurements of $\Delta Y_{\pi^+\pi^-}$ performed separately in subsamples corresponding to different trigger requirements and detector occupancies (and, for each subsample, separately for different data-taking years and magnet polarities). The p-value of the dispersion of the measurements around the baseline one is displayed as well.

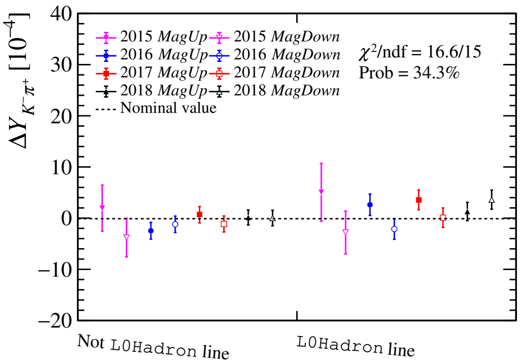

Figure 8.7: Measurements of $\Delta Y_{K^-\pi^+}$ performed separately in the subsample where the L0 hadronic trigger line is fired by the D^0 candidate and in its complimentary (and, for each of them, separately for different data-taking years and magnet polarities). The weights are calculated independently for each subsample. The p-value of the dispersion of the measurements around the baseline one is displayed as well.

Chapter 9

Results

This chapter reports the results of the measurement. Their combination with previous LHCb measurements and their impact on the knowledge of the parameters that quantify mixing and time-dependent CP violation in D^0-meson decays are described. Finally, the dissertation concludes by highlighting the importance of the work detailed in the present thesis in the context of the future experimental program of the LHCb experiment, and by summarising the prospects for the improvements in precision expected in the next years for the ΔY parameter.

The linear fits to the time-dependent asymmetry of the signal $D^0 \to K^+K^-$ and $D^0 \to \pi^+\pi^-$ candidates are displayed, for the whole data sample and after the kinematic weighting and the subtraction of the contribution from secondary decays, in Fig. 9.1. The resulting slopes are

$$\Delta Y_{K^+K^-} = (-2.3 \pm 1.5 \pm 0.3) \times 10^{-4},$$
$$\Delta Y_{\pi^+\pi^-} = (-4.0 \pm 2.8 \pm 0.4) \times 10^{-4},$$

where the first uncertainties are statistical and the second are systematic. Assuming all systematic uncertainties are 100% correlated, except those on the background under the D^0-meson mass

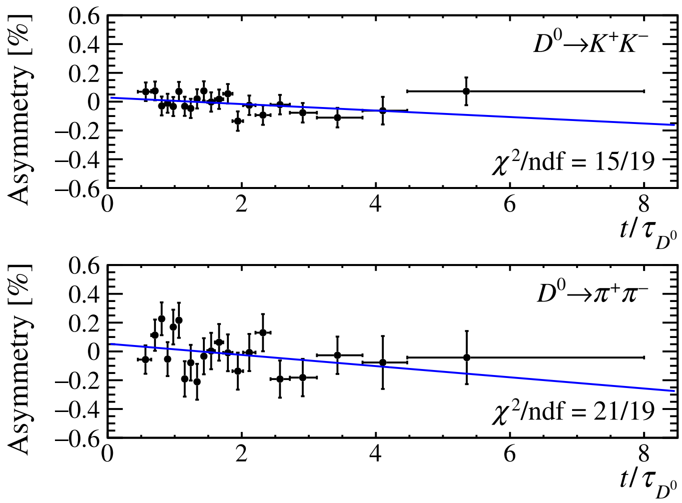

Figure 9.1: Linear fit to the time-dependent asymmetry of the (top) $D^0 \to K^+K^-$ and (bottom) $D^0 \to \pi^+\pi^-$ candidates.

peak, which are taken to be uncorrelated, the difference of ΔY between the two final states is equal to

$$\Delta Y_{K^+K^-} - \Delta Y_{\pi^+\pi^-} = (1.7 \pm 3.2 \pm 0.1) \times 10^{-4},$$

and is consistent with zero within 0.5σ. Neglecting final-state dependent contributions, the two values are combined by using the best linear unbiased estimator [180, 181]. The result,

$$\Delta Y = (-2.7 \pm 1.3 \pm 0.3) \times 10^{-4},$$

is consistent with zero within 2σ, and both its statistical and systematic uncertainties are smaller by a factor larger than two than those of the previous most precise measurement of the ΔY parameter [114].

As a by-product of the main measurement, the analogue of ΔY for right-sign $D^0 \to K^-\pi^+$ decays is measured to be $\Delta Y_{K^-\pi^+} = (-0.4 \pm 0.5 \pm 0.2) \times 10^{-4}$. However, the strategy adopted for this measurement was developed by analysing the same data which were used to perform the measurement itself.

9.1 Combination with previous LHCb measurements

The results are combined with previous LHCb measurements [114, 116, 118], with which they are consistent, yielding

$$\begin{aligned} \Delta Y_{K^+K^-} &= (-0.3 \pm 1.3 \pm 0.3) \times 10^{-4}, \\ \Delta Y_{\pi^+\pi^-} &= (-3.6 \pm 2.4 \pm 0.4) \times 10^{-4}, \\ \Delta Y_{K^+K^-} - \Delta Y_{\pi^+\pi^-} &= (+3.3 \pm 2.7 \pm 0.2) \times 10^{-4}, \\ \Delta Y &= (-1.0 \pm 1.1 \pm 0.3) \times 10^{-4}, \end{aligned}$$

which are the LHCb legacy results for the 2011–2012 and 2015–2018 data samples. They are consistent with the *CP*-invariance hypothesis for both $D^0 \to K^+K^-$ and $D^0 \to \pi^+\pi^-$ decays, and improve on the precision of the previous world average [47], which is shown in Fig. 2.2 in Sect. 2.2, by nearly a factor of two. Finally, the arithmetic average of $\Delta Y_{K^+K^-}$ and $\Delta Y_{\pi^+\pi^-}$, which would allow to suppress final-state dependent contributions to ΔY by a factor of ϵ [28], where ϵ is the parameter quantifying the breaking of $SU(3)_{\mathrm{F}}$ symmetry in the decay, is equal to

$$\tfrac{1}{2}(\Delta Y_{K^+K^-} + \Delta Y_{\pi^+\pi^-}) = (-1.9 \pm 1.3 \pm 0.4) \times 10^{-4}.$$

Figure 9.2 displays the new world average of ΔY after the measurement presented in this thesis. Here, the systematic uncertainty of the LHCb measurements are assumed to be uncorrelated with those of the BaBar, CDF and Belle experiments, whose inclusion modifies the average calculated from the LHCb measurements only marginally. The improvements in the knowledge of the parameters quantifying mixing and time-dependent *CP* violation in D^0-meson decays that follow from the present measurement, instead, are displayed in Figure 9.3. The precision on the dispersive mixing phase ϕ_2^M improves by around 35%, but smaller improvements concern other parameters as well, and in particular y_{12}, $A_{K\pi}$ and $\Delta_{K\pi}$. The analogue of the plots in Fig. 9.3 for the superweak approximation and for the phenomenological parametrisation are displayed in Appendix B.

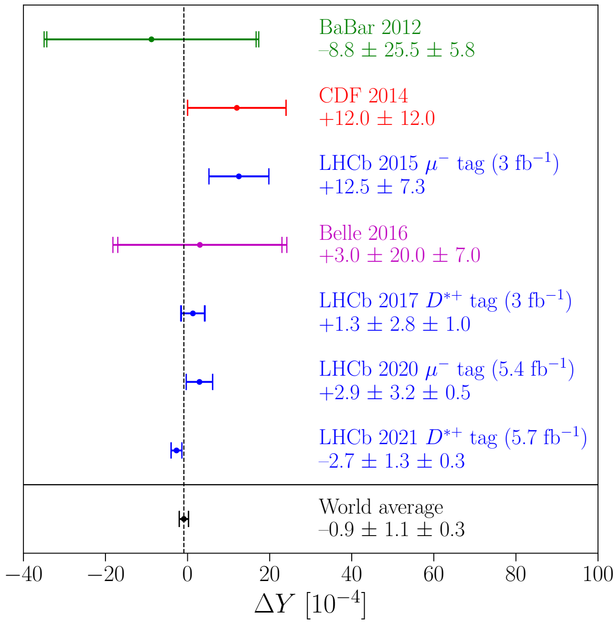

Figure 9.2: Summary of the most precise measurements of the parameter ΔY to date, including the present one. The measurements are compatible with each other, with a p-value of 38%. The world average without including the present measurement was $\Delta Y = (3.1 \pm 2.0 \pm 0.5) \times 10^{-4}$. Measurements references, from top to bottom: BaBar 2012 [57], CDF 2014 [115], LHCb 2015 μ^- tag [116], Belle 2016 [59], LHCb 2017 D^{*+} tag [114], LHCb 2020 μ^- tag [118], LHCb 2021 D^{*+} tag [133].

9.2 Conclusions and future prospects

The measurement presented in this thesis improves by nearly a factor of two the precision of the world average of the *CP* violation parameter ΔY, which is approximately equal to the negative of the parameter A_Γ. Thus, it sets the strongest bound to date on the value of the phase ϕ_2^M, which parametrises dispersive *CP*-violating contributions to D^0-meson mixing. At the same time, it represents the most precise measurement of *CP* violation in *D*-meson decays and, more in general, the most precise measurement of *CP* violation ever performed at the LHCb experiment. An article summarising the analysis method and the results presented in this thesis will be submitted shortly to the journal *Physical Review D* [133].

The unprecedented precision achieved is relevant also from another point of view. In fact, the measurement represents an encouraging example of the effectiveness of the *Turbo* data-taking paradigm pioneered by the LHCb experiment during 2015–2018 to perform high-precision measurements. As detailed in Sect. 3.3.2, the excellent performance of the nearly real-time trigger reconstruction since 2015 offers the opportunity to perform physics analyses directly using candidates reconstructed at the trigger level, which the present measurement exploits. The storage of only the triggered candidates enables a reduction in the event size by an order of magnitude. This is particularly important for heavy-hadron decays that are abundantly produced at the LHC and can selected with high purity, like most *D*-meson decays into charged hadrons. In fact, the main limitation in selecting and recording these decays is given by the resources available for permanent data storage. However, without a safety net of *post-hoc* reprocessing, errors are not tolerable and the reconstruction and selections must be designed to guarantee

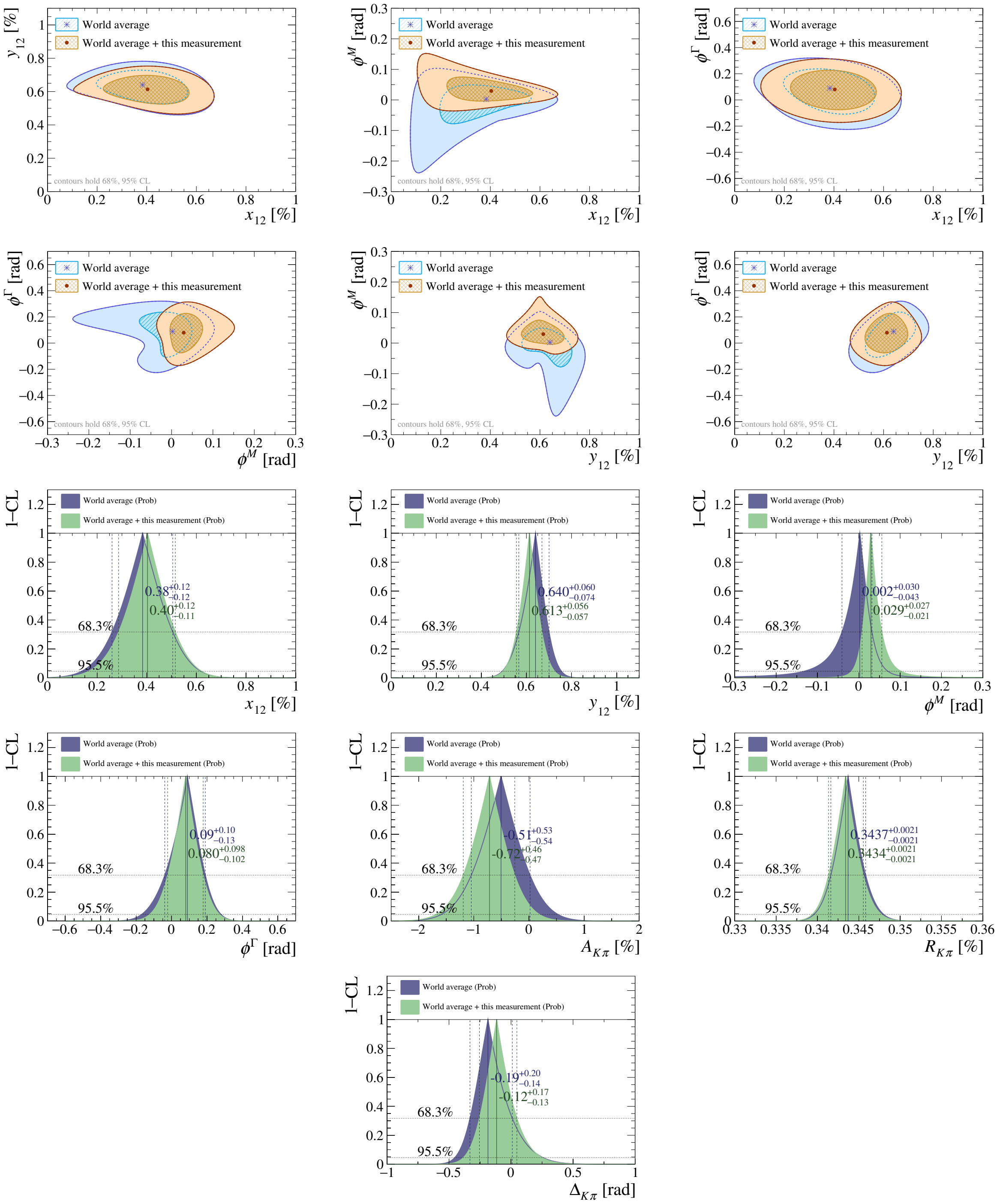

Figure 9.3: Impact of the present measurement on the knowledge of mixing and time-dependent *CP* violation in D^0-meson decays. The parameters $A_{K\pi}$ and $\Delta_{K\pi}$ are defined as $A_{K\pi} \equiv (R^+_{K^-\pi^+} - R^-_{K^-\pi^+})/(R^+_{K^-\pi^+} + R^-_{K^-\pi^+})$ and $\Delta_{K\pi} \equiv \Delta_{K^-\pi^+}$. The details of the fits performed to obtain these results are reported in Appendix B.

the possibility of keeping the systematic uncertainties below the statistical ones. High-precision measurements like the present one represent an important test bed of this paradigm, which will be the core of the future research program of the LHCb experiment, and will be adopted by most measurements of B-meson decays starting from 2022. In particular, the control sample of $D^0 \to K^-\pi^+$ decays that is used to prove the effectiveness of the measurement method in this thesis, corresponding to 519 million decays, is the largest sample ever analysed at the LHCb experiment. The precision of the measurement of $\Delta Y_{K^-\pi^+}$, whose compatibility with zero is determined with a precision of 0.5×10^{-4}, suggests that there are no intrinsic limitations in performing *CP* violation measurements with *Turbo* data. This precision will likely be reached by B-meson measurements only after 2030.

Before that date, steady progress in the study of D-meson decays is expected as well. The present measurement is expected to represent the most precise measurement of the ΔY parameter at least until the end of the next LHCb data taking period, in 2025. The Belle II experiment is expected to measure it by employing electron–positron collision data corresponding to an integrated luminosity of $50\,\text{ab}^{-1}$ within the next ten years. However, the predicted uncertainty is approximately equal to 2×10^{-4} [182]. Thus, while the Belle II measurement will provide a useful cross-check of the LHCb results thanks to the very different experimental environment of B-factory colliders, it is not expected to reduce the uncertainty on the ΔY world average significantly. On the other hand, in 2022 the Upgrade I of the LHCb experiment will start its data-taking recording pp collisions at an increased instantaneous luminosity of $2 \times 10^{33}\,\text{cm}^{-2}\,\text{s}^{-1}$, which is a factor of five larger than the current one, at an increased centre-of-mass energy of 14 TeV [183, 184]. This is foreseen to increase the total integrated luminosity of pp collisions recorded by the LHCb experiment to $25\,\text{fb}^{-1}$ ($50\,\text{fb}^{-1}$) by the end of its third (fourth) data-taking period, corresponding to the years 2022–2024 (2027–2030). Finally, the LHCb collaboration recently proposed an Upgrade II of the experiment, to allow the possibility of recording collisions at an instantaneous luminosity equal to $2 \times 10^{34}\,\text{cm}^{-2}\,\text{s}^{-1}$, a factor of ten higher than in the Upgrade I [185, 186]. If this proposal was approved, the total recorded integrated luminosity could increase to $300\,\text{fb}^{-1}$ by around 2037. This may allow to increase the number of recorded $D^0 \to K^+K^-$ decays to more than 5 billions, and to reduce the statistical precision on ΔY below 0.2×10^{-5}, a value comparable or less than the SM predictions [28, 29].

Of course, these projections do not take into account possible irreducible systematic uncertainties, which are hard to predict before performing the measurements. However, the precision of the present result, which reduces the systematic uncertainty by around a factor of three with respect to the previous measurement employing D^{*+}-tagged data [114], suggests that precisions of the order of 0.1×10^{-4} could actually be reached. In particular, the estimate of the largest systematic uncertainty, arising from the removal of the background under the D^{*+}-meson mass peak, suffers from large statistical fluctuations and is expected to be reducible. The uncertainty on the subtraction of secondary decays is already at the level of 0.1×10^{-4}, and might be further reduced by more detailed simulation studies and by employing further discriminating variables in addition to the IP of the D^0 meson, at the price of increased analysis complexity. For example, the vector momentum of primary and secondary D^0 mesons is known to differ due to different kinematics distributions of D^{*+} and B mesons produced in the pp collision. Furthermore, the IP of the π^+_{tag} meson and a careful analysis of the uncertainty on the IP of the D^0 meson might be used as further handles to increase the purity of the sample of primary decays. The contribution to the systematic uncertainty from biases due to background under the D^0-meson mass peak and to a time-dependent shift of the D^{*+}-meson mass peak are equal or less than the previous ones. Furthermore, they are equal to the total estimated size of the bias, and can be easily reduced by subtracting the bias. All in all, the biggest challenge of the measurement is related to the removal of the nuisance detection asymmetries. The method described in Chapter 5 is currently found to be effective for this aim. In addition, it may be used also to perform other time-dependent measurements, like that of the parameter $\Delta Y_{K\pi}$ introduced in Sect. 2.1.4 in untagged $D^0 \to K^{\mp}\pi^{\pm}$ decays. However, it is not guaranteed to work at arbitrary precision and further studies will be needed in the future to ensure that nuisance detection asymmetries are removed to the desired precision. To this regard, the quantification of the correlations between the decay kinematics and decay time described in Sect. 5.1 and in Appendix D.1 are an important step forward, and are currently been used in the design of the trigger for the next data taking.

Finally, a lower profile but essential result presented in this thesis is the observation that biases in the measurement of the y_{CP} parameter as large as 6% have been neglected until today, as shown in Sect. 2.1.2. The future world averages of the parameters quantifying mixing and CP violation in D^0-meson decays will need to take into account the deviations of the decay-time distribution of $D^0 \to K^-\pi^+$ decays from an exponential function, which are quantified by the parameter $y_{CP}^{K^-\pi^+}$ defined in Eq. (1.54) and are already of the same order of the statistical precision on the y_{CP} parameter. This discussion will be reported in an article in the next few weeks [187].

Appendix A

Phenomenological parametrisation of CP violation in $D^0 \to h^+h^-$ decays

This appendix reports the expressions for the CP-violation observables of $D^0 \to h^+h^-$ decays in the phenomenological parametrisation employed by Refs. [36, 47]. The notation for the weak angles follows that of Ref. [28].

In the phenomenological parametrisation, the time-dependent decay rates of D^0 and $\overline{D}^0$ mesons into the final state f are obtained by substituting Eq. (1.20) into Eq. (1.37), yielding

$$\Gamma(D^0 \to f, t) = \mathcal{N}_f \left| g_+(t) A_f + \frac{q}{p} g_-(t) \bar{A}_f \right|^2, \qquad \Gamma(\overline{D}^0 \to f, t) = \mathcal{N}_f \left| \frac{p}{q} g_-(t) A_f + g_+(t) \bar{A}_f \right|^2. \tag{A.1}$$

The analogue of Eq. (1.40) is obtained by substituting the definitions of $g_\pm(t)$, given in Eqs. (1.17) and (1.21), and by using the definition of the parameter λ_f in Eq. (1.34), giving

$$\begin{aligned}
\Gamma(D^0 \to f, t) = \frac{\mathcal{N}_f}{2} e^{-\tau} |A_f|^2 \big[&(1 + |\lambda_f|^2) \cosh(y\tau) + (1 - |\lambda_f|^2) \cos(x\tau) \\
&+ 2\,\mathcal{R}e(\lambda_f) \sinh(y\tau) - 2\,\mathcal{I}m(\lambda_f) \sin(x\tau) \big], \\
\Gamma(\overline{D}^0 \to f, t) = \frac{\mathcal{N}_f}{2} e^{-\tau} \big|\bar{A}_f\big|^2 \big[&(1 + \big|\lambda_f^{-1}\big|^2) \cosh(y\tau) + (1 - \big|\lambda_f^{-1}\big|^2) \cos(x\tau) \\
&+ 2\,\mathcal{R}e(\lambda_f^{-1}) \sinh(y\tau) - 2\,\mathcal{I}m(\lambda_f^{-1}) \sin(x\tau) \big].
\end{aligned} \tag{A.2}$$

As for the theoretical parametrisation, these formulas can be expanded to quadratic order in the mixing parameters, yielding

$$\begin{aligned}
\Gamma(D^0 \to f, t) = \mathcal{N}_f e^{-\tau} |A_f|^2 \big\{ 1 &+ \big[y\mathcal{R}e(\lambda_f) - x\mathcal{I}m(\lambda_f) \big] \tau, \\
&+ \tfrac{1}{4} \big[y^2 (1 + \big|\lambda_f\big|^2) - x^2 (1 - \big|\lambda_f\big|^2) \big] \tau^2 \big\} \\
\Gamma(\overline{D}^0 \to f, t) = \mathcal{N}_f e^{-\tau} \big|\bar{A}_f\big|^2 \big\{ 1 &+ \big[y\mathcal{R}e(\lambda_f^{-1}) - x\mathcal{I}m(\lambda_f^{-1}) \big] \tau, \\
&+ \tfrac{1}{4} \big[y^2 (1 + \big|\lambda_f^{-1}\big|^2) - x^2 (1 - \big|\lambda_f^{-1}\big|^2) \big] \tau^2 \big\}.
\end{aligned} \tag{A.3}$$

The expressions for the decay rates into the final state $\bar{f}$ are obtained from the expressions above through the substitution $f \to \bar{f}$. Their specialisation to the cases of CS, RS and WS decays is provided in the following sections.

A.1 Cabibbo-suppressed decays

For the Cabibbo-suppressed decays $f = K^+K^-$ or $f = \pi^+\pi^-$, the λ_f parameter is conventionally parametrised as

$$\lambda_f \equiv \frac{q}{p}\frac{\bar{A}_f}{A_f} \equiv -|\lambda_f| e^{i\phi_{\lambda_f}}, \tag{A.4}$$

where the minus sign ensures that the angle ϕ_{λ_f} equals zero rather than π in the limit of no *CP* violation. Substituting this definition in Eq. (A.3) yields the following expressions for the parameters $c_f^{\pm}$ and $c_f'^{\pm}$ defined in Eq. (1.43),

$$\begin{aligned}
c_f^{\pm} &= \left|\frac{q}{p}\right|^{\pm 1} \left|\frac{\bar{A}_f}{A_f}\right|^{\pm 1} (\pm x \sin\phi_{\lambda_f} - y\cos\phi_{\lambda_f}) \\
&\approx -y \pm x\phi_{\lambda_f} \pm y\left[a_f^d - \left(\left|\frac{q}{p}\right| - 1\right)\right], \\
c_f'^{\pm} &= \frac{1}{4}\left[y^2\left(\left|\frac{q}{p}\right|^{\pm 2}\left|\frac{\bar{A}_f}{A_f}\right|^{\pm 2} + 1\right) + x^2\left(\left|\frac{q}{p}\right|^{\pm 2}\left|\frac{\bar{A}_f}{A_f}\right|^{\pm 2} - 1\right)\right] \\
&\approx \frac{1}{2}y^2 \pm \frac{1}{2}(x^2+y^2)\left[\left(\left|\frac{q}{p}\right| - 1\right) - a_f^d\right],
\end{aligned} \tag{A.5}$$

where in the approximate expressions terms of order higher than one in the *CP* violation parameters ϕ_{λ_f}, $|q/p| - 1$ and a_f^d are neglected. The parameters ΔY_f and y_{CP}^f defined in Eqs. (1.46) and (1.47) are equal to

$$\begin{aligned}
\Delta Y_f &= \frac{1}{2}\left[\left(\left|\frac{q}{p}\right|\left|\frac{\bar{A}_f}{A_f}\right| + \left|\frac{p}{q}\right|\left|\frac{A_f}{\bar{A}_f}\right|\right) x\sin\phi_{\lambda_f} - \left(\left|\frac{q}{p}\right|\left|\frac{\bar{A}_f}{A_f}\right| - \left|\frac{p}{q}\right|\left|\frac{A_f}{\bar{A}_f}\right|\right) y\cos\phi_{\lambda_f}\right] \\
&\approx x\phi_{\lambda_f} - y\left(\left|\frac{q}{p}\right| - 1\right) + y a_f^d, \\
y_{CP}^f &= \frac{1}{2}\left[\left(\left|\frac{q}{p}\right|\left|\frac{\bar{A}_f}{A_f}\right| + \left|\frac{p}{q}\right|\left|\frac{A_f}{\bar{A}_f}\right|\right) y\cos\phi_{\lambda_f} - \left(\left|\frac{q}{p}\right|\left|\frac{\bar{A}_f}{A_f}\right| - \left|\frac{p}{q}\right|\left|\frac{A_f}{\bar{A}_f}\right|\right) x\sin\phi_{\lambda_f}\right] \\
&\approx y.
\end{aligned} \tag{A.6}$$

The approximate expression for ΔY displays explicitly that this observable receives a contribution of *CP* violation to mixing, which is proportional to y and vanishes only if $|q| = |p|$, one from *CP* violation in the interference, which is proportional to x and vanishes only if $\phi_f = 0$, and finally a contribution from *CP* violation in the decay, proportional to y. The measurements of y_{CP}^f indicate that y_{CP}^f is approximately equal to y rather than to $-y$, and imply that the angle ϕ_{λ_f} is approximately equal to zero rather than to π (while in the theoretical parametrisation they implied that ϕ_f^{Γ} was approximately equal to zero), justifying the first-order approximations $\sin\phi_{\lambda_f} \approx \phi_{\lambda_f}$ and $\cos\phi_{\lambda_f} \approx 1$ above.

A.2 Right-sign and wrong-sign decays

For the wrong-sign and right-sign final states $\bar{f} = K^+\pi^-$ and $f = K^-\pi^+$, the λ_f and $\lambda_{\bar{f}}$ parameters are parametrised as

$$\lambda_f \equiv \frac{q}{p}\frac{\bar{A}_f}{A_f} \equiv |\lambda_f| e^{i(\phi_{\lambda_f} + \Delta_f)}, \qquad \lambda_{\bar{f}} \equiv \frac{q}{p}\frac{\bar{A}_{\bar{f}}}{A_{\bar{f}}} \equiv |\lambda_f| e^{i(\phi_{\lambda_f} - \Delta_f)}, \tag{A.7}$$

where the strong phase Δ_f is the same as in Eq. (1.48), and the phase ϕ_{λ_f} in general differs from that of the previous section owing to different final-state dependent contributions from *CP* violation in the decay amplitude. The parameters $c_f^{\pm}$ and $c_f'^{\pm}$ defined in Eq. (1.51) are equal to

$$\begin{aligned} c_f^{\pm} &= \sqrt{\frac{R_f^{\pm}}{R_f}} \left|\frac{\bar{A}_f}{A_{\bar{f}}}\right|^{\pm 1} \left|\frac{q}{p}\right|^{\pm 1} \left[y\cos(\Delta_f \pm \phi_{\lambda_f}) - x\sin(\Delta_f \pm \phi_{\lambda_f})\right] \\ &\approx \left[1 \pm \left(\left|\frac{q}{p}\right| - 1\right) \mp \frac{1}{2}(a_{\bar{f}}^d + a_f^d)\right](y\cos\Delta_f - x\sin\Delta_f) \mp (x\cos\Delta_f + y\sin\Delta)\phi_{\lambda_f}, \\ c_f'^{\pm} &= \frac{1}{4}(y^2 - x^2) + \frac{1}{4}R_f^{\pm}\left|\frac{\bar{A}_f}{A_{\bar{f}}}\right|^{\pm 2}\left|\frac{q}{p}\right|^{\pm 2}(x^2 + y^2) \\ &\approx \frac{1}{4}(y^2 - x^2) + \frac{1}{4}R_f\left[1 \pm 2\left(\left|\frac{q}{p}\right| - 1\right) \mp (a_{\bar{f}}^d + a_f^d)\right](x^2 + y^2), \end{aligned} \tag{A.8}$$

where in the approximate expressions terms of order higher than one in the *CP* violation parameters ϕ_{λ_f}, $|q/p| - 1$, a_f^d and $a_{\bar{f}}^d$ are neglected. The observables ΔY_f and y_{CP}^f defined in Eqs. (1.53) and (1.54) are equal to

$$\begin{aligned} \Delta Y_f &\approx \frac{\sqrt{R_f}}{2}\Bigg[- (x\cos\Delta_f + y\sin\Delta_f)\sin\phi_{\lambda_f}\left(\left|\frac{q}{p}\right| + \left|\frac{p}{q}\right|\right) \\ &\qquad + (y\cos\Delta_f - x\sin\Delta_f)\cos\phi_{\lambda_f}\left(\left|\frac{q}{p}\right| - \left|\frac{p}{q}\right| - (a_f^d + a_{\bar{f}}^d)\right)\Bigg] \\ &\approx \sqrt{R_f}\Bigg\{ - (x\cos\Delta_f + y\sin\Delta_f)\phi_{\lambda_f} \\ &\qquad + (y\cos\Delta_f - x\sin\Delta_f)\left[\left(\left|\frac{q}{p}\right| - 1\right) - \frac{1}{2}(a_f^d + a_{\bar{f}}^d)\right]\Bigg\}, \\ y_{CP}^f &\approx \frac{\sqrt{R_f}}{2}\Bigg[(x\sin\Delta_f - y\cos\Delta_f)\cos\phi_{\lambda_f}\left(\left|\frac{q}{p}\right| + \left|\frac{p}{q}\right|\right) \\ &\qquad + (x\cos\Delta_f + y\sin\Delta_f)\sin\phi_{\lambda_f}\left(\left|\frac{q}{p}\right| - \left|\frac{p}{q}\right|\right)\Bigg] \\ &\approx \sqrt{R_f}(x\sin\Delta_f - y\cos\Delta_f), \end{aligned} \tag{A.9}$$

where the same approximations as in Eq. (A.8) are employed, and additionally terms proportional to a_f^d or to $a_{\bar{f}}^d$ are expanded to zeroth order in the other *CP* violation parameters starting from the first expressions.

For WS decays, instead, the parameters $c_{\bar{f}}^{\pm}$ and $c_{\bar{f}}'^{\pm}$ defined in Eq. (1.55) are equal to

$$\begin{aligned} c_{\bar{f}}^{\pm} &= \left|\frac{\bar{A}_{\bar{f}}}{A_f}\right|^{\pm 1}\left|\frac{q}{p}\right|^{\pm 1}\left[y\cos(\Delta_f \mp \phi_{\lambda_f}) + x\sin(\Delta_f \mp \phi_{\lambda_f})\right] \\ &\approx \left[1 \pm \left(\left|\frac{q}{p}\right| - 1\right) \mp a_f^d\right](y\cos\Delta_f + x\sin\Delta_f) \mp (x\cos\Delta_f - y\sin\Delta_f)\sin\phi_{\lambda_f}, \\ c_{\bar{f}}'^{\pm} &= \frac{1}{4}(y^2 + x^2)\left|\frac{q}{p}\right|^{\pm 2}\left|\frac{\bar{A}_{\bar{f}}}{A_f}\right|^{\pm 2} + \frac{1}{4}R_{\bar{f}}^{\pm}(y^2 - x^2) \\ &\approx \frac{1}{4}\left[1 \pm 2\left(\left|\frac{q}{p}\right| - 1\right) \mp 2a_f^d\right](x^2 + y^2) + \frac{1}{4}R_{\bar{f}}^{\pm}(y^2 - x^2). \end{aligned} \tag{A.10}$$

Again, terms of order higher than one in the *CP* violation parameters ϕ_{λ_f}, $|q/p|-1$ and a_f^d are neglected in the approximate expressions.

A.3 Approximate universality and final-state dependence

For a fixed final state f, the parametrisation of time-dependent *CP* violation in terms of the parameters q/p and ϕ_{λ_f} is equivalent to that in terms of the angles ϕ_f^M and ϕ_f^Γ of the theoretical parametrisation. The relation between these sets of parameters are given by Eq. (1.30), which in the limit of small *CP* violation simplifies to Eq. (1.31), and by the following expression,

$$\tan 2\phi_{\lambda_f} = -\left(\frac{x_{12}^2 \sin 2\phi_f^M + y_{12}^2 \sin 2\phi_f^\Gamma}{x_{12}^2 \cos 2\phi_f^M + y_{12}^2 \cos 2\phi_f^\Gamma}\right), \tag{A.11}$$

which is obtained by multiplying both sides of Eq. (1.16) by $(\bar{A}_f/A_f)^2$ for CS decays, and by $(\bar{A}_f\bar{A}_{\bar{f}}/A_f A_{\bar{f}})$ for RS and WS decays. In the limit that ϕ_f^M and ϕ_f^Γ are small, or in other words that *CP* violation is small and that the parameters x and y have the same sign — a scenario that is now favoured at approximately 3σ [47] —, this expression is simplified and the angle ϕ_{λ_f} can be written as a weighted sum of the angles ϕ_f^M and ϕ_f^Γ,

$$\phi_{\lambda_f} \approx -\frac{x_{12}^2}{x_{12}^2+y_{12}^2}\phi_f^M - \frac{y_{12}^2}{x_{12}^2+y_{12}^2}\phi_f^\Gamma. \tag{A.12}$$

Analogously to Sect. 1.3.4, it is possible also in the phenomenological parametrisation to introduce an intrinsic phase of *CP* violation in the mixing [28], which is approximately equal to ϕ_{λ_f} in the limit of no *CP* violation in the decay. This is defined as

$$\phi_2 \equiv \arg\left[\frac{q}{p}\frac{(\lambda_{cu}^s - \lambda_{cu}^d)^2\Gamma_2}{4}\right], \tag{A.13}$$

where λ_{cu}^i is defined as $\lambda_{cu}^i \equiv V_{ci}V_{ui}^*$ and Γ_2 is the dominant $\Delta U = 2$ amplitude (excluding the CKM coefficients) contributing to the absorptive-mixing transition Γ_{12}, defined in Sect. 1.3.4. The phase ϕ_2, which is usually named ϕ by the HFLAV collaboration [47], is related to ϕ_2^M and to ϕ_2^Γ by Eq. (A.11), with the substitution λ_f, $f \to 2$. The final-state dependent corrections to ϕ_2 are equal in magnitude but opposite in sign with respect to those of $\phi_2^{M(\Gamma)}$. In other words, the following expression holds, $\phi_{\lambda_f} = \phi_2 - \delta\phi_f$, with $\delta\phi_f$ the same as in Sect. 1.3.4. The limit of approximate universality is implemented by substituting $\phi_{\lambda_f} \to \phi_2$ in all of the expressions above, like it is currently done by the HFLAV collaboration [47].

Finally, the final-state dependent contribution to ΔY_f in the phenomenological parametrisation can be divided from the final-state independent contribution as done in Eq. (1.71) for the theoretical parametrisation, yielding

$$\Delta Y_f \approx x\phi_2 - y\left(\left|\frac{q}{p}\right| - 1\right) + y a_f^d \left(1 + \frac{x}{y}\cot\delta_f\right). \tag{A.14}$$

Appendix B

Fit to the charm *CP*-violation and mixing observables

This appendix reports the details of the fit of the parameters that quantify time-dependent CP violation and mixing in D^0 mesons to all the measurements available to date. The results of the fit are employed in the main body of the thesis to estimate the size of the observable $\Delta Y_{K^-\pi^+}$, and to assess the impact of the present measurement of ΔY on the world average of the aforementioned parameters. The expressions of all the relevant experimental observables are provided both in terms of the theoretical and phenomenological parameters. Finally, the impact of neglecting the parameter $y_{CP}^{K^-\pi^+}$ in the interpretation of the measurements of the parameter y_{CP} is discussed.

The estimate of the value of the observable $\Delta Y_{K^-\pi^+}$ presented in Sect. 5 is obtained through a fit of the parameters quantifying time-dependent *CP* violation and mixing of D^0 mesons to all of the relative measurements performed to date worldwide. The fit is performed with an approach similar to that adopted by the HFLAV and UTfit collaborations [28, 47, 122, 123]. However, it does not include the measurements of time-integrated *CP* asymmetries that are employed by the HFLAV collaboration, since they have a negligible impact on the knowledge of the parameters of time-dependent measurements. In addition, contrary to both the aforementioned references, it takes into account the measurement of the strong phase $\Delta_{K\pi}$ performed by the BESIII experiment [126], as well as the contribution of the parameter $y_{CP}^{K^-\pi^+}$ to the determination of the y_{CP} parameter through the observables in Eqs. (2.6) and (2.7). The impact of the latter improvement with respect to the fits of the HFLAV and UTfit collaborations is discussed in Sect. B.4. Finally, this fit is employed also to estimate the impact of the present measurement of ΔY on the world average of the parameters of time-dependent *CP* violation and mixing in Sect. 9.1.

The fit is based on the frequentist framework for statistical analysis GammaCombo, developed by the LHCb collaboration to combine its measurements of the angle γ of the CKM unitary triangle [188, 189]. To reduce the computing time needed to calculate the confidence intervals on the parameters, the profile likelihood ratio (Prob) method is employed rather than the pseudoexperiment-based (Plugin) method. While the coverage properties of the Prob method are known to be nonoptimal, they generally provide results accurate within 10% uncertainty, and are thus sufficient to estimate the impact of single measurements on the fit results and to set a rough limit on the magnitude of the $\Delta Y_{K^-\pi^+}$ observable.

The experimental inputs employed in the fit are listed in Table B.1. In the following, the parameters $R_{K^-\pi^+}$, $R^+_{K^-\pi^+}$, $R^-_{K^-\pi^+}$ and $\Delta_{K^-\pi^+}$ introduced in Sect. 1.3.3 are denoted with

$R_{K\pi}$, $R^+_{K\pi}$, $R^-_{K\pi}$ and $\Delta_{K\pi}$, respectively, to keep the notation compact. The parameters $\Delta_{K\pi}$, $R_{K\pi}$, $A_{K\pi} \equiv (R^+_{K\pi} - R^-_{K\pi})/(R^+_{K\pi} + R^-_{K\pi}) \approx a^d_{K^+\pi^-} - a^d_{K^-\pi^+}$ are shared by the theoretical and phenomenological parametrisations. The remaining mixing and time-dependent *CP* violation parameters, instead, depend on the parametrisation. The expressions of the experimental observables in terms of the two alternative sets of parameters are listed in the next sections, where the *CP* violation in the decay of the Cabibbo-favoured channel, $a^d_{K^-\pi^+}$, is neglected, implying the equality $A_{K\pi} \approx a^d_{K^+\pi^-}$. The code employed to perform the fit will be made publicly available contemporaneously with the publication of Ref. [187].

Table B.1: Observables used in the fit. The observables $R^+_{K\pi}$ and $R^-_{K\pi}$ are related to the parameters $R_{K\pi}$ and $A_{K\pi}$ *via* $R^\pm_{K\pi} = R_{K\pi}(1 \pm A_{K\pi})$. Both the world averages of ΔY excluding and including the present measurement are listed. The parameter $y^{K\pi}_{CP}$ is the analogue of the parameter $y^{K^-\pi^+}_{CP}$ for untagged $D^0 \to K^-\pi^+$ decays, or in other words for the sum of $D^0 \to K^-\pi^+$ and $\overline{D}{}^0 \to K^+\pi^-$ decays.

Decay mode	Observable	Values	Correlation coefficients
$D^0 \to K^+K^-$ (E791) [119]	$y_{CP} - y^{K\pi}_{CP}$	$(7.32 \pm 30.68) \times 10^{-3}$	
$D^0 \to K^0_S K^+K^-/K^+K^-/\pi^+\pi^-/K^0_S\pi^0\pi^0/$ $K^0_S\pi^0/K^0_S\omega/K^0_S\eta$ (Belle, BESIII) [190, 191]	y_{CP}	$(-3.70 \pm 7.04) \times 10^{-3}$	
$D^0 \to K^+K^-/\pi^+\pi^-$ (Mainly from LHCb, BaBar, Belle) [57, 59, 61, 120, 121]	$y_{CP} - y^{K^-\pi^+}_{CP}$	$(7.42 \pm 1.12) \times 10^{-3}$	
$D^0 \to K^0_S\omega$ (Belle) [192]	$y_{CP} + y^{K^-\pi^+}_{CP}$	$(9.60 \pm 11.14) \times 10^{-3}$	
$D^0 \to K^+K^-/\pi^+\pi^-$ (Mainly from LHCb) [57, 59, 114–116, 118] Second line adds Ref. [133]	ΔY ΔY	$(3.09 \pm 2.04) \times 10^{-4}$ $(-0.92 \pm 1.11 \pm 0.33) \times 10^{-4}$	
$D^0 \to K^+\ell^-\bar{\nu}$ (Mainly BaBar, Belle) [193–197]	$(x^2+y^2)/2$	$(0.0130 \pm 0.0269)\%$	
$D^0 \to K^+\pi^-\pi^+\pi^-$ (LHCb 2011–2012) [130]	$(x^2+y^2)/4$	$(4.8 \pm 1.8) \times 10^{-5}$	
$D^0 \to K^+\pi^-$ (BaBar 384 fb^{-1}) [135]	$R_{K\pi}$ $(x'^+)^2$ y'^+	$(3.03 \pm 0.189) \times 10^{-3}$ $(-2.4 \pm 5.2) \times 10^{-4}$ $(9.8 \pm 7.8) \times 10^{-3}$	$\begin{Bmatrix} 1 & 0.77 & -0.87 \\ & 1 & -0.94 \\ & & 1 \end{Bmatrix}$
$\overline{D}{}^0 \to K^-\pi^+$ (BaBar 384 fb^{-1}) [135]	$A_{K\pi}$ $(x'^-)^2$ y'^-	$(-2.1 \pm 5.4)\%$ $(-2.0 \pm 5.0) \times 10^{-4}$ $(9.6 \pm 7.5) \times 10^{-3}$	same as above
$D^0 \to K^+\pi^-$ (Belle 976 fb^{-1}) [134]	$R_{K\pi}$ x'^2 y'	$(3.53 \pm 0.013) \times 10^{-3}$ $(0.9 \pm 2.2) \times 10^{-4}$ $(4.6 \pm 3.4) \times 10^{-3}$	$\begin{Bmatrix} 1 & 0.737 & -0.865 \\ & 1 & -0.948 \\ & & 1 \end{Bmatrix}$
$D^0 \to K^+\pi^-$ (CDF 9.6 fb^{-1}) [136]	$R_{K\pi}$ x'^2 y'	$(3.51 \pm 0.35) \times 10^{-3}$ $(0.8 \pm 1.8) \times 10^{-4}$ $(4.3 \pm 4.3) \times 10^{-3}$	$\begin{Bmatrix} 1 & 0.90 & -0.967 \\ & 1 & -0.975 \\ & & 1 \end{Bmatrix}$

— continued from previous page.

$D^0 \to K^\pm \pi^\mp$ (LHCb 2011–2016) [60]	$R^+_{K\pi}$	$(3.454 \pm 0.045) \times 10^{-3}$	$\begin{Bmatrix} 1 & -0.935 & 0.843 & -0.012 & -0.003 & 0.002 \\ & 1 & -0.963 & -0.003 & 0.004 & -0.003 \\ & & 1 & 0.002 & -0.003 & 0.003 \\ & & & 1 & -0.935 & 0.846 \\ & & & & 1 & -0.964 \\ & & & & & 1 \end{Bmatrix}$
	y'^+	$(5.01 \pm 0.74) \times 10^{-3}$	
	$(x'^+)^2$	$(0.61 \pm 0.37) \times 10^{-4}$	
	$R^-_{K\pi}$	$(3.454 \pm 0.045) \times 10^{-3}$	
	y'^-	$(5.54 \pm 0.74) \times 10^{-3}$	
	$(x'^-)^2$	$(0.16 \pm 0.39) \times 10^{-4}$	
$\psi(3770) \to D^0 \overline{D}^0$ (CLEOc) [125]	$R_{K\pi}$	$(0.533 \pm 0.107 \pm 0.045)\%$	$\begin{Bmatrix} 1 & 0 & 0 & -0.42 & 0.01 \\ & 1 & -0.73 & 0.39 & 0.02 \\ & & 1 & -0.53 & -0.03 \\ & & & 1 & 0.04 \\ & & & & 1 \end{Bmatrix}$
	x^2	$(0.06 \pm 0.23 \pm 0.11)\%$	
	y	$(4.2 \pm 2.0 \pm 1.0)\%$	
	$\cos \Delta_{K\pi}$	$0.81\,^{+0.22}_{-0.18}\,^{+0.07}_{-0.05}$	
	$\sin \Delta_{K\pi}$	$0.01 \pm 0.41 \pm 0.04$	
$\psi(3770) \to D^0 \overline{D}^0$ (BESIII) [126]	$A^{K\pi}_{CP}$	$(12.7 \pm 1.3 \pm 0.7)\%$	
$D^0 \to K^0_S \pi^+\pi^- / K^0_S K^+K^-$ (BaBar) [56]	x	$(0.16 \pm 0.23 \pm 0.12 \pm 0.08)\%$	$+0.0615$
	y	$(0.57 \pm 0.20 \pm 0.13 \pm 0.07)\%$	
$D^0 \to \pi^0 \pi^+\pi^-$ (BaBar) [198]	x	$(1.5 \pm 1.2 \pm 0.6)\%$	-0.006
	y	$(0.2 \pm 0.9 \pm 0.5)\%$	
$D^0 \to K^0_S \pi^+\pi^-$ (Belle) [58]	x	$(5.8 \pm 1.9^{+0.734}_{-1.177}) \times 10^{-3}$	$\begin{Bmatrix} 1 & 0.054 & -0.074 & -0.031 \\ & 1 & 0.034 & -0.019 \\ & & 1 & 0.044 \\ & & & 1 \end{Bmatrix}$
	y	$(2.7 \pm 1.6^{+0.546}_{-0.854}) \times 10^{-3}$	
	$\lvert q/p \rvert$	$0.82\,^{+0.20}_{-0.18}\,^{+0.0807}_{-0.0645}$	
	ϕ_2	$(-13\,^{+12}_{-13}\,^{+4.15}_{-4.77})^\circ$	
$D^0 \to K^0_S \pi^+\pi^-$ (LHCb 2011–2012) [62]	x_{CP}	$(2.7 \pm 1.6 \pm 0.4) \times 10^{-3}$	$\begin{Bmatrix} 1 & (-0.17+0.15) & (0.04+0.01) & (-0.02-0.02) \\ & 1 & (-0.03-0.05) & (0.01-0.03) \\ & & 1 & (-0.13+0.14) \\ & & & 1 \end{Bmatrix}$ Notation: above coefficients are (statistical+systematic).
	y_{CP}	$(7.4 \pm 3.6 \pm 1.1) \times 10^{-3}$	
	Δx	$(-0.53 \pm 0.70 \pm 0.22) \times 10^{-3}$	
	Δy	$(0.6 \pm 1.6 \pm 0.3) \times 10^{-3}$	

B.1 Theoretical parametrisation and superweak approximation

The expressions of the experimental observables in Table B.1 in terms of the theoretical parameters x_{12}, y_{12}, ϕ_2^M, ϕ_2^Γ, $\Delta_{K\pi}$, $R_{K\pi}$ and $A_{K\pi}$ are

$$x = \mathrm{sign}\big[\cos\big(\phi_2^M - \phi_2^\Gamma\big)\big] \times \frac{1}{\sqrt{2}}\left(x_{12}^2 - y_{12}^2 + \sqrt{(x_{12}^2 + y_{12}^2)^2 - 4x_{12}^2 y_{12}^2 \sin^2(\phi_2^M - \phi_2^\Gamma)}\right)^{1/2}, \tag{B.1}$$

$$y = \frac{1}{\sqrt{2}}\left(y_{12}^2 - x_{12}^2 + \sqrt{(x_{12}^2 + y_{12}^2)^2 - 4x_{12}^2 y_{12}^2 \sin^2(\phi_2^M - \phi_2^\Gamma)}\right)^{1/2}, \tag{B.2}$$

$$\left|\frac{q}{p}\right| = \left(\frac{x_{12}^2 + y_{12}^2 + 2x_{12}y_{12}\sin\big(\phi_2^M - \phi_2^\Gamma\big)}{\sqrt{(x_{12}^2 + y_{12}^2)^2 - 4x_{12}^2 y_{12}^2 \sin^2(\phi_2^M - \phi_2^\Gamma)}}\right)^{1/2}, \tag{B.3}$$

$$\phi_2 = -\frac{1}{2}\,\mathrm{atan}\left(\frac{x_{12}^2 \sin 2\phi_2^M + y_{12}^2 \sin 2\phi_2^\Gamma}{x_{12}^2 \cos 2\phi_2^M + y_{12}^2 \cos 2\phi_2^\Gamma}\right), \tag{B.4}$$

$$
\begin{aligned}
x_{CP} &= x_{12}\cos\phi_2^M, && \text{(B.5)}\\
y_{CP} &= y_{12}\cos\phi_2^\Gamma, && \text{(B.6)}\\
\Delta x &= -y_{12}\sin\phi_2^\Gamma, && \text{(B.7)}\\
-\Delta Y = \Delta y &= x_{12}\sin\phi_2^M, && \text{(B.8)}\\
x' &= [\text{sign}(\cos\phi_2^M)x_{12}\cos\Delta_{K\pi} - \text{sign}(\cos\phi_2^\Gamma)y_{12}\sin\Delta_{K\pi}](1\mp A_{K\pi}), && \text{(B.9)}\\
y' &= [\text{sign}(\cos\phi_2^\Gamma)y_{12}\cos\Delta_{K\pi} + \text{sign}(\cos\phi_2^M)x_{12}\sin\Delta_{K\pi}](1\mp A_{K\pi}), && \text{(B.10)}\\
x'^{\pm} &= x_{12}\cos\big(\Delta_{K\pi}\pm\phi_2^M\big) - y_{12}\sin\big(\Delta_{K\pi}\pm\phi_2^\Gamma\big), && \text{(B.11)}\\
y'^{\pm} &= y_{12}\cos\big(\Delta_{K\pi}\pm\phi_2^\Gamma\big) + x_{12}\sin\big(\Delta_{K\pi}\pm\phi_2^M\big), && \text{(B.12)}\\
A_{CP}^{K\pi} &= \frac{2\sqrt{R_{K\pi}}\cos\Delta_{K\pi}+y_{12}}{1+R_{K\pi}+\sqrt{R_{K\pi}}(y_{12}\cos\Delta_{K\pi}+x_{12}\sin\Delta_{K\pi})+\frac{1}{2}(x_{12}^2+y_{12}^2)}, && \text{(B.13)}\\
y_{CP}^{K\pi} &= -2\sqrt{R_{K\pi}}\,y_{12}\cos\Delta_{K\pi}\cos\phi_2^\Gamma, && \text{(B.14)}\\
y_{CP}^{K^-\pi^+} &= \sqrt{R_{K\pi}}\Big[x_{12}\sin\Delta_{K\pi}\cos\phi_2^M - y_{12}\cos\Delta_{K\pi}\cos\phi_2^\Gamma\Big], && \text{(B.15)}\\
\Delta Y_{K^-\pi^+} &= \sqrt{R_{K\pi}}\Big[\;x_{12}\sin\phi_f^M\cos\Delta_{K\pi}+y_{12}\sin\phi_f^\Gamma\sin\Delta_{K\pi} && \text{(B.16)}\\
&\qquad +\tfrac{1}{2}A_{K\pi}(x_{12}\sin\Delta_{K\pi}\cos\phi_f^M - y_{12}\cos\Delta_{K\pi})\Big].
\end{aligned}
$$

The confidence regions of the theoretical parameters are compared, before and after the ΔY measurement presented in this thesis, in Fig. 9.3 of Sect. 9.1.

The superweak approximation [85] consists in the assumption that the only source of *CP* violation in D^0-meson decays is given by *CP*-violating interactions with new particles whose mass scale is much higher than that of D^0 mesons. Consequently, the only parameter responsible for *CP* violation would be the mixing-matrix element M_{12} or, equivalently, the weak angle ϕ_2^M [42, 43, 199]. In the fit, this limit is implemented by using the same parameters and expressions as the theoretical parametrisation, with the exception that the asymmetry $A_{K\pi}$ and the angle ϕ_2^Γ are fixed to zero. The results are displayed in Fig. B.1. Since the number of free parameters to fit to the same experimental results is lower, the improvement due to the measurement presented in this thesis on the knowledge of the *CP*-violation parameter ϕ_2^M is smaller than that achieved in the theoretical parametrisation for the parameters ϕ_2^M and ϕ_2^Γ.

B.2 Phenomenological parametrisation

The expressions of the experimental observables in Table B.1 in terms of the phenomenological parameters x, y, ϕ_2, $|q/p|$, $\Delta_{K\pi}$, $R_{K\pi}$ and $A_{K\pi}$ are

$$
\begin{aligned}
x_{CP} &= \frac{1}{2}\left[+x\cos\phi_2\left(\left|\frac{q}{p}\right|+\left|\frac{p}{q}\right|\right)+y\sin\phi_2\left(\left|\frac{q}{p}\right|-\left|\frac{p}{q}\right|\right)\right], && \text{(B.17)}\\
y_{CP} &= \frac{1}{2}\left[-x\sin\phi_2\left(\left|\frac{q}{p}\right|-\left|\frac{p}{q}\right|\right)+y\cos\phi_2\left(\left|\frac{q}{p}\right|+\left|\frac{p}{q}\right|\right)\right], && \text{(B.18)}\\
\Delta x &= \frac{1}{2}\left[+x\cos\phi_2\left(\left|\frac{q}{p}\right|-\left|\frac{p}{q}\right|\right)+y\sin\phi_2\left(\left|\frac{q}{p}\right|+\left|\frac{p}{q}\right|\right)\right], && \text{(B.19)}\\
-\Delta Y = \Delta y &= \frac{1}{2}\left[-x\sin\phi_2\left(\left|\frac{q}{p}\right|+\left|\frac{p}{q}\right|\right)+y\cos\phi_2\left(\left|\frac{q}{p}\right|-\left|\frac{p}{q}\right|\right)\right], && \text{(B.20)}
\end{aligned}
$$

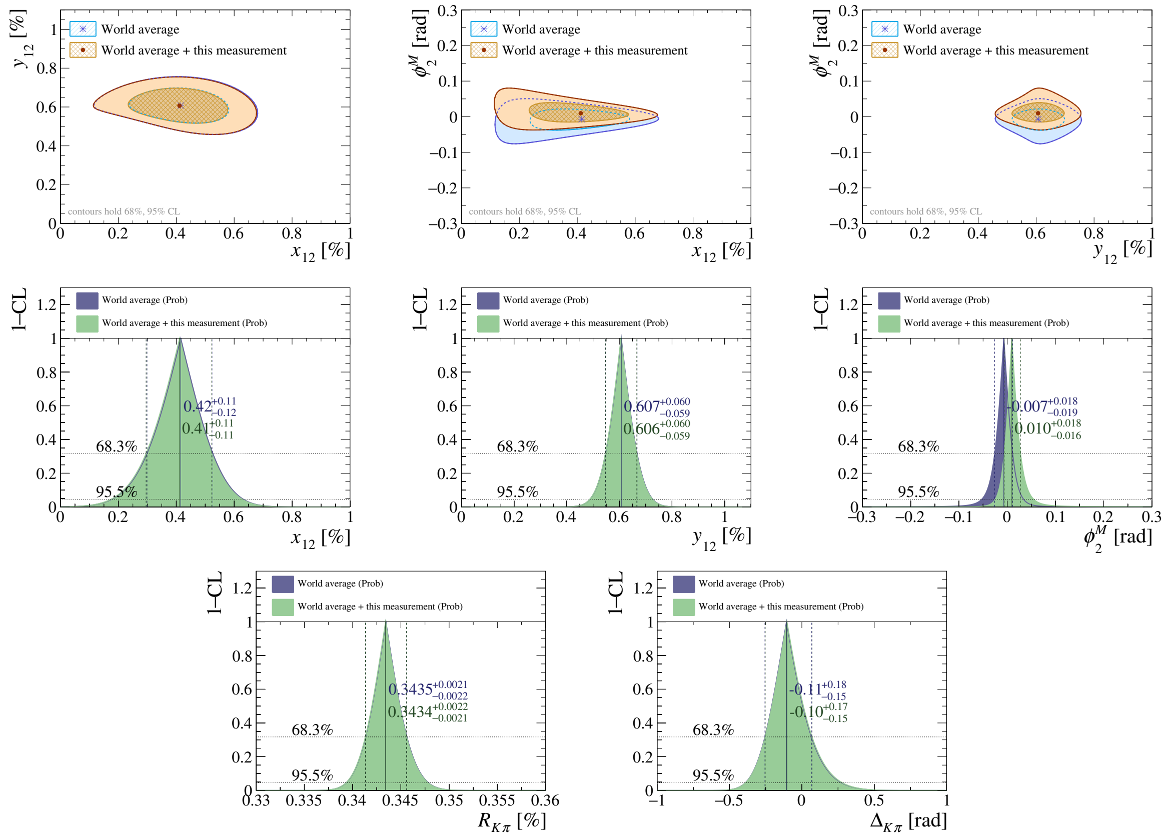

Figure B.1: Impact of the present measurement of ΔY on the knowledge of the parameters quantifying mixing and time-dependent CP violation in D^0 mesons, in the superweak approximation.

$$x' = x\cos\Delta_{K\pi} - x\sin\Delta_{K\pi}, \tag{B.21}$$

$$y' = x\sin\Delta_{K\pi} + y\cos\Delta_{K\pi}, \tag{B.22}$$

$$x'^{\pm} = \left|\frac{q}{p}\right|^{\pm 1}(1 \mp A_{K\pi})\left[x\cos\!\left(\Delta_{K\pi} \mp \phi_{\lambda_f}\right) - y\sin\!\left(\Delta_{K\pi} \mp \phi_{\lambda_f}\right)\right], \tag{B.23}$$

$$y'^{\pm} = \left|\frac{q}{p}\right|^{\pm 1}(1 \mp A_{K\pi})\left[x\sin\!\left(\Delta_{K\pi} \mp \phi_{\lambda_f}\right) + y\cos\!\left(\Delta_{K\pi} \mp \phi_{\lambda_f}\right)\right], \tag{B.24}$$

$$\begin{aligned}\Delta Y_{K^-\pi^+} \approx \frac{\sqrt{R_{K\pi}}}{2}\Bigg[&-(x\cos\Delta_{K\pi} + y\sin\Delta_{K\pi})\sin\phi_2\left(\left|\frac{q}{p}\right| + \left|\frac{p}{q}\right|\right) \\ &+ (y\cos\Delta_{K\pi} - x\sin\Delta_{K\pi})\cos\phi_2\left(\left|\frac{q}{p}\right| - \left|\frac{p}{q}\right| - A_{K\pi}\right)\Bigg],\end{aligned} \tag{B.25}$$

$$y_{CP}^{K\pi} = \sqrt{R_{K\pi}}\cos\Delta_{K\pi}\left[-y\cos\phi_2\left(\left|\frac{q}{p}\right| + \left|\frac{p}{q}\right|\right) + x\sin\phi_2\left(\left|\frac{q}{p}\right| - \left|\frac{p}{q}\right|\right)\right], \tag{B.26}$$

$$\begin{aligned}y_{CP}^{K^-\pi^+} = \frac{\sqrt{R_{K\pi}}}{2}\Bigg[&\ (x\sin\Delta_{K\pi} - y\cos\Delta_{K\pi})\cos\phi_2\left(\left|\frac{q}{p}\right| + \left|\frac{p}{q}\right|\right) \\ &+ (x\cos\Delta_{K\pi} + y\sin\Delta_{K\pi})\sin\phi_2\left(\left|\frac{q}{p}\right| - \left|\frac{p}{q}\right|\right)\Bigg],\end{aligned} \tag{B.27}$$

$$A_{CP}^{K\pi} = \frac{2\sqrt{R_{K\pi}}\cos\Delta_{K\pi} + y}{1 + R_{K\pi} + \sqrt{R_{K\pi}}(y\cos\Delta_{K\pi} + x\sin\Delta_{K\pi}) + \frac{1}{2}(x^2+y^2)}. \tag{B.28}$$

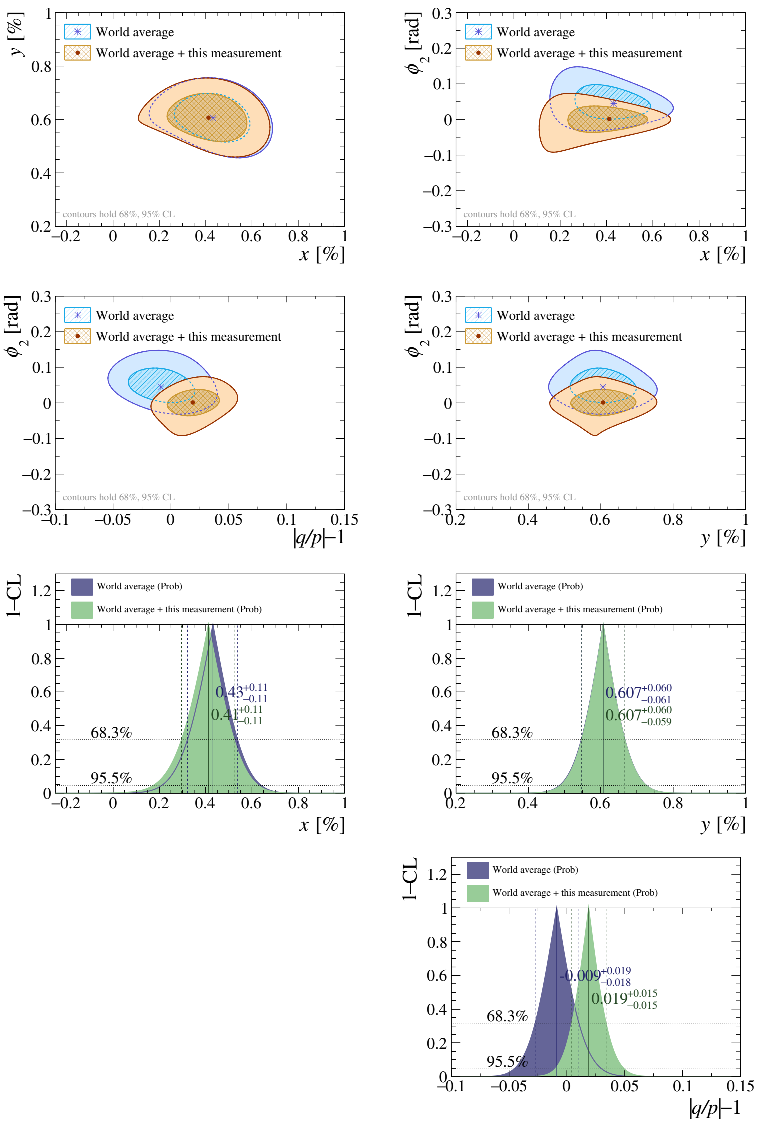

Figure B.2: Impact of the present measurement of ΔY on the knowledge of the parameters quantifying mixing and time-dependent *CP* violation in D^0 mesons, in the phenomenological approximation. The results for the parameters $A_{K\pi}$, $R_{K\pi}$ and $\Delta_{K\pi}$ are the same as in Fig. 9.3.

The confidence regions for all the parameters, compared before and after the ΔY measurement presented in this thesis, are displayed in Fig. B.2.

B.3 Upper estimate on the magnitude of $\Delta Y_{K^-\pi^+}$

An upper limit on the magnitude of the observable $\Delta Y_{K^-\pi^+}$ is obtained by adding it as nuisance parameter to the set of theoretical parameters. Then, a fictitious measurement is added to those of Table B.1, constraining the difference between the magnitudes of the left- and right-hand sides of Eq. (B.16) to coincide within an uncertainty much smaller than the experimental precision on $\Delta Y_{K^-\pi^+}$. The confidence interval for the magnitude of $\Delta Y_{K^-\pi^+}$, evaluated based on a fit

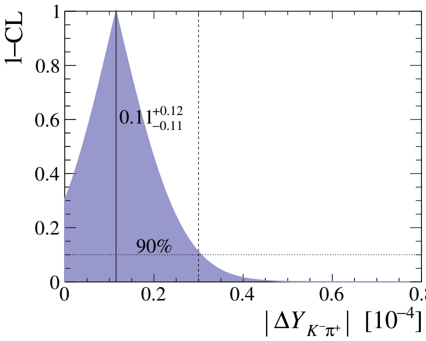

Figure B.3: Lower confidence interval on the absolute value of $\Delta Y_{K^-\pi^+}$, obtained with all measurements in Table B.1, (left) except and (right) including the one presented in this thesis.

that does not employ the measurement of the ΔY observable presented in this thesis as input, is displayed in Fig. B.3. The magnitude of $\Delta Y_{K^-\pi^+}$ is estimated to be less than 0.3×10^{-4} at 90% confidence level.

B.4 Impact of neglecting $y_{CP}^{K^-\pi^+}$ in the measurement of y_{CP}

All the studies of D^0-meson decays to date have neglected the contribution of the parameter $y_{CP}^{K^-\pi^+}$ to the measurements of the parameter y_{CP} that are performed through the procedure of Sect. 2.1.2, *cf.* the Eqs. (2.6) and (2.7). This holds also for the world-average fits used to estimate the values of the mixing and *CP*-violation parameters [28, 47, 122, 123]. The impact of this approximation is shown for the current world average of the mixing and *CP* violation parameters — including the measurement presented in this thesis — in Fig. B.4. The most precise measurements of the y_{CP} parameter employ the K^+K^- and $\pi^+\pi^-$ final states, as shown in Table B.1. Therefore, they actually measure the difference $y_{CP} - y_{CP}^{K^-\pi^+}$. Since the value of $y_{CP}^{K^-\pi^+}$ is negative, the world average of the parameter $y_{12} \approx y_{CP}$ is biased to larger values when $y_{CP}^{K^-\pi^+}$ is neglected. This bias is currently small — it corresponds to around $+0.07 \times 10^{-3}$, that is 12% of the precision on the parameter y_{12} —, since the knowledge of y_{12} is driven by the precise measurement of the parameter y' from the time-dependent analysis of WS/RS $D^0 \to K^\pm\pi^\mp$ decays. The precision of the latter measurement is dominated by the latest measurement by the LHCb collaboration, performed using the D^{*+}-tagged data collected during 2011–2012 and 2015–2016 [60]. On the contrary, while the most precise measurement of the y_{CP} parameter was also performed by the LHCb collaboration, it employs only the much smaller sample of μ^--tagged data collected during 2011–2012 [61]. The precision on y_{CP} is expected to improve considerably in the next years. For example, the statistical precision achievable by measuring it with the 2015–2018 D^{*+}-tagged data sample is as low as 0.22×10^{-3} [138]. This value is a factor of 5 smaller than that of the current world average of y_{CP}, and corresponds to around 3.6% of the world-average value of the parameter y_{12}, $(6.1 \pm 0.6) \times 10^{-3}$. Therefore, it would be be smaller by a factor of 1.6 than the bias from neglecting $y_{CP}^{K^-\pi^+}$, which is approximately equal to $\sqrt{R_{K\pi}} \approx 5.7\%$ of the value of y_{12}. Considering the contribution from $y_{CP}^{K^-\pi^+}$ to the measurements of y_{CP} performed with the method described in Sect. 2.1.2 will thus be crucial in all future fits to the parameters quantifying mixing and *CP* violation in D^0 mesons.

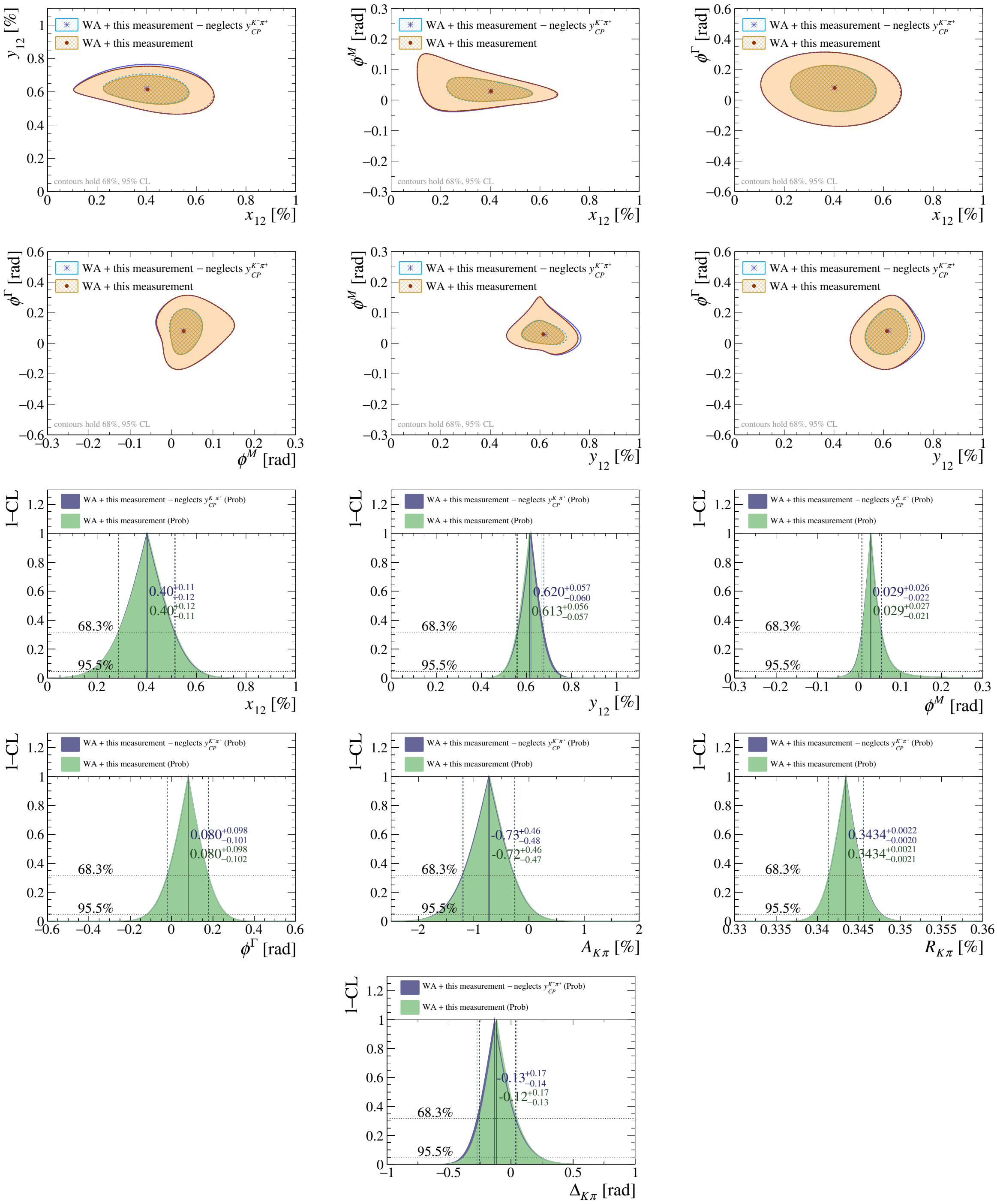

Figure B.4: Impact of neglecting the contribution of $y_{CP}^{K^-\pi^+}$ in the measurement of the y_{CP} parameter on the knowledge of the parameters quantifying charm mixing and time-dependent CP violation, in the theoretical parametrisation.

Appendix C

Definition of the trigger variables

This appendix reports the definition of the variables that are used in the software-trigger selection of Sects. 4.1.2 and 4.1.3, but are not defined there.

- **Track-based ghost probability**: output of a neural network quantifying the probability that the track does not correspond to the passage of any real particles [200]. Possible causes of misreconstruction include the wrong association of hits belonging to two or more different tracks or that are due to detector noise, the association of two segments belonging to two different tracks in the VELO and in the T-stations, and the persistence of real tracks in more than one event — the so-called *spillover* — for detectors whose time response is comparable or longer than the time between two consecutive collisions of the proton bunches (25 ns). If this is the case, some hits might occasionally be taken into consideration in more than one event.

- **PV of a particle**: in the first-stage (second-stage) software trigger, it is defined as the PV to which the particle IP (χ^2_{IP}) is the smallest.

- **Direction angle (θ_{DIRA})**: the angle between the momentum of a particle and the vector connecting its PV to its decay vertex (DV). It is expected to be zero within experimental uncertainty for particles originating from the PV. It can be used to discriminate primary $D^0 \to h^+h^-$ decays from secondary decays, for which the momentum of the D^0 is not necessarily aligned to that of its parent B meson, and from D-meson partially reconstructed decays, where the D momentum is wrongly calculated from a subset of the final-state particles of its decay.

- $\eta = -\log(\tan\theta/2)$: in the two-track line of the first-stage software trigger, it denotes the parametrisation *via* pseudorapidity of the polar angle, *i.e.* the angle with respect to the z axis, of the displacement vector between the PV and the two-track vertex.

- **Corrected mass**: it is defined as $m_{\mathrm{corr}} = \sqrt{m^2 + p_{\mathrm{T}}^2} + p_{\mathrm{T}}$, where p_{T} is the component of the sum of the momenta of the two tracks transverse to the displacement vector connecting their PV to their fitted vertex. Thus, the p_{T} is equal to $p_{\mathrm{T}} = p\sin\theta_{\mathrm{DIRA}}$, where p and θ_{DIRA} are referred to the combination of the two tracks. The corrected mass partially corrects the value of the measured mass of long-lived particles that are not entirely reconstructed, for example because they decayed semileptonically with the emission of a neutrino. It corresponds to the minimum mass of the reconstructed particle, obtained by adding to its measured momentum some transverse momentum from massless undetected particles, that is needed to set θ_{DIRA} equal to zero. In the case of $D^0 \to h^+h^-$ decays, it is equal to the measured invariant mass within experimental resolution.

- in the two-track line of the first-stage software trigger, the requirement $\theta_{\mathrm{DIRA}}(\mathrm{trk}_1 + \mathrm{trk}_2) < \pi/2$ ensures that the measured vertex of the two tracks does not lie behind their PV.

Appendix D

Kinematic weighting

This appendix provides further details on the kinematic weighting described in Sect. 5.2, as well as additional studies on the nuisance asymmetries and on the interplay of the kinematic weighting with the subtraction of the contribution to the asymmetry from secondary decays.

D.1 Impact of the first-stage software-trigger requirements on the measurement

During the 2015–2018 data-taking, the first-stage software-trigger requirements had a larger impact in the determination of the correlation of the kinematics of the event with the D^0 decay time than those of the second-stage software trigger. This is a consequence of the fact that these lines were designed to select a pure sample of B-meson decays. On the contrary, decays of primary D mesons were employed as background in the training of the classifier of the two-track line. Figure D.1 displays the correlations of decay time with the D^0-meson momentum, as a function of the first-stage software-trigger requirement, both for the single- and the two-track lines. The two-track trigger line introduced in 2015 allows for smaller correlations with respect to the single-track trigger line updated starting from that used during 2011–2012. Furthermore, the value of the thresholds for the parameter α_0 of Eq. (4.1) and for the classifier output have a large impact on the correlations. Feasibility studies are currently ongoing to introduce a two-track first-stage software-trigger line dedicated to D^0-meson two-body decays starting from 2022, designed to minimise the correlations. Thus, it would allow to minimise the nuisance time-dependent asymmetries and to maximise the statistical precision at equal decay yield, by minimising the dilution due to the kinematic weighting described in Sect. 5.4. In fact, the latter can increase significantly also for small changes of the selection requirements, *cf.* for example Ref. [117].

D.2 Weighting details

The distribution of the weights of the kinematic equalisation of Sect. 5.2 is shown in Fig. D.2 for all D^0-meson decay channels, while the distribution of the candidates with nonzero weights is displayed in Fig. D.3. The absolute value of the coefficient used to remove the $m(D^0\pi^+_{\text{tag}})$ background, as described in Sect. 4.3, is shown in Fig. D.4 for raw data and after each of the two steps of the kinematic weighting.

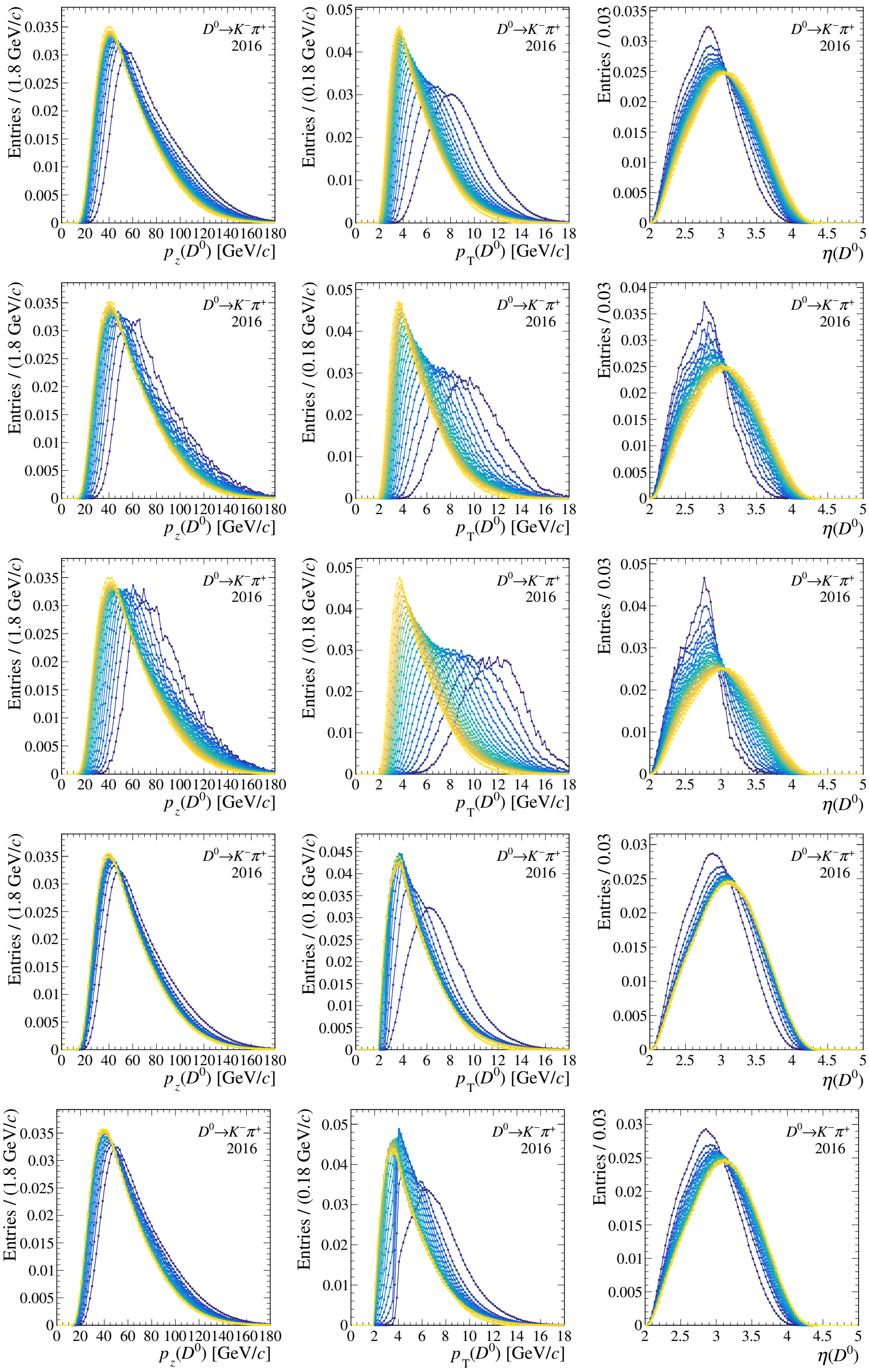

Figure D.1: Normalised distributions of the z and transverse components and of the pseudorapidity of the D^0 momentum, in different colours for different decay time bins, and for different first-stage software-trigger requirements. Blue (yellow) dots correspond to low (high) decay times, see Fig. 5.3 for the legend. The plots are produced using events where the D^0 meson was responsible for the first-stage software-trigger decision, for the following trigger lines, from top to bottom: the single-track line, with the α_0 parameter equal to 1.1, 1.6 and 2.3, and the two-track line with the classifier threshold equal to 0.95 and 0.97.

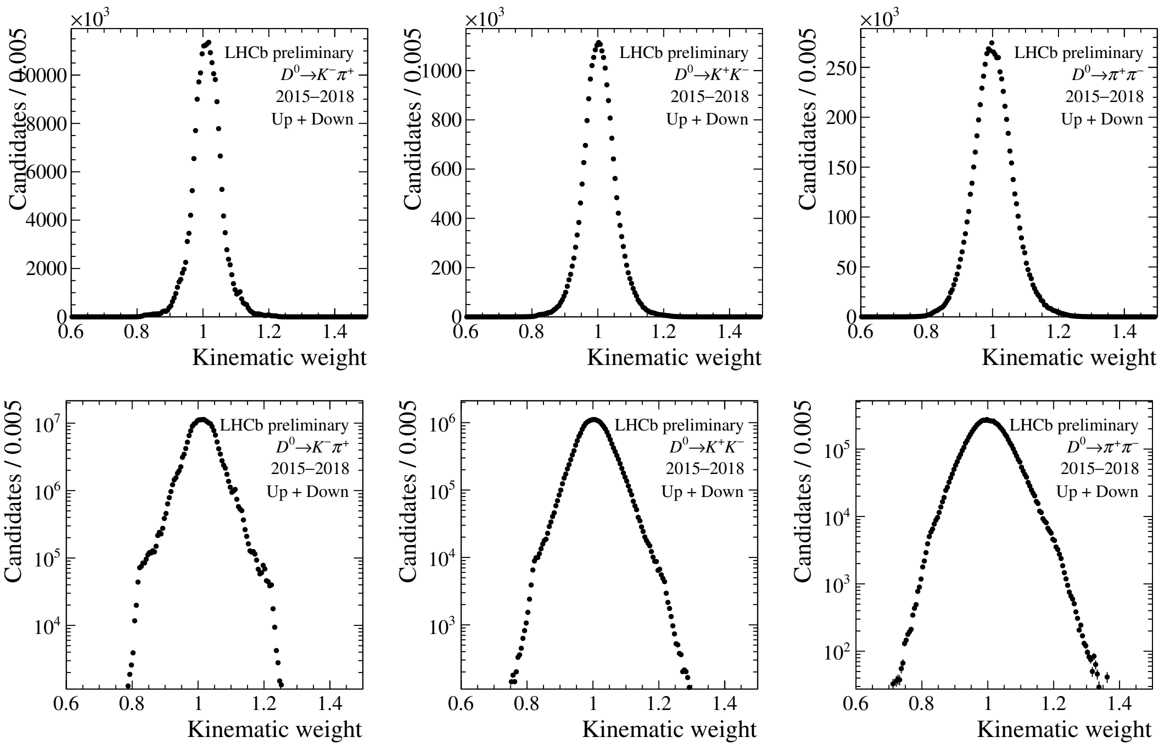

Figure D.2: Distribution of the weights of the kinematic equalisation of Sect. 5.2 for the (left) $K^-\pi^+$, (centre) K^+K^- and (right) $\pi^+\pi^-$ decay channels, in (top) linear and (bottom) logarithmic scale.

D.3 Additional studies

Alternative configurations for the kinematic weighting of Sect. 5.2 have been studied. All of them employ equally spaced binnings. Furthermore, the studies were carried out without correcting for the dilution of the measured value of ΔY discussed in Sect. 5.4, nor for the contribution to the asymmetry from secondary decays. In fact, the first effect is nearly negligible, while the subtraction of the bias from secondary decays provokes a shift of $\Delta Y_{K^-\pi^+}$ equal to -0.25×10^{-4}, independently of the configuration of the kinematic weighting. In fact, the weighting does not modify the flavour-integrated fraction of secondary decays in the sample, and to first order it does not modify the difference between the asymmetry of secondary and primary decays, either, as shown in Fig. D.5. Since these two quantities are the only ones determining the size of the bias, this is not affected by the kinematic weighting. Therefore, in the following the results should be compared with those reported in Sect. 5.2, and the compatibility of $\Delta Y_{K^-\pi^+}$ with zero should be be tested after a shift of -0.25×10^{-4}.

The analysed weighting configurations are listed below. In all cases, in each step of the weighting at least 40 entries for both D^0 and $\overline{D}^0$ candidates and an asymmetry less than 20% are always required in each three-dimensional bin, otherwise the corresponding weight is set to zero.

1. Two weightings, the first of the D^0 kinematics and the second of the kinematics of the D^0 and of the $\pi^+_{\rm tag}$ at the same time:

   - the first weighting equalises the $(\theta_x(D^0), \theta_y(D^0), k(D^0))$ distribution by employing 36, 27 and 40 bins in the ranges $[-0.27, 0.27]\,\text{rad}$, $[-0.27, 0.27]\,\text{rad}$ and $[0., 0.06]\,c/\text{GeV}$,

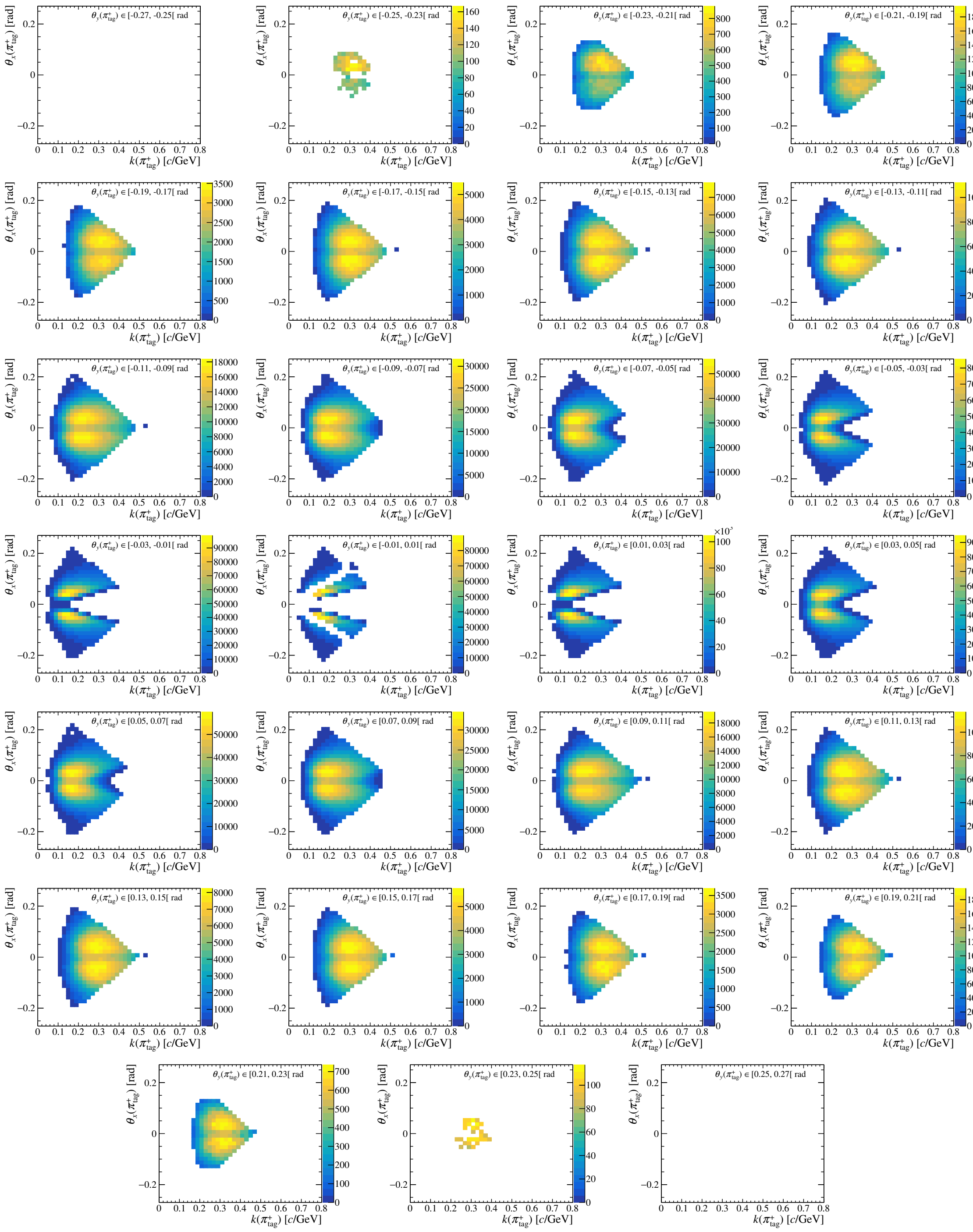

Figure D.3: Distribution of θ_x *versus* k of the candidates of the $K^-\pi^+$ subsample, collected during 2017 with the *MagUp* polarity, which are not rejected by the requirements on the minimum number of events and maximum asymmetry per bin in the first step of the kinematic weighting. The distributions are shown for each bin of the third weighted variable, θ_y. The requirements reject many of the candidates with low curvature (*cf.* Fig. 5.1), as well as those that are deflected into the LHC beam pipe by the magnet, corresponding to the empty diagonal bands of the plot corresponding to $\theta_y \in [-10, 10]$ mrad.

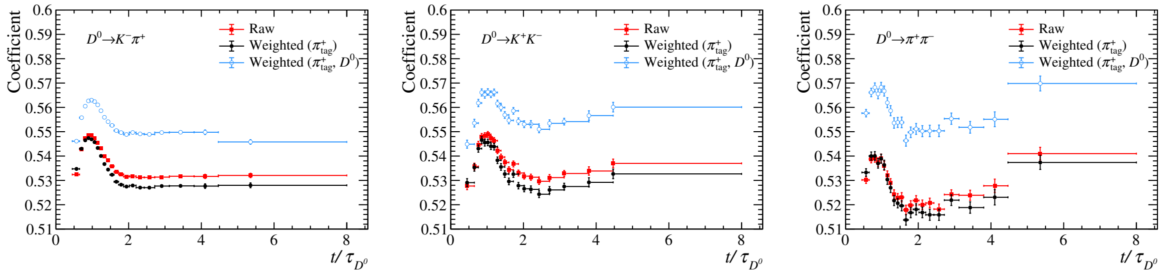

Figure D.4: Absolute value of the coefficient used in the subtraction of the $m(D^0\pi^+_{\rm tag})$ background described in Sect. 4.3, for raw data and after each of the two steps of the kinematic weighting, for the (left) $K^-\pi^+$, (centre) K^+K^- and (right) $\pi^+\pi^-$ decay channels.

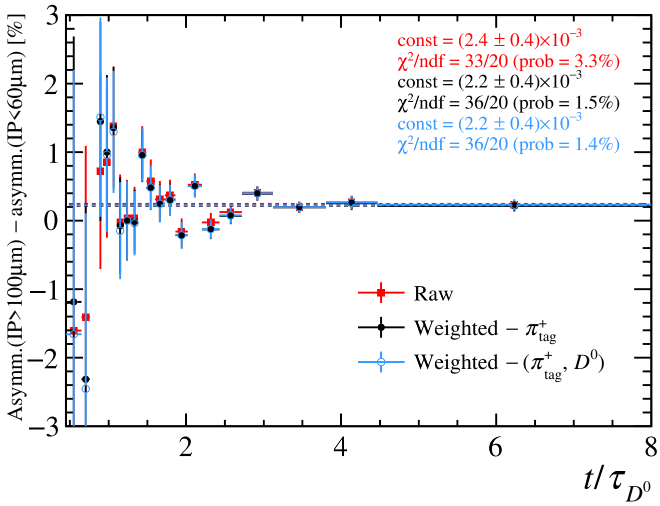

Figure D.5: Asymmetry difference of secondary and primary $K^-\pi^+$ candidates, before and after the kinematic weighting. This is calculated as the difference of the asymmetry of the candidates with IP $> 100\,\mu$m and those satisfying IP$(D^0) < 60\,\mu$m. These categories are good proxies of secondary and primary decays, while the subtraction allows to cancel the nuisance detection asymmetries also before the kinematic weighting. A constant fit is superimposed. The results show that the asymmetry difference changes by less than 10% after the kinematic weighting.

respectively;

- the second weighing equalises the $(p_{\rm T}(D^0), \eta(D^0), \eta(\pi^+_{\rm tag}))$ distribution by employing 32, 25 and 22 bins in the ranges $[2, 18]$ GeV/c, $[2, 4.5]$ and $[2, 4.2]$, respectively.

The results are $(-0.11 \pm 0.49) \times 10^{-4}$, $(-1.89 \pm 1.50) \times 10^{-4}$ and $(-3.07 \pm 2.78) \times 10^{-4}$, corresponding to a shift from the baseline value of 0.00×10^{-4}, -0.03×10^{-4} and 0.34×10^{-4} for the $K^-\pi^+$, K^+K^- and $\pi^+\pi^-$ channels, respectively.

2. Two weightings, the first of the D^0 kinematics and the second of the $\pi^+_{\rm tag}$ kinematics:

   - the first weighting equalises the $(\theta_x(D^0), \theta_y(D^0), k(D^0))$ distribution employing 36, 27 and 40 bins in the ranges $[-0.27, 0.27]$ rad, $[-0.27, 0.27]$ rad and $[0., 0.06]$ c/GeV, respectively.
   - the second weighting equalises the $(\theta_x(\pi^+_{\rm tag}), \theta_y(\pi^+_{\rm tag}), k(\pi^+_{\rm tag}))$ distribution employing

36, 27 and 40 bins in the ranges $[-0.27, 0.27]$ rad, $[-0.27, 0.27]$ rad and $[0., 0.8]$ c/GeV, respectively;

The results are $(-0.40 \pm 0.50) \times 10^{-4}$, $(-1.15 \pm 1.53) \times 10^{-4}$ and $(-2.13 \pm 2.87) \times 10^{-4}$, corresponding to a shift from the baseline value of 0.51×10^{-4}, 0.70×10^{-4} and 1.28×10^{-4} for the $K^-\pi^+$, K^+K^- and $\pi^+\pi^-$ channels, respectively.

3. Two weightings, the first of the $\pi^+_{\rm tag}$ kinematics and the second of the D^0 kinematics:
   - the first weighting equalises the $(\theta_x(\pi^+_{\rm tag}), \theta_y(\pi^+_{\rm tag}), k(\pi^+_{\rm tag}))$ distribution employing 36, 27 and 40 bins in the ranges $[-0.27, 0.27]$ rad, $[-0.27, 0.27]$ rad and $[0., 0.8]$ c/GeV, respectively;
   - the second weighting equalises the $(\theta_x(D^0), \theta_y(D^0), k(D^0))$ distribution employing 36, 27 and 40 bins in the ranges $[-0.27, 0.27]$ rad, $[-0.27, 0.27]$ rad and $[0., 0.06]$ c/GeV, respectively.

   The results are $(0.01 \pm 0.48) \times 10^{-4}$, $(-1.47 \pm 1.49) \times 10^{-4}$ and $(-2.89 \pm 2.80) \times 10^{-4}$, corresponding to a shift from the baseline value of 0.10×10^{-4}, 0.38×10^{-4} and 0.53×10^{-4} for the $K^-\pi^+$, K^+K^- and $\pi^+\pi^-$ channels, respectively.

4. Four weightings, the first and the third of the $\pi^+_{\rm tag}$ kinematics and the second and fourth of the D^0 kinematics, using the same binning of the previous configuration. The results are $(-0.02 \pm 0.48) \times 10^{-4}$, $(-1.40 \pm 1.49) \times 10^{-4}$ and $(-2.76 \pm 2.80) \times 10^{-4}$, corresponding to a shift from the baseline value of 0.13×10^{-4}, 0.45×10^{-4} and 0.65×10^{-4} for the $K^-\pi^+$, K^+K^- and $\pi^+\pi^-$ channels, respectively.

The results for the four configurations are displayed for the $K^-\pi^+$ decay channel and all data subsamples in Fig. D.6. The baseline configuration of the weighting minimises the detection asymmetries of the D^0 and $\pi^+_{\rm tag}$ kinematics. The configurations (2) and (3) minimise by construction the detection asymmetries of the last-weighted particle; however, the particle that was weighted first displays larger asymmetries. Finally, the asymmetries are not reduced by iterating the weightings as done in the configuration (4) — in particular, the results after the third weighting are very similar to those after the first one and the results after the fourth weighting are very similar to those after the second one —, suggesting the need of a simultaneous weighting of the D^0 and $\pi^+_{\rm tag}$ kinematics, like that of the baseline configuration.

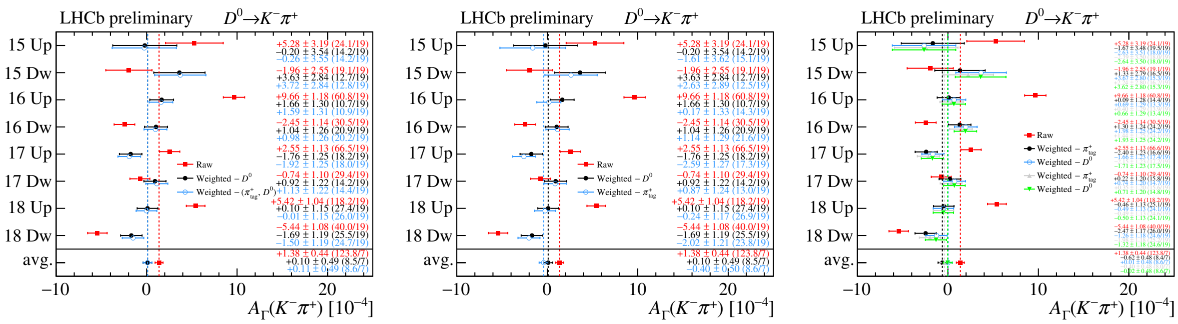

Figure D.6: Results for $\Delta Y_{K^-\pi^+}$ when adopting the alternative kinematic weightings described in the item (left) 1, (centre) 2 and (right) 3 and 4 of the list in Sect. D.2.

It is interesting to note that all configurations that weight the D^0 meson kinematics last (*e.g.* configurations number (1), (3) and (4)) display numerical results very similar to the baseline one

— the deviation of $\Delta Y_{K^-\pi^+}$ from the baseline result is always below 0.13×10^{-4} — , even if the residual asymmetries on the π^+_{tag} kinematics are larger. On the contrary, residual asymmetries of the D^0 kinematics, like those found for the configuration (2), correspond to much larger deviations of the results from the baseline ones.

D.4 Residual asymmetries

This section reports the plots of the measured asymmetry of the distributions of the momenta of the D^0 and π^+_{tag} mesons and of the D^0 flight distance for the $K^-\pi^+$ decay channel. The plots are produced by employing the whole 2015–2018 data sample, for the *MagUp* and *MagDown* polarities combined. The results for the signal channels K^+K^- and $\pi^+\pi^-$ are compatible with those of the $K^-\pi^+$ channel, but are characterised by larger statistical uncertainties. Therefore, they are not displayed for the sake of brevity.

The largest residual asymmetries are those of the $\eta(D^0)$ and $\eta(\pi^+_{\text{tag}})$ distributions. They display a sawtooth behaviour, with a maximum value of around 4×10^{-3} and opposite tooth slopes for the D^0 and π^+_{tag} mesons. In the plots each tooth spans four bins, which correspond to a single bin of the kinematic weighting. One possible explanation of these asymmetries is that there is a different bias in the measurement of the pseudorapidity of π^+_{tag} and π^-_{tag} mesons, and this bias is opposite in sign with respect to that of D^0 and $\overline{D}^0$ mesons. Equalising the kinematics of π^+_{tag} and π^-_{tag} mesons may thus increase the asymmetry between the D^0 and $\overline{D}^0$ kinematic distributions, and *vice versa*. Therefore, a simultaneous weighting of $\eta(D^0)$ and $\eta(\pi^+_{\text{tag}})$, like that of the second kinematic weighting, would be needed to keep the effect under control. In any case, these residual asymmetries have a negligible effect on the measurement. In fact, in Sect. 7.4 the width of the bins of the kinematic weighting is decreased up to a factor of 4 for each variable, and the width of the asymmetry tooth of the two pseudorapidities is reduced accordingly, but the shift of the measured value of $\Delta Y_{K^-\pi^+}$ remains below 0.05×10^{-4}.

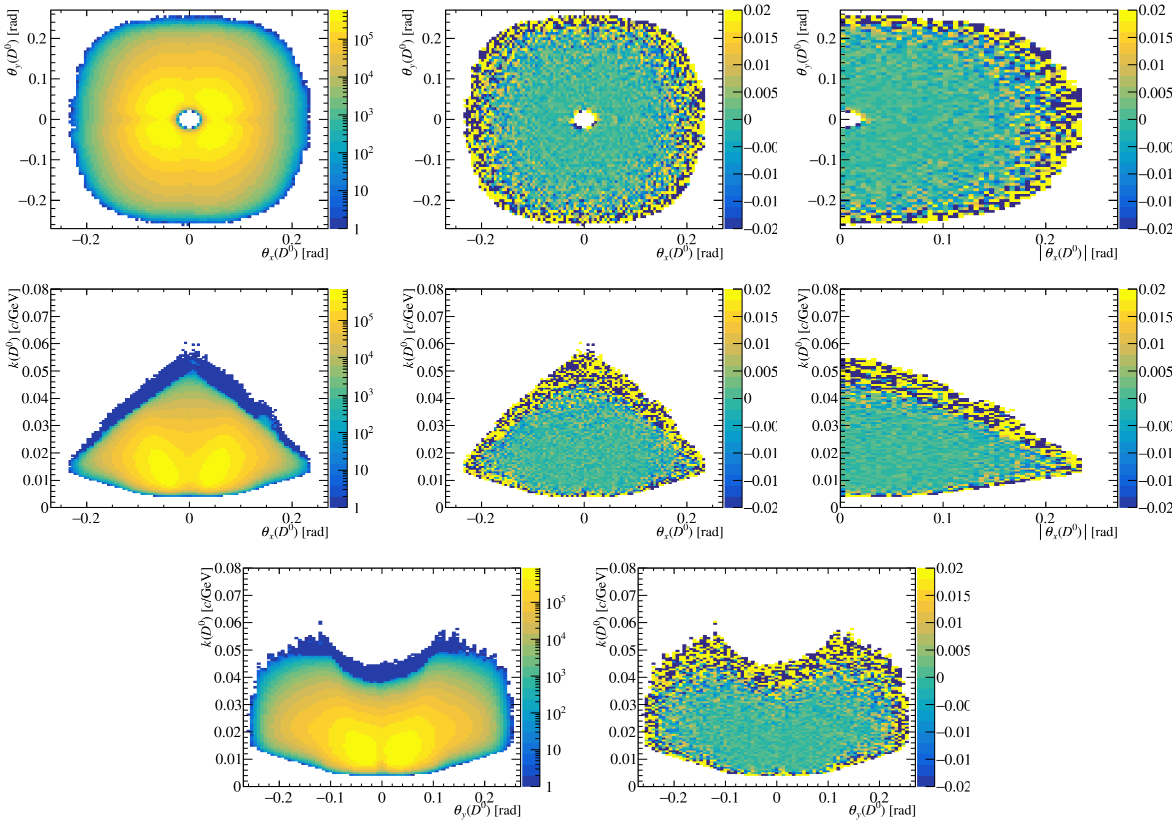

Figure D.7: Two-dimensional distributions and asymmetries of the vector momentum of the D^0 meson, for the full $D^0 \to K^-\pi^+$ data sample.

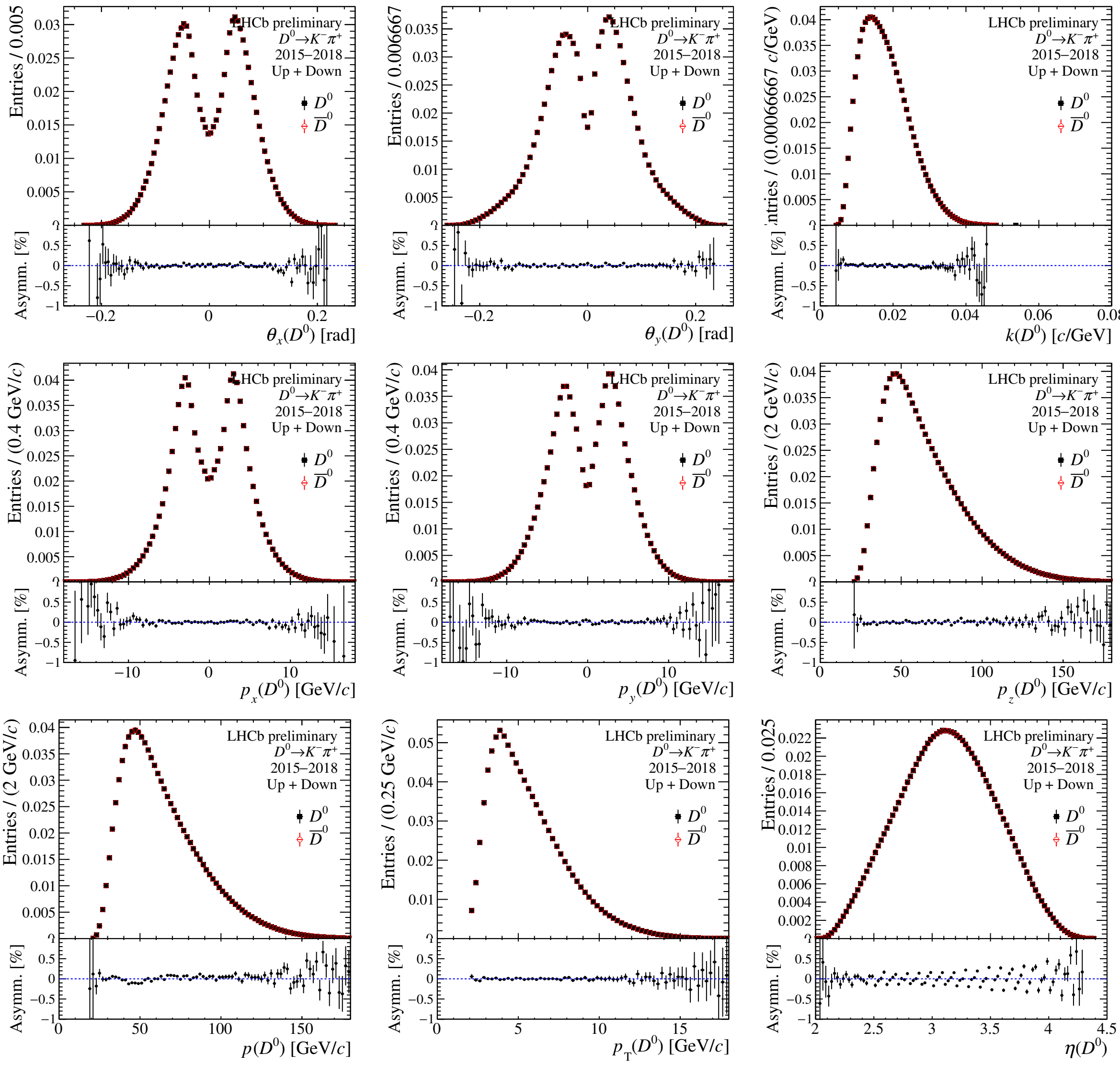

Figure D.8: Distributions and asymmetries of the momentum of the D^0 meson for the full $D^0 \to K^-\pi^+$ data sample.

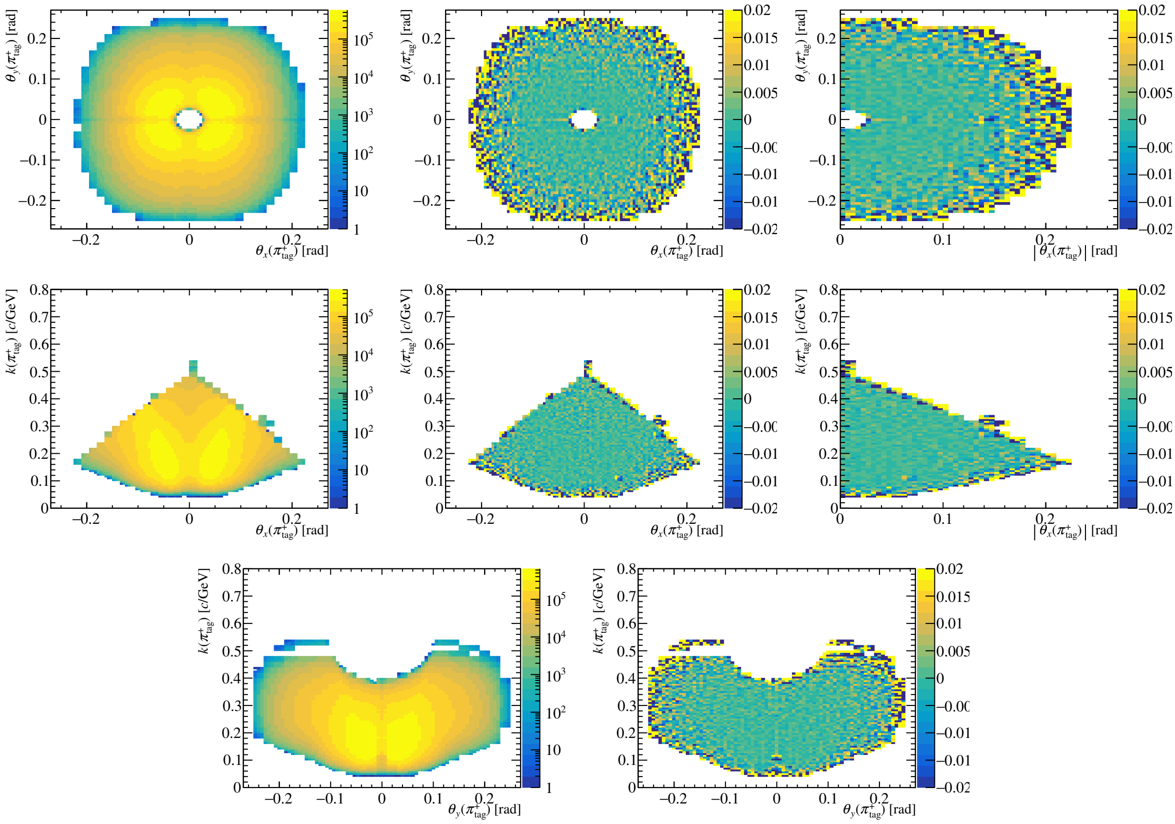

Figure D.9: Two-dimensional distributions and asymmetries of the vector momentum of the π^+_{tag} meson, for the full $D^0 \to K^-\pi^+$ data sample.

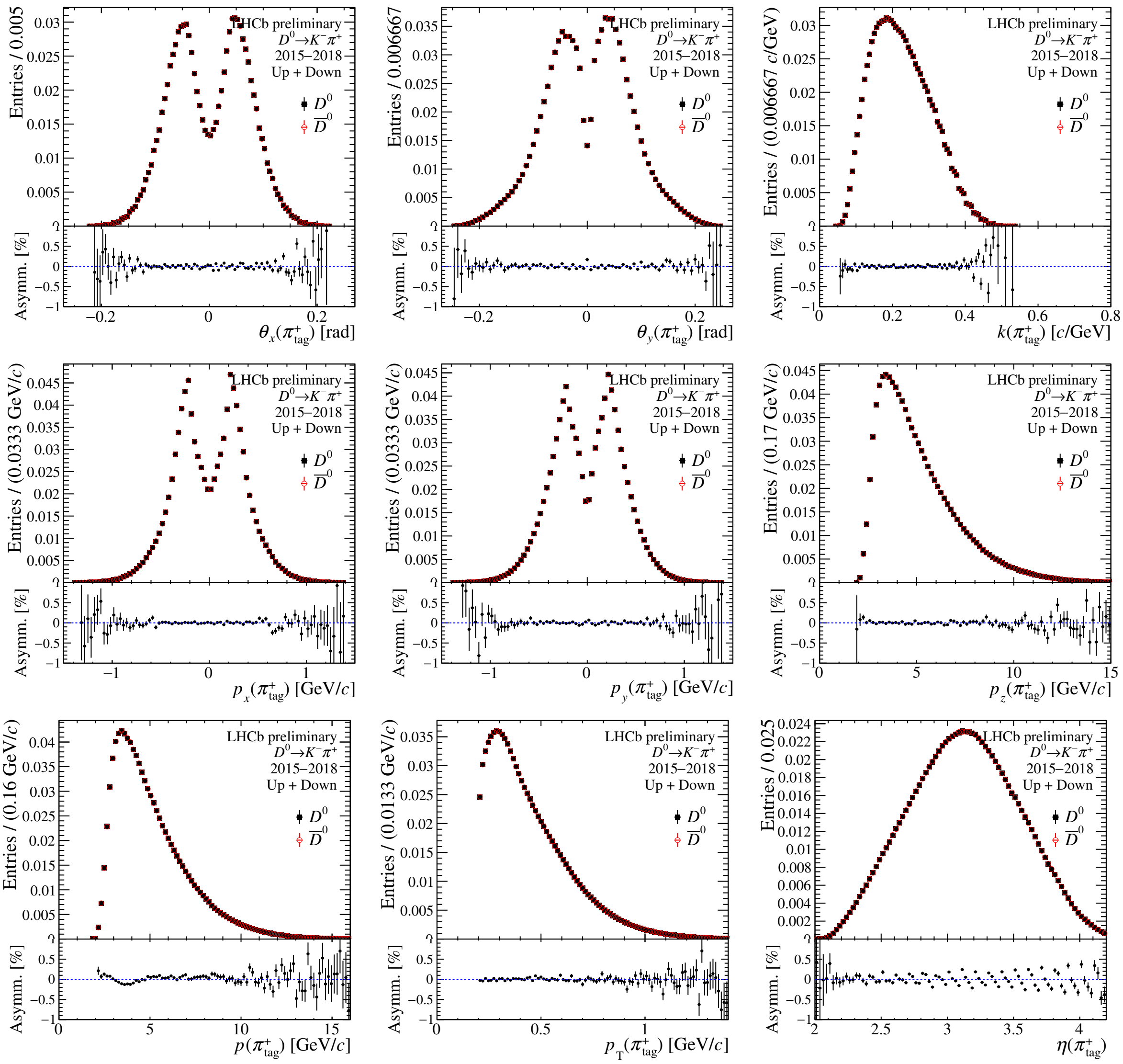

Figure D.10: Distributions and asymmetries of the momentum of the $\pi^+_{\rm tag}$ meson for the full $D^0 \to K^-\pi^+$ data sample.

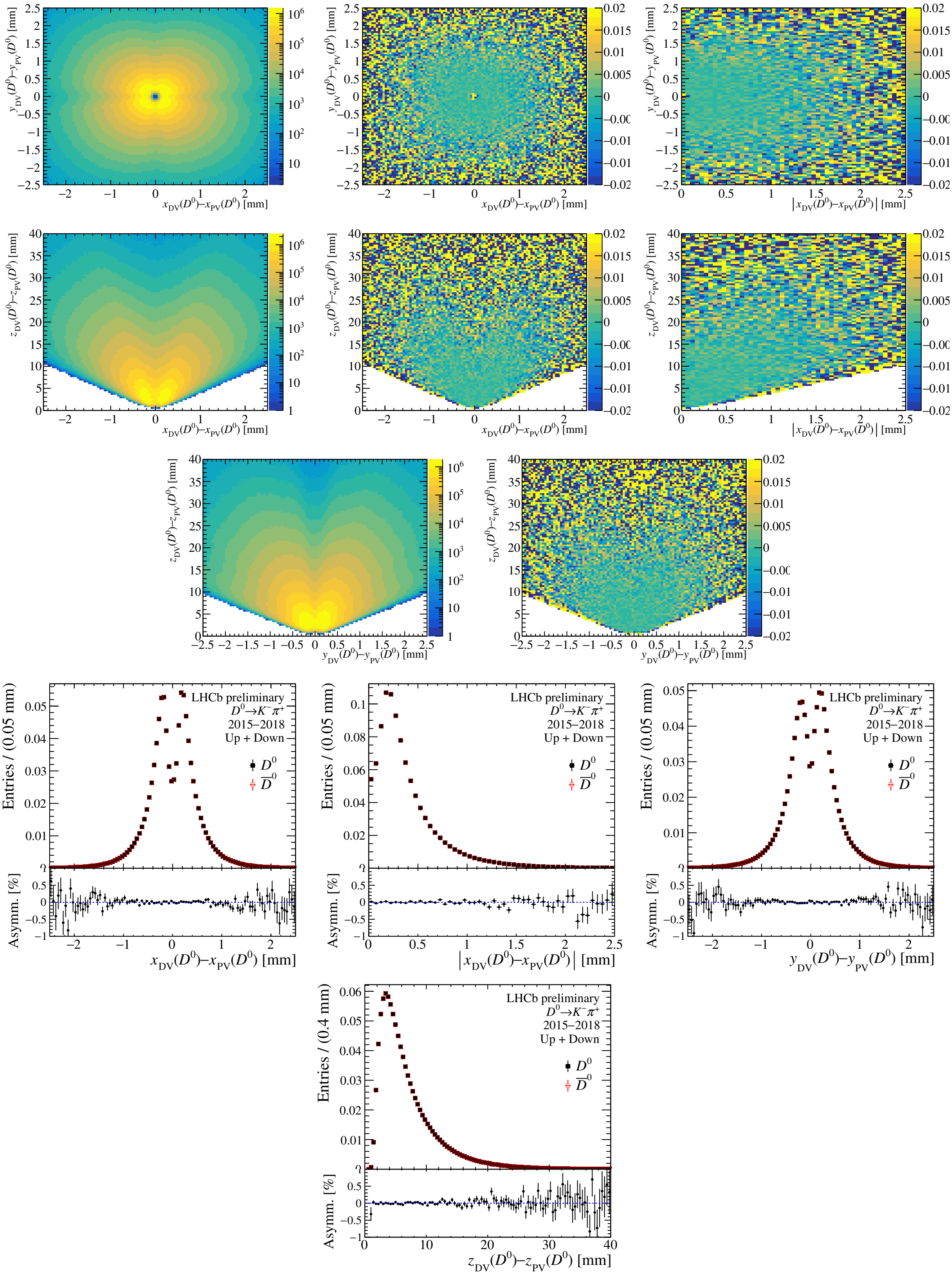

Figure D.11: Distributions and asymmetries of the D^0 flight distance for the full $D^0 \to K^-\pi^+$ data sample.

D.5 Correlation of $m(D^0\pi^+_{\rm tag})$ with the weighting variables

The distributions of the variables employed in the kinematic weighting of Sect. 5.2 are displayed for the $m(D^0\pi^+_{\rm tag})$ signal window and for the baseline and alternative lateral windows defined in Sect. 7.1 in Fig. D.12. Whereas the signal distributions (red points) differ significantly from those of the $m(D^0\pi^+_{\rm tag})$ lateral windows, the background distributions in the various lateral windows are nearly indistinguishable. The only exception is the $p_{\rm T}(D^0)$ distribution of the leftmost window, which displays and intermediate shape between the signal one and that of the other lateral windows. This behaviour is probably due to the larger contamination of signal events in the leftmost window. Furthermore, the contamination of secondary decays, whose $p_{\rm T}(D^0)$ is larger on average than that of primary decays and whose $m(D^0\pi^+_{\rm tag})$ distribution has a long left tail, might play a role, too.

In any case, this is not expected to have a significant impact on the measurement. In fact, the background asymmetry in both the leftmost and baseline lateral windows is less than 5×10^{-3}, as shown in Fig. D.13. Therefore, it is reasonable to assume that the background under the signal

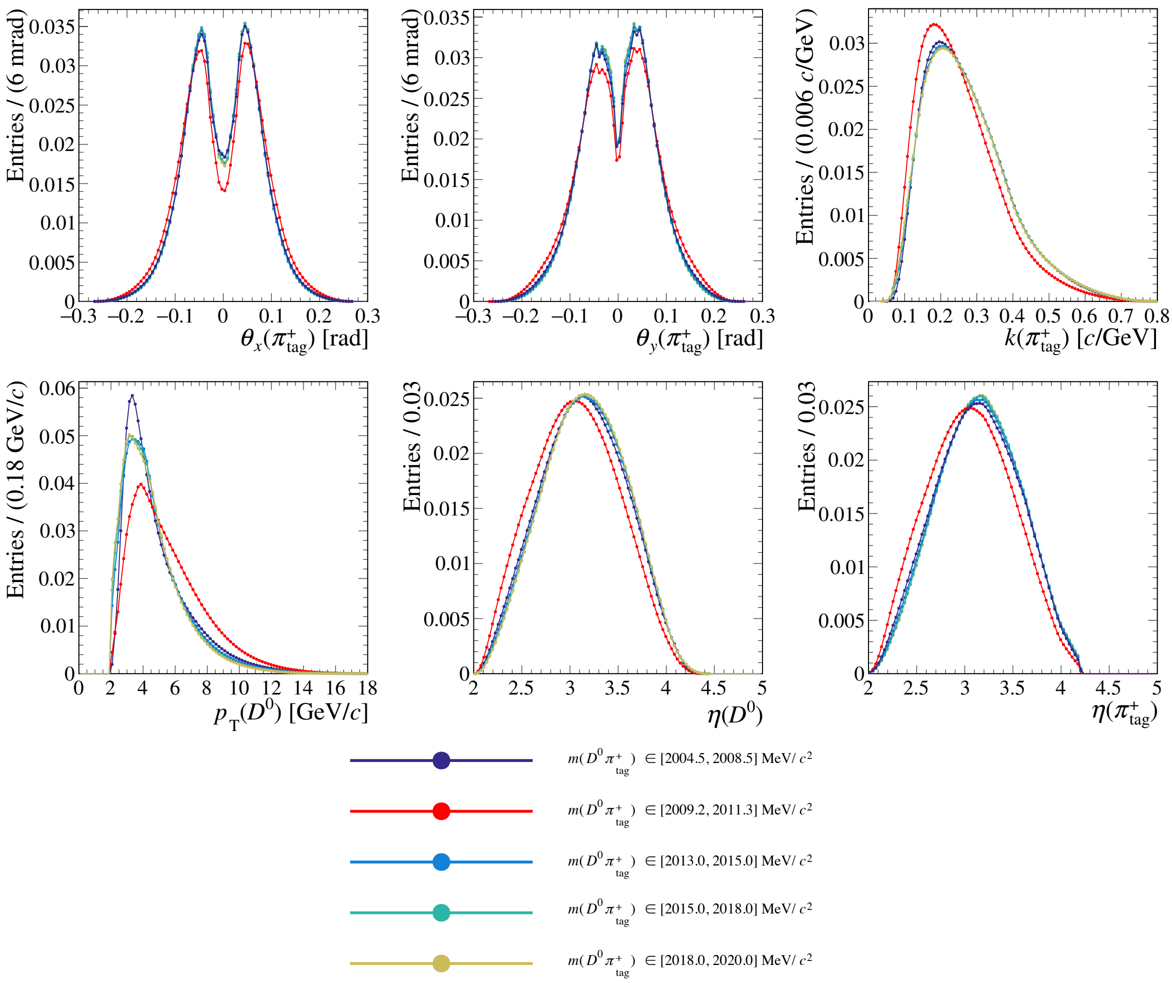

Figure D.12: Normalised distributions of the kinematic variables employed in the weighting of Sect. 5.2 in the $m(D^0\pi^+_{\rm tag})$ signal window and in the baseline and alternative lateral windows defined in Sect. 7.1.

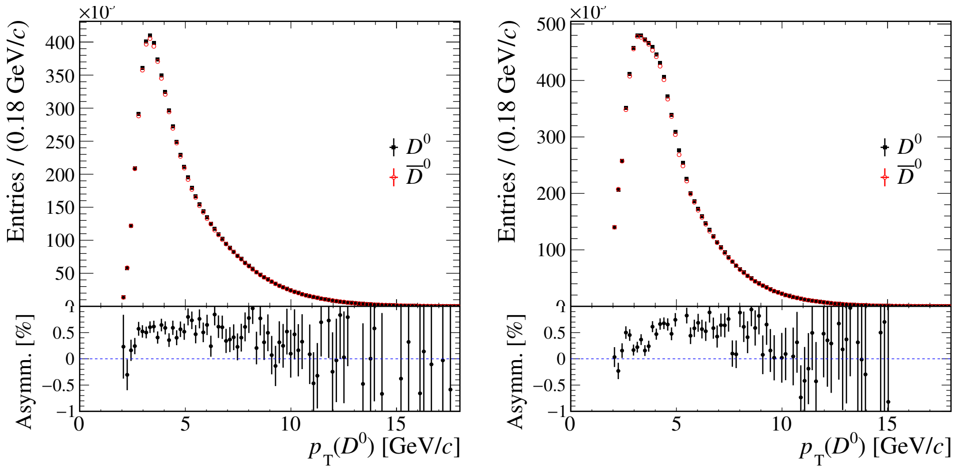

Figure D.13: Asymmetry of the $p_{\mathrm{T}}(D^0)$ kinematically weighted distribution in the (left) leftmost and (right) baseline $m(D^0\pi^+_{\mathrm{tag}})$ sidebands.

peak has a similar asymmetry. Its contribution to the total asymmetry, if it was not subtracted, would be $(5 \times 10^{-3}) \times 5\% = 2.5 \times 10^{-4}$, where 5% is the fraction of background events in the signal window for the K^+K^- and $\pi^+\pi^-$ channels. Even in the unreasonable assumption that

- the background was not subtracted (whereas the background contribution to the asymmetry is removed by using the background decays in the lateral window);
- the asymmetry varied by its whole size (5×10^{-3}) over the $p_{\mathrm{T}}(D^0)$ range (whereas it is nearly constant as a function of $p_{\mathrm{T}}(D^0)$);
- $p_{\mathrm{T}}(D^0)$ was 100% correlated with D^0 decay time (whereas it is not);

the bias on ΔY would be $(2.5 \times 10^{-4})/5 = 0.5 \times 10^{-4}$, where 5 is the analysed decay time range in τ_{D^0} units. This number is approximately equal to the statistical uncertainty of the $K^-\pi^+$ channel. The real effect is likely smaller by at least one order of magnitude, and therefore negligible with respect to both the statistical uncertainty and the assigned systematic uncertainty on the removal of the $m(D^0\pi^+_{\mathrm{tag}})$ background discussed in Sect. 7.1, which is probably overestimated.

Appendix E

Background under the D^0 mass peak

This appendix provides further details on the background decays whose $m(h^+h^-)$ distribution differs from that of the D^0 meson.

E.1 Particle-identification selection requirements

The selection efficiency of $D^0 \to \pi^+\pi^-$ candidates in the $m(\pi^+\pi^-)$ signal window and in the $m(\pi^+\pi^-) \in [1750, 1800]\,\mathrm{MeV}/c^2$ lateral window — mainly populated by $D^0 \to K^-\pi^+$ misidentified decays — is plotted as a function of the $\mathrm{DLL}_{K\pi}(\pi^\pm)$ requirement in Fig. E.1. The baseline requirement $\mathrm{DLL}_{K\pi}(\pi^\pm) < -5$ rejects 95.4% (retains 75.2%) of the candidates in the lateral (signal) window. The selection efficiency of $D^0 \to K^+K^-$ candidates in the $m(K^+K^-)$ signal window and in the $m(K^+K^-) \in [1750, 1800]\,\mathrm{MeV}/c^2$ lateral window is plotted as a function of the `ProbNNe`$(K^\pm)$ requirement in Fig. E.2. The baseline requirement `ProbNNe`$(K^\pm) < 0.2$ rejects 4.6% (retains 99.6%) of the candidates in the lateral (signal) window.

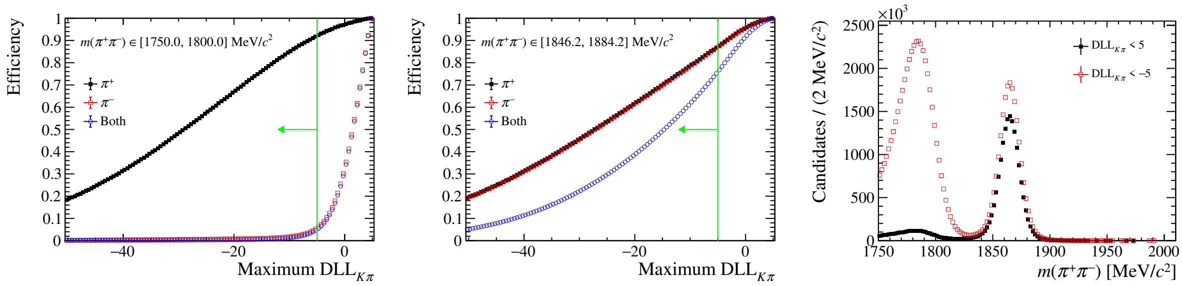

Figure E.1: Selection efficiency of the requirement $\mathrm{DLL}_{K\pi}(\pi^\pm) < -5$, normalised to that of the requirement $\mathrm{DLL}_{K\pi}(\pi^\pm) < 5$ which is implemented at the trigger level, for candidates in the (left) $m(\pi^+\pi^-) \in [1750, 1800]\,\mathrm{MeV}/c^2$ lateral window and (centre) signal window. The green vertical lines indicate the baseline requirement. (Right) $m(\pi^+\pi^-)$ distribution of the candidates before and after the $\mathrm{DLL}_{K\pi}(\pi^\pm) < -5$ requirement.

E.2 Particle-identification efficiency

Figure E.3 displays the probability of identifying kaon mesons, pion mesons, muons or electrons as kaon mesons from $D^0 \to K^+K^-$ decays, kaon mesons from $D^0 \to K^-\pi^+$ decays or pion mesons,

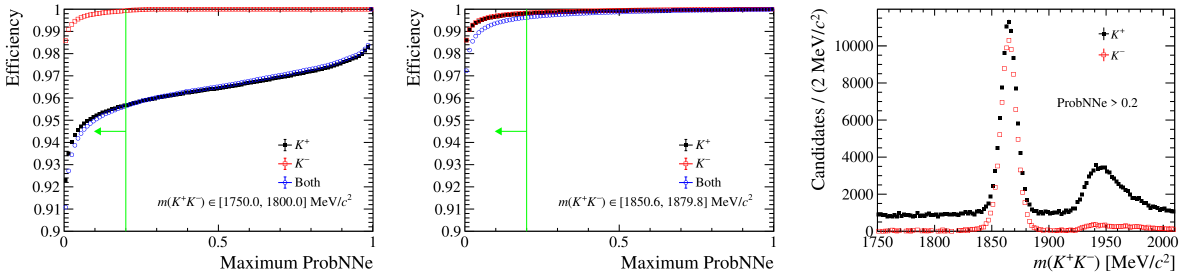

Figure E.2: Selection efficiency of the requirement `ProbNNe`$(K^{\pm}) < 0.2$ for the candidates in the (left) $m(K^+K^-) \in [1750, 1800]\,\text{MeV}/c^2$ lateral window and (centre) signal window. The green vertical lines indicate the baseline requirement. (Right) $m(K^+K^-)$ distribution of the candidates rejected by the `ProbNNe`$(K^{\pm}) < 0.2$ requirement.

as a function of momentum and pseudorapidity. The corresponding particle-identification requirements are $\text{DLL}_{K\pi} > 5$ `&&` `ProbNNe`$(K^{\pm}) < 0.2$, $\text{DLL}_{K\pi} > 5$ and $\text{DLL}_{K\pi} < -5$, respectively. All probabilities are calculated according to the procedure described in Ref. [201]. The binning of the two variables is chosen so as that the difference in efficiency between two adjacent bins differs from zero with a significance of around 2σ.

E.3 Estimate of the background size

The overall agreement between data and expectations is checked in a fit, whose results are shown in Fig. E.4, where the relative normalisation of all background components with respect to the signal are fixed to the expectations from RapidSim. Even if the fit has only three free parameters — the mean and width of the signal resolution and the overall normalisation of the fit function —, the main characteristics of the data distribution are well reproduced. In particular, the largest discrepancies between fit and data are probably due to a poor reproduction of the left (right) tail of the $D^0 \to K^-\pi^+$ distribution in the K^+K^- ($\pi^+\pi^-$) decay channel. On the other hand, Figure E.5 shows the results of the template fits to the $m(K^+K^-)$ and $m(\pi^+\pi^-)$ distributions where, differently from the baseline fit, the normalisation of the $D^0 \to h^-\ell^+\nu_\ell$ background decays are left free to float just as those of the other background components. This results into an overestimation of the fraction of the background from semileptonic decays, whose size is artificially increased to compensate for the imprecise reproduction of the tail of the distribution of $D^0 \to K^-\pi^+$ decays.

The results of the linear fits to the time-dependent fraction of background components in the $m(h^+h^-)$ signal window for the baseline template fit of Sect. 7.5 are shown in Figs. E.6, E.7 and E.8 for the $K^-\pi^+$, K^+K^- and $\pi^+\pi^-$ decay channels, respectively. The fractions are calculated based on the RapidSim distributions of $m(h^+h^-)$-*versus*-$t(D^0)$, scaled using the time-integrated relative normalisations between the background components and the signal from the time-integrated fits of Sect. 7.5. The agreement between the decay-time distributions of data and RapidSim is checked by measuring the time-dependent fraction of signal in the $m(h^+h^-)$ signal region as the ratio of the RapidSim template — normalised according to the results of the fit — to the data, as shown in Fig. E.9. The fraction varies from around 80% to 120% from low to high decay times, for all three decay channels, corresponding to discrepancies of up to 20% from the expectations, which are approximately given by a constant function equal to unity.

Finally, the results of the linear fits to the time-dependent asymmetry of the candidates in the

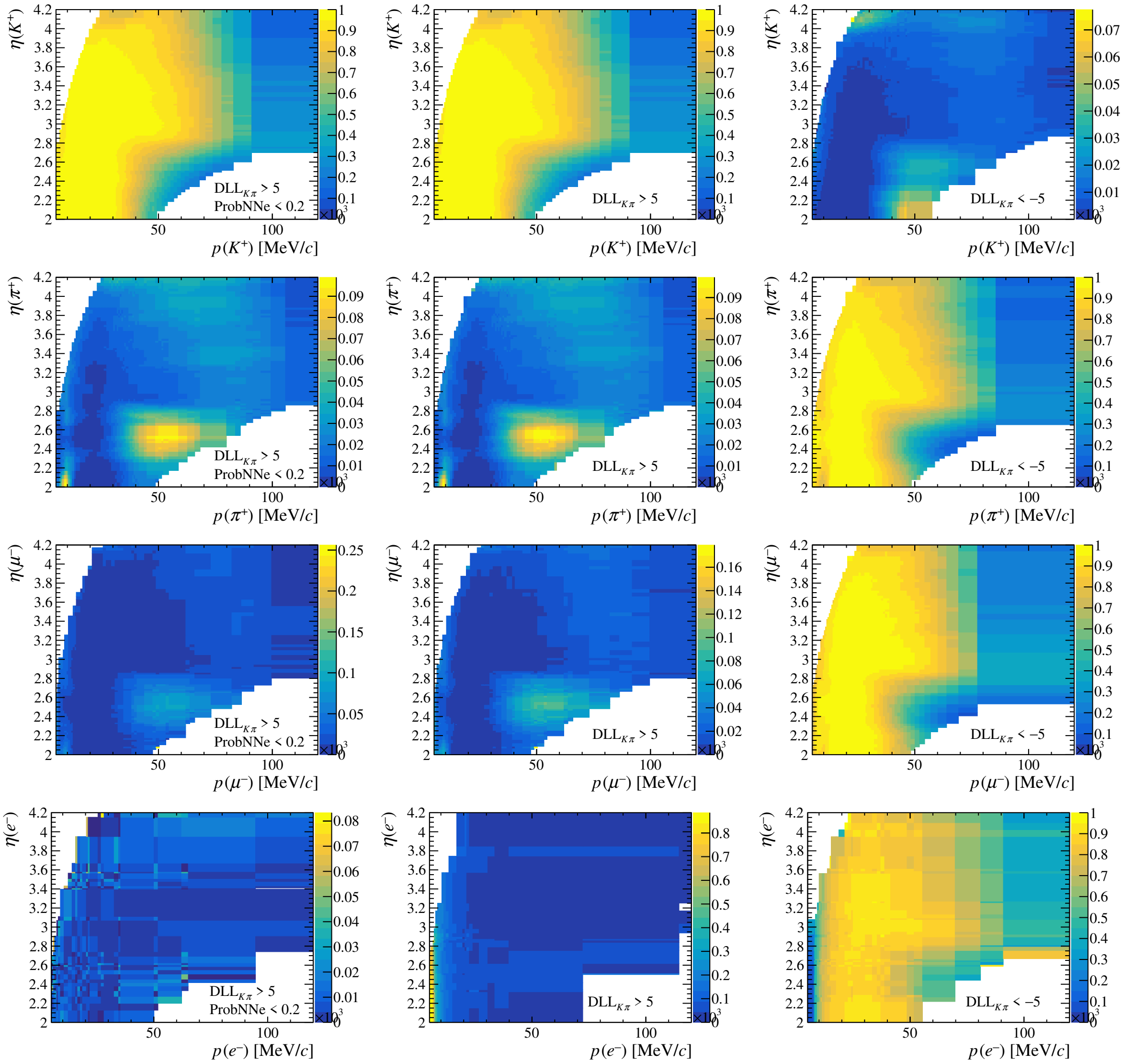

Figure E.3: PID efficiency for identifying a (top) K meson, (centre-top) π meson, (centre-bottom) muon or (bottom) electron as (left) a charged kaon with electron veto, (centre) a charged kaon without electron veto or (right) a pion, as a function of the momentum and pseudorapidity.

$m(h^+h^-)$ lateral windows are shown in Figs. E.10 and E.11 for the $K^-\pi^+$ and K^+K^- decay channels, respectively.

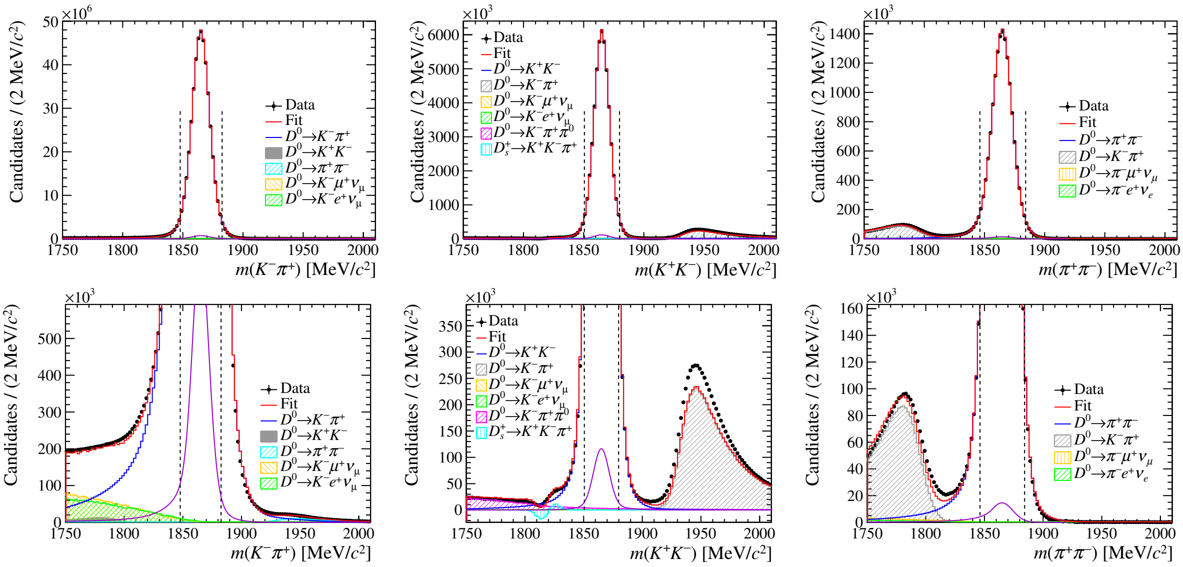

Figure E.4: Template fit to the time and flavour integrated $m(h^+h^-)$ distributions of (left) $K^-\pi^+$, (centre) K^+K^- and (right) $\pi^+\pi^-$ decays. The relative normalisation between the background components and the signal is fixed to the expectations of RapidSim and PIDCalib; the signal component due to decays in flight of D^0 daughter mesons into muons is shown in violet. Bottom plots are magnified to put the background components in evidence.

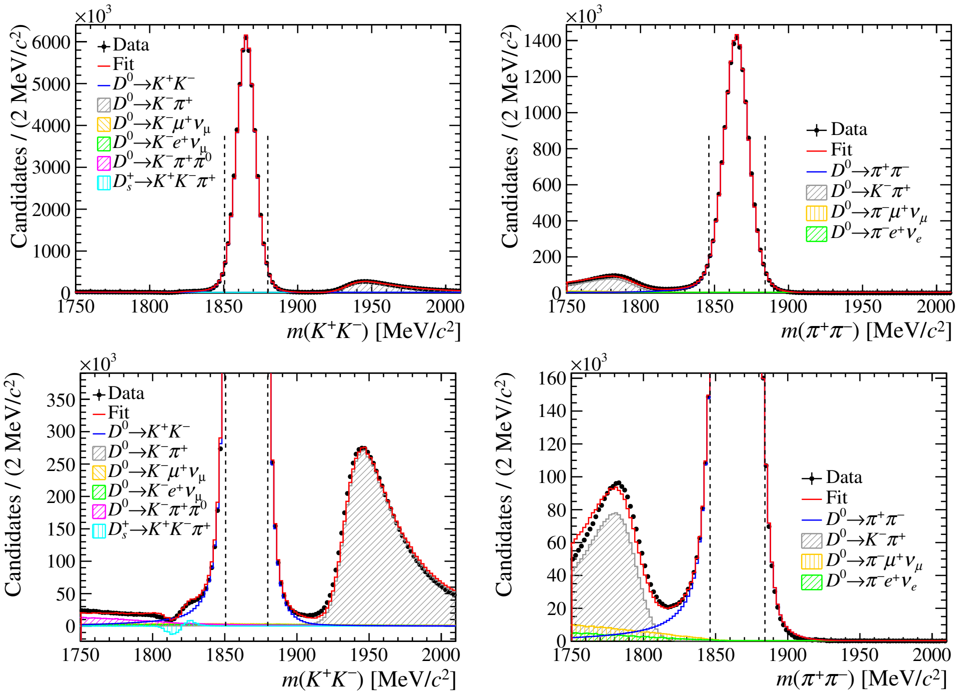

Figure E.5: Template fit to the time-integrated $m(h^+h^-)$ distribution of (left) $D^0 \to K^+K^-$ and (right) $D^0 \to \pi^+\pi^-$ decays, where all background normalisations are left free to vary, with the exception of the ratio between the normalisations of $D^0 \to h^-e^+\nu_e$ and $D^0 \to h^-\mu^+\nu_\mu$ decays, which is fixed to expectations. Bottom plots are magnified to put the background components in evidence.

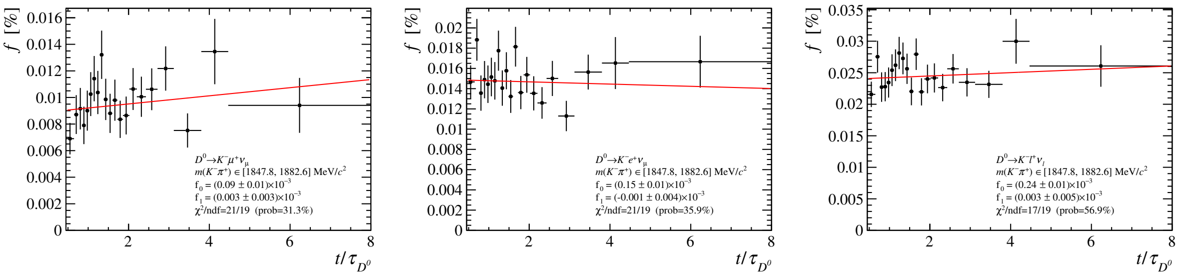

Figure E.6: Linear fit to the time-dependent fraction of background candidates in the $m(K^{-}\pi^{+})$ signal region, for all relevant backgrounds components.

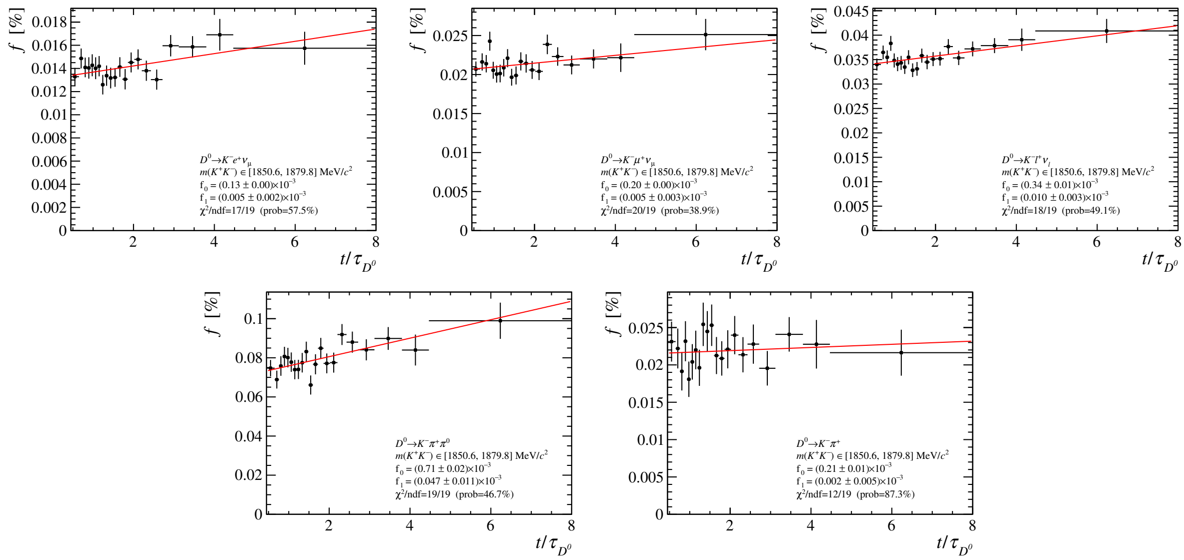

Figure E.7: Linear fit to the time-dependent fraction of background candidates in the $m(K^{+}K^{-})$ signal region, for all relevant backgrounds components.

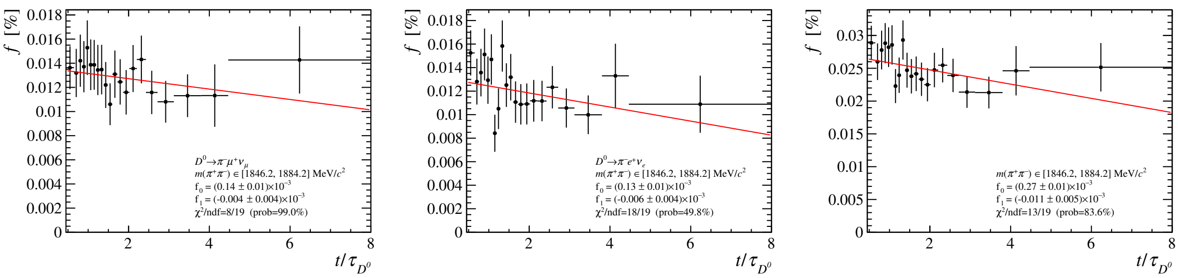

Figure E.8: Linear fit to the time-dependent fraction of background candidates in the $m(\pi^{+}\pi^{-})$ signal region, for all relevant backgrounds components.

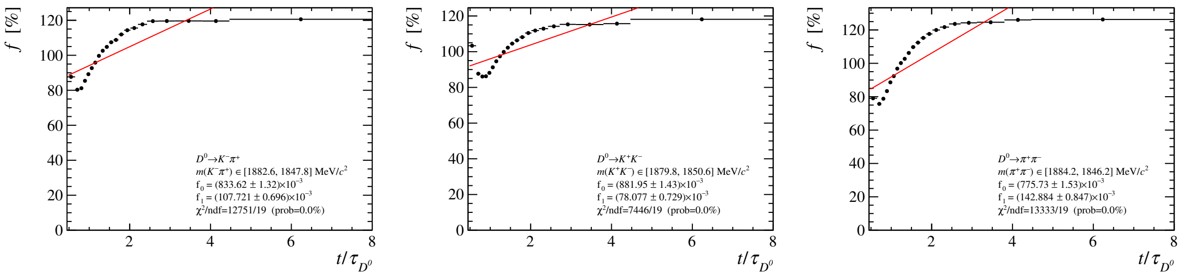

Figure E.9: Linear fit to the time-dependent fraction of signal candidates in the $m(h^+h^-)$ signal region, for the (left) $K^-\pi^+$, (centre) K^+K^- and (right) $\pi^+\pi^-$ decay channels. The fractions are calculated as the ratio of the RapidSim template (with the normalisation taken from the results of the template fit of Sect. 7.5) to the data.

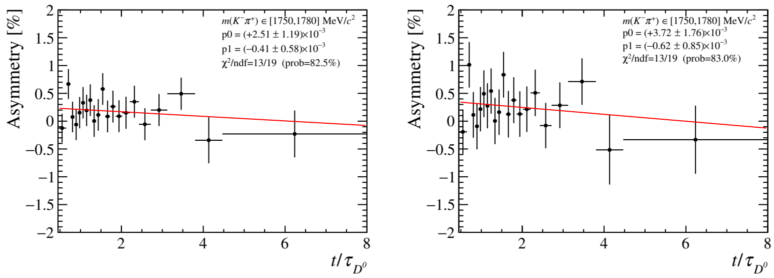

Figure E.10: Linear fit to the time-dependent asymmetry (left) in the $m(K^-\pi^+) \in [1750, 1780]\,\mathrm{MeV}/c^2$ window and (right) of the $D^0 \to K^-\ell^+\nu_\ell$ background, calculated by dividing the asymmetry by the $D^0 \to K^-\ell^+\nu_\ell$ fraction in the corresponding window.

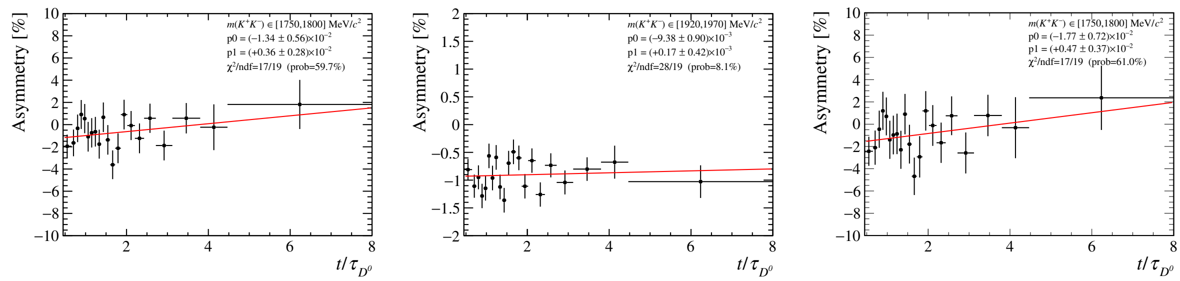

Figure E.11: Linear fit to the time-dependent asymmetry (left) in the $m(K^+K^-) \in [1750, 1800]\,\mathrm{MeV}/c^2$ window, (centre) in the $m(K^+K^-) \in [1920, 1970]\,\mathrm{MeV}/c^2$ window and (right) of the $D^0 \to K^-\pi^+\pi^0$ background, calculated by dividing the asymmetry of the left plot by the $D^0 \to K^-\pi^+\pi^0$ background fraction in the corresponding window.

References

[1] A. D. Sakharov, *Violation of CP Invariance, C asymmetry, and baryon asymmetry of the universe*, Sov. Phys. Usp. **34** (1991) 392.

[2] N. Cabibbo, *Unitary symmetry and leptonic decays*, Phys. Rev. Lett. **10** (1963) 531.

[3] M. Kobayashi and T. Maskawa, *CP-violation in the renormalizable theory of weak interaction*, Prog. Theor. Phys. **49** (1973) 652.

[4] J. H. Christenson, J. W. Cronin, V. L. Fitch, and R. Turlay, *Evidence for the 2π Decay of the K_2^0 Meson*, Phys. Rev. Lett. **13** (1964) 138.

[5] KTeV collaboration, *Observation of direct CP violation in $K_{S,L} \to \pi\pi$ decays*, Phys. Rev. Lett. **83** (1999) 22, `arXiv:hep-ex/9905060`.

[6] NA48 collaboration, *A Precise measurement of the direct CP violation parameter $Re(\epsilon'/\epsilon)$*, Eur. Phys. J. C **22** (2001) 231, `arXiv:hep-ex/0110019`.

[7] BaBar collaboration, *Observation of CP violation in the B^0 meson system*, Phys. Rev. Lett. **87** (2001) 091801, `arXiv:hep-ex/0107013`.

[8] Belle collaboration, *Observation of large CP violation in the neutral B meson system*, Phys. Rev. Lett. **87** (2001) 091802, `arXiv:hep-ex/0107061`.

[9] BaBar collaboration, *Observation of direct CP violation in $B^0 \to K^+\pi^-$ decays*, Phys. Rev. Lett. **93** (2004) 131801, `arXiv:hep-ex/0407057`.

[10] Belle collaboration, *Evidence for direct CP violation in $B^0 \to K^+\pi^-$ decays*, Phys. Rev. Lett. **93** (2004) 191802, `arXiv:hep-ex/0408100`.

[11] LHCb collaboration, *Observation of CP violation in $B^\pm \to DK^\pm$ decays*, Phys. Lett. **B712** (2012) 203, Erratum ibid. **B713** (2012) 351, `arXiv:1203.3662`.

[12] LHCb collaboration, *First observation of CP violation in the decays of B_s^0 mesons*, Phys. Rev. Lett. **110** (2013) 221601, `arXiv:1304.6173`.

[13] M. Dine and A. Kusenko, *The origin of the matter–antimatter asymmetry*, Rev. Mod. Phys. **76** (2003) 1, `arXiv:hep-ph/0303065`.

[14] Y. Grossman, A. L. Kagan, and Y. Nir, *New physics and CP violation in singly Cabibbo suppressed D decays*, Phys. Rev. **D75** (2007) 036008, `arXiv:hep-ph/0609178`.

[15] N. Carrasco *et al.*, *D^0–$\bar{D}^0$ mixing in the standard model and beyond from $N_f = 2$ twisted mass QCD*, Phys. Rev. D **90** (2014) 014502, `arXiv:1403.7302`.

[16] C. Alpigiani *et al.*, *Unitarity Triangle Analysis in the Standard Model and Beyond*, in *5th Large Hadron Collider Physics Conference*, 2017, `arXiv:1710.09644`.

[17] LHCb collaboration, *Observation of D^0–$\overline{D}^0$ oscillations*, Phys. Rev. Lett. **110** (2013) 101802, `arXiv:1211.1230`.

[18] LHCb collaboration, *Observation of CP violation in charm decays*, Phys. Rev. Lett. **122** (2019) 211803, `arXiv:1903.08726`.

[19] F. Buccella, A. Paul, and P. Santorelli, *$SU(3)_F$ breaking through final state interactions and CP asymmetries in $D \to PP$ decays*, Phys. Rev. D **99** (2019) 113001, `arXiv:1902.05564`.

[20] M. Chala, A. Lenz, A. V. Rusov, and J. Scholtz, *ΔA_{CP} within the Standard Model and beyond*, JHEP **07** (2019) 161, `arXiv:1903.10490`.

[21] H.-N. Li, C.-D. Lü, and F.-S. Yu, *Implications on the first observation of charm CPV at LHCb*, `arXiv:1903.10638`.

[22] Y. Grossman and S. Schacht, *The emergence of the $\Delta U = 0$ rule in charm physics*, JHEP **07** (2019) 020, `arXiv:1903.10952`.

[23] A. Soni, *Resonance enhancement of charm CP*, `arXiv:1905.00907`.

[24] H.-Y. Cheng and C.-W. Chiang, *Revisiting CP violation in $D \to PP$ and VP decays*, Phys. Rev. D **100** (2019) 093002, `arXiv:1909.03063`.

[25] A. Dery and Y. Nir, *Implications of the LHCb discovery of CP violation in charm decays*, JHEP **12** (2019) 104, `arXiv:1909.11242`.

[26] D. Wang, C.-P. Jia, and F.-S. Yu, *A self-consistent framework of topological amplitude and its $SU(N)$ decomposition*, `arXiv:2001.09460`.

[27] R. Bause, H. Gisbert, M. Golz, and G. Hiller, *Exploiting CP-asymmetries in rare charm decays*, Phys. Rev. D **101** (2020) 115006, `arXiv:2004.01206`.

[28] A. L. Kagan and L. Silvestrini, *Dispersive and Absorptive CP Violation in $D^0 - \overline{D^0}$ Mixing*, `arXiv:2001.07207`.

[29] Y. Grossman, *Charming CP violation*, contribution at the workshop *Implications of LHCb measurements and future prospects*, 2020.

[30] LHCb collaboration, *Measurement of CP asymmetry in $D^0 \to K^+K^-$ decays*, Phys. Lett. **B767** (2017) 177, `arXiv:1610.09476`.

[31] T. D. Lee and C.-N. Yang, *Question of Parity Conservation in Weak Interactions*, Phys. Rev. **104** (1956) 254.

[32] C. S. Wu *et al.*, *Experimental Test of Parity Conservation in β Decay*, Phys. Rev. **105** (1957) 1413.

[33] R. L. Garwin, L. M. Lederman, and M. Weinrich, *Observations of the Failure of Conservation of Parity and Charge Conjugation in Meson Decays: The Magnetic Moment of the Free Muon*, Phys. Rev. **105** (1957) 1415.

[34] R. D. Peccei, *The Strong CP problem and axions*, Lect. Notes Phys. **741** (2008) 3, `arXiv:hep-ph/0607268`.

[35] C. A. Baker *et al.*, *An Improved experimental limit on the electric dipole moment of the neutron*, Phys. Rev. Lett. **97** (2006) 131801, `arXiv:hep-ex/0602020`.

[36] Particle Data Group, *Review of particle physics*, Prog. Theor. Exp. Phys. **2020** (2020) 083C01.

[37] R. Barbieri, *Ten Lectures on the ElectroWeak Interactions*, Scuola Normale Superiore, 2007.

[38] L.-L. Chau and W.-Y. Keung, *Comments on the Parametrization of the Kobayashi-Maskawa Matrix*, Phys. Rev. Lett. **53** (1984) 1802.

[39] L. Wolfenstein, *Parametrization of the Kobayashi-Maskawa Matrix*, Phys. Rev. Lett. **51** (1983) 1945.

[40] A. J. Buras, M. E. Lautenbacher, and G. Ostermaier, *Waiting for the top quark mass, $K^+ \to \pi^+\nu\overline{\nu}$, $B^0_{(s)}$–$\overline{B}^0_{(s)}$ mixing and CP asymmetries in B decays*, Phys. Rev. D **50** (1994) 3433, `arXiv:hep-ph/9403384`.

[41] CKMfitter group, *CP violation and the CKM matrix: Assessing the impact of the asymmetric B factories*, Eur. Phys. J. **C41** (2005) 1, `arXiv:hep-ph/0406184`, updated results and plots available at `http://ckmfitter.in2p3.fr/`.

[42] Y. Grossman, Y. Nir, and G. Perez, *Testing new indirect CP Violation*, Phys. Rev. Lett. **103** (2009) 071602, `arXiv:0904.0305`.

[43] A. L. Kagan and M. D. Sokoloff, *Indirect CP violation and implications for D^0–$\overline{D}^0$ and B^0_s–$\overline{B}^0_s$ mixing*, Phys. Rev. **D80** (2009) 076008, `arXiv:0907.3917`.

[44] V. Weisskopf and E. Wigner, *Berechnung der natürlichen linienbreite auf grund der diracschen lichttheorie*, Zeitschrift für Physik **63** (1930) 54; V. Weisskopf and E. Wigner, *Über die natürliche linienbreite in der strahlung des harmonischen oszillators*, Zeitschrift für Physik **65** (1930) 18.

[45] K. Konishi and G. Paffuti, in *Quantum Mechanics*, pp. 228–230, Oxford University Press, 2009.

[46] M. Sozzi, in *Discrete Symmetries and CP Violation*, pp. 280–281, Oxford University Press, 2008.

[47] Heavy Flavor Averaging Group, *Averages of b-hadron, c-hadron, and τ-lepton properties as of 2018*, `arXiv:1909.12524`, updated results and plots available at `https://hflav.web.cern.ch`.

[48] A. Buras, in *Gauge Theories of Weak Decays*, pp. 181–212, Cambridge University Press, 2020.

[49] S. L. Glashow, J. Iliopoulos, and L. Maiani, *Weak Interactions with Lepton-Hadron Symmetry*, Phys. Rev. D **2** (1970) 1285.

[50] A. Buras, in *Gauge Theories of Weak Decays*, pp. 71–73, Cambridge University Press, 2020.

[51] A. J. Buras, *Weak Hamiltonian, CP violation and rare decays*, in *Les Houches Summer School in Theoretical Physics, Session 68: Probing the Standard Model of Particle Interactions*, 281–539, 1998, `arXiv:hep-ph/9806471`.

[52] L. Maiani, *The GIM Mechanism: origin, predictions and recent uses*, in *48*$^{\rm th}$ *Rencontres de Moriond on Electroweak Interactions and Unified Theories*, 3–16, 2013, `arXiv:1303.6154`.

[53] A. F. Falk, Y. Grossman, Z. Ligeti, and A. A. Petrov, *$SU(3)$ breaking and D^0–$\bar{D}^0$ mixing*, Phys. Rev. D **65** (2002) 054034, `arXiv:hep-ph/0110317`.

[54] M. Gronau and J. L. Rosner, *Revisiting D^0–$\bar{D}^0$ mixing using U-spin*, Phys. Rev. D **86** (2012) 114029, `arXiv:1209.1348`.

[55] BaBar collaboration, *Measurement of $D^0 - \bar{D}^0$ mixing from a time-dependent amplitude analysis of $D^0 \to K^+\pi^-\pi^0$ decays*, Phys. Rev. Lett. **103** (2009) 211801, `arXiv:0807.4544`.

[56] BaBar collaboration, *Measurement of $D^0 - \overline{D}^0$ mixing parameters using $D^0 \to K^0_S\pi^+\pi^-$ and $D^0 \to K^0_S K^+K^-$ decays*, Phys. Rev. Lett. **105** (2010) 081803, `arXiv:1004.5053`.

[57] BaBar collaboration, *Measurement of D^0–$\overline{D}^0$ mixing and CP violation in two-body D^0 decays*, Phys. Rev. **D87** (2013) 012004, `arXiv:1209.3896`.

[58] Belle collaboration, *Measurement of $D^0 - \bar{D}^0$ mixing and search for indirect CP violation using $D^0 \to K^0_S\pi^+\pi^-$ decays*, Phys. Rev. D **89** (2014) 091103, `arXiv:1404.2412`.

[59] Belle collaboration, *Measurement of D^0–$\overline{D}^0$ mixing and search for CP violation in $D^0 \to K^+K^-, \pi^+\pi^-$ decays with the full Belle data set*, Phys. Lett. **B753** (2016) 412, `arXiv:1509.08266`.

[60] LHCb collaboration, *Updated determination of D^0–$\overline{D}^0$ mixing and CP violation parameters with $D^0 \to K^+\pi^-$ decays*, Phys. Rev. **D97** (2018) 031101, `arXiv:1712.03220`.

[61] LHCb collaboration, *Measurement of the charm-mixing parameter y_{CP}*, Phys. Rev. Lett. **122** (2019) 011802, `arXiv:1810.06874`.

[62] LHCb collaboration, *Measurement of the mass difference between neutral charm-meson eigenstates*, Phys. Rev. Lett. **122** (2019) 231802, `arXiv:1903.03074`.

[63] M. D. Schwartz, in *Quantum Field Theory and the Standard Model*, ch. 35, Cambridge University Press, 2013.

[64] A. Lenz and T. Rauh, *D-meson lifetimes within the heavy quark expansion*, Phys. Rev. D **88** (2013) 034004, `arXiv:1305.3588`.

[65] M. Kirk, A. Lenz, and T. Rauh, *Dimension-six matrix elements for meson mixing and lifetimes from sum rules*, JHEP **12** (2017) 068, `arXiv:1711.02100`, [Erratum: JHEP 06, 162 (2020)].

[66] ETM collaboration, *ΔS=2 and ΔC=2 bag parameters in the standard model and beyond from N_f=2+1+1 twisted-mass lattice QCD*, Phys. Rev. D **92** (2015) 034516, `arXiv:1505.06639`.

[67] A. Bazavov *et al.*, *Short-distance matrix elements for D^0-meson mixing for $N_f = 2+1$ lattice QCD*, Phys. Rev. D **97** (2018) 034513, `arXiv:1706.04622`.

[68] A. Lenz, M. L. Piscopo, and C. Vlahos, *Renormalization scale setting for D-meson mixing*, Phys. Rev. D **102** (2020) 093002, `arXiv:2007.03022`.

[69] T. Jubb, M. Kirk, A. Lenz, and G. Tetlalmatzi-Xolocotzi, *On the ultimate precision of meson mixing observables*, Nucl. Phys. B **915** (2017) 431, `arXiv:1603.07770`.

[70] H. Georgi, *D–$\overline{D}$ mixing in heavy quark effective field theory*, Phys. Lett. B **297** (1992) 353, `arXiv:hep-ph/9209291`.

[71] T. Ohl, G. Ricciardi, and E. H. Simmons, *D–$\overline{D}$ mixing in heavy quark effective field theory: The Sequel*, Nucl. Phys. B **403** (1993) 605, `arXiv:hep-ph/9301212`.

[72] I. I. Y. Bigi and N. G. Uraltsev, *D^0–$\overline{D}^0$ oscillations as a probe of quark hadron duality*, Nucl. Phys. B **592** (2001) 92, `arXiv:hep-ph/0005089`.

[73] M. Bobrowski, A. Lenz, J. Riedl, and J. Rohrwild, *How Large Can the SM Contribution to CP Violation in $D^0 - \bar{D}^0$ Mixing Be?*, JHEP **03** (2010) 009, `arXiv:1002.4794`.

[74] M. Bobrowski, A. Lenz, and T. Rauh, *Short distance D^0–$\overline{D}^0$ mixing*, in *5th International Workshop on Charm Physics*, 2012, `arXiv:1208.6438`.

[75] H. M. Asatrian, A. Hovhannisyan, U. Nierste, and A. Yeghiazaryan, *Towards next-to-next-to-leading-log accuracy for the width difference in the $B_s - \bar{B}_s$ system: fermionic contributions to order $(m_c/m_b)^0$ and $(m_c/m_b)^1$*, JHEP **10** (2017) 191, `arXiv:1709.02160`.

[76] H. M. Asatrian *et al.*, *Penguin contribution to the width difference and CP asymmetry in B_q-$\bar{B}_q$ mixing at order $\alpha_s^2 N_f$*, Phys. Rev. D **102** (2020) 033007, `arXiv:2006.13227`.

[77] L. Wolfenstein, *D^0–$\bar{D}^0$ Mixing*, Phys. Lett. B **164** (1985) 170.

[78] J. F. Donoghue, E. Golowich, B. R. Holstein, and J. Trampetic, *Dispersive Effects in D^0–$\bar{D}^0$ Mixing*, Phys. Rev. D **33** (1986) 179.

[79] H.-Y. Cheng and C.-W. Chiang, *Long-Distance Contributions to $D^0 - \bar{D}^0$ Mixing Parameters*, Phys. Rev. D **81** (2010) 114020, `arXiv:1005.1106`.

[80] H.-Y. Jiang *et al.*, *D^0-$\overline{D}^0$ mixing parameter y in the factorization-assisted topological-amplitude approach*, Chin. Phys. C **42** (2018) 063101, `arXiv:1705.07335`.

[81] M. T. Hansen and S. R. Sharpe, *Multiple-channel generalization of Lellouch-Luscher formula*, Phys. Rev. D **86** (2012) 016007, `arXiv:1204.0826`.

[82] A. F. Falk *et al.*, *D^0–$\bar{D}^0$ mass difference from a dispersion relation*, Phys. Rev. D **69** (2004) 114021, `arXiv:hep-ph/0402204`.

[83] E. Golowich, J. Hewett, S. Pakvasa, and A. A. Petrov, *Implications of D^0–$\bar{D}^0$ Mixing for New Physics*, Phys. Rev. D **76** (2007) 095009, `arXiv:0705.3650`.

[84] UTfit collaboration, *Model-independent constraints on $\Delta F = 2$ operators and the scale of new physics*, JHEP **03** (2008) 049, `arXiv:0707.0636`.

[85] L. Wolfenstein, *Violation of CP Invariance and the Possibility of Very Weak Interactions*, Phys. Rev. Lett. **13** (1964) 562.

[86] S. Bianco, F. L. Fabbri, D. Benson, and I. Bigi, *A Cicerone for the physics of charm*, Riv. Nuovo Cim. **26N7** (2003) 1, `arXiv:hep-ex/0309021`.

[87] A. Lenz and G. Wilkinson, *Mixing and CP violation in the charm system*, `arXiv:2011.04443arXiv:2011.04443`.

[88] J. Brod, Y. Grossman, A. L. Kagan, and J. Zupan, *A Consistent Picture for Large Penguins in $D \to \pi^+\pi^-, K^+K^-$*, JHEP **10** (2012) 161, `arXiv:1203.6659`.

[89] CKMfitter group, *Current status of the standard model CKM fit and constraints on $\Delta F = 2$ new physics*, Phys. Rev. **D91** (2015) 073007, `arXiv:1501.05013`, updated results and plots available at `http://ckmfitter.in2p3.fr/`.

[90] U. Nierste and S. Schacht, *CP Violation in $D^0 \to K_S K_S$*, Phys. Rev. D **92** (2015) 054036, `arXiv:1508.00074`.

[91] U. Nierste and S. Schacht, *Neutral $D \to KK^*$ decays as discovery channels for charm CP violation*, Phys. Rev. Lett. **119** (2017) 251801, `arXiv:1708.03572`.

[92] H.-n. Li, C.-D. Lu, and F.-S. Yu, *Branching ratios and direct CP asymmetries in $D \to PP$ decays*, Phys. Rev. D **86** (2012) 036012, `arXiv:1203.3120`.

[93] H.-Y. Cheng and C.-W. Chiang, *Direct CP violation in two-body hadronic charmed meson decays*, Phys. Rev. D **85** (2012) 034036, `arXiv:1201.0785`, [Erratum: Phys.Rev.D 85, 079903 (2012)].

[94] A. Khodjamirian and A. A. Petrov, *Direct CP asymmetry in $D \to \pi^-\pi^+$ and $D \to K^-K^+$ in QCD-based approach*, Phys. Lett. B **774** (2017) 235, `arXiv:1706.07780`.

[95] M. Golden and B. Grinstein, *Enhanced CP Violations in Hadronic Charm Decays*, Phys. Lett. B **222** (1989) 501.

[96] D. Pirtskhalava and P. Uttayarat, *CP Violation and Flavor SU(3) Breaking in D-meson Decays*, Phys. Lett. B **712** (2012) 81, `arXiv:1112.5451`.

[97] T. Feldmann, S. Nandi, and A. Soni, *Repercussions of Flavour Symmetry Breaking on CP Violation in D-Meson Decays*, JHEP **06** (2012) 007, `arXiv:1202.3795`.

[98] G. Hiller, M. Jung, and S. Schacht, *SU(3)-flavor anatomy of nonleptonic charm decays*, Phys. Rev. D **87** (2013) 014024, `arXiv:1211.3734`.

[99] Y. Grossman and D. J. Robinson, *SU(3) Sum Rules for Charm Decay*, JHEP **04** (2013) 067, `arXiv:1211.3361`.

[100] S. Müller, U. Nierste, and S. Schacht, *Sum Rules of Charm CP Asymmetries beyond the $SU(3)_F$ Limit*, Phys. Rev. Lett. **115** (2015) 251802, `arXiv:1506.04121`.

[101] F. Buccella *et al.*, *Nonleptonic weak decays of charmed mesons*, Phys. Rev. D **51** (1995) 3478, `arXiv:hep-ph/9411286`.

[102] E. Franco, S. Mishima, and L. Silvestrini, *The Standard Model confronts CP violation in $D^0 \to \pi^+\pi^-$ and $D^0 \to K^+K^-$*, JHEP **05** (2012) 140, arXiv:1203.3131.

[103] LHCb collaboration, *Measurement of CP asymmetry in $D^0 \to K^-K^+$ and $D^0 \to \pi^-\pi^+$ decays*, JHEP **07** (2014) 041, arXiv:1405.2797.

[104] LHCb collaboration, *Evidence for CP violation in time-integrated $D^0 \to h^-h^+$ decay rates*, Phys. Rev. Lett. **108** (2012) 111602, arXiv:1112.0938.

[105] A. Buras, in *Gauge Theories of Weak Decays*, pp. 265–269, Cambridge University Press, 2020.

[106] D. Atwood and A. Soni, *Searching for the Origin of CP violation in Cabibbo Suppressed D-meson Decays*, PTEP **2013** (2013) 093B05, arXiv:1211.1026.

[107] U. Nierste, *Charm decays*, PoS **Beauty2019** (2020) 048, arXiv:2002.06686.

[108] LHCb collaboration, *Search for CP violation in $D_s^+ \to K_S^0\pi^+$, $D^+ \to K_S^0K^+$ and $D^+ \to \phi\pi^+$ decays*, Phys. Rev. Lett. **122** (2019) 191803, arXiv:1903.01150.

[109] I. I. Bigi, A. Paul, and S. Recksiegel, *Conclusions from CDF Results on CP Violation in $D^0 \to \pi^+\pi^-, K^+K^-$ and Future Tasks*, JHEP **06** (2011) 089, arXiv:1103.5785.

[110] H.-N. Li, H. Umeeda, F. Xu, and F.-S. Yu, *D meson mixing as an inverse problem*, Phys. Lett. B **810** (2020) 135802, arXiv:2001.04079.

[111] LHCb collaboration, *Measurement of mixing and CP violation parameters in two-body charm decays*, JHEP **04** (2012) 129, arXiv:1112.4698.

[112] LHCb collaboration, *Measurements of indirect CP asymmetries in $D^0 \to K^-K^+$ and $D^0 \to \pi^-\pi^+$ decays*, Phys. Rev. Lett. **112** (2014) 041801, arXiv:1310.7201.

[113] V. V. Gligorov *et al.*, *Swimming: A data driven acceptance correction algorithm*, J. Phys. Conf. Ser. **396** (2012) 022016.

[114] LHCb collaboration, *Measurement of the CP violation parameter A_Γ in $D^0 \to K^+K^-$ and $D^0 \to \pi^+\pi^-$ decays*, Phys. Rev. Lett. **118** (2017) 261803, arXiv:1702.06490.

[115] CDF collaboration, *Measurement of indirect CP-violating asymmetries in $D^0 \to K^+K^-$ and $D^0 \to \pi^+\pi^-$ decays at CDF*, Phys. Rev. **D90** (2014) 111103, arXiv:1410.5435.

[116] LHCb collaboration, *Measurement of indirect CP asymmetries in $D^0 \to K^-K^+$ and $D^0 \to \pi^-\pi^+$ decays using semileptonic B decays*, JHEP **04** (2015) 043, arXiv:1501.06777.

[117] T. Pajero and M. J. Morello on behalf of the LHCb collaboration, *Search for time-dependent CP violation in $D^0 \to K^+K^-$ and $D^0 \to \pi^+\pi^-$ decays*, LHCb-CONF-2019-001, 2019.

[118] LHCb collaboration, *Updated measurement of decay-time-dependent CP asymmetries in $D^0 \to K^+K^-$ and $D^0 \to \pi^+\pi^-$ decays*, Phys. Rev. **D101** (2020) 012005, arXiv:1911.01114.

[119] E791 collaboration, *Measurements of lifetimes and a limit on the lifetime difference in the neutral D meson system*, Phys. Rev. Lett. **83** (1999) 32, arXiv:hep-ex/9903012.

[120] FOCUS collaboration, *A Measurement of lifetime differences in the neutral D meson system*, Phys. Lett. B **485** (2000) 62, `arXiv:hep-ex/0004034`.

[121] CLEO collaboration, *Lifetime differences, direct CP violation and partial widths in D^0 meson decays to K^+K^- and $\pi^+\pi^-$*, Phys. Rev. D **65** (2002) 092001, `arXiv:hep-ex/0111024`.

[122] UTfit collaboration, *The unitarity triangle fit in the standard model and hadronic parameters from lattice QCD: A reappraisal after the measurements of Δm_s and $BR(B \to \tau\nu_\tau)$*, JHEP **10** (2006) 081, `arXiv:hep-ph/0606167`, updated results and plots available at `http://www.utfit.org/`.

[123] UTfit collaboration, *Neutral charm mixing results from the UTfit collaboration*, PoS **CKM2016** (2017) 143.

[124] LHCb collaboration, *Measurements of prompt charm production cross-sections in pp collisions at $\sqrt{s} = 13$ TeV*, JHEP **03** (2016) 159, Erratum ibid. **09** (2016) 013, Erratum ibid. **05** (2017) 074, `arXiv:1510.01707`.

[125] CLEO collaboration, *Updated Measurement of the Strong Phase in $D^0 \to K^+\pi^-$ Decay Using Quantum Correlations in $e^+e^- \to D^0\bar{D}^0$ at CLEO*, Phys. Rev. D **86** (2012) 112001, `arXiv:1210.0939`.

[126] BESIII collaboration, *Measurement of the $D \to K^-\pi^+$ strong phase difference in $\psi(3770) \to D^0\overline{D}^0$*, Phys. Lett. B **734** (2014) 227, `arXiv:1404.4691`.

[127] BESIII collaboration, *Model-independent determination of the relative strong-phase difference between D^0 and $\bar{D}^0 \to K^0_{S,L}\pi^+\pi^-$ and its impact on the measurement of the CKM angle γ/ϕ_3*, Phys. Rev. D **101** (2020) 112002, `arXiv:2003.00091`.

[128] BESIII collaboration, *Determination of Strong-Phase Parameters in $D \to K^0_{S,L}\pi^+\pi^-$*, Phys. Rev. Lett. **124** (2020) 241802, `arXiv:2002.12791`.

[129] A. Di Canto *et al.*, *Novel method for measuring charm-mixing parameters using multibody decays*, Phys. Rev. D **99** (2019) 012007, `arXiv:1811.01032`.

[130] LHCb collaboration, *First observation of $D^0 - \overline{D}^0$ oscillations in $D^0 \to K^+\pi^+\pi^-\pi^-$ decays and a measurement of the associated coherence parameters*, Phys. Rev. Lett. **116** (2016) 241801, `arXiv:1602.07224`.

[131] LHCb collaboration, *Studies of the resonance structure in $D^0 \to K^\mp\pi^\pm\pi^+\pi^-$ decays*, Eur. Phys. J. **C78** (2018) 443, `arXiv:1712.08609`.

[132] D. Muller, *Measurements of production cross-sections and mixing of charm mesons at LHCb*, 2017. Presented 23 Oct 2017.

[133] LHCb collaboration, *Search for time-dependent CP violation in $D^0 \to K^+K^-$ and $D^0 \to \pi^+\pi^-$ decays*, LHCb-PAPER-2020-045, To be submitted to *Physical Review D*.

[134] Belle collaboration, *Observation of $D^0 - \bar{D}^0$ Mixing in e^+e^- Collisions*, Phys. Rev. Lett. **112** (2014) 111801, `arXiv:1401.3402`, [Addendum: Phys.Rev.Lett. 112, 139903 (2014)].

[135] BaBar collaboration, *Evidence for $D^0 - \overline{D}^0$ Mixing*, Phys. Rev. Lett. **98** (2007) 211802, `arXiv:hep-ex/0703020`.

[136] CDF collaboration, *Observation of D^0–$\bar{D}^0$ Mixing Using the CDF II Detector*, Phys. Rev. Lett. **111** (2013) 231802, `arXiv:1309.4078`.

[137] CDF collaboration, *Measurement of CP-violation asymmetries in $D^0 \to K_S\pi^+\pi^-$*, Phys. Rev. D **86** (2012) 032007, `arXiv:1207.0825`.

[138] T. Pajero, *Mixing and CP violation in charm at LHCb*, review talk at the workshop *Implications of LHCb measurements and future prospects*. On behalf of the LHCb collaboration.

[139] LHCb collaboration, *Measurement of B meson production cross-sections in proton-proton collisions at $\sqrt{s}$ =7 TeV*, JHEP **08** (2013) 117, `arXiv:1306.3663`.

[140] LHCb collaboration, *Measurements of prompt charm production cross-sections in pp collisions at $\sqrt{s}$ =5 TeV*, JHEP **06** (2017) 147, `arXiv:1610.02230`.

[141] Belle-II collaboration, *The Belle II Physics Book*, PTEP **2019** (2019) 123C01, `arXiv:1808.10567`, [Erratum: PTEP 2020, 029201 (2020)], p. 377.

[142] L. Evans and P. Bryant (editors), *LHC Machine*, JINST **3** (2008) S08001.

[143] T. Sjöstrand, S. Mrenna, and P. Skands, *A brief introduction to PYTHIA 8.1*, Comput. Phys. Commun. **178** (2008) 852, `arXiv:0710.3820`; T. Sjöstrand, S. Mrenna, and P. Skands, *PYTHIA 6.4 physics and manual*, JHEP **05** (2006) 026, `arXiv:hep-ph/0603175`.

[144] C. Elsässer, *$\bar{b}b$ production angle plots*, `https://lhcb.web.cern.ch/lhcb/speakersbureau/html/bb_ProductionAngles.html`. Accessed 22 October 2020.

[145] LHCb collaboration, *The LHCb detector at the LHC*, JINST **3** (2008) S08005.

[146] LHCb collaboration, *LHCb detector performance*, Int. J. Mod. Phys. **A30** (2015) 1530022, `arXiv:1412.6352`.

[147] L. S. T. Group, *Material for publications*, `http://lhcb.physik.uzh.ch/ST/public/material/index.php`, 2006. Accessed 13 August 2017.

[148] R. Arink *et al.*, *Performance of the LHCb Outer Tracker*, JINST **9** (2014) P01002, `arXiv:1311.3893`.

[149] LHCb collaboration, S. Amato *et al.*, *LHCb RICH: Technical Design Report*, CERN-LHCC-2000-037, 2000.

[150] M. Adinolfi *et al.*, *Performance of the LHCb RICH detector at the LHC*, Eur. Phys. J. **C73** (2013) 2431, `arXiv:1211.6759`.

[151] LHCb collaboration, *Current status and performance of the LHCb electromagnetic and hadron calorimeters*, J. Phys. Conf. Ser. **293** (2011) 012052.

[152] LHCb collaboration, *LHCb preshower(PS) and scintillating pad detector (SPD): Commissioning, calibration, and monitoring*, J. Phys. Conf. Ser. **160** (2009) 012046.

[153] LHCb collaboration, *LHCb muon system technical design report*, CERN-LHCC-2001-010, 2001.

[154] R. Fruhwirth, *Application of Kalman filtering to track and vertex fitting*, Nucl. Instrum. Meth. A **262** (1987) 444.

[155] G. Dujany and B. Storaci, *Real-time alignment and calibration of the LHCb Detector in Run II*, J. Phys. Conf. Ser. **664** (2015) 082010.

[156] R. Aaij *et al.*, *The LHCb trigger and its performance in 2011*, JINST **8** (2013) P04022, `arXiv:1211.3055`.

[157] R. Aaij *et al.*, *Tesla: an application for real-time data analysis in High Energy Physics*, Comput. Phys. Commun. **208** (2016) 35, `arXiv:1604.05596`.

[158] A. Hoecker *et al.*, *TMVA 4 — Toolkit for Multivariate Data Analysis with ROOT. Users Guide.*, `arXiv:physics/0703039`.

[159] V. V. Gligorov and M. Williams, *Efficient, reliable and fast high-level triggering using a bonsai boosted decision tree*, JINST **8** (2013) P02013, `arXiv:1210.6861`.

[160] J. Van Tilburg, *Information on the absorption of hadrons*, `https://twiki.cern.ch/twiki/bin/view/LHCb/TrackingEffAbsLength`, 2011.

[161] G. Corti and F. Ferrari, *Measurement of the position of the UX85-1 beampipe with Run-1 and Run-2 data*, LHCb-INT-2018-001, 2018.

[162] W. D. Hulsbergen, *Decay chain fitting with a Kalman filter*, Nucl. Instrum. Meth. **A552** (2005) 566, `arXiv:physics/0503191`.

[163] M. Needham, *Clone track identification using the Kullback–Liebler distance*, LHCb-2008-002.

[164] N. L. Johnson, *Systems of frequency curves generated by methods of translation*, Biometrika **36** (1949) 149.

[165] LHCb collaboration, *Prompt charm production in pp collisions at $\sqrt{s} = 7$ TeV*, Nucl. Phys. **B871** (2013) 1, `arXiv:1302.2864`.

[166] I. Belyaev *et al.*, *Handling of the generation of primary events in Gauss, the LHCb simulation framework*, J. Phys. Conf. Ser. **331** (2011) 032047.

[167] D. J. Lange, *The EvtGen particle decay simulation package*, Nucl. Instrum. Meth. **A462** (2001) 152.

[168] P. Golonka and Z. Was, *PHOTOS Monte Carlo: A precision tool for QED corrections in Z and W decays*, Eur. Phys. J. **C45** (2006) 97, `arXiv:hep-ph/0506026`.

[169] Geant4 collaboration, *Geant4 developments and applications*, IEEE Trans. Nucl. Sci. **53** (2006) 270; Geant4 collaboration, *Geant4: A simulation toolkit*, Nucl. Instrum. Meth. **A506** (2003) 250.

[170] M. Clemencic *et al.*, *The LHCb simulation application, Gauss: Design, evolution and experience*, J. Phys. Conf. Ser. **331** (2011) 032023.

[171] LHCb collaboration, *Measurement of the $B^{\pm}$ production cross-section in pp collisions at $\sqrt{s} = 7$ and 13 TeV*, JHEP **12** (2017) 026, `arXiv:1710.04921`.

[172] A. Rogozhnikov, *Reweighting with Boosted Decision Trees*, J. Phys. Conf. Ser. **762** (2016) 012036, `arXiv:1608.05806`, `https://github.com/arogozhnikov/hep_ml`.

[173] L. Dufour and J. Van Tilburg, *Decomposition of simulated detection asymmetries in LHCb*, LHCb-INT-2018-006, document accessible only by the members of the LHCb collaboration.

[174] P. Marino and M. J. Morello, *Measurement of the CP violation parameter A_Γ in $D^0 \to K^+K^-$ and $D^0 \to \pi^+\pi^-$ decays*, CERN-THESIS-2017-007.

[175] LHCb collaboration, *Measurements of charm mixing and CP violation using $D^0 \to K^\pm\pi^\mp$ decays*, Phys. Rev. **D95** (2017) 052004, Erratum ibid. **D96** (2017) 099907, `arXiv:1611.06143`.

[176] G. A. Cowan, D. C. Craik, and M. D. Needham, *RapidSim: an application for the fast simulation of heavy-quark hadron decays*, Comput. Phys. Commun. **214** (2017) 239, `arXiv:1612.07489`.

[177] M. Cacciari, M. Greco, and P. Nason, *The p_T spectrum in heavy-flavour hadroproduction*, JHEP **05** (1998) 007, `arXiv:hep-ph/9803400`.

[178] L. Anderlini *et al.*, *The PIDCalib package*, LHCb-PUB-2016-021, 2016.

[179] T. Skwarnicki, *A study of the radiative cascade transitions between the Upsilon-prime and Upsilon resonances*, PhD thesis, Institute of Nuclear Physics, Krakow, 1986, DESY-F31-86-02.

[180] L. Lyons, D. Gibaut, and P. Clifford, *How to combine correlated estimates of a single physical quantity*, Nucl. Instrum. Meth. **A270** (1988) 110.

[181] R. Nisius, *BLUE: combining correlated estimates of physics observables within ROOT using the Best Linear Unbiased Estimate method*, SoftwareX **11** (2020) 100468, `arXiv:2001.10310`.

[182] Belle-II collaboration, *The Belle II Physics Book*, PTEP **2019** (2019) 123C01, `arXiv:1808.10567`, pp. 379–388, [Erratum: PTEP 2020, 029201 (2020)].

[183] LHCb collaboration, *Framework TDR for the LHCb Upgrade: Technical Design Report*, CERN-LHCC-2012-007, 2012.

[184] LHCb collaboration, *LHCb Trigger and Online Upgrade Technical Design Report*, CERN-LHCC-2014-016, 2014.

[185] LHCb collaboration, *Expression of Interest for a Phase-II LHCb Upgrade: Opportunities in flavour physics, and beyond, in the HL-LHC era*, CERN-LHCC-2017-003, 2017.

[186] LHCb collaboration, *Physics case for an LHCb Upgrade II — Opportunities in flavour physics, and beyond, in the HL-LHC era*, `arXiv:1808.08865`.

[187] T. Pajero and M. J. Morello, *Implications of the contribution of doubly Cabibbo-suppressed decays to right-sign $D^0 \to K^-\pi^+$ decays*, In preparation.

[188] LHCb collaboration, *Measurement of the CKM angle γ from a combination of LHCb results*, JHEP **12** (2016) 087, `arXiv:1611.03076`.

[189] M. Kenzie *et al.*, *GammaCombo: A statistical analysis framework for combining measurements, fitting datasets and producing confidence intervals*, doi: 10.5281/zenodo.3371421.

[190] Belle collaboration, *Measurement of y_{CP} in D^0 meson decays to the $K^0_S K^+ K^-$ final state*, Phys. Rev. D **80** (2009) 052006, `arXiv:0905.4185`.

[191] BESIII collaboration, *Measurement of y_{CP} in $D^0 - \overline{D}^0$ oscillation using quantum correlations in $e^+e^- \to D^0\overline{D}^0$ at $\sqrt{s} = 3.773\,GeV$*, Phys. Lett. B **744** (2015) 339, `arXiv:1501.01378`.

[192] Belle collaboration, *Measurement of the charm-mixing parameter y_{CP} in $D^0 \to K^0_S\omega$ decays at Belle*, Phys. Rev. D **102** (2020) 071102, `arXiv:1912.10912`.

[193] E791 collaboration, *Search for $D^0 - \overline{D}^0$ mixing in semileptonic decay modes*, Phys. Rev. Lett. **77** (1996) 2384, `arXiv:hep-ex/9606016`.

[194] CLEO collaboration, *Limits on neutral D mixing in semileptonic decays*, Phys. Rev. D **71** (2005) 077101, `arXiv:hep-ex/0502012`.

[195] BaBar collaboration, *Search for $D^0 - \bar{D}^0$ mixing using semileptonic decay modes*, Phys. Rev. D **70** (2004) 091102, `arXiv:hep-ex/0408066`.

[196] BaBar collaboration, *Search for $D^0 - \overline{D}^0$ mixing using doubly flavor tagged semileptonic decay modes*, Phys. Rev. D **76** (2007) 014018, `arXiv:0705.0704`.

[197] Belle collaboration, *Improved search for D^0–$\bar{D}^0$ mixing using semileptonic decays at Belle*, Phys. Rev. D **77** (2008) 112003, `arXiv:0802.2952`.

[198] BaBar collaboration, *Measurement of the neutral D meson mixing parameters in a time-dependent amplitude analysis of the $D^0 \to \pi^+\pi^-\pi^0$ decay*, Phys. Rev. D **93** (2016) 112014, `arXiv:1604.00857`.

[199] M. Ciuchini *et al.*, *D–$\bar{D}$ mixing and new physics: General considerations and constraints on the MSSM*, Phys. Lett. **B655** (2007) 162, `arXiv:hep-ph/0703204`.

[200] M. De Cian, S. Farry, P. Seyfert, and S. Stahl, *Fast neural-net based fake track rejection in the LHCb reconstruction*, LHCb-PUB-2017-011, 2017.

[201] R. Aaij *et al.*, *Selection and processing of calibration samples to measure the particle identification performance of the LHCb experiment in Run 2*, Eur. Phys. J. Tech. Instr. **6** (2018) 1, `arXiv:1803.00824`.